Exploring active site structural dynamics in NiFe-hydrogenases with ultrafast pump-probe and two-dimensional infrared spectroscopy

Solomon Wrathall

Doctor of Philosophy

University of York

Chemistry

September 2022

Contents

Acknowledgements

Firstly, I would like to thank my PhD supervisors, Neil Hunt and Alison Parkin, for their unwavering patience, kindness and support. Specific thanks are owed to Barbara Procacci and Marius Horch, whose enthusiasm and good humour were a particular tonic in stressed times. I would also like to thank my colleagues, Chris Furlan, Pete Howe and Tom Ward, the technical staff at York University, Julia Walton, Danny Shaw, Stuart Murray, Chris Rhodes and Mark Roper, and the technical staff at the Rutherford Appleton Laboratory, Greg Greetham and Paul Donaldson. Without their support and insight this project would not have been possible.

Declaration

I declare that this thesis is a presentation of original work and I am the sole author. This work has not previously been presented for an award at this, or any other, University. All sources are acknowledged as References.

1 Abstract

NiFe hydrogenases are promising candidates for sustainable energy approaches using H_2 as a clean fuel. Comparison with the rare earth metal containing H_2-conversion catalysts that are used industrially highlights a number of distinct advantages in the use of NiFe hydrogenases or hydrogenase-inspired catalysts. They are able to catalyse H_2-conversion with high turnover frequencies while containing only base metals, they tolerate a greater variety of conditions and don't require the use of fossil fuel derived feedstocks. However, implementation of hydrogenase-based catalysts is hampered by the incomplete understanding of some of the aspects of its catalysis. While a general outline for its catalytic mechanism has been established, the specific determinants for efficient H_2-cleavage and H^+-reduction remain vague. NiFe hydrogenases with different activity profiles, physiological functions and parent organisms all display a highly conserved active site environment yet the way in which the active site chemistry is modulated by the surrounding protein architecture is poorly understood. The importance of understanding this modulation is demonstrated by the small molecule hydrogenase-inspired catalysts that do exhibit efficient H_2-conversion invariably featuring either a significant second coordination sphere, or are cofactors implanted within a protein matrix.

The carbonyl and cyanide ligands present in the NiFe hydrogenase active site are ideal probes for IR experiments, indeed vibrational spectroscopy has been used extensively to identify and monitor the interconversion of redox structural states formed by NiFe hydrogenases. Conventional IR approaches use the fundamental frequencies of the carbonyl and the two cyanide stretching modes (ν_{CO}, ν_{CN1} and ν_{CN2}, respectively) as fingerprints to identify specific redox states.

When evaluated in isolation these frequencies can provide only limited catalytically relevant insight as they are subject to a variety of structural and electronic factors including the ligands present in the particular active site state, H-bonding and long range electrostatic interactions with the protein matrix. The interpretation of ν_{CO} and ν_{CN} mode frequencies is hampered by uncertainty in the anharmonicities along the CO and CN stretching coordinates, in addition to the precise composition of their associated normal modes. While the ν_{CN1} mode is generally acknowledged to have greater symmetric stretching character and the ν_{CN2} mode to have greater asymmetric stretching character, a thorough understanding of their potential energy surfaces (contributions from each cyanide ligand) has yet to be established. This situation is further complicated by the highly localised nature of the ν_{CO} and ν_{CN} modes to their respective bond coordinates, which results in their stretching frequencies being insensitive to isotopic substitution of adjacent atoms, which would otherwise provide useful information relating to the molecular composition proximal to the [NiFe] site. Here, ultrafast pump-probe and 2D-IR spectroscopy are used to characterise the ν_{CO} and ν_{CN} modes of the regulatory hydrogenase from *Ralstonia eutropha*, the membrane bound hydrogenase (Hyd-1) from *Escherichia coli* and the Fe-site mimic $K[CpFe(CO)(CN)_2]$. A number of previously unexplored spectroscopic parameters are evaluated and a high degree of similarity is observed between different redox states and enzymes, implying an evolutionarily selected active site environment. Via comparison of these observables with those from the Fe-site mimic dissolved in a variety of solvents, some parameters can be ascribed to intrinsic properties of the active site $Fe(CO)(CN)_2$ moiety, whilst others are indicative of the protein scaffold forming a highly specialized environment that tightly controls the structure of the active site. This situation is similar to that observed in both native [FeFe]-hydrogenase and in active site mimics, for which

the spectroscopy of the isolated active site is distinctly different to that of the active site implanted within the protein matrix.

2 Introduction and theory

2.1 Hydrogen as a sustainable fuel

The combustion of H_2 releases a very large amount of energy without any long-lived intrinsic greenhouse gas emissions, as such H_2 has been heralded as a fuel of the future from as early as 1874 in the writings of Jules Verne.[1]

$$H_2 + \tfrac{1}{2}O_2 \rightarrow H_2O \qquad \textbf{(1)}$$

$$\Delta G^o = -237\ kJ\ mol^{-1}$$

However, the ostensibly simple reaction by which H_2 is split into protons and electrons is complicated by the H-H bond being remarkably strong and non-polar,[2] activating H_2 thus requires a suitable catalyst. Platinum electrodes have typically been used for this purpose, however, Pt is expensive, resource limited and energy intensive to mine.[3] A number of nickel containing catalysts are also used for H_2-conversion and while Ni is cheaper and more abundant than Pt, these catalysts are significantly less efficient than their noble metal containing counterparts.[4] Pt-based H_2 conversion catalysts are also subject to irreversible poisoning by trace impurities such as CO and H_2S necessitating the use of high-purity feedstock which exacerbates the environmental toll of such an approach.[3,4] It is apparent that the development of cheaper and more sustainable H_2-conversion catalysts would be broadly beneficial.

2.2 Hydrogenases

Hydrogenases are the hydrogen converting enzymes that have been produced by microorganisms to enable the use of H_2 as a fuel since the early stages of life on earth.[5] There are three phylogenetically unrelated categories of hydrogenases that are designated according to the metal content of their active

sites: NiFe-,[6,7] FeFe-[8,9] and Fe-hydrogenases.[10] This project is focussed on the study of NiFe-hydrogenases.

Most FeFe- and NiFe-hydrogenases catalyse both the reduction of protons to H_2 (**Equation (*2*)**) and also the oxidation of H_2 to protons and electrons (**Equation (3)**).[11] Remarkably, some hydrogenases have been shown to convert hydrogen at rates approaching, and in some cases even exceeding, those reported for their

$$2H^+ + 2e^- \rightarrow H_2 \qquad \textbf{(2)}$$

$$H_2 \rightarrow 2H^+ + 2e^- \qquad \textbf{(3)}$$

synthetic Pt-containing counterparts (measured electrochemically).[12] Notably, these enzymes do not contain any rare earth metals and are tolerant of more diverse conditions than Pt-containing catalysts, with some able to maintain and/or recover activity following exposure to inhibitory H_2S, CO and O_2.

2.2.1 Physiological context

The NiFe-hydrogenases can be categorised into four groups according to their functions and cellular contexts.[5,13]

Group 1 – Membrane-bound H_2-uptake enzymes

Typically located on the periplasmic side of the membrane, these enzymes are generally coupled to additional electron transfer and/or transmembrane proteins (**Figure 1** and **Figure 2**).[11]

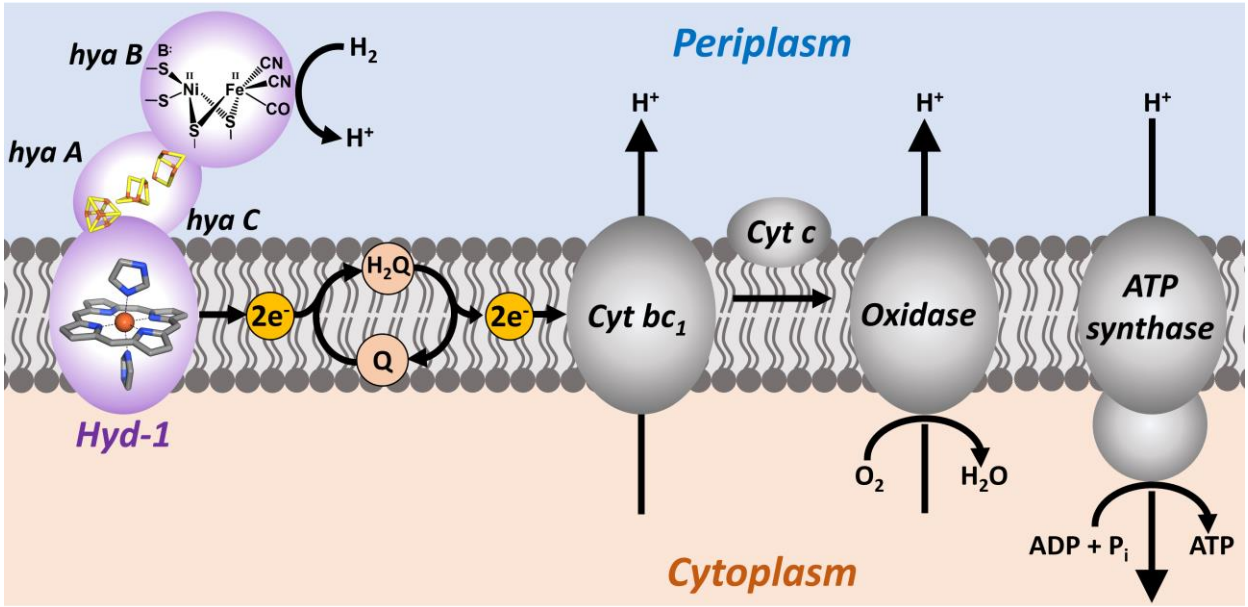

Figure 1. *Schematic diagram showing how EcHyd-1, an O_2-tolerant group 1 [NiFe]-hydrogenase, couples H_2-oxidation to aerobic respiration via the quinone (Q/H_2Q) pool.*

Group 2 – Cytosolic H_2-uptake and sensory enzymes

These enzymes fulfil varying and some partially unknown functions,[13] with notable examples including the cyanobacterial uptake hydrogenases that catalyse the oxidation of H_2 produced by processes including photosynthesis and N_2-fixation, and H_2-sensing enzymes that exhibit low H_2-oxidation activity but function to regulate expression of more catalytically active hydrogenases.[13]

Group 3 – Cytosolic bidirectional enzymes

These enzymes typically exist as large multisubunit assemblies that resemble respiratory complex I.[5] Most group 3 hydrogenases are soluble, but some are associated with the cytosolic or thylakoid membranes.[5] Generally, these enzymes couple the oxidation of H_2 to the reduction of respiratory cofactors including NAD^+, $NADP^+$, F_{420}.[5,13] They are termed bidirectional as they are also able to perform the reverse reaction, coupling cofactor oxidation to H_2-

production, under physiological conditions.[14] The cellular functions performed by group 3 hydrogenases are diverse and depend upon the enzyme, host organism and its current metabolic state. H_2 production could act as a sink for disposal of excess electrons produced by fermentation or photosynthesis, whereas H_2-oxidation can serve as a source of energy and reducing equivalents (e.g., NADH, NADPH).

Group 4 – Membrane-bound H_2-evolving enzymes

These enzymes are large multisubunit assemblies typically comprising six or more subunits.[11] Group 4 hydrogenases bear some similarities with their group 1 counterparts, they are both membrane bound and involved in energy conversion. However, group 4 enzymes are localised on the cytoplasmic (rather than periplasmic) side of the membrane and do not use H_2 as an electron source, instead coupling the oxidation of low-potential one-carbon containing molecules (such as carbon monoxide or formate) to H_2-production (via $CO + H_2O \rightarrow CO_2 + 2H^+ + 2e^-$ and $HCOO^- \rightarrow CO_2 + H^+ + 2e^-$).[5,11]

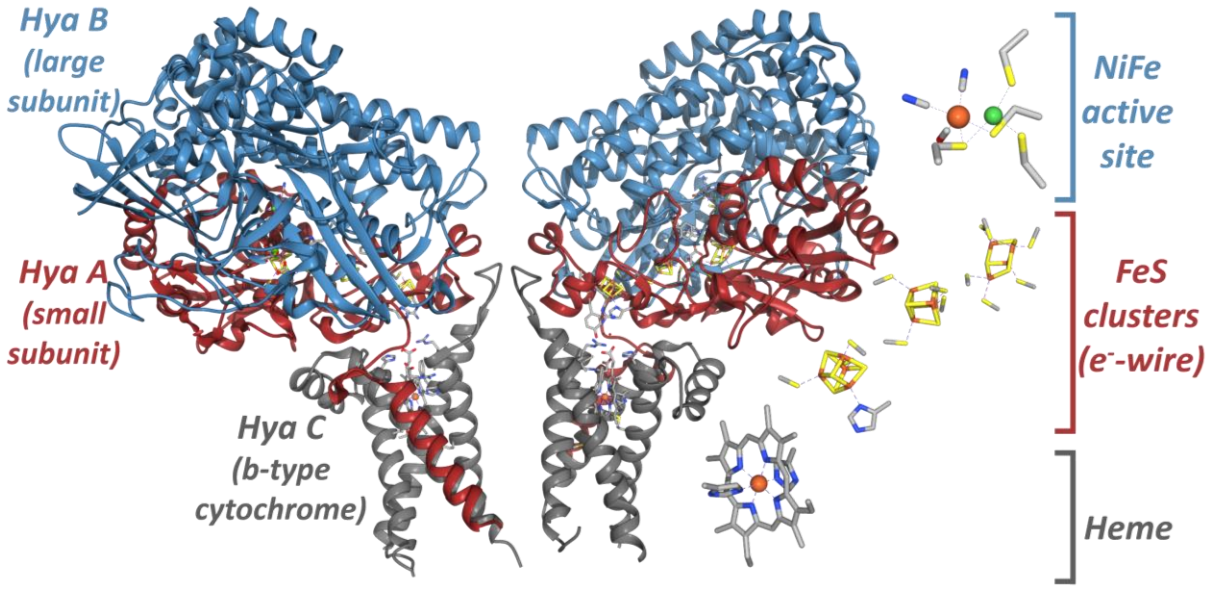

Figure 2. *(Left) Ribbon diagram for the EcHyd-1 dimer (PDB: 6FPO[15]) and (right) ball-and-stick schematics of the key cofactors ligated by each subunit.*

NiFe hydrogenases can be further separated into two categories according to their interaction with oxygen. Hydrogenases that maintain some level of activity in the presence of O_2, and quickly return to pre-exposure levels of activity when the O_2 is removed, are termed O_2-tolerant hydrogenases.[11,16] In the literature, prominent examples of O_2-tolerant NiFe-hydrogenases include: *Escherichia coli* Hydrogenase-1 (*Ec*Hyd-1[17,18]), *Aquifex aeolicus* Hydrogenase-I (*Aa*Hase-I[19,20]), *Ralstonia eutropha* membrane bound hydrogenase (*Re*MBH[16]), regulatory hydrogenase (*Re*RH[21]) and soluble hydrogenase (*Re*SH[22,23]). For O_2-sensitive hydrogenases their activity is completely abrogated by O_2-exposure and following the removal of O_2 they reactivate slowly if at all (however certain hydrogenases will reactivate upon application of a reducing potential).[11,16] Prominent examples of O_2-sensitive hydrogenases include: *Desulfovibrio vulgaris* Miyazaki F (*Dv*MF[16]), *Desulfovibrio gigas* hydrogenase (*Dg*H[16,24]), *Allochromatium vinosum* membrane bound hydrogenase (*Av*MBH[16]) and *E. coli* Hydrogenase-2 (*Ec*Hyd-2[25]).

2.2.2 Structural features of MBH

The minimal functional unit of a NiFe-hydrogenase comprises a heterodimer of so-called 'large' and 'small' subunits, with masses of typically ~65 and ~30 kDa, repectively.[5,11] The large subunit coordinates the bimetallic NiFe active site, and the small subunit harbours an electron relay that is composed of FeS clusters.[5,11] There also exists several proton transfer pathways and hydrophobic gas channels that connect the deeply buried NiFe active site to the protein surface.[5,11]

The NiFe active site

The NiFe active site features a ferrous iron ion and a nickel ion with an oxidation state that varies with the catalytic substate of the enzyme (between Ni^{I}, Ni^{II}, and Ni^{III}).[11,17,26,27] These metal ions are coordinated by seven strictly conserved ligands; one carbon monoxide (CO), two cyanide (CN^-) and four cysteine thiolate ligands ($Cys\text{-}S^-$). Two of the cysteine thiolates terminally coordinate the Ni ion, and the remaining two are present in positions that bridge the metal ions. The Fe ion is further coordinated by CO and the pair of CN^- ligands. A third bridging position is also present, although the ligand that occupies this position varies with the catalytic substate of the enzyme, in some states it is vacant, whilst in others it is occupied by an OH^- or H^- ligand. The coordination geometry for the metal ions

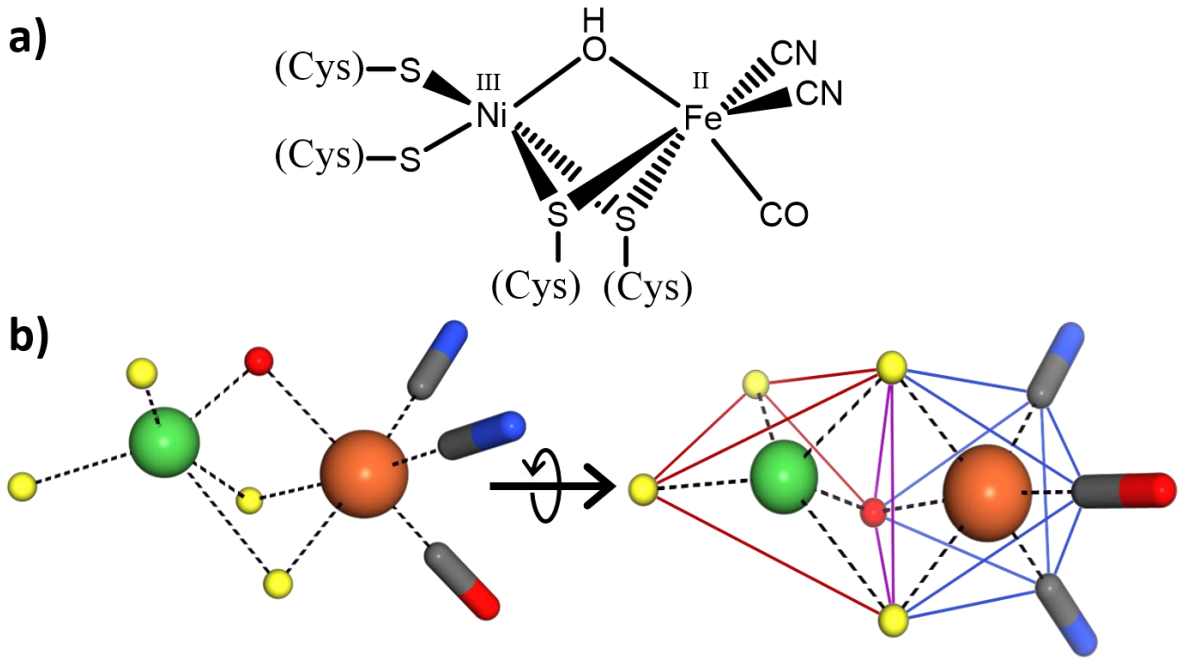

Figure 3 (a) *Skeletal structure of the NiFe cluster.* ***(b)*** *<u>Ec</u>Hyd-1 crystal structure data (PDB: 6FPO[15]) showing the showing the geometry around the active site Ni- and Fe-ions, shown as balls and sticks coloured by heteroatom.*

of a NiFe hydrogenase with an occupied third bridging site can be seen in **Figure 3**, these are distorted square-based pyramidal for the Ni-ion and octahedral for the Fe-ion (**Figure 3(b)**). For an active site state with a vacant third bridging site (**Figure 4(b)** and **Figure 9**) the geometries are see-saw shaped and square pyramidal for Ni- and Fe-ions, respectively.

The active site environment of the bimetallic cluster is highly conserved, both among NiFe-hydrogenases of different classes and from different organisms. This can be seen below in **Figure 4** which compares the binding pocket of five hydrogenases of three classes from four different organisms.

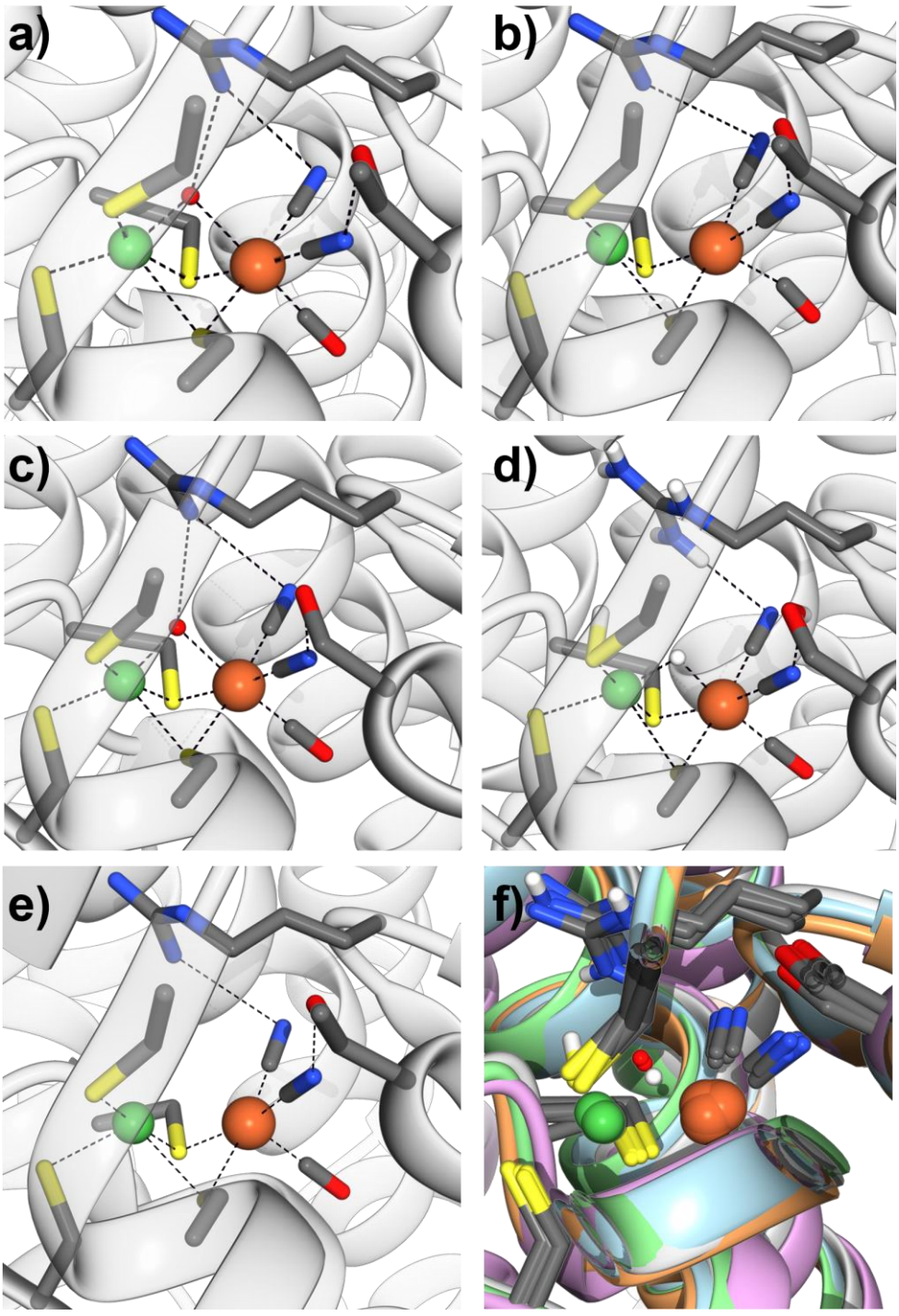

Figure 4 *Crystal structure data showing the active site environment of the NiFe hydrogenases:* ***(a)*** *oxidised EcHyd-1 (PDB: 6FPO[15]),* ***(b)*** *reduced ReMBH (PDB: 7ODG[28]),* ***(c)*** *oxidised EcHyd-2 (PDB: 6EHQ[29]),* ***(d)*** *reduced DvMF (PDB: 4U9I[30]),* ***(e)*** *as-isolated M. marburgensis F_{420}-reducing hydrogenase (PDB: 4OMF[37]) and* ***(f)*** *an overlay. Selected side chains/groups are shown in ball and stick form, coloured by heteroatom (blue = N, red = O, yellow = S, green = Ni and orange = Fe).*

The active site environment is largely hydrophobic, with crystal structures indicating that no water molecules are present within H-bonding range of the active site ligands (not counting the H_2O present in the variable third bridging position of some active site states, **Figure 4(a)**, **(b)** and **Figure 9**).[15,28–30]

Iron-sulfur (FeS) clusters

The small protein subunit of NiFe-hydrogenases commonly ligates three FeS cluster cofactors which form a relay to shuttle electrons between the NiFe active site and the surface of the small subunit, thus providing a means by which the hydrogenase minimal functional unit can electrochemically interface with auxiliary electron transfer protein subunits. Some examples of redox active auxiliary subunits found in NiFe hydrogenases include: cytochrome in membrane bound hydrogenases (*Re*MBH,[31] *Ec*Hyd-1,[32] *Av*MBH,[33] etc), histidine kinase in *Re*RH,[34] NAD^+-reductase in *Re*SH,[35] coenzyme-F_{420} reductase in soluble hydrogenases of *Methanosarcina barkeri* (*Mb*SH)[36] and *Methanothermobacter marburgensis* (*Mm*SH),[37] NADPH-oxidase in *Pyrococcus furiosus* soluble hydrogenase (*Pf*SH),[38] formate dehydrogenase in *Ec*Hyd-3.[39] The FeS clusters in the small subunit are regularly interspaced and close together (~ 8-12 Å) to facilitate the efficient transfer of electrons (**Figure 5**). The FeS clusters are designated proximal, medial and distal according to their proximity to the NiFe active site (**Figure 5**). At a pH of 7.0 the oxidation of H_2 can occur at any potential higher than that of the H_2/H^+ couple (-413 mV), likewise the reduction of H^+ to H_2 should occur at more negative potentials than that of the H_2/H^+ couple. The potential of the FeS clusters of group 1 (i.e., H_2-uptake membrane bound) NiFe hydrogenases are all more positive than -413 mV,[40] and their potentials are even higher for O_2-tolerant group 1 hydrogenases.[41,42] The potentials of the FeS clusters relative to that of the H_2/H^+ couple likely contributes towards the

catalytic bias of a particular hydrogenase towards oxidation or evolution of H_2.[17,18,20]

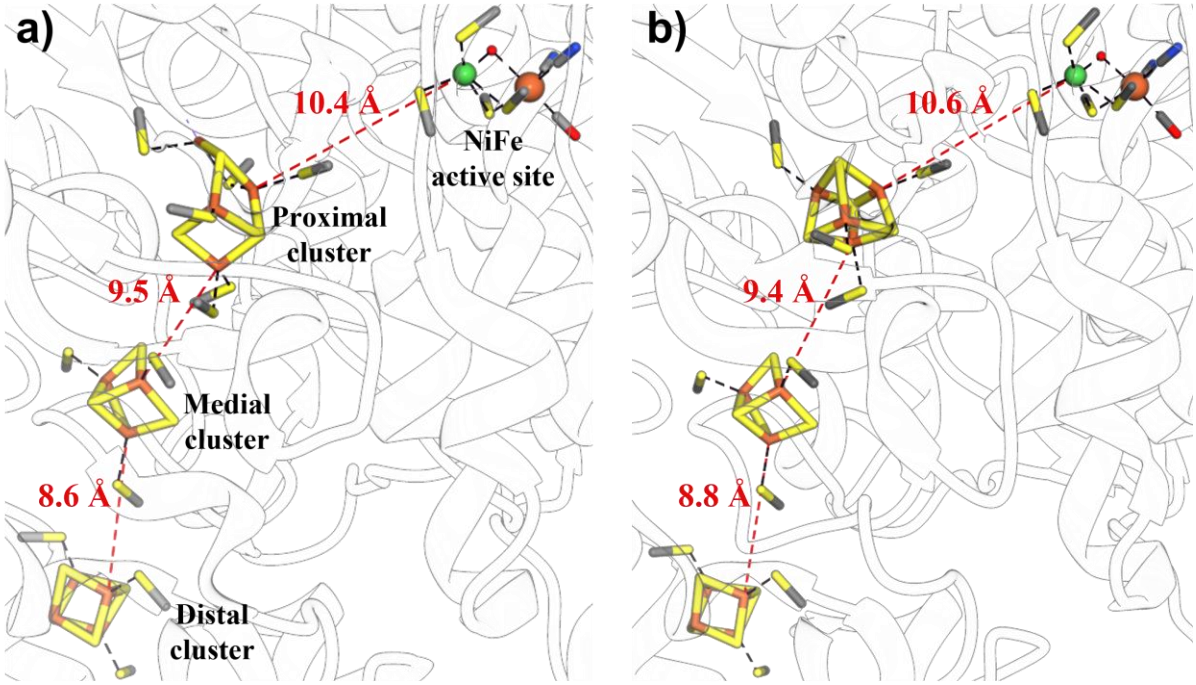

Figure 5 *Crystal structure data showing the electron relay formed by the FeS clusters and the NiFe active site for* ***(a)*** *EcHyd-1 (PDB: 6FPO[15]) and* ***(b)*** *EcHyd-2 (PDB: 6EHQ[29]). The protein is shown as transparent white ribbon with selected groups in ball and stick form, coloured by heteroatom.*

The proximal, medial and distal FeS clusters can differ in the number of constituent Fe and S atoms in addition to the number of coordinating cysteine thiolate ligands, the differences are outlined below in **Table 1**.

Table 1 Comparing the composition and reduction potentials of FeS-clusters in O_2-tolerant and O_2-sensitive hydrogenases. Listed potentials refer to the midpoint reduction potentials for the $[FeS]^{4+/3+}$ (and $[FeS]^{5+/4+}$) transitions of the proximal cluster and the $[FeS]^{+/0}$ transition of the medial cluster, determined for the wild type (O_2-tolerant) and C19G mutant (O_2-sensitive) of *Ec*Hyd-1.[42,48]

Hydrogenase type	**Cluster**	**FeS composition**	**Number of cysteine ligands**	**Potential / mV vs SHE**
O_2-tolerant	Proximal	4Fe3S	6	30 (230)
	Medial	3Fe4S	3	190
	Distal	4Fe4S	3	
O_2-sensitive	Proximal	4Fe4S	4	240
	Medial	3Fe4S	3	160
	Distal	4Fe4S	3	

The proximal cluster of O_2-sensitive hydrogenases is a standard 4Fe4S cluster coordinated by four cysteine ligands, whereas O_2-tolerant hydrogenases have a unique proximal 4Fe3S cluster with six cysteine ligands,[18,43–47] this is shown below in **Figure 6**.

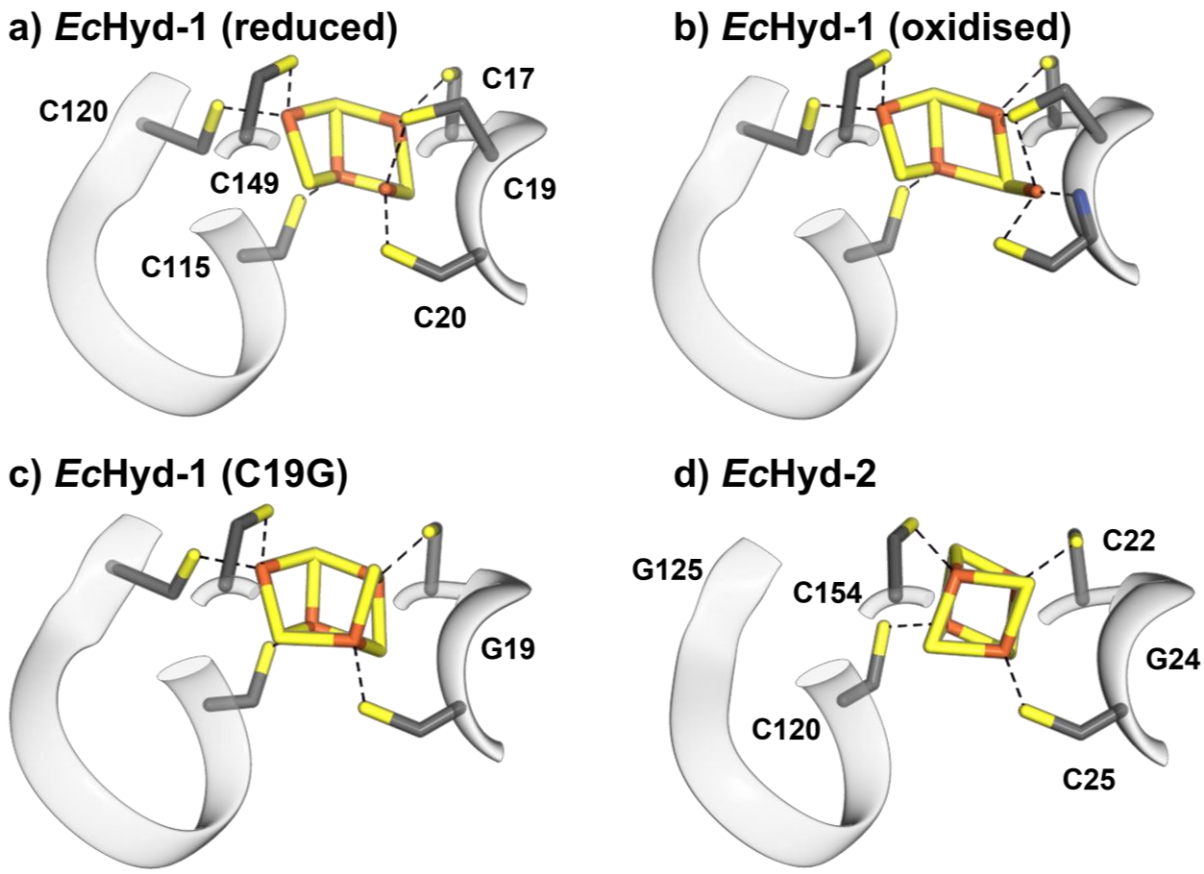

Figure 6 *Crystal structure data comparing the proximal FeS clusters of the O_2-tolerant EcHyd-1 in its* ***(a)*** *reduced and* ***(b)*** *superoxidised states with that of the O_2-sensitive* ***(c)*** *C19G mutant of EcHyd-1 and* ***(d)*** *native EcHyd-2 (PDB: 6FPW, 6FPO, 6G94 and 6EN9, respectively).*[15,29,48]

The unusual proximal clusters of O_2-tolerant hydrogenases are able to form an additional 'superoxidised' redox state that is one electron more oxidised than that formed by the proximal clusters of O_2-sensitive hydrogenases.[15] The release of this additional electron ensures that O_2-tolerant hydrogenases are able to rapidly reactivate following exposure to inhibitory O_2 (**Figure 9**).[15] Crystal structure data (**Figure 6(a)** and **(b)**) shows that this over-oxidation of the proximal cluster is accompanied by a structural transition in which the cluster opens up, one of the Fe atoms rotates and is ligated by the main chain N atom of Cys20 (**Figure 6(b)**).[15]

The additional cysteine residues that coordinate the proximal cluster have been shown to be crucial factors in determining whether a NiFe hydrogenase can support this structural transition when exposed to O_2.[15,44] The *Ec*Hyd-1 mutant C19G (**Figure 6(c)**) demonstrated O_2-sensitivity similar to that observed in *Ec*Hyd-2, whereas *Ec*Hyd-1 mutant C120G had minimal reduction in O_2-tolerance,[18] which is likely a consequence of the C19G mutation causing the proximal 4Fe3S cluster to be replaced with a 4Fe4S cluster,[48] like that present in *Ec*Hyd-2. It was hypothesised that the *Ec*Hyd-2 mutant G24C would have enhanced O_2-tolerance, however both G24C and G125C mutations rendered the protein unstable.[18]

The medial FeS cluster is also implicated in the mechanism by which inhibitory O_2 is removed from the active site of NiFe hydrogenases. While over-oxidation of the proximal cluster of O_2-tolerant hydrogenases provides two electrons, the final electron is likely supplied by the medial FeS cluster.[42,49]

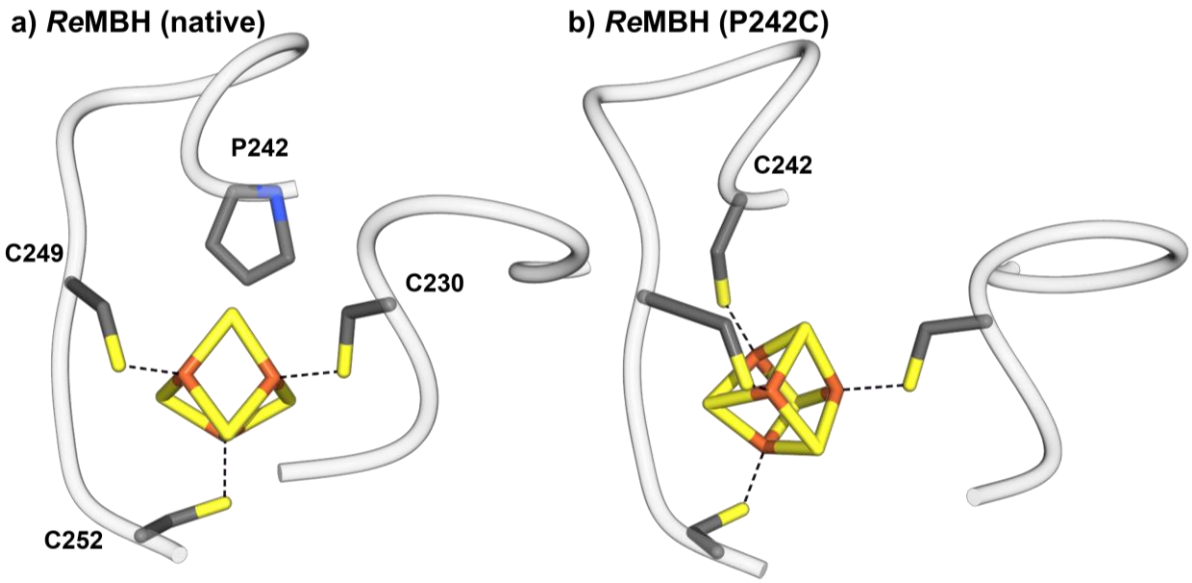

Figure 7 *Crystal structure data comparing the medial FeS clusters of* ***(a)*** *native ReMBH (PDB: 5MDK)*[50]*, and* ***(b)*** *ReMBH mutant P242C (PDB: 7ODH).*[28]

In both O_2-tolerant and O_2–sensitive hydrogenases the medial cluster is a 3Fe4S cluster coordinated by three cysteine residues (**Table 1**). Introduction of an additional coordinating cysteine residue at the medial cluster, via the P242C mutation, has been shown to increase the O_2 sensitivity of the O_2-tolerant hydrogenases *Ec*Hyd-1 and *Re*MBH. Crystal structure data shows that this mutation causes the hydrogenase to incorporate a 4Fe4S cluster rather than the normal 3Fe4S cluster (**Figure 7**), which likely causes enhanced O_2-sensitivity by lowering the potential of the medial cluster, which in turn results in it losing electrons to the distal cluster too readily to act as a reservoir for reduction of the proximal cluster.[28,51]

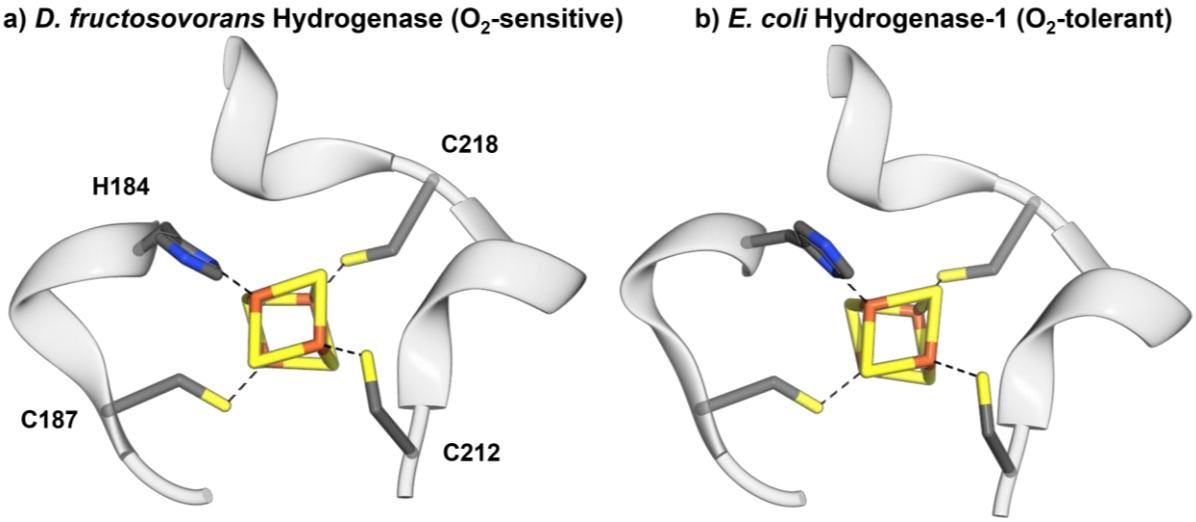

Figure 8 *Crystal structure data comparing the distal FeS clusters of* ***(a)*** *D. fructosovorans Hydrogenase (PDB: 1YRQ[52]) and,* ***(b)*** *EcHydrogenase-1 (PDB: 6FPO[15]).*

The distal FeS cluster is located furthest from the NiFe active site and forms the final part of the electron transfer chain, interfacing with the hydrogenase's physiological partner (e.g. cytochrome in *Ec*Hyd-1) or solvent molecules in the case of the hydrogenase minimal functional unit (i.e., heterodimer of large and small subunits). The structure of the distal FeS cluster is highly conserved (**Figure 8**) among O_2-tolerant and O_2-sensitive hydrogenases, it features a cubane 4Fe4S

cluster coordinated by three cysteine ligands and a histidine. The distal cluster is thought to control the catalytic bidirectionality of hydrogenases via its role as the 'gateway' cluster.[53] For instance, *Ec*Hyd-1 exhibits considerable H_2-evolution activity at low pH but negligible H_2-evolution at physiological pH, this has been attributed to the distal cluster having a pH-independent potential while the potential of the H^+/H_2 couple is highly pH dependent, so below a certain pH the transfer of electrons from distal cluster towards the NiFe active site becomes favourable.[53–56] The role of the distal cluster in determining the catalytic directionality has been highlighted by a study on the O_2-sensitive bidirectional hydrogenase from *Desulfovibrio fructosovorans* in which mutation of the coordinating histidine residue (H184 in **Figure 8(a)**) to glycine or cysteine resulted in a substantial drop in H_2-evolution activity (to 75% and 45% of that of WT, respectively), and an even larger decrease in H_2-oxidation activity (to 3% and 2%, respectively).[57] The activity of the variants was observed to recover in the presence of imidazole. The authors attribute the slower electron transfer observed in these variants to unfavourable contributions to electronic coupling and reorganisation energy, rather than substantial changes in the potential of the distal cluster.[57]

2.2.3 Catalytic cycle

NiFe hydrogenases transition through a number of active site states, the putative structures of these states are shown below in **Figure 9**. These states can be separated into two categories, i) "on-cycle" states formed during catalytic activity (whether H_2-oxidation or production), and ii) catalytically inactive "off-cycle" states formed following exposure of the active site to inhibitory O_2.[11]

State dependent variation in the structure of the NiFe centre includes changes to the Ni-ion oxidation state, the presence/identity of the ligand in the third bridging site, the protonation state of the terminal cysteine thiolate ligands and the sulphoxygenation state of the bridging cysteine thiolate ligands.[11,26,58,59]

Macroscopically the off-cycle states differ in whether they are slow or fast to reactivate. The generally accepted naming convention for active site states of NiFe hydrogenases follows the form Ni_x-Y_z. The subscript *'x'* denotes the catalytic competence of the state, with Ni_a states being catalytically *active* (sunburst colours in **Figure 9**), the Ni_r *ready* states are catalytically inactive but fast to reactivate (light blue in **Figure 9**) and the Ni_u *unready* states are inactive and slow to reactivate (dark blue and purple in **Figure 9**).[11,60] The *'Y'* designation of Ni_x-Y_z is largely historical, with the Ni_x-A, -B and -C following the original assignment of these states when they were first detected using EPR spectroscopy.[51–53] The L of Ni_a-L derives from this state first being observed in samples under intense illumination. The S of Ni_r-S, Ni_a-S and Ni_a-SR shows that these states are EPR silent, and the R indicates that Ni_a-SR is reduced. The subscript *'z'* designation of Ni_x-Y_z is used to distinguish substates that are very closely related, two substates of Ni_r-S have been identified (Ni_r-S_I and Ni_r-S_{II}), and three for Ni_a-L (Ni_a-$L_{I \rightarrow III}$) and Ni_a-SR (Ni_a-$SR_{I \rightarrow III}$). Ni_r-S_I and Ni_r-S_{II} states are thought to differ in terms of the protonation state of the third bridging ligand. The precise structural differences between Ni_a-$L_{I \rightarrow III}$ and Ni_a-$SR_{I \rightarrow III}$ states (respectively) have not been elucidated, however due to their very similar IR signatures it is believed that these states may differ in terms of protonation of terminal cysteines, rotation of terminal cysteines or the orientation of nearby H-bonding side chains. [11,26,27,58–60]

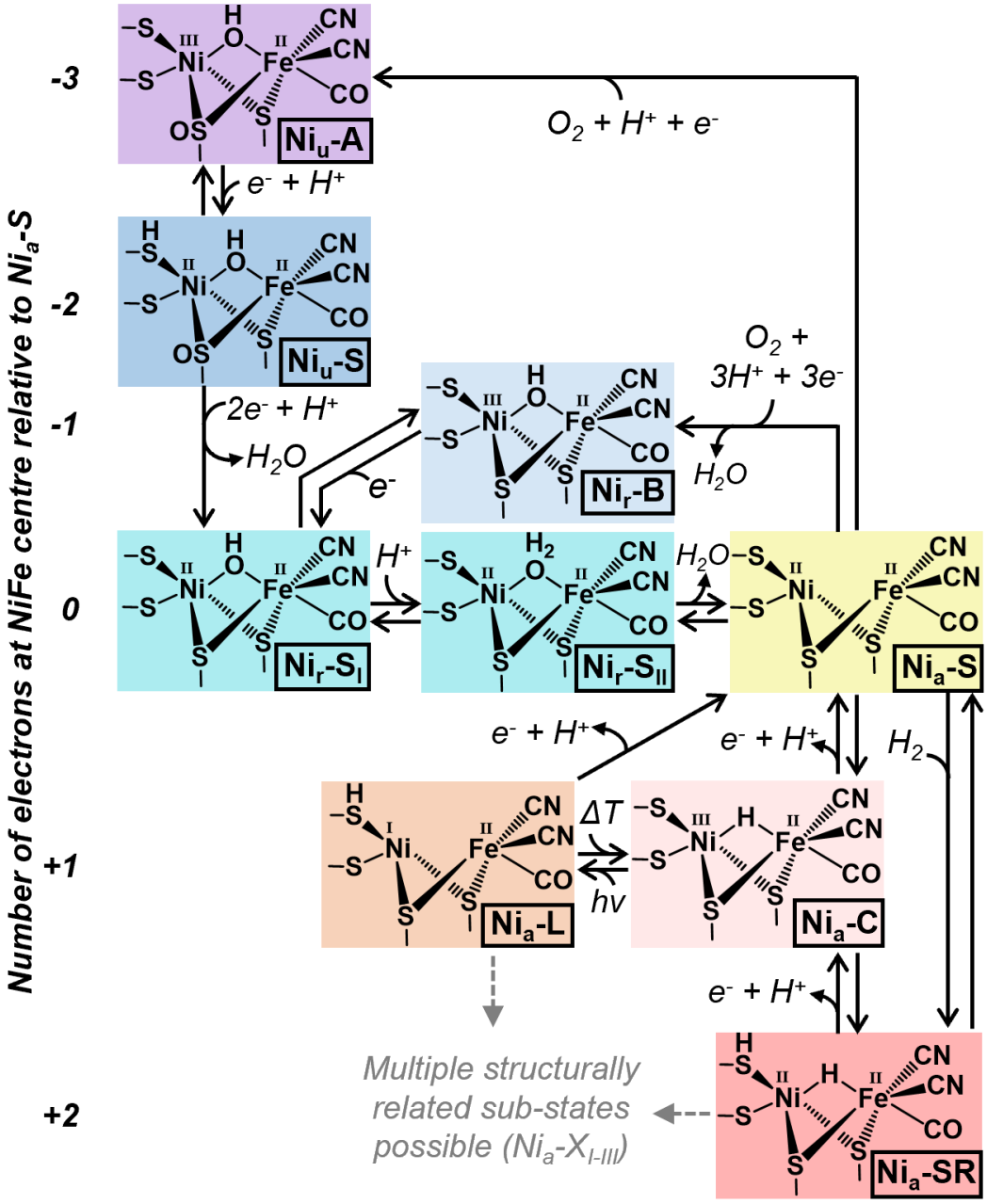

Figure 9 *[NiFe]-hydrogenase active site state structures and corresponding labels. States that differ in only the subscript (Ni$_a$-L$_{III}$ and Ni$_a$-L$_{II}$ or Ni$_a$-SR$_{III}$ and Ni$_a$-SR$_{II}$) are thought to represent closely related conformers of the same state.*

The Ni$_a$-S state is a key catalytic intermediate and the most oxidised of the on-cycle active site states. Exposure of Ni$_a$-S to O_2 converts it from an S=0 Ni^{II} state into the Ni^{III} containing S=1/2 states Ni$_r$-B or Ni$_u$-A, both of these states feature a bridging $^-$OH ligand, however the Ni$_u$-A state is also thought to have a sulfoxygenated bridging cysteine.[58,61–64] Whether Ni$_r$-B or Ni$_u$-A forms depends

upon the number of protons and electrons supplied by the enzyme to the NiFe centre, the preferential formation of Ni_r-B by O_2-tolerant enzymes is thought be caused by their proximal FeS clusters being able to supply more electrons.[18,45,51,55] One electron reduction of Ni_u-A and Ni_r-B yields the Ni^{II} containing Ni_u-S[58] and Ni_r-S_I[61] states (respectively), and while the precise structure of these states are not known they have been assumed to retain structural similarity to Ni_u-A and Ni_r-B.[11,65] Two electron reduction converts the Ni_u-S state into Ni_r-S_I and eliminates H_2O with the O and an H atom supplied by the cysteine residues.[24] Protonation of the bridging $^-$OH ligand converts the Ni_r-S_I state into Ni_r-S_{II}, which can then rapidly form Ni_a-S via loss of the bridging H_2O ligand.[66] For NiFe hydrogenase molecules performing H_2-oxidation the vacant bridging site of Ni_a-S serves as the binding site for H_2.[27,67,68] H-H bond cleavage is generally accepted to occur via a heterolytic mechanism,[2,67,69–72] producing the Ni_a-SR state which features a bridging hydride and a protonated terminal cysteine residue.[73–75] Activation of the H-H bond has been proposed to occur via mechanisms featuring a frustrated Lewis pair (FLP)[27,76–78] or oxidative addition,[27,79–81] as shown in **Figure 10**.

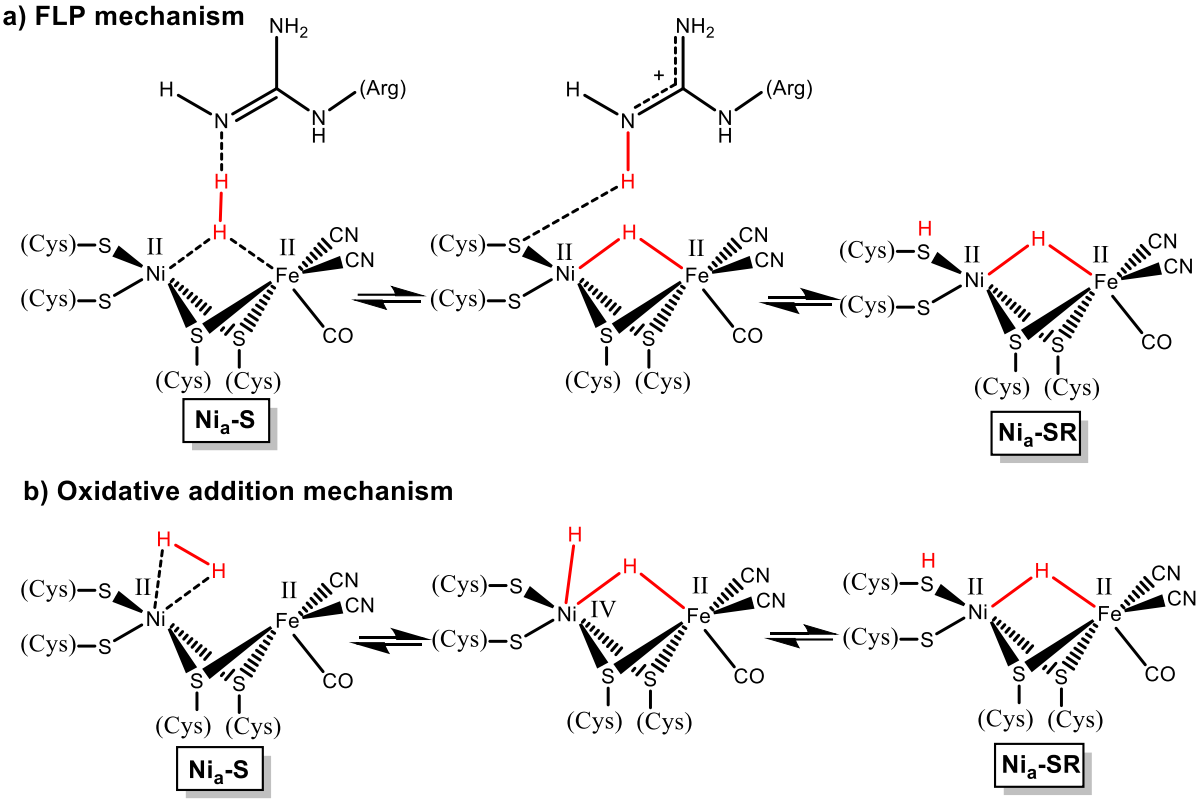

Figure 10 *H_2-activation via* ***(a)*** *heterolytic frustrated Lewis pair and* ***(b)*** *oxidative addition mechanisms.*

In the FLP mechanism (**Figure 10(b)**) the transiently deprotonated guanidinium group of an arginine side chain, suspended ~4 Å above the variable bridging position, acts as a strong base for H-H bond cleavage.[27,77,78] Alternatively, H_2 could bind to the Ni ion in a side-on arrangement producing a Kubas-complex (**Figure 10(b)**), oxidative addition occurs and a transient Ni(IV)-dihydride is formed, this is followed by proton transfer to a terminal cysteine thiolate ligand.[27,79,81] The importance of the arginine residue to H_2 activation has been demonstrated in computational[82,83] and mutational[77] studies on hydrogenases, however the structures of the earliest intermediates in H_2 binding and cleavage have yet to be elucidated. In the conversion of the Ni_a-SR to the Ni_a-C state a proton is released from a terminal cysteine residue as well as an electron from the Ni-ion via its oxidation to the Ni(III) state (S=1/2),[71,81] likely occurring in two sequential steps.[84] Ni_a-C can then either tautomerise to the Ni_a-L state, or

transition back to the Ni_a-S state via the concerted release of a proton and an electron.[11,27,85] The tautomerisation of Ni_a-C involves the Ni(III) ion accepting two electrons from the bridging hydride ligand to form an S=1/2 Ni(I) ion, and the transfer of the nascent H^+ to one of the terminal cysteine thiolate ligands.[2,11,14,27] Ni_a-L can transform into Ni_a-S via the release of one proton and one electron, the proton is released from the terminal cysteine thiolate ligand and the electron via one-electron oxidation of the Ni(I) ion.[11,59]

2.2.4 Characterisation of NiFe hydrogenases – insight from vibrational spectroscopy

IR spectroscopy has played a pivotal role in the characterisation of NiFe hydrogenase active site states, and even formed the basis for the initial identification of the carbonyl and cyanide ligands detected in early crystal structures of hydrogenase from *D. gigas*.[24,86,87] The $Fe(CO)(CN)_2$ unit present in the NiFe-hydrogenase active site produces an IR absorption spectrum featuring three signals corresponding to the fundamental (v=0-1) transitions of the stretching modes of the carbonyl and cyanide ligands, these are labelled ν_{CO}, ν_{CN1} and ν_{CN2} in **Figure 11**.[88] The ν_{CN1} and ν_{CN2} modes are generally assigned to the symmetric and asymmetric stretching modes of the cyanide ligands, respectively.[63,88–90] However, normal mode analysis indicates that some degree of delocalisation occurs, so for the purposes of this project they are referred to as ν_{CN1} and ν_{CN2}.[91] The carbonyl and cyanide ligands are π acidic and so their stretching frequencies are sensitive to the level of electron density at the metal centre to which they are bound, as such the positions of the ν_{CO} and ν_{CN} bands are effective diagnostics for identifying the redox structural states of NiFe hydrogenases. The position of the ν_{CO} band is particularly sensitive to changes

at the NiFe centre as carbonyl ligands are more effective π-acceptors than cyanide ligands (which are more potent σ-donors). Cyanide ligands are more potent σ-donors than carbonyl ligands as the negative charge on their C atoms results in a higher energy HOMO, this negative charge also raises the energy of the π* orbitals (relative to CO) causing CN^- to be a weaker π-acceptor. While CO/CN^- ligands can stabilise H_2 binding by limiting back donation into the σ* orbitals of H_2,[79] establishing the precise role of the CO/CN^- ligands in hydrogenase catalysis is complicated by H_2 binding and activation likely occurring at the Ni centre.[81] Considering the conserved nature of the protein architecture around the CO/CN^- ligands (**Figure 4**) and the sensitivity of their vibrational frequencies to relatively long range structural changes (comparing Ni_r-S_I and Ni_r-B in **Figure 9** for instance), it is probable that they have a more subtle role in catalysis than simply stabilising the Fe(II) ion in a low spin state.

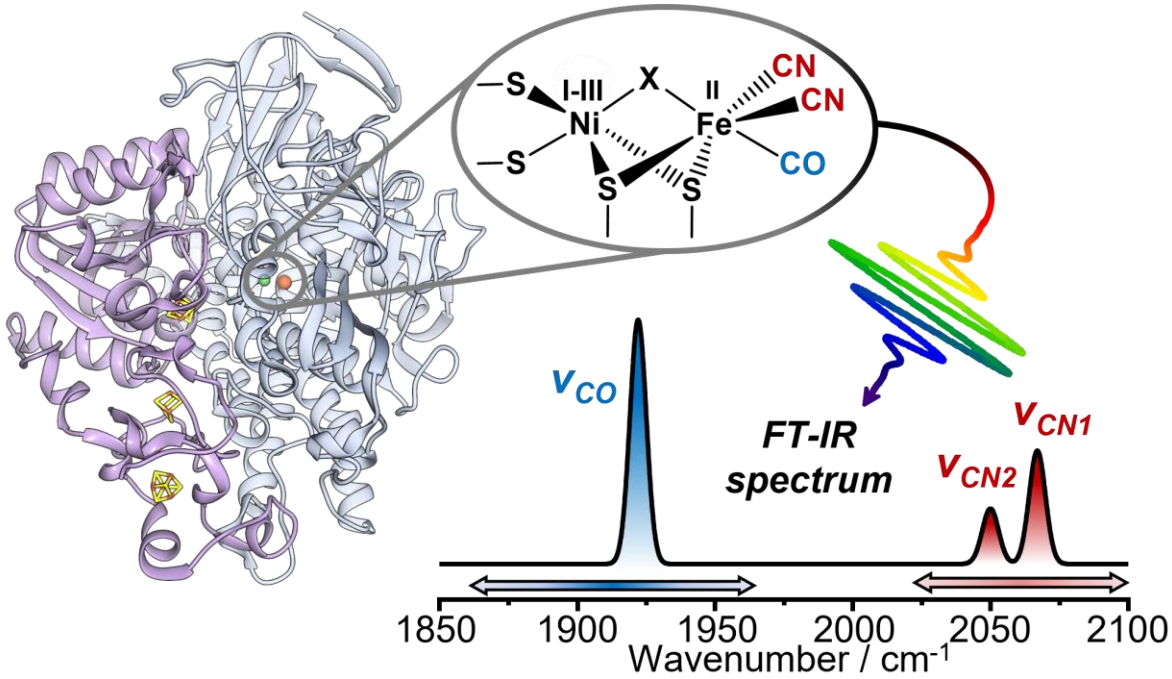

Figure 11 *NiFe hydrogenase heterodimer (EcHyd-1, PDB: 6FPO[15]), shown as coloured ribbon, with generic skeletal structure of the active site and labelled FT-IR spectrum for a single active site state (Ni_r-S).*

IR spectroscopy, and the spectroelectrochemical variant in particular, have been used extensively to identify and monitor the interconversion of hydrogenase redox structural states.[15,25,66,68,85,88,92–96] Valuable insight has also been provided by a variety of more complex variants of vibrational spectroscopy. The bridging hydride ligand present in Ni_a-SR states has been detected using nuclear resonance vibrational spectroscopy (NRVS).[97] Resonance Raman spectroscopy has been used to investigate the electronic configurations of the metal ions as well as metal-ligand bonding.[95,98,99] The association of cysteinyl S-Fe modes with the bending and stretching modes of the $[Fe(CO)(CN^-)_2]^{+/0}$ moiety have been confirmed in studies using NRVS and resonance Raman (RR) spectroscopy.[99,100] Photogated and potential jump transient IR absorption approaches have been used to investigate short-lived intermediates and explore the coupling of proton and electron transfer steps during the transition between active site states at sub-turnover frequency timescales.[84,101–107] This approach was also used in a mutational study to identify a role for the conserved arginine residue (R509 in *Ec*Hyd-1 numbering) in modulating the equilibrium between the tautomeric Ni_a-C and Ni_a-L states.[101]

Despite the wealth of information provided by vibrational spectroscopy in existing hydrogenase studies, the current approaches have some significant limitations. The fundamental frequencies of the ν_{CO} and ν_{CN} modes are typically the only quantity evaluated (excluding RR and NRVS studies), and these frequencies are subject to a number of structural and electronic factors that haven't been fully characterised.[108] While the conditions that govern the interconversion of redox states have been explored in depth, a dynamic picture of the vibrational properties of individual redox states has yet to emerge. Obtaining a more thorough understanding of the potential energy surfaces and

vibrational dynamics of the ν_{CO} and ν_{CN} modes may contribute to unravelling some of the central unknowns in hydrogenase research:

1) The poor catalytic activity exhibited by small biomimetic models of the NiFe- and FeFe-hydrogenase active sites demonstrates the functional importance of the protein matrix, how does the protein matrix tune the chemistry at the active site and what are the key determinants for efficient H_2-conversion?
2) Does H_2-bond cleavage occur via oxidative addition or an FLP mechanism?
3) Considering that H_2 likely binds at the Ni-centre, what is the role of the $Fe(CO)(CN^-)_2$ unit in H_2-cleavage?

2.3 Pump-probe and 2D-IR spectroscopy

2.3.1 Fundamentals of IR spectroscopy

The vibrations of a pair of atoms joined by a covalent bond can be modelled by a Morse anharmonic potential.[109] In this description the potential energy (*V(r)*) is at a minimum when the interatomic separation (*r*) is equal to the equilibrium bond length (r_0). A Morse anharmonic potential is shown in **Figure 12**.

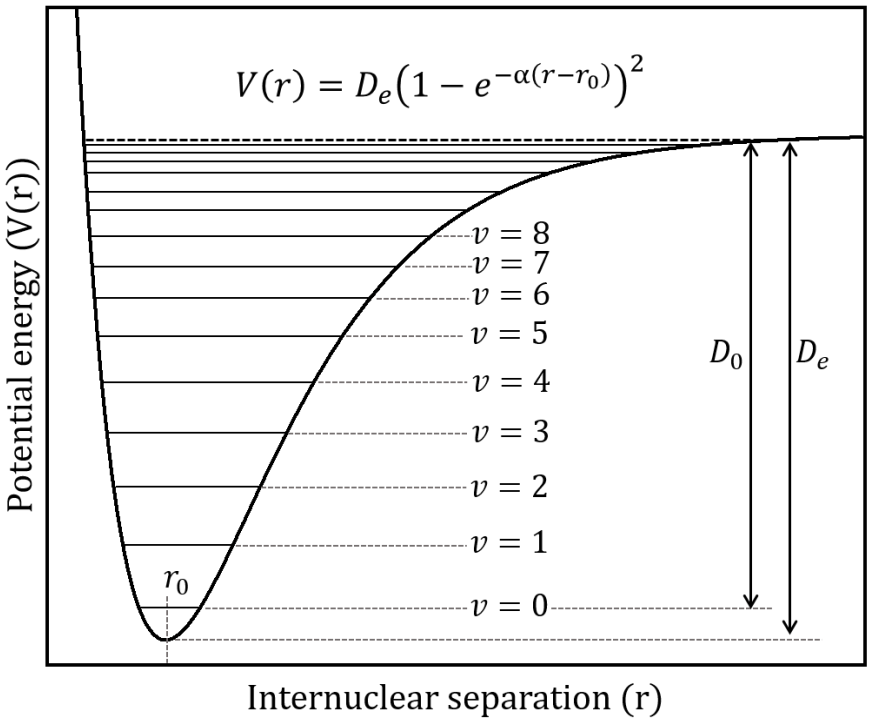

Figure 12 *Morse potential for a pair of covalently bonded atoms. The ground state ($v = 0$) and vibrationally excited states ($v = 1, 2, 3, ..$) are shown along with the equilibrium bond length (r_0), dissociation energy (D_e), and dissociation limit (D_0).*[109]

The energy (E_v) of vibrational levels is described by:

$$E_v = hv_0\left(v + \frac{1}{2}\right) - \frac{\left[hv_0\left(v + \frac{1}{2}\right)\right]^2}{4D_e} \qquad \textbf{(4)}$$

The harmonic frequency (v_0) is related to the mass of the particles (*m*), the dissociation energy and the curvature of the potential well (*a*) via:

$$v_0 = \frac{a}{2\pi}\sqrt{\frac{2D_e}{\mu}} \quad \textbf{(5)}$$

Where μ is calculated from the masses of bonded atoms:

$$\mu = \frac{m_1 m_2}{m_1 + m_2} \quad \textbf{(6)}$$

The curvature of the potential well relates to the bond's force constant (k_e) via:

$$a = \sqrt{\frac{k_e}{2D_e}} \quad \textbf{(7)}$$

The difference in energy for a pair of adjacent energy levels can be calculated from **Equation (4)**, giving:

$$E_{v+1} - E_v = hv_0 - \frac{(v+1)(hv_o)^2}{2D_e} \quad \textbf{(8)}$$

Equation (4) can be alternatively expressed to include the anharmonicity constants ω_e and χ_e (as wavenumbers):

$$\frac{E_v}{hc} = \omega_e\left(v + \frac{1}{2}\right) - \omega_e\chi_e\left(v + \frac{1}{2}\right)^2 \quad \textbf{(9)}$$

In IR absorption experiments the excitation field, *E(t)*, induces polarisation, *P(t)*, of the sample which gives rise to emission of the signal field, $E_{sig}(t)$.[110] The signal field is phase shifted by π/2 relative to the polarisation which results in destructive interference between excitation and signal fields at energies corresponding to bond frequencies, thereby giving rise to the features detected in absorption spectra.[111,112]

The polarisation induced by the excitation field for a given dielectric medium is described by:

$$P(t) = \varepsilon_0 \chi E(t) = \varepsilon_0 \left(\chi^{(1)} E(t) + \chi^{(2)} E^2(t) + \chi^{(3)} E^3(t) + \cdots \chi^{(n)} E^n(t) \right) \quad \textbf{(10)}$$

Where ε_0 denotes the permittivity of free space and χ is the optical susceptibility of the medium which describes the extent to which its dipoles are induced by an excitation field. Since χ is related to the polarizability of the molecules that comprise the medium so too is it related to the transition dipole moment of the fundamental transition, μ_{01}.[111,113] The transition dipole describes the change in a molecule's charge distribution caused by excitation of a vibrational mode.[111] In the quantum mechanical description a coherent superposition between the ground and first vibrationally excited states is created by the excitation field, this causes macroscopic polarisation of the medium oscillating at the frequency of the fundamental transition, which in turn causes the emission of the signal field at this energy.[111,112,114] Maxwell's equations stipulate that the signal field is emitted π/2 out of phase relative to the polarisation, causing it to destructively interfere with the excitation field at energies corresponding to the vibrational transition.[111,115] For the case of linear spectroscopies such as FT-IR spectroscopy the polarisation function can be truncated to only the first order terms:

$$P(t) = \varepsilon_0 \chi^{(1)} E(t) \quad \textbf{(11)}$$

The macroscopic polarisation decays to equilibrium according to the molecular response function, *R(t)*. The molecular response function contains information describing the evolution of molecular structure. Fourier transformation of *R(t)* yields the frequency domain signal field, *S(ω)*, which is comprised of both real and imaginary parts. The imaginary component describes the dispersive lineshape *D(ω)*, and the real component describes the absorptive lineshape *A(ω)*. The phase of real and imaginary components is such that only *A(ω)* interferes with *E(t)* and so can be detected.[111,112,114]

$$D(\omega) \propto \frac{-\mu_{01}^2(\omega - \omega_{01})}{(\omega - \omega_{01})^2 + (0.5\gamma)^2} \quad \textbf{(12)}$$

$$A(\omega) \propto \frac{\mu_{01}^2(0.5\gamma)}{(\omega - \omega_{01})^2 + (0.5\gamma)^2} \quad \textbf{(13)}$$

Here ω is the frequency of light emitted, ω_{01} is the frequency of the fundamental and γ is the natural linewidth of the transition. The resulting absorption spectrum, $A(\omega)$, has a Lorentzian distribution (**Figure 13**).

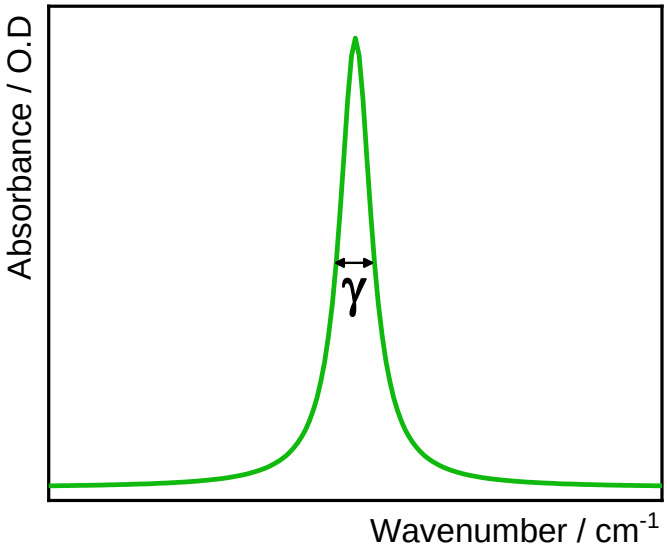

Figure 13 *An absorption peak with a Lorentzian distribution.*

The natural linewidth of a distribution cannot be infinitely narrow, rather it has a finite value arising due to the quantum properties of the system. For example, the first vibrationally excited state (v=1) is a transient state with a finite vibrational lifetime, T_1.[111] The lifetime has an associated error according to the Heisenberg uncertainty principle:

$$\partial E \, \partial t \geq \frac{h}{4\pi} \quad \textbf{(14)}$$

Where ∂t is the length of time that the v=1 state is occupied (i.e., T_1) and ∂E is the uncertainty in its energy level, and h is Planck's constant. Since the vibrational frequency of a transition is dependent on the separation in energies of the associated energy levels (here v=0 and v=1), error in the energy levels impacts the vibrational frequency of the transition via:

$$\partial E = hc\ \partial v \quad \textbf{(15)}$$

Substituting **(15)** into **(14)** and rearranging for ∂v gives:

$$\partial v \geq \frac{1}{4\pi c\ \partial t} \quad \textbf{(16)}$$

It is apparent from **(16)** that the error in the frequency of the vibration, ∂v, is directly affected by the vibrational lifetime. The decay of the macroscopic polarisation is subject to more rapid dephasing processes in addition to the intrinsic lifetime of the excited state. The vibrations of each molecule may occur at a narrow range of frequencies determined by the lifetimes of the vibrations, the instantaneous frequencies may fluctuate rapidly within these bounds. These fluctuations can cause the phase relationship of ground and excited states to change such that coherence is lost and the polarisation decays, this is termed pure dephasing and occurs with a timescale of T_2^*.[111,113] Vibrational lifetime and pure dephasing both contribute to the minimum width of vibrational transition:

$$\gamma \sim \frac{1}{2T_1} + \frac{1}{T_2^*} = \frac{1}{T_2} \quad \textbf{(17)}$$

T_2 is the homogenous dephasing time, which incorporates contributions from both pure dephasing and vibrational relaxation. A homogeneously broadened transition is one whose width is solely determined by T_2.[111]

Transitions observed in IR spectra for molecules in the solution phase are routinely much broader than the natural linewidth, with Gaussian rather than Lorentzian distributions. This is because the distribution of electrons between the vibrating atoms is influenced by interactions with solvent molecules leading to changes in the potential energy surface (**Figure 12**) for the vibration and its associated transition energies. The vibrational frequency of an oscillator falls within a Gaussian distribution determined by the conformation dependent interactions with its solvent environment. This is because for a molecular

ensemble each accessible conformation is occupied, leading to a Gaussian lineshape composed of a series of overlapping Lorentzian lineshapes representing each of the accessed conformations. These lineshapes are said to be inhomogeneously broadened, an example is shown in **Figure 14**.

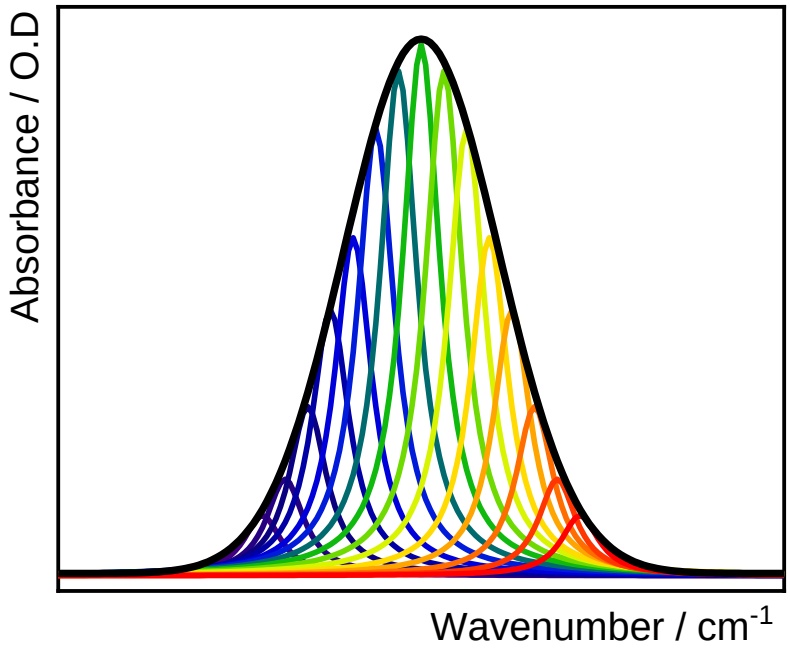

Figure 14 *An inhomogeneously broadened Gaussian lineshape composed of a series of Lorentzian lineshapes representing the different molecular conformations available to an oscillator in the solution phase.*

Considering an oscillation of a molecule dissolved in water, the subpicosecond fluctuations in the hydrogen bonding network formed by solvating water molecules causes the instantaneous frequency of a single oscillator to vary on the same timescale as its solvent environment. This variation in vibrational frequency with time is termed spectral diffusion. The changes in solvation environment can thus be probed by analysing the evolution in lineshape caused by spectral diffusion. However, analysing the spectral diffusion of a transition via linear IR spectroscopy is not possible because it is ensemble averaged. Analysis of spectral diffusion is more facile with 2D-IR spectroscopy as it has greater time resolution, and the spectral response is spread over an additional axis.[111]

2.3.2 Non-linear IR spectroscopy

2.3.3 3rd order spectroscopy

Investigating the changes in structure and dynamics that impact a molecular vibration requires the use of laser pulses with duration shorter than that of these processes. For very short duration laser pulses the induced polarisation is no longer linear with respect to the optical suscpetibility and higher order terms must be considered. For very short duration laser pulses the molecular response function has contributions from $\chi^{(1)}$ and $\chi^{(3)}$, the contribution from higher order odd-power terms is sufficiently small to not be considered. For non-centrosymmetric media (e.g., non-crystalline solutions) the contributions from even power terms is zero.[111,113]

Four wave mixing is the most common approach by which 3rd order signals are extracted. In this approach three laser pulses incident on the sample are separated in time by t_1, t_2 and t_3. The resulting 3rd order polarisation is related to the molecular response function via:

$$P^{(3)}(t) \propto \int_0^\infty dt_3 \int_0^\infty dt_2 \int_0^\infty dt_1 E_3(t-t_3)E_2(t-t_3-t_2)E_1(t-t_3-t_2-t_1)R^{(3)}(t_3,t_2,t_1) \qquad \textbf{(18)}$$

The 3rd order response function, $R^{(3)}(t_3, t_2, t_1)$, is deconvoluted from the excitation fields, $E_{1\text{-}3}$, by using the phase matching properties of the pulse sequence.[111] In the four-wave mixing approach the pulses are referred to by their wavevectors ($2\pi/\lambda$) $\vec{k}_1$, $\vec{k}_2$, $\vec{k}_3$ and $\vec{k}_4$, where $\vec{k}_4$ is the emitted signal field and the subscript numbers indicate the time ordering of the pulses.

To describe how the laser pulses interact with an ensemble of oscillators a combined statistical and quantum mechanical approach is used. The statistical

average of the ensemble is described using a density matrix representation. For each interaction of a pulse with the ensemble, the transition dipole moment operator, μ, is applied to the density matrix. With negative wave vectors (-$\vec{k}$) exciting the bra state $\langle x|$ and positive wave vectors (+$\vec{k}$) exciting the ket state $|x\rangle$ of the ensemble. The converse is true for de-excitation, with positive wave vectors de-exciting the bra state $\langle x|$ and negative wave vectors de-exciting the ket states.[111,112,114]

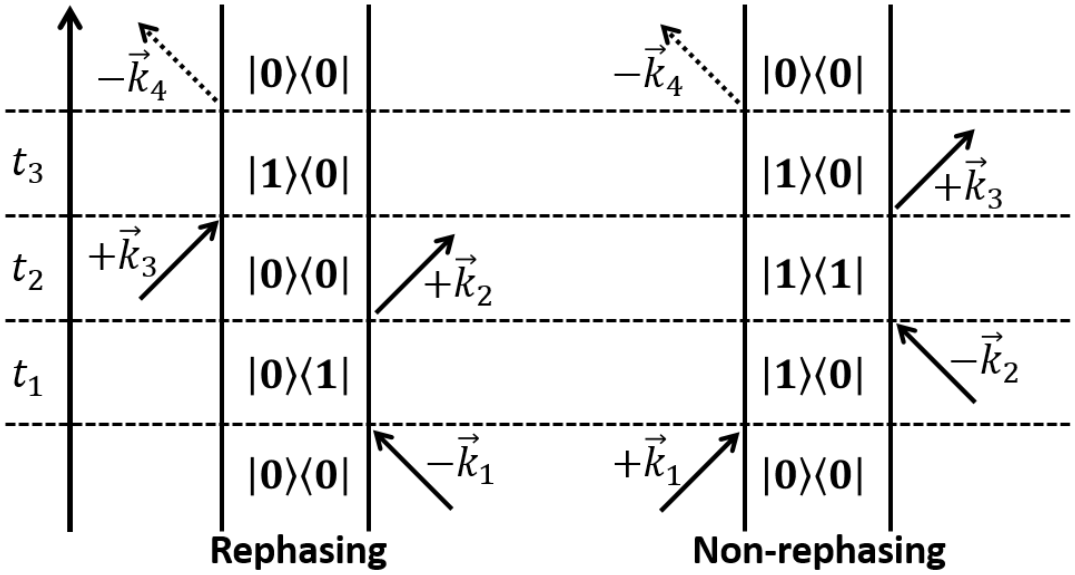

Figure 15 *Feynman diagrams for rephasing and non-rephasing pathways.*

The excitation fields can interact with the sample via several pathways. These pathways are said to be rephasing if the signal field $\vec{k}_4$ is emitted via de-excitation of the opposite state that was initially excited by the first excitation field, $\vec{k}_1$. For the example of a rephasing pathway in **Figure 15** the first excitation field excites the ket state of the ensemble and the signal is emitted via de-excitation of the bra state. Similarly, pathways are said to be non-rephasing if the signal field is emitted via de-excitation of the same state that was initially excited by the first excitation field. For the example of a non-rephasing pathway in **Figure 15** the first excitation field excites the bra state and the signal is

emitted via de-excitation of the bra state of the ensemble. Rephasing pathways in the response function restore the macroscopic polarisation initially imparted by the first excitation field and result in the emission of a "photon echo" signal field. Non-rephasing signals are sensitive to only homogeneous dephasing so collection of data from both rephasing and non-rephasing pathways is necessary for distinguishing homogeneous and inhomogeneous contributions to linewidths, and also for preventing the distortion of lineshapes caused by third order responses.[111]

The process for how 3rd-order signals are emitted from a sample is as follows:

i. The first excitation field, $\vec{k}_1$, interacts with either the bra or ket state of the ensemble creating a coherent superposition of the ground and first excited states oscillating with a frequency of ω_{01}.
ii. During the first coherence time t_1 which is the time between the first and second pulses, the macroscopic polarisation decays due to dephasing.
iii. The second excitation field, $\vec{k}_2$, either de-excites the bra or ket state initially excited by $\vec{k}_1$, or excites the opposite state, and so converts the coherent superposition state into a population state.
iv. During the population waiting time, t_2, which is the time between the second and third pulses, the population state evolves via spectral diffusion, vibrational relaxation, or energy transfer between coupled vibrations.
v. The third excitation field, $\vec{k}_3$, arrives at the sample and creates a second superposition state, which restores the macroscopic polarisation. For rephasing pathways, the coherence is restored after the second coherence time, t_3. The length of t_3 is approximately equal length to t_1 as

it amounts to the time taken to restore the coherence lost during t_1. The second coherence time culminates in the emission of the signal field, $\vec{k}_4$.

The emitted signal field contains all of the information relating to the pathways explored by the ensemble during its interactions with the pulse sequence. A selection of rephasing pathways are shown below in **Figure 16**.[111,112,114]

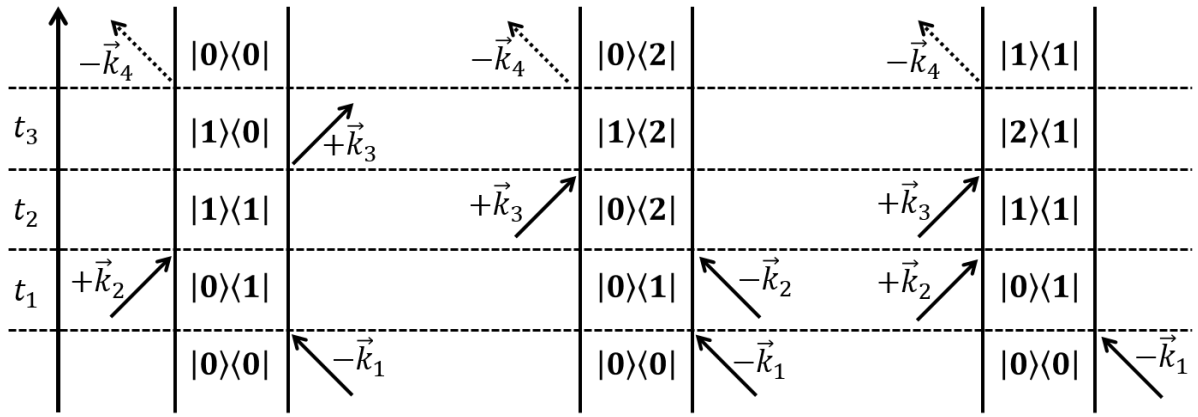

Figure 16 *Feynman diagrams for three possible rephasing pathways in 2D-IR spectroscopy.*

Since the pathways explored by the ensemble are dependent upon the sign of the wave vector, some of the pathways can be selected for via phase matching.[111] The experiments in this thesis used a geometry in which the first and second pulses are collinear (i.e., $\vec{k}_1 = \vec{k}_2$), this simplifies the experimental setup as it causes the emission of the signal field from both rephasing and non-rephasing pathways to be collinear. The phase matching condition used in this thesis is:

$$\vec{k}_4 = -\vec{k}_1 + \vec{k}_2 + \vec{k}_3 \qquad \textbf{(19)}$$

This pulse sequence is advantageous because i) the collinearity of $\vec{k}_1$ and $\vec{k}_2$ simplifies the collection of purely absorptive spectra and ii) the collinearity of $\vec{k}_3$ and $\vec{k}_4$ enables $\vec{k}_3$ to act as a local oscillator to self-heterodyne the signal field.

2.3.4 2D-IR spectroscopy

2D-IR spectroscopy is a four-wave mixing approach using ultrashort duration laser pulses with the molecular response is spread over a second frequency axis. The additional frequency axis can be generated via two methods. The first method, termed the frequency domain approach, uses narrow bandwidth pump pulses where the central frequency is scanned to produce the second frequency axis.[116] While the frequency domain approach is simpler experimentally, it is less suitable for studying ultrafast processes as narrowband pulses have increased pulse duration and so lower time resolution (pulse duration and bandwidth are related properties with limits intrinsic to the shape of the pulse).[117] The second approach, termed the time domain approach, was used for all 2D-IR experiments for this thesis. For this approach broadband pump pulses are used, and the second frequency axis is generated by scanning the delay between pump pulses (t_1) and Fourier transformation to convert it into the frequency domain.[118] The time delay between pump pulses can be controlled with optical delay lines, an interferometer, or via acousto-optic modulation with a pulse shaper (which also enables narrowband ultrashort pulses to be produced).[119,120] The spectra presented here were collected using a setup with a pulse shaper. Further details of the experimental setup are discussed in 3.2.2.

Example data including linear IR and 2D-IR spectra as well as an energy level scheme for a pair of coupled vibrational modes are shown below in **Figure 17**. Anharmonic coupling occurs as a result of the coupled vibrational modes either sharing atoms or having atoms sufficiently close in space for their orbitals to interact thereby altering their vibrational potentials, causing perturbation of their transition energies relative to the uncoupled scenario.[111,112,114] Coupled vibrational modes are considered to share a ground state. The example 2D-IR

spectrum corresponds to data recorded at a short population time (t_2), this quantity is also referred to as the waiting time (T_w) and the pump-probe delay time. The energy level scheme features six energy levels including the ground state, $|00\rangle$, the first excited states, $|10\rangle$ and $|01\rangle$, the second excited states, $|20\rangle$ and $|02\rangle$, and the two-quantum combination state, $|11\rangle$.

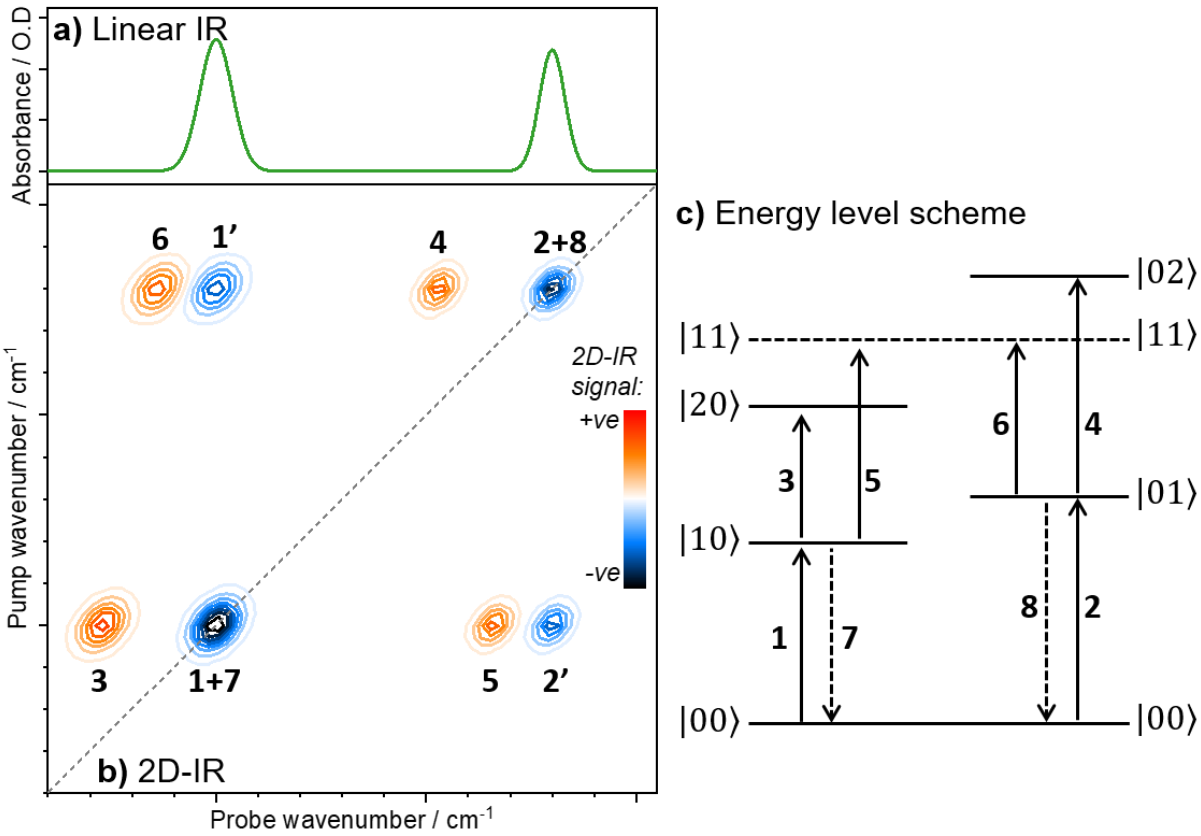

Figure 17 *Example data showing the* ***(a)*** *linear IR spectrum (top panel) and corresponding 2D-IR spectrum (bottom panel) and* ***(b)*** *energy level scheme for a pair of coupled vibrational modes.*

The linear IR spectrum in **Figure 17(a)** contains two peaks corresponding to the v=0-1 transitions (termed ground state absorptions) **1** and **2**, no excited state transitions are present as only the ground state has significant population at room temperature. The 2D-IR spectrum in **Figure 17(b)** can be separated into diagonal and off-diagonal regions. The diagonal region contains the four bands

labelled: **3**, **1+7**, **4** and **2+8**, and the off-diagonal region contains peaks labelled: **6**, **1**, **5** and **2**. The corresponding energy level scheme is shown in **Figure 17(c)**.

2D-IR spectra are recorded as difference spectra, with spectra recorded in the absence of pump-pulses (i.e., $\vec{k}_1$ and $\vec{k}_2$) subtracted from those recorded with all of the pulses. This causes the ground state absorption peaks (**1+7** and **2+8**) to have negative intensity because the pump pulses deplete the population of the ground state, stimulated emission (**7** and **8**) also contributes to their negative intensity.

The rephasing Feynman pathways that give rise to the peaks in **Figure 17** when using the pulse sequence outlined in **Equation (14)** are shown in **Figure 18**.

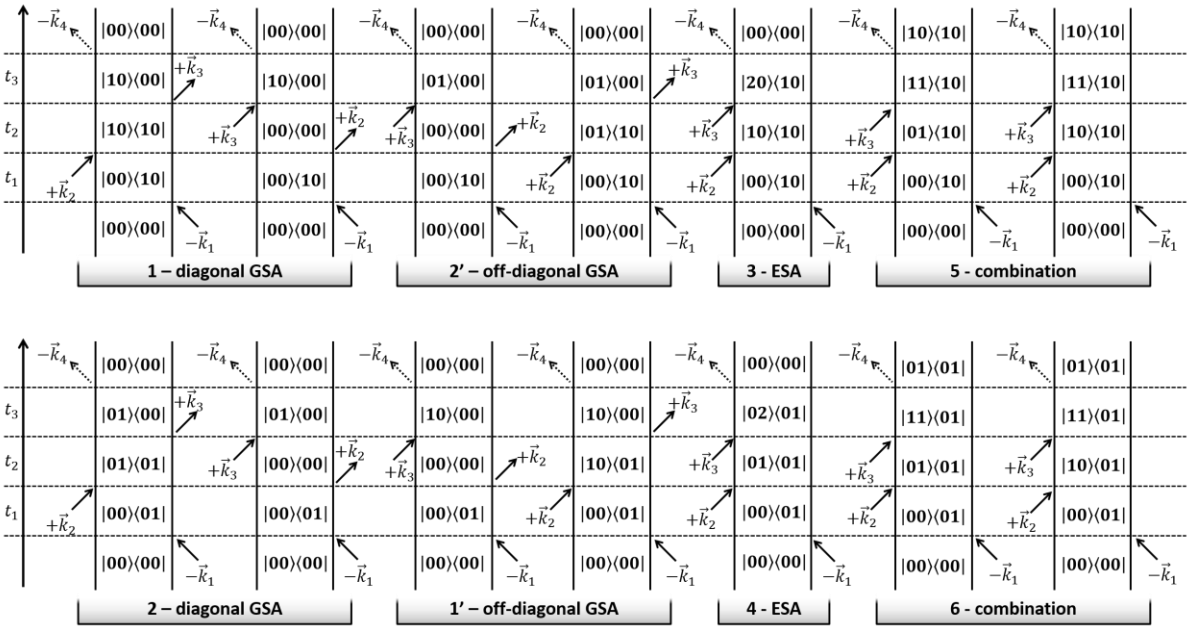

Figure 18 *Feynman diagrams for the allowed rephasing pathways that give rise to the peaks in Figure 17 using the pulse sequence described in* ***Equation (14)****.*

The pathways that give rise to the on-diagonal peaks **1+7** and **2+8** are very similar, with each pathway maintaining the same relationship in coherencies during t_1 and t_3, i.e., $|00\rangle\langle 10|$ to $|10\rangle\langle 00|$ for peak **1+7** and $|00\rangle\langle 01|$ to $|01\rangle\langle 00|$ for peak **2+8**. The pattern is not maintained for the off-diagonal bleaches **1'** and

2', instead having $|00\rangle\langle 01|$ and $|01\rangle\langle 00|$ (during t_1 and t_3) for peak **1'** and $|00\rangle\langle 10|$ and $|10\rangle\langle 00|$ for **2'**. This is because **1'** and **2'** are caused by coupling, the coupled modes have a common ground state so the pump pulse can generate a coherence with the coupled mode. The excited state absorption peaks (v=1-2) labelled **3** and **4** result from pathways that create v=1 population states ($|10\rangle\langle 10|$ and$|01\rangle\langle 01|$, respectively) during t_2, this allows the third excitation field to create a coherence between v=1 and v=2 ($|20\rangle\langle 10|$ and $|02\rangle\langle 01|$, respectively) during t_3, the resulting signal field is down shifted from the corresponding v=0-1 peak by the anharmonicity of the vibrational mode. If the system were completely harmonic then the v=1-2 peak would not be shifted from the v=0-1 peak and they would cancel out. Like the off-diagonal bleaches, the two-quantum combination bands (**5** and **6**) are caused by coupling. However, for combination bands the signal field is emitted from a state with one-quantum of excitation in each of the coupled modes ($|11\rangle\langle 10|$ and$|11\rangle\langle 01|$ for **5** and **6**, respectively), this results in the shifting of its signal to lower wavenumber (relative to its partnered off-diagonal bleach) by an amount proportional to the coupling strength.[111]

While the position of a peak is dependent on the factors governing transition energy, the amplitude is determined by the strength of the transition dipole moment (μ), and its angle relative to that of interacting transition dipoles. The angle between transition dipole moments of coupled vibrational modes (θ) can be determined by analysing the peak amplitudes in spectra recorded with different pulse polarisation geometries. The ratio of amplitudes (A_{perp}/A_{para}) of off-diagonal fundamental transitions varies with the pump-probe polarisation geometry (ZZYY for perpendicular, and ZZZZ for parallel) and θ according to **Equation (20)**.[121]

$$\frac{A_{perp}}{A_{para}} = \frac{1 - cos^2\theta}{1 + 2\,cos^2\theta} \qquad \textbf{(20)}$$

This is shown graphically below in **Figure 19**.

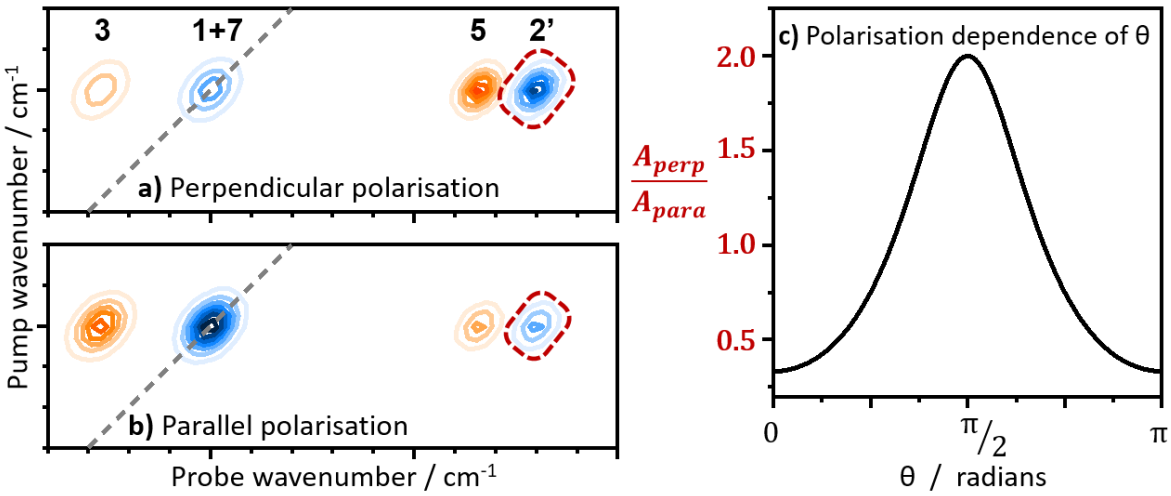

Figure 19 *Example data showing the lower half of 2D-IR spectra recorded with an early T_w and* ***(a)*** *perpendicular and* ***(b)*** *parallel polarisation geometries (i.e., ZZYY and ZZZZ, respectively). (c) Plot showing the relationship between the ratio of cross peak amplitudes (A_{perp}/A_{para}) and the angle between coupled transition dipole moments (θ).*

Each 2D-IR spectrum is recorded at a single pump-probe delay time (T_w). Dynamic information can be determined from the analysis of spectra recorded at a range of values for T_w. For 2D-IR spectra featuring coupled vibrations, additional off-diagonal peaks may emerge in spectra recorded at later waiting times, this is shown in the example spectra below in **Figure 20**.

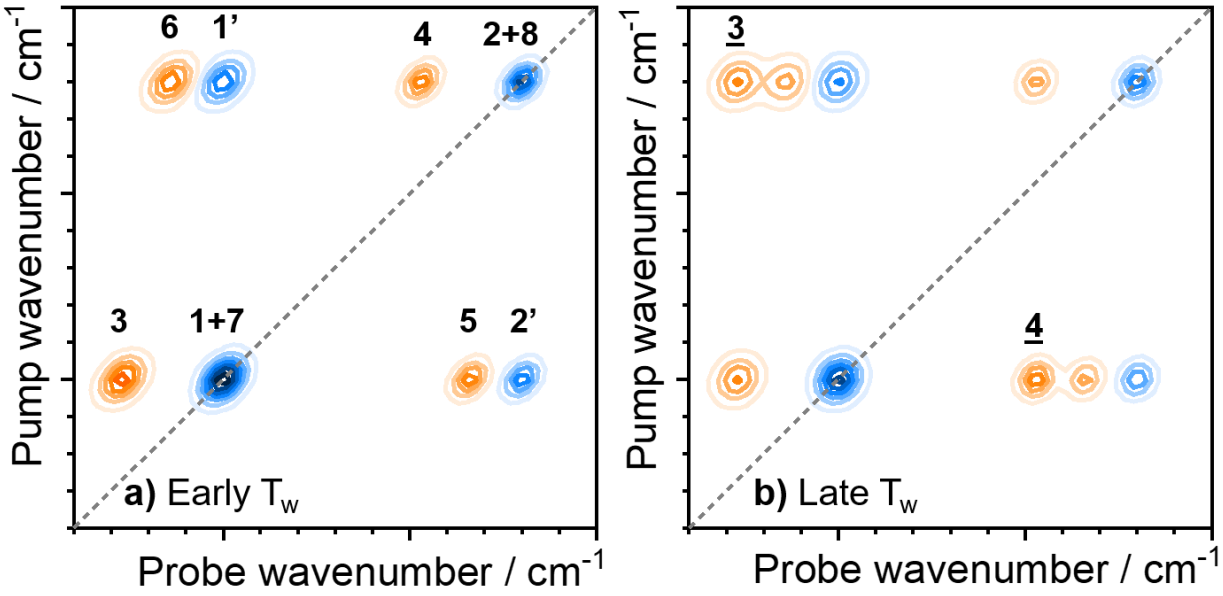

Figure 20 *Example 2D-IR spectra recorded at* ***a)*** *early and* ***b)*** *late values of T_w. peaks are numbered according to the energy level scheme in* ***Figure 17(c)****. Excited state absorption peaks caused by energy transfer are indicated by the underlined numbers.*

In the example 2D-IR spectrum recorded at a later T_w (**Figure 20(b)**) two additional peaks, labelled **3** and **4**, appear in the off-diagonal regions. Peak **3** is at a pump frequency resonant with the $|00\rangle \rightarrow |01\rangle$ transition (i.e., peak **2**) and a probe frequency consistent with the $|10\rangle \rightarrow |20\rangle$ transition (i.e., peak **3**). This is because peak **3** is caused by pumping of the $|00\rangle \rightarrow |01\rangle$ mode, followed by energy transfer from $|01\rangle$ to $|10\rangle$ during the population waiting time (t_2 i.e., T_w), and subsequent excited state absorption $|10\rangle \rightarrow |20\rangle$ via the probe pulse. The converse is true for peak **4**. Feynman diagrams for rephasing pathways that give rise to peaks **3** and **4** are shown below in **Figure 21**.

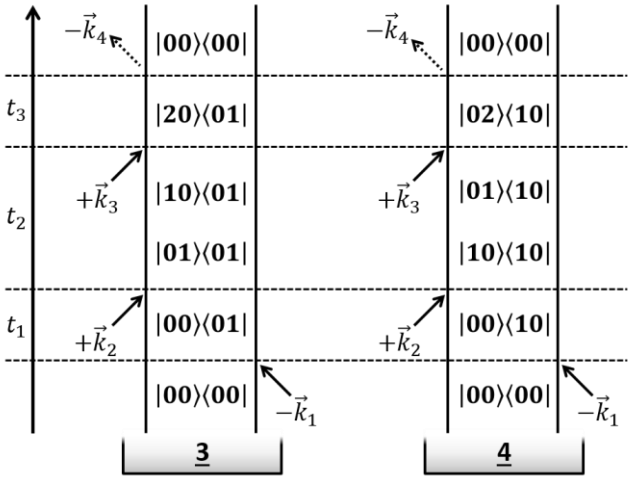

Figure 21 *Feynman diagrams for rephasing pathways that give rise to energy transfer peaks* ***3*** *and* ***4*** *that can be seen in* ***Figure 20(b)****.*

As T_w is increased, on-diagonal peaks decrease in intensity as the likelihood increases that the population state relaxes to the ground state prior to the arrival of the probe pulse at the sample. For sufficiently large values of T_w the diagonal peaks will not be visible as the population state will have completely decayed prior to the arrival of the third pulse. The lifetime of a vibrational mode can be determined by analysing the decay in amplitude of the corresponding peaks. As T_w advances, the intensity of off-diagonal peaks initially increases due to energy transfer between coupled modes, before decaying on a timescale in accordance with their on-diagonal counterparts.

2D-IR spectra recorded at advancing waiting times are also useful for the information they reveal through the changes in lineshape of peaks. This is shown in the example 2D-IR spectra in **Figure 22** for a diagonal peak pair recorded at a series of values of T_w.

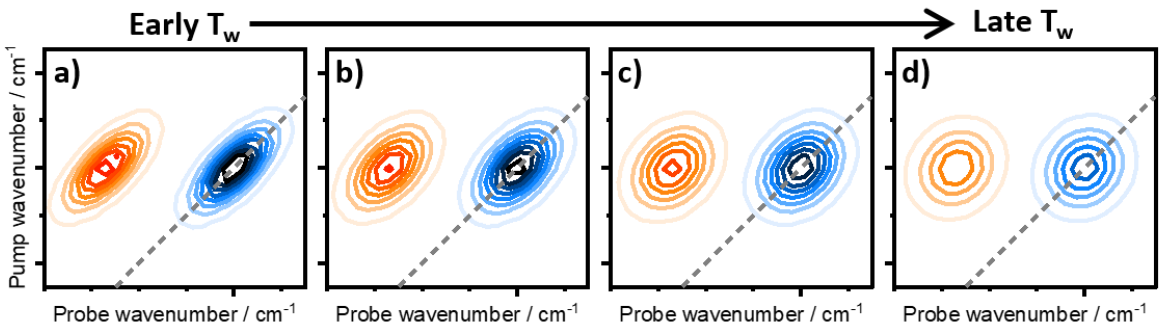

Figure 22 *Example 2D-IR spectra showing how the lineshape of a diagonal peak pair evolves from early (**a**) to late **(b)** values of T_w.*

The diagonal width of a peak (i.e., along the grey dotted line in **Figure 22**) represents the total linewidth (which is the convolution of homogeneous and inhomogeneous linewidths), and the anti-diagonal width of a peak reflects the homogeneous linewidth. If the only contribution to linewidth was from homogeneous broadening then the diagonal width would equal the anti-diagonal width and the peak would be perfectly circular. The peak pair in the low T_w spectrum in **Figure 22(a)** are said to be inhomogeneously broadened because their widths along the diagonal are much larger than on the anti-diagonal. For low values of T_w the anti-diagonal width is narrow because the vibrating atoms are unable to exchange energy with molecules in their surroundings (i.e., solvent molecules), as such the spectra can be considered static snapshots of the system. When the T_w exceeds the rate of fluctuation of molecules in the environment, the frequency of the vibrating atoms can evolve due to energy transfer with solvent molecules leading to the probe pulse detecting a different vibrational frequency to that which was excited by the pump pulse, leading to increased anti-diagonal linewidth and more circular peaks (as in **Figure 22(d)**). This process is termed spectral diffusion. The rate of spectral diffusion can be quantified by analysing the lineshape of peaks via the central line slope (CLS) and nodal line slope (NLS) approaches (as shown below in **Figure 23**), or by fitting the peaks to 2D-Gaussian functions. These approaches

measure how well the detected frequency of a vibration correlates with the frequency at which it was initially excited, resulting in a frequency-frequency correlation function (FFCF).

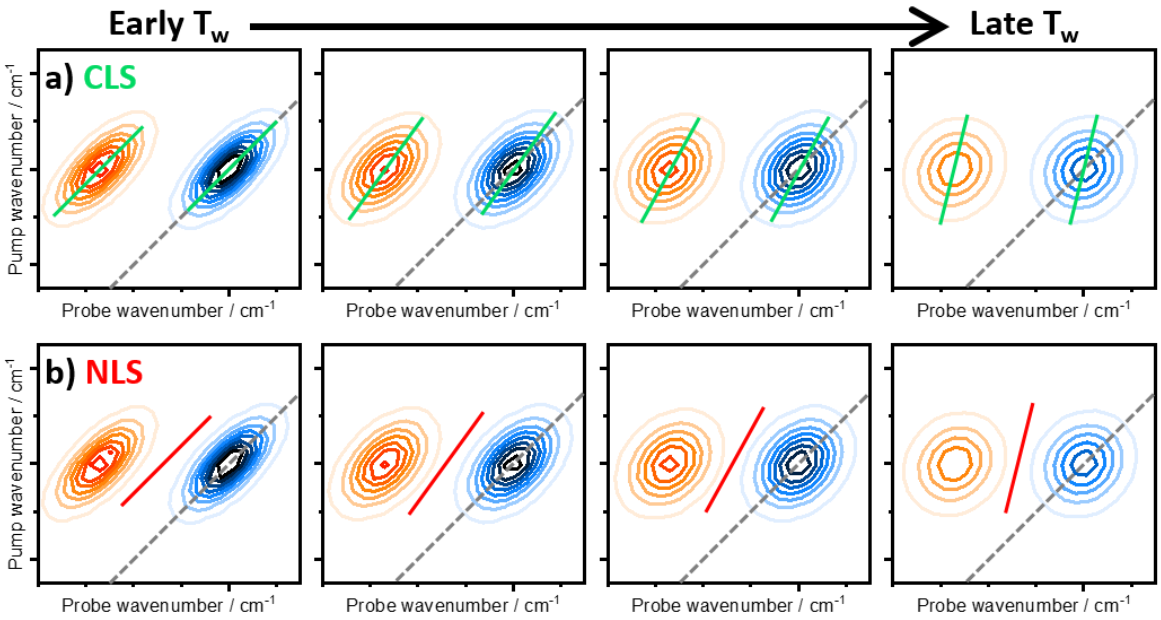

Figure 23 *Example data showing the* ***(a)*** *CLS and* ***(b)*** *NLS approaches to spectral diffusion analysis.*

In CLS analysis (**Figure 23(a)**) straight lines that bisect each peak are defined by determining the probe wavenumber at which each transition has maximum amplitude for each pump wavenumber in which that transition appears. At short waiting times this line is parallel to the spectral diagonal, and as the waiting time advances spectral diffusion causes the line to tilt towards the vertical. When the line reached the vertical, correlation between pumped and probed vibrational frequencies is zero. In the NLS approach (**Figure 23(b)**) an equivalent straight line is define by determining the probe wavenumber between v=0-1 and v=1-2 peaks at which the sign flips from positive to negative.

Alternatively, each peak can be fitted to a two-dimensional Gaussian function like that shown below in equation **(21)**. In this approach each peak is defined by

the sum of a number of Gaussian lineshapes along pump and probe wavenumber axes, and the resulting correlation parameter (C_{2D}) extracted directly.

$$f(x,y) = A\ \text{e}\text{^}\left[-\frac{1}{2\left(1-{C_{2D}}^2\right)}\left(\left(\frac{x-x_0}{\sigma_x}\right)^2+\left(\frac{y-y_0}{\sigma_y}\right)^2-\frac{2C_{2D}(y-x_0)(x-y_0)}{\sigma_y\sigma_x}\right)\right] \quad \textbf{(21)}$$

Where:

f(x,y) = signal amplitude at pump wavenumber, probe wavenumber of (x,y)

x = probe wavenumber

y = pump wavenumber

A = amplitude of peak

C_{2D} = cross correlation parameter

x_0 = central wavenumber of peak along probe axis

y_0 = central wavenumber of peak along probe axis

σ_x = standard deviation along probe axis

σ_y = standard deviation along pump axis

$$\sigma_x = \frac{FWHM_x}{2\sqrt{2\ ln(2)}}$$

Each of these approaches can give an equivalent measure of the FFCF, however the suitability of each approach varies with the particular 2D-IR to be analysed. Fitting spectra with overlapping peaks to 2D Gaussian functions can be unreliable and/or highly labour intensive. Likewise, CLS analysis can be unreliable for overlapping peaks. NLS analysis is more suitable for systems with sufficiently low anharmonicity that there is some overlap between v=0-1 and v=1-2 peaks. In the example shown above in **Figure 23** the most suitable approaches would be CLS or 2D-Gaussian fitting, in fact all of the example 2D-IR spectra shown in this chapter were generated using **Equation (21)**.

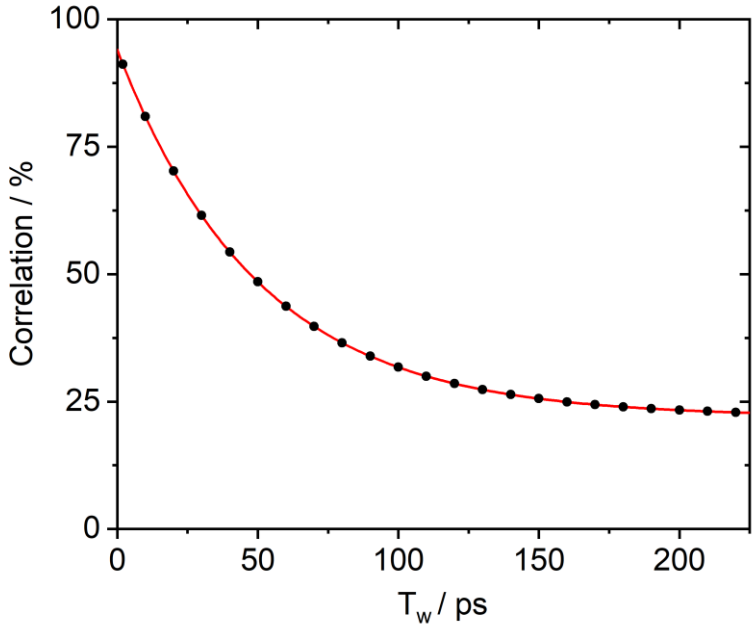

Figure 24 *Example of an FFCF plot for data obtained from spectral diffusion analysis. Black dots indicate correlation data points obtained from 2D-IR spectra, and the red line corresponds to the monoexponential fit.*

The example FFCF shown above in **Figure 24** is typical of a vibrational mode undergoing spectral diffusion and can provide a number of pieces of useful information about the system. Firstly the time constants obtained from fitting the exponential decay can inform on the rate of physical processes in the surroundings of the probed vibrational mode, this could be the reorganisation of solvent molecules or main chain fluctuations of the protein matrix.[122–125] Secondly, the timescale with which the correlation levels off is informative as theoretically it should reach zero if given sufficient time, however plateauing at a non-zero correlation as in **Figure 24** is often observed. This indicates the occurrence of processes too slow for the experimental timescale to observe. Thirdly, if the initial correlation value is less than one (i.e., when $T_w = 0$) then this indicates the occurrence of structural fluctuations that are too rapid for the experiment to observe (i.e., faster than the laser pulse duration).[111,112,114]

2.3.5 Pump-probe IR spectroscopy

While both pump-probe and 2D-IR spectroscopy use a four-wave mixing approach, their key differences lie in the implementation of the pump pulse and the pump-probe delay time. Essentially, in 2D-IR spectroscopy a narrowband pump pulse is scanned to generate the second frequency axis forming a two-dimensional plot at a fixed T_w, while in pump-probe IR spectroscopy a broadband pump pulse is used and an overlay plot is formed by varying the value of T_w, an example of which can be seen below in **Figure 25**. More specifically pump-probe spectroscopy uses a four wave mixing approach in which the first two excitation fields ($\vec{k}_1$ and $\vec{k}_2$) are degenerate and temporally overlapped. [111] Collectively the first two excitation fields are referred to as the pump pulse and the third excitation field ($\vec{k}_3$) is the probe pulse.[111]

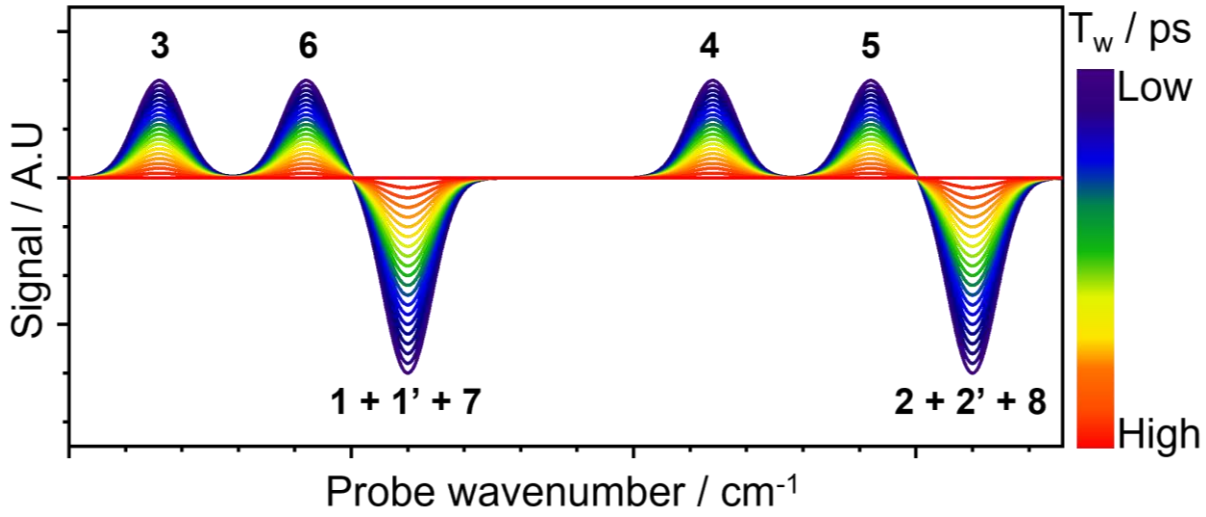

Figure 25 *Example of idealised pump-probe spectra coloured by pump-probe delay time (T_w) as indicated by the scale bar. The positions of peaks and their assignments (shown in bold) are consistent with the 2D-IR spectra shown in* ***Figure 17*** *and* ***Figure 20****.*

As the pump pulses are temporally overlapped (i.e., t_1=0) Feynman pathways for the excitation process cannot be separated, and a population state is created. Following the pump-probe delay time (T_w or t_2) the probe pulse can interact with either of the population states, $|0\rangle\langle 0|$ or $|1\rangle\langle 1|$. Vibrational relaxation can occur

during the pump-probe delay time, the probability of vibrational relaxation occurring increases with advancing T_w. It follows that the final coherent state created by the probe pulse depends upon the extent of vibrational relaxation that occurred during T_w thus by varying T_w the vibrational lifetime (T_1) of a mode can be measured.[126–128]

Pump-probe and 2D-IR spectroscopy are complementary techniques. In distinguishing coupling peaks (e.g., $|10\rangle \rightarrow |11\rangle$) in pump-probe spectra from excited state absorption peaks (e.g., $|10\rangle \rightarrow |20\rangle$) it is often necessary to reference the corresponding 2D-IR spectra, however the true utility of pump-probe spectroscopy is in the analysis of signal decay. By plotting the decay in amplitude of a particular signal as a function of T_w and fitting the resultant plot to an appropriate exponential function, time constants (T_1) can be obtained that reflect the intrinsic vibrational lifetime of the mode, this provides a useful metric for the efficiency with which energy is dissipated from the vibrating atoms.[126–128] An example of a kinetics plot derived from pump-probe data is shown below in **Figure 26**. The same information can also be obtained via 2D-IR spectroscopy, however collecting 2D-IR spectra for a representative series of T_w values would be prohibitively time consuming.

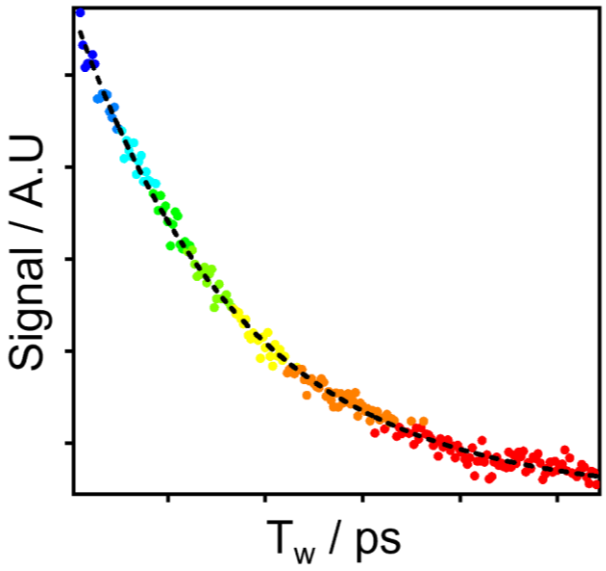

Figure 26 *Plot of the intensity of pump-probe peak* ***5*** *from* ***Figure 25*** *as a function of T_w (coloured dots) and fitted monoexponential function (dashed black line).*

2.3.6 Pump-probe and 2D-IR spectroscopy of simple proteins

There are two general approaches for analysing proteins with IR spectroscopy, the local approach and the global approach. In the local approach a functional group with a single vibrational mode that is not obscured by overlap with solvent or main chain protein vibrations is selected to use as a local reporter of biomolecular structure. It is necessary that the local reporter is close to sites of functional relevance in the protein so the way this approach is implemented varies with the system being studied. Some systems naturally have an active site ligand with an intrinsic vibrational mode that can act as an effective local reporter, for instance Fe-bound CO and CN^- groups in NiFe-hydrogenases[11] and FeFe-hydrogenases,[129] and the Fe-bound NO in NO reductase[130] and nitrosylated catalase.[126,131] Other systems have been analysed after incorporating a local reporter, for instance the N_3^- group of azidophenylalanine in myoglobin[132] and BLUF[133] (blue light using flavin) proteins, and C^{13}=O^{18} labelled glycine in the M2 proton channel protein.[134,135] While non-canonical amino acids have been used

successfully, particular care must be employed that the functionality of the protein is not perturbed by incorporation of the amino acid.

In the global approach, the spectroscopy of the entire protein is analysed usually via the main-chain amide I mode by making use of the coupling patterns that are characteristic of each of the secondary structural motifs. This is demonstrated in **Figure 27** for β-sheets and α-helices. The peptide groups of α-helices couple to form a single extended vibrational mode with its transition dipole moment oriented along the helix direction, there are also modes perpendicular to the helix axis but these are much lower in intensity. The 2D-IR spectra of the amide I region of α-helices (**Figure 27(b)**) comprise a diagonal peak pair centred around

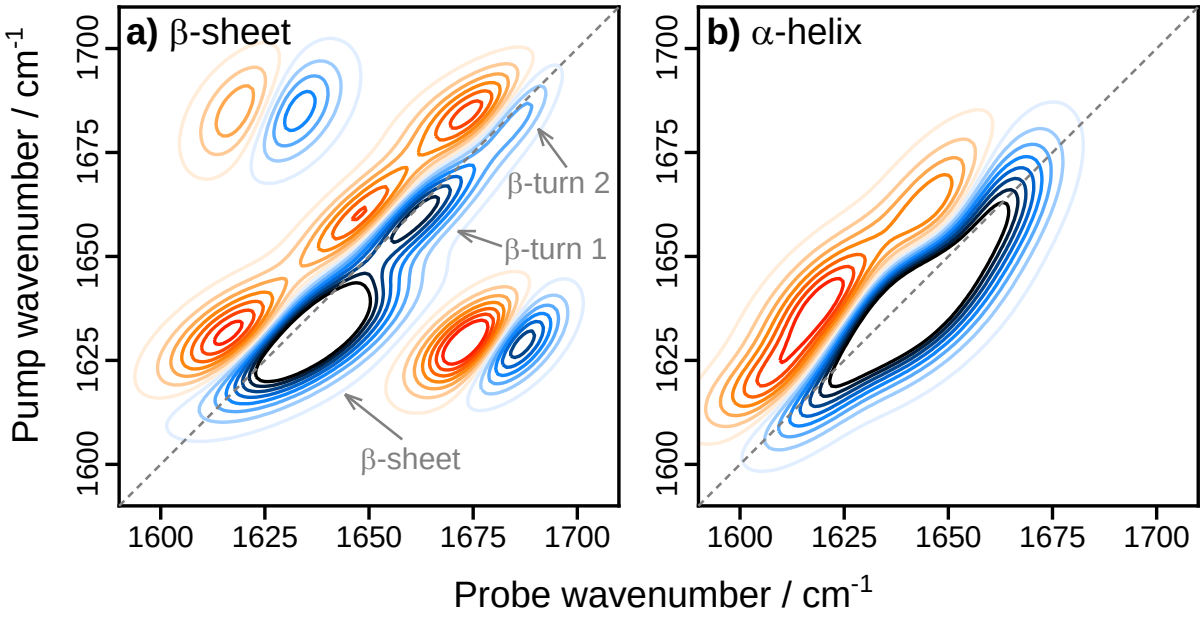

Figure 27 *Example data showing the 2D-IR spectrum of the amide I region of a protein containing* ***(a)*** *β-sheet and* ***(b)*** *α-helix secondary structures.*

1650 cm^{-1} that is very broad and distorted in shape. The 2D-IR spectra of the amide I region of β-sheets (**Figure 27(a)**) comprises three diagonal peak pairs centred around 1630, 1660 and 1690 cm^{-1} corresponding to the β-sheet, β-turn 1 and β-turn 2 amide I modes, respectively.[136] Coupling between β-sheet and β-

turn 2 amide I modes causes off-diagonal peaks that give β-sheet proteins their characteristically Z-shaped amide I spectra.[136]

Binding of the anti-HIV drug rilpivirine to HIV reverse transcriptase (HIV-RT) has been studied with 2D-IR spectroscopy via the local approach by using rilpivirine's chemically distinct CN moieties as local reporters. It was found that the CN groups of complexed rilpivirine/HIV-RT (**Figure 28**) displayed complex vibrational dynamics and spectral diffusion spanning from hundreds of femtoseconds to tens of picoseconds. The CN mode for the right hand arm of rilpivirine (**Figure 28(b)**) was shown to display very slow dynamics which was attributed to interactions with the backbone and side chains of HIV-RT in a

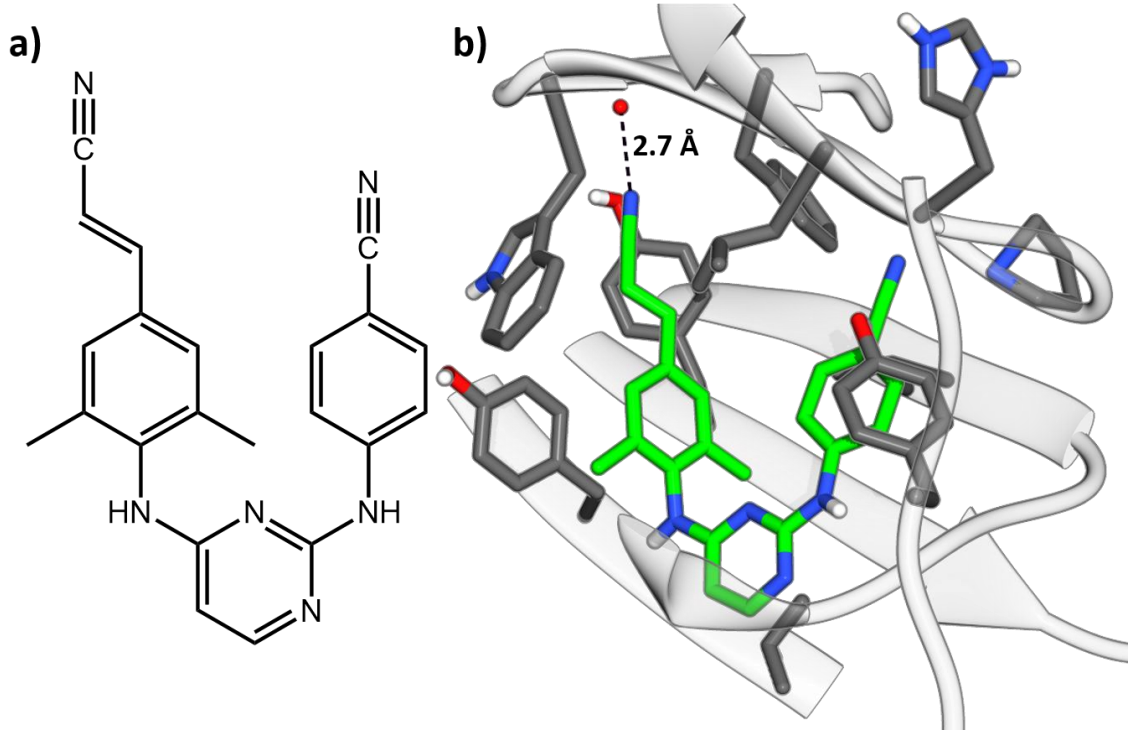

Figure 28 (a) *Skeletal structure of rilpivirine.* ***(b)*** *Crystal structure data (PDB: 4G1Q[137]) of rilpivirine in complex with the active site of HIV-RT, rilpivirine is shown in green stick-form and HIV-RT as white ribbon with selected side chains in grey stick-form, coloured by heteroatom. An H-bond between rilpivirine and an active site water molecule is indicated by a dashed line and the N-O distance stated.*

hydrophobic region of the binding pocket.[138] Whereas the very rapid dynamics observed for the left hand arm of rilpivirine (**Figure 28(b)**) were attributed to H-bonding interactions with a mobile water molecule. The authors postulate that this anchoring H-bond helps to preserve the activity of rilpivirine in active site mutants of HIV-RT.[137]

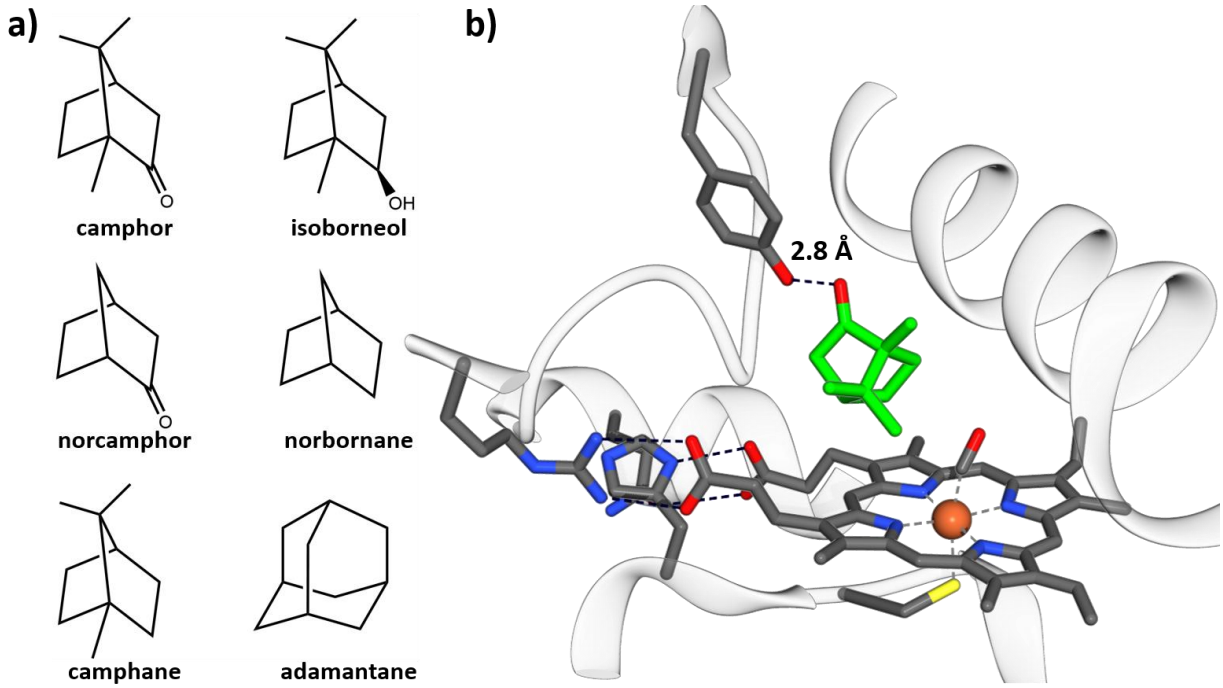

Figure 29 (a) *Skeletal structures of substrates whose complexes with cytochrome P450 were tested with 2D-IR spectroscopy.*[139,140] ***(b)*** *Crystal structure data (PDB: 1T87*[141]*) showing the active site of CO-bound cytochrome P450 in complex with camphor. Cytochrome P450 is shown as white ribbon with the heme group and selected side chains in grey-stick form, coloured by heteroatom. Camphor is shown in green stick form. Selected H-bonds are shown as black dashed lines and the camphor-tyrosine distance (O-O) indicated.*

The binding of a range of substrates to cytochrome P450 (**Figure 29**) was studied with 2D-IR spectroscopy by using the spectral diffusion of a ferrous heme bound CO ligand as a local reporter.[139,140] The spectra of substrate-free cytochrome P450 contain three CO signals that were shown to interconvert relatively slowly (nanoseconds or longer), indicating the presence of three distinct

conformational states. [140] The presence of substrate molecules stabilises a single conformational state of cytochrome P450 (leading to the spectra comprising a single CO signal), and within this conformational state the rate of interconversion between structural substates was shown to be increased relative to each of the three conformational states seen in the spectra of substrate-free cytochrome P450. The authors posit that substrate binding lowers the activation energy barrier between structural substates, which facilitates accession of the transition state. The rate of structural interconversion for enzyme complexed with its natural substrate camphor was shown to be up to threefold slower than in the presence of unnatural substrates, the authors postulate that this may account for the lower stereo-/regiospecificity observed for these substrates. In a subsequent study the H-bonding tyrosine residue (**Figure 29(b)**) was mutated to a cyanophenylalanine as an additional active site probe to monitor the influence of the tyrosine-substrate H-bond on molecular recognition.[139] It was found that the tyrosine-substrate H-bond is not crucial to molecular recognition but does however contribute to binding affinity.

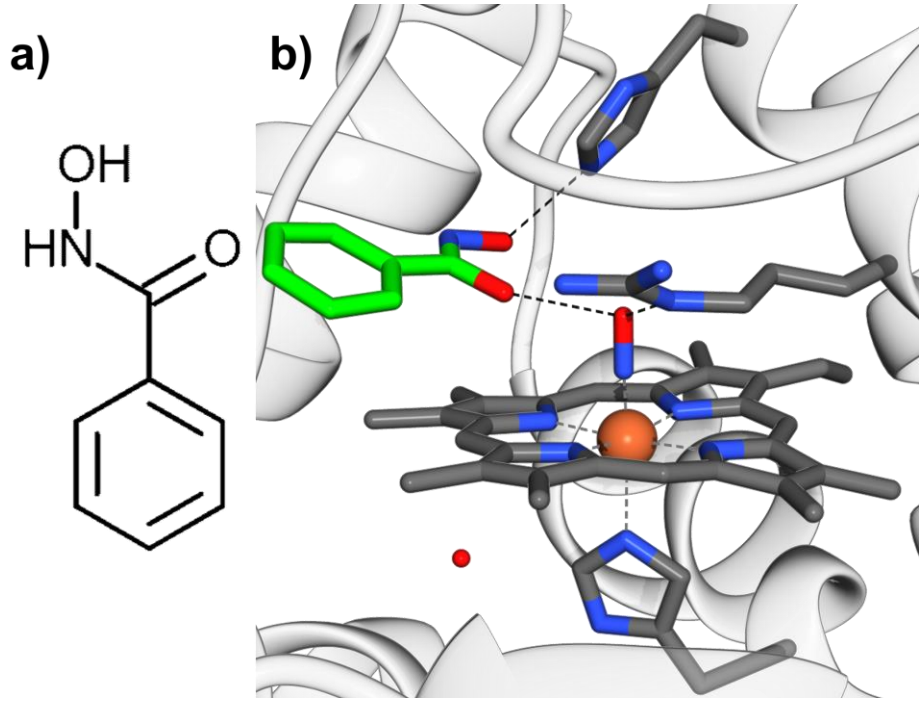

Figure 30 *(a) Skeletal structure of benzohydroxamic acid (BHA) and* ***(b)*** *crystal structure data (PDB: 2ATJ*[142]*) showing the active site of NO-bound horseradish peroxidase (HRP) in complex with BHA. HRP is shown as white ribbon with the heme group and selected sidechains in grey stick form, coloured by heteroatom. BHA is shown in green stick form.*

The active site dynamics of horseradish peroxidase have also been studied using the local approach by means of the ferric heme-bound NO ligand.[143] In this study they demonstrated how the presence of the benzohydroxamic acid ligand (**Figure 30**) could be detected via the spectral diffusion and T_1 time of the NO vibration. Additionally, it was found that for BHA-free enzyme the NO vibrational dynamics were sensitive to H/D solvent isotope exchange, whereas binding of BHA elicited insensitivity to H/D exchange. This showed that solvent can access the active site heme group and that this access is prevented by the presence of the substrate.[143]

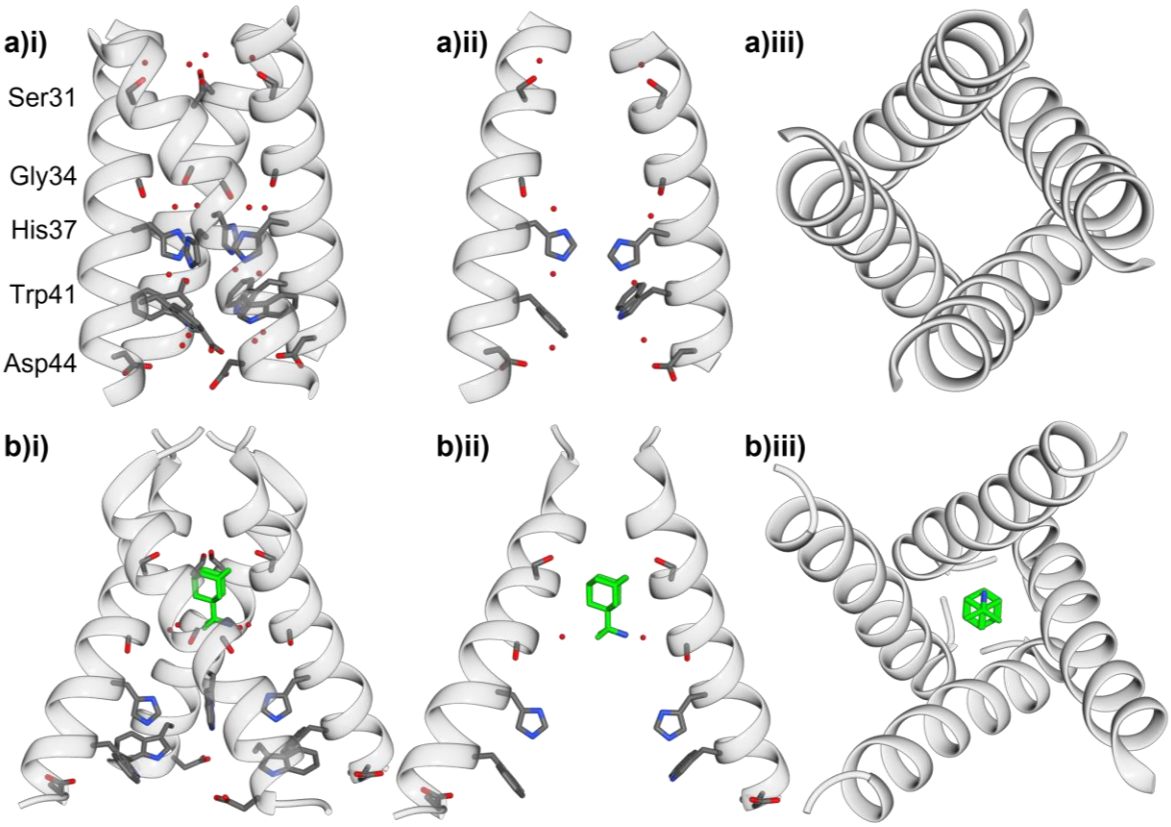

Figure 31 *Crystal structure data showing the M2 proton channel from influenza A in its* ***(a)*** *closed conformation and* ***(b)*** *rimantadine-bound open conformation (PDB: 3LBW*[144] *and 6BOC*[145]*, respectively), viewed as a tetramer* ***(i)****, in cross-section* ***(ii)*** *and down the tunnel axis* ***(iii)****. The protein is depicted in white ribbon form with selected sidechains/groups (labelled) shown as grey sticks, coloured by heteroatom. The rimantadine ligand is shown as green sticks, coloured by heteroatom.*

Influenza A can infect host cells by using the host's endocytosis pathways. Cell surface receptors recognise proteins on the viral envelope and trigger encapsulation of the virus within a lysosome.[146] The acidity of the lysosome interior triggers a conformational change in the M2 channel protein (**Figure 31**), enabling it to transmit protons to the interior of the viral capsid which in turn causes the uncoating and release of viral ribonucleoproteins, thus activating the virus.[146] The structure of the M2 channel protein at various solution pH values and the mechanism of inhibition by rimantidine and 7,7-spiran amine was studied with 2D-IR spectroscopy by using $C^{13}=O^{18}$ isotope labelled Gly34 as a local probe.[134,135] The $C^{13}=O^{18}$ labelling of a particular residue causes a 60-70 cm^{-}

[1] downshift in its amide I vibration (depending on the extent of H-bonding) as well as decoupling it from the exciton with which it would normally associate, making it an effective and non-perturbative local reporter.[147] By analysing the spectral diffusion of the reporter group it was found that acidification caused water molecules within the channel to transition from an ice-like state to a much more mobile state like that in bulk-solvent.[134] This effect was accentuated by the presence of channel blocking drugs, indicating an entropic component to their binding.[135]

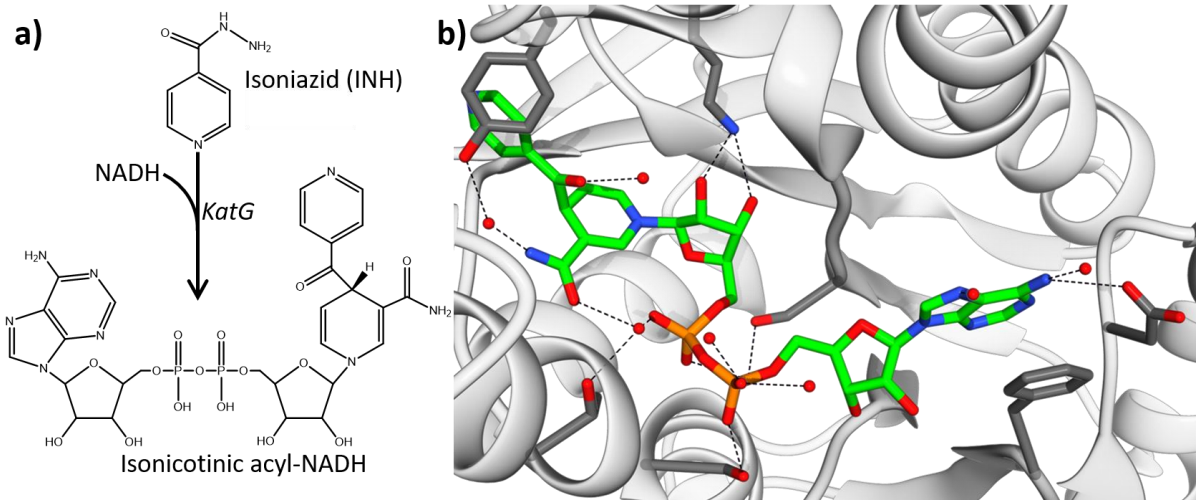

Figure 32 (a) *Skeletal structure of prodrug isoniazid and its activated form as a nicotinoyl-NAD adduct.* ***(b)*** *Crystal structure data (PDB: 4TRO[148]) showing the binding pocket of InhA in complex with nicotinoyl-NAD adduct. InhA is shown as white ribbon with selected side chains as grey sticks, coloured by heteroatom. The ligand is shown as green sticks, coloured by heteroatom. Selected H-bonds are shown as black dashed lines connecting heteroatoms.*

InhA is a carrier protein reductase that is involved in the biosynthesis of the *Mycobacterium tuberculosis* cell wall. Isoniazid is an antibiotic prodrug that when activated, via *KatG* catalysed reaction with NADH, inhibits formation of the mycobacterium cell wall by tightly binding to the InhA active site.[148] Inhibitor binding to InhA, and to antibiotic-resistant mutants of InhA, has been explored

with 2D-IR spectroscopy using the amide I vibration as a global reporter.[149,150] While inhibitor binding is not associated with significant structural changes in InhA, it was found to cause significant changes in the vibrational coupling associated with β-strand components of the active site Rossman fold of InhA, and these changes in coupling were found to permeate much further than the active site. The authors used molecular dynamics simulations to show that this inhibitor-mediated enhancement of coupling is associated with restriction of the enzyme's flexibility, suggesting that the inhibitors work by locking InhA into an inactive conformation.[149,150] This coupling enhancement was reduced in the spectra of antibiotic-resistant mutants of InhA, suggesting that the resistance mechanism could involve enhancing the enzyme's flexibility in the presence of the inhibitor.[149,150]

2.3.7 Research objectives for pump-probe and 2D-IR spectroscopy of NiFe hydrogenases

From a broad perspective the two principal objectives of this research project are i) to characterise novel spectroscopic markers for active site states under physiologically relevant conditions, and ii) to interpret the structural/functional relevance of the spectral data without relying on extensive computation.

More specifically pump-probe and 2D-IR spectroscopy will be useful for:

i) Assigning transitions of the ν_{CO} and ν_{CN} modes originating from enzyme in the same active site state via the observation of coupling peaks. This process is essential for the detailed evaluation of vibrational transitions. However, unambiguous assignment of transitions originating from the same redox state is not always possible with linear IR experiments, because of the crowded spectra produced by samples

comprising mixtures of states and the difficulties inherent to producing samples containing a single redox state.

ii) Using the polarisation dependence of coupling peaks to extract geometric information relating to the relative orientation of the transition dipole moments of the ν_{CO} and ν_{CN} modes for hydrogenase molecules in solution. This process will serve as a useful adjunct to existing crystallographic data, either validating the orthogonal orientations CO and CN ligands, or by providing examples of enzymes/states for which the solution phase structure diverges from that in the crystal. State specific variation in the geometry of the $Fe(CO)(CN)_2$ moiety could have far-reaching ramifications for our understanding of NiFe hydrogenase catalysis.

iii) Determination of coupling strength between ν_{CO} and ν_{CN} modes via the separation between combination and fundamental bands. While coupling has been inferred from the FT-IR spectra of isotopically labelled hydrogenase,[88] quantifying the differences in coupling strength between active site states could contribute to understanding the roles of CO and CN^- ligands in catalysis.

iv) Quantifying the anharmonicities of ν_{CO} and ν_{CN} modes via the separation between excited state and fundamental transitions will provide information relating to the shape of the potential energy surfaces along CO and CN^- coordinates.

v) Evaluating the waiting time dependence of the 2D lineshapes (inhomogeneous and homogeneous linewidths) for ν_{CO} and ν_{CN} transitions will inform on the rate of structural fluctuations in the local environment of CO and CN^- ligands, providing a measure of the

protein's plasticity in this region and the extent of the conformational constraints it imposes on the $Fe(CO)(CN)_2$ unit.

vi) Assessing the waiting time (T_w) dependence of pump-probe signals will provide vibrational lifetimes for transitions of the ν_{CO} and ν_{CN} modes, providing a metric for the efficiency of energy dissipation away from these coordinates. This will complement existing RR and NRVS data, providing insight in to the extent of association between ν_{CO}/ν_{CN} modes and those in their surroundings (Fe-C/S, main chain amide, etc).

3 Materials and Methods

3.1 Preparation and characterisation of *Ec*Hyd-1

3.1.1 Preparation protocol

Growth

E. coli cells (K12 strain, LF03[55] mutant), featuring a His_6 tag at the 3'-terminus of the gene encoding the Hyd-1 large subunit (HyaB), were streaked onto a lysogeny broth (LB) agar plate (absent antibiotics) and grown at 37°C overnight (~18 hours). A single colony was used to inoculate a starter culture comprising 100 mL of LB media, which was then grown at 37 °C with 180 rpm shaking for 7-8 hours. Four sterile 6 L bottles of LB supplemented with 0.5% (w/v) sodium fumarate and 0.5% (v/v) glycerol were prewarmed at 37 °C without agitation. Each 6 L bottle was inoculated with 25 mL of starter culture and topped up with LB such that only 5 mL of headspace remained. Cells were grown overnight at 37 °C under anaerobic conditions in a stationary incubator (Gallenkamp), until an OD_{600} > 1.5 was reached (typically 18-20 hours).

Isolation

Cells were harvested by centrifugation at 6000 x *g* for 20 minutes at 4 °C (Sorvall Lynx 4000 centrifuge, F-12-6x500 LEX rotor). Each 24 L cell growth produced ~72 g of well cell pellet. The cell pellets from two 24 L cell growths were resuspended in 300 mL of resuspension buffer (0.15 M NaCl, 0.1 M Tris, pH 7.6) and stirred at 4 °C. Once the cells were resuspended sucrose was added (20 g per 100 mL), and the mixture stirred for 30 minutes at 4 °C. Cells were harvested by centrifugation at 8000 x *g* for 30 minutes at 4 °C. Cell pellets were subjected to osmotic shock by resuspension in 600 mL of ice cold water (Pur1te), with stirring at 4 °C for 40 minutes. The solution was adjusted to 0.3 M NaCl, 3% (w/v) Triton X-100, 0.1 M Tris (pH 7.6), 500 µM AEBSF, 50 µM Leupeptin, 1 µM

pepstatin, 10 µg mL^{-1} benzonase, 50 µg mL^{-1} lysozyme, and stirred overnight at 4 °C. The mixture was split into 4 aliquots (~150 mL) and sonicated (Soniprep 150) on ice for 10 x 30 seconds (2 cm probe diameter, amplitude set to 15). Cellular debris was pelleted by centrifugation at 30,000 x *g* for 35 minutes. The supernatant was diluted to 0.15 M NaCl with an equal volume of 0.1 M Tris (pH 7.6), and then made up to 30 mM imidazole.

Purification

Using an Äkta Start (GE Life Sciences), lysate (chilled on ice) was loaded (at 5 mL min^{-1}) using the sample pump onto a pair of 5 mL HisTrap FF Crude column (GE Life Sciences) that had been equilibrated in buffer A (0.15 M NaCl, 0.1 M Tris, 30 mM imidazole, pH 7.6). The column was washed (at 5 mL min^{-1}) with 16 column volumes of buffer A to remove non-specifically bound protein. Specifically bound protein was eluted (at 5 mL min^{-1}) with a 0-100% linear gradient of buffer B (0.15 M NaCl, 0.1 M Tris, 0.5 M imidazole, pH 7.6) over 10 column volumes. Progress was monitored via the 280 nm absorption of elutants. Protein was eluted in 2 mL fractions. Hydrogenase containing fractions were dialysed at 4 °C overnight (for ~18 hours) into imidazole-free buffer (0.15 M NaCl, 0.1 M Tris, pH 7.6) and then concentrated to a volume of 4 mL with a 10 kDa MWCO centrifugal concentrator (Vivaspin 20, GE Healthcare). Using an ÄKTA Explorer (GE Life Sciences) the sample was loaded in 2 mL aliquots at 1 mL min^{-1} onto an S200 16/600 gel filtration column that had been equilibrated in imidazole-free buffer (0.15 M NaCl, 0.1 M Tris, pH 7.6). The sample was eluted in 0.5 mL fractions over a single 120 mL column volume at 1 mL min^{-1}. Hydrogenase containing fractions were identified by native- and SDS-PAGE and then pooled and concentrated to 0.5-1 mM using a 10 kDa MWCO centrifugal concentrator. Protein concentration was determined using the Coomassie (Bradford) Protein Assay using bovine serum albumin (BSA) as calibrant.

3.1.2 Gel electrophoresis

SDS-PAGE samples were prepared using 5xSDS gel loading buffer and boiled prior to loading on to 12 % acrylamide gels. SDS-PAGE gels were run at 150 V for 45-60 minutes, bands were stained using Coomassie Brilliant Blue R-250 dye and SDS-PAGE low-range standards (Bio-Rad) were used as markers.

Precast Native-PAGE gels (Bio-Rad Mini-PROTEAN® TGX™) were run at 150 V for 1-2 hours using Tris-glycine buffer, and either stained using Coomassie Brilliant Blue R-250 dye to reveal all protein bands, or transported into a glove box (Faircrest, O_2 < 10 ppm) and placed overnight in a sealed box containing H_2-saturated buffer comprising 50 mM potassium phosphate (pH 7.6), 90 µM phenazine methosulfate and 60 µM nitroblue tetrazolium. Active hydrogenase present in gel bands oxidises H_2 and transmits electrons via phenazine carrier molecules to the nitroblue blue tetrazolium dye, ensuring only protein bands that contain active hydrogenase are stained.[2] For Coomassie stained native gels the NativeMark Unstained Protein Standard (ThermoFisher) was used.

3.1.3 UV/vis spectroscopy

UV/vis spectra (250-700 nm) were collected using a DeNovix (DS-11 FX+) spectrophotometer using quartz cuvettes with a pathlength of 1 cm. For H_2 gas incubation experiments, samples were exposed to H_2 inside a glovebox and then ported out in stoppered cuvettes for recording UV/vis spectra.

3.1.4 Activity assays

Hydrogen oxidation kinetics were monitored spectrophotometrically at room temperature via the reductive decolourisation of methylene blue inside a glove box (Faircrest, O_2 < 10 ppm).[56,152] First, the extinction coefficient at approximately 626 nm of fully oxidised methylene blue was determined by

measuring the absorbance of methylene blue solutions of different concentration (0, 2, 5, 8, 10, 14, 22 and 25 µM) in mixed buffer (15 mM MES, CHES, TAPS, HEPES and Na acetate at pH 7.6) using a custom-built spectrophotometer containing a narrow band LED.[55] Then, a 2 mL aliquot of H_2-saturated solution containing 25 µM methylene blue in mixed buffer (pH 7.6) was injected into a cuvette (polystyrene, 3 mL volume, 10 mm optical path length, Fisher) through a subaseal-lid. To the cuvette was added 10 µL of enzyme solution. The cuvette was placed inside the custom-built spectrophotometer. The H_2-oxidation activity was monitored via the concomitant reduction of methylene blue.

3.1.5 Cyclic voltammetry (CV)

Electrochemical experiments were performed in a similar manner to those described previously.[56] A glovebox (Faircrest, O_2 < 10 ppm) with a three-electrode setup featuring a saturated calomel reference, platinum counter and pyrolytic graphite edge (PGE) working electrode (0.03 cm^{-2} geometric disk area) was used. Experiments were performed using a water-jacketed, gas-tight glass electrochemical cell filled with mixed buffer comprising 100 mM NaCl and 15 mM MES, CHES, TAPS, HEPES and Na acetate at pH 7.6. The temperature of the cell was maintained at 30°C using a water circulator and the atmosphere maintained with a flow of approximately 1 cm^3 s^{-1} of 100% H_2 gas. The (PGE) electrode surface was prepared by abrasion with sandpaper (Norton) before application of 2 µL of 20 µM enzyme solution, the enzyme was left to adhere to the surface for approximately 30 s before rinsing off the excess using 200 µL of buffer. The working electrode was rotated at 3000 rpm using an Origatrod rotator (Origalys) to ensure that catalysis was not rate limited by mass transport

of substrate/product. Measurements were performed using an Ivium CompactStat potentiostat using IviumSoft software.

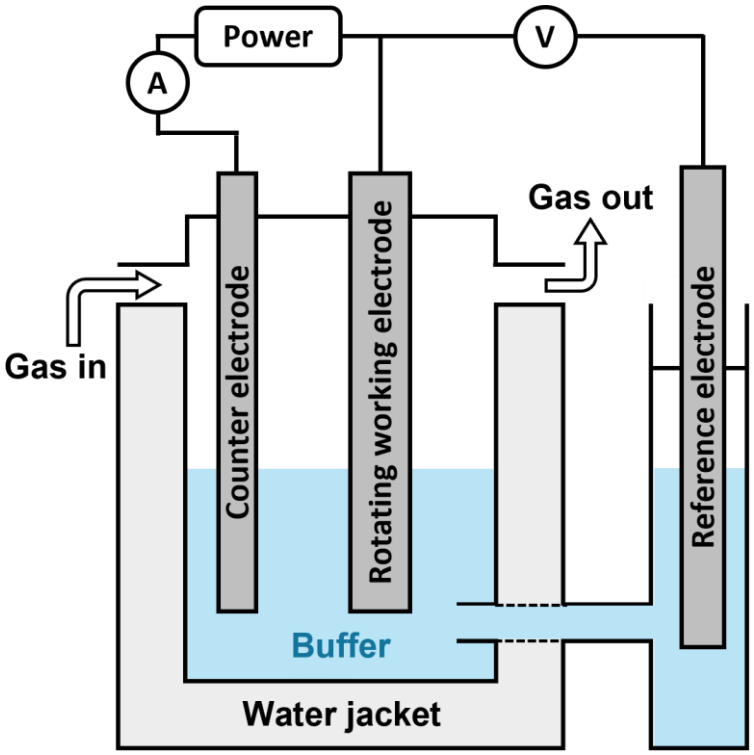

Figure 33 *Schematic of the experimental setup used for protein film electrochemistry experiments.*

3.1.6 Cryo-electron microscopy

1.2/1.3 UltrAuFoil grids were glow discharged (PELCO easiGlow) for 90 s on each side using atmospheric gas before mounting in Vitrobot tweezers. 1 mg mL^{-1} Hyd-1 aliquots were defrosted and 2.5 µL placed onto the grid, blotted (4°C, 100% humidity), and plunged into liquid ethane. Blot time was 3 s and blot force was constant at -5. Data collection was performed on a Glacios microscope operated at 200 kV. One exposure was collected per hole, and the autofocus routine was run every 10 µm. A nominal magnification of 120K, spot size of 6, illuminated area of 1 µm were used and data were collected at a calibrated pixel size of 1.2 Å. The total fluence was of 50.0 electrons/ $Å^2$. A total of 921 EER movies were collected. The Relion pipeline was used for all image processing. Whole micrograph motion correction and damage weighting were performed

using the implementation of MotionCor2 in Relion. Initial CTF values were determined with CTFFIND4 and the Laplacian-of-Gaussian (LoG) filter was used to select an initial set of particles. 2D classification was used in multiple rounds.

3.2 IR spectroscopy of *Ec*Hyd-1 and *Re*RH

3.2.1 FT-IR

FT-IR spectra of *Ec*Hyd-1 samples were collected in transmission mode using a Bruker Vertex 70 spectrometer featuring a Michelson interferometer and a single element detector, as shown below in **Figure 34**.

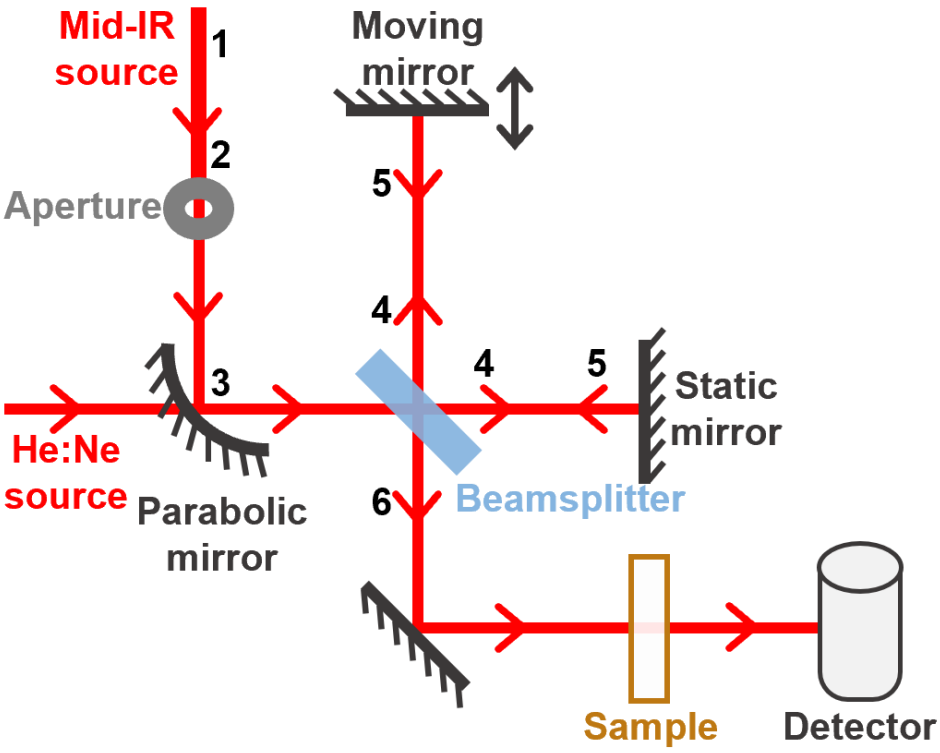

Figure 34 *Schematic of an FT-IR spectrometer featuring a Michelson interferometer.*

Infrared spectroscopy experiments on *Ec*Hyd-1 were conducted using a Harrick cell featuring CaF_2 windows and a PTFE spacer that gave an optical pathlength

of 50 µm. The Harrick cell was filled with 25 µL of 1.0 mM *Ec*Hyd-1. IR absorption spectra were recorded in transmission mode at room temperature with a spectrometer resolution of 2 cm^{-1}. The empty spectrometer was used as a background. Sample and background spectra were averaged over 400-800 scans (the same number for each), corrected for contributions from residual water vapour before fitting and subtracting a polynomial baseline to remove the effects of absorptions due to the solvent. The FT-IR data processing procedure is shown in **Figure 35**.

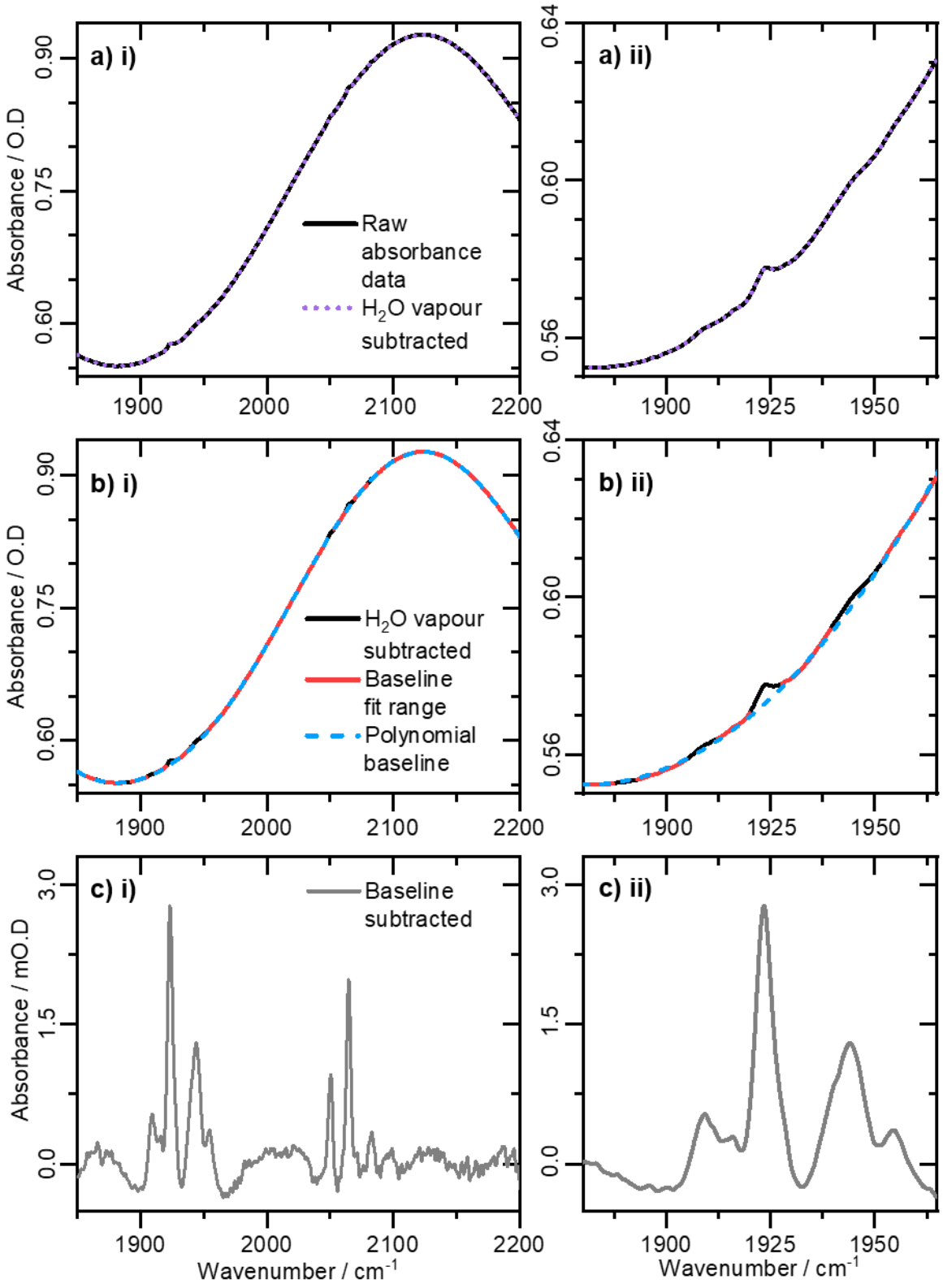

Figure 35 *FT-IR data processing, showing* ***(a)*** *the removal of residual water vapour,* ***(b)*** *the fitting of a polynomial baseline and* ***(c)*** *the spectrum following baseline subtraction for* ***(i)*** *the full range and* ***(ii)*** *a zoomed in view of the CO region.*

For FT-IR gas cycling experiments approximately 25 µL of 1 mM as-isolated *Ec*Hyd-1, pH 7.6, was used to fill a Harrick cell and IR absorption spectra were collected (***Figure 69*** in 5.3.2). Gas cycling experiments were then performed on the same sample of enzyme by first porting a 75 µL aliquot of *Ec*Hyd-1 into a glovebox (Faircrest, O_2 < 10 ppm) and exposing it to an active flow of 100% H_2 for 2 hours and then leaving the enzyme under a quiescent 100% H_2 atmosphere for 18 hours at 4 ^oC. The Harrick IR cell was then filled (approx. 25 µL) with H_2-exposed *Ec*Hyd-1 inside the glovebox, before it was ported out and the FT-IR was recorded (***Figure 69*** in 5.3.2). A 25 µL aliquot of the H_2-saturated *Ec*Hyd-1 was then ported out of the glovebox and exposed to a flow of 100% O_2 for 1 hour at room temperature. The FT-IR absorption spectra of this sample were then recorded and processed using the same method as described above (**Figure 35**).

3.2.2 2D-IR spectroscopy

The ULTRA B spectrometer at the STFC Rutherford Appleton laboratory was used for obtaining all 2D-IR spectra collected during this project.[153] The experimental setup is divided into four stages, i) generation of laser pulses in the oscillator, ii) chirped pulse amplification of laser pulses, iii) conversion of laser pulses into mid-IR via optical parametric amplification-difference frequency generation (OPA-DFG), and iv) 2D-IR beam path. A simplified schematic of the experimental setup can be seen in **Figure 36**.

i) The oscillator

ULTRA uses a custom built titanium sapphire oscillator that produces a train of laser pulses to seed the amplifier.[153] The pulses have a repetition rate of 65 MHz, a duration of 20 fs, and a bandwidth of 50 nm which is centred at 800 nm.

ii) The amplifier

The amplifier (Coherent Legend Elite Duo) is a chirped pulse amplifier that increases the energy of pulses emitted by the oscillator.[153] The amplifier is composed of three parts, i) the stretcher, ii) the regenerative amplification cavity, and iii) the compressor.

The stretcher consists of a pair of gratings arranged such that components of the pulses become temporally separated in a frequency specific manner (chirped), this increases the duration of pulses (from 20 fs to ~1 ps) and decreases the peak pulse power. Decreasing the peak pulse power is critical to preventing damage to optics in the amplification stage.

The regenerative amplification cavity features a cryogenically cooled Ti:Sapphire crystal pumped by the second harmonic ($\lambda/2$=526.5 nm) of a Q-switched Nd:YLF (neodymium-doped yttrium lithium fluoride) laser. A pair of electro-optic modulators (Pockels cells) are used as polarisation gates at the termini of the cavity. A single pulse from the oscillator pulse train is propagated into the amplification cavity where it resonates, making multiple passes through the Ti:Sapphire gain medium. After 10-11 round trips of the cavity maximum amplification is achieved, the Pockels cells then switch the polarisation of the pulse ejecting it from the amplification cavity and onto the compressor gating.

The compression stage consists of a grating and set of optics that reverses the separation caused by the stretcher prior to ejection of the pulse from the amplifier. The amplifier produces a train of pulses with duration ~50 fs, average power 5 W, at a repetition rate of 10 kHz.

iii) OPA-DFG

The (Light Conversion, Topas-C) OPA-DFG converts the 800 nm light from the amplifier into the mid-IR via the process of optical parametric amplification.[113] The key principle of optical parametric amplification is that a non-linear optical

crystal (β-barium borate; BBO) can convert single photons into two photons of lower energy (**Equations (22)** and ***(23)***).

$$\omega_{pump} + \omega_{signal} \rightarrow \omega_{idler} + 2\omega_{signal} \quad \textbf{(22)}$$

$$\omega_{pump} = \omega_{idler} + \omega_{signal} \quad \textbf{(23)}$$

The OPA-DFG composed of three parts, the pre-amplification stage (**1**), the power amplification stage (**2**), and the difference frequency generation (DFG) stage (**3**).

Inside the OPA, the 800 nm output from the Ti:Sapphire is split by a beam splitter into a high intensity pump pulse (a) and lower intensity pulse (b). The lower intensity pulse (b) is split by an additional beam splitter into a higher intensity pump pulse (c) and lower intensity pulse (d). White light is generated from pulse d using a sapphire plate. In the pre-amplification stage (**1**), pump pulse c is used to pump the first BBO crystal and the white light pulse is used to seed the optical parametric amplification process, providing a wide range of potential signal (and idler) frequencies. The desired signal frequency is obtained by adjusting the time delay between pump and white light pulses. In the power amplification stage (**2**), the signal pulse is used to seed the second BBO crystal which is pumped by pump pulse a, giving rise to amplification of the signal pulse and generation of an idler pulse. The signal and idler pulses are separated and transmitted into the difference frequency generation stage (**3**). In this stage the pulses are recombined in a silver gallium sulphide ($AgGaS_2$) crystal, resulting in a broadband, lower frequency pulse with central frequency determined by the angle with which the pulses are incident on the $AgGaS_2$ crystal.

iv) The 2D-IR beam path

2D-IR spectra were acquired using the pseudo pump-probe geometry, as shown in **Figure 36**.[154]

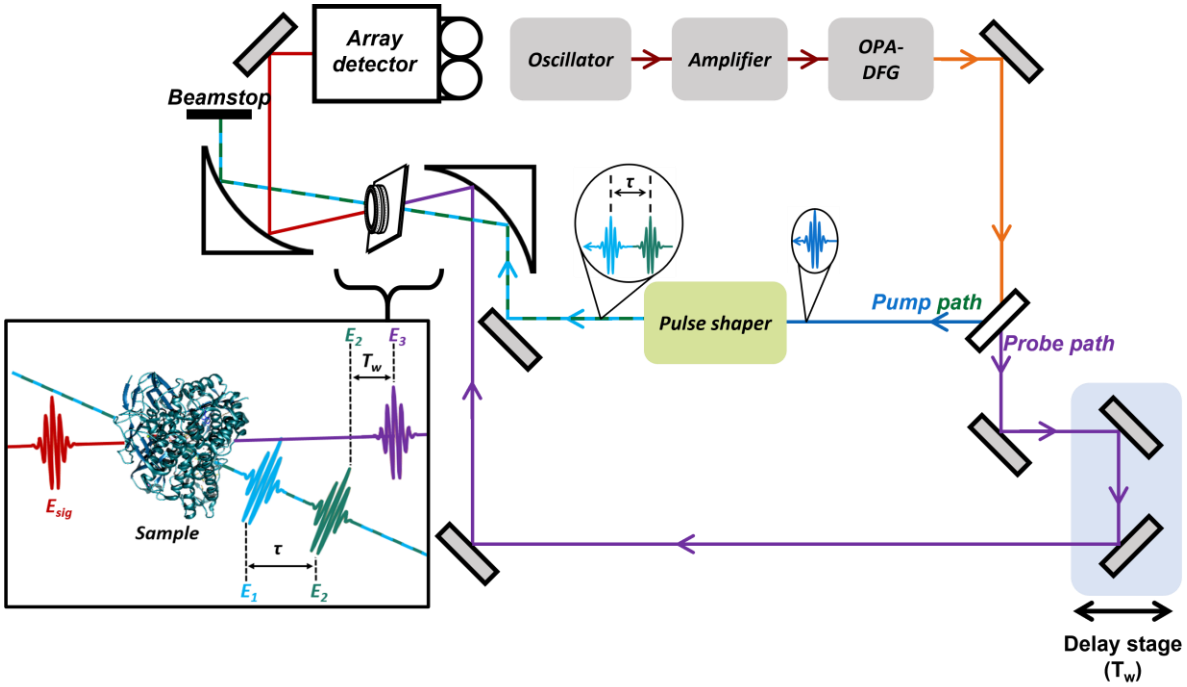

Figure 36 *Schematic of the experimental setup used for collection of time-domain 2D-IR spectra in the pseudo pump-probe geometry at the Rutherford Appleton Laboratory. E_1 and E_2 denote the pump pulses, and E_3 the probe pulse, and E_{sig} the signal pulse. The signal pulse is emitted collinearly with residual probe light.*

The optical parametric amplifier (OPA) generated a train of pulses (300 cm^{-1} bandwidth, centred at 2050 cm^{-1}, with a repetition rate of 10 kHz) that were directed onto a potassium bromide beam splitter (orange segment of beam path in **Figure 36**) which divides the beam into an intense pump-pulse and a less intense probe-pulse. The probe is directed onto an optical delay stage (**Figure 36**, purple beam path) whose position defines the T_w for the experiment, and the pump-pulse is directed into the pulse shaper (**Figure 36**, dark blue beam path). A schematic of the pulse shaper is shown below in **Figure 37**.

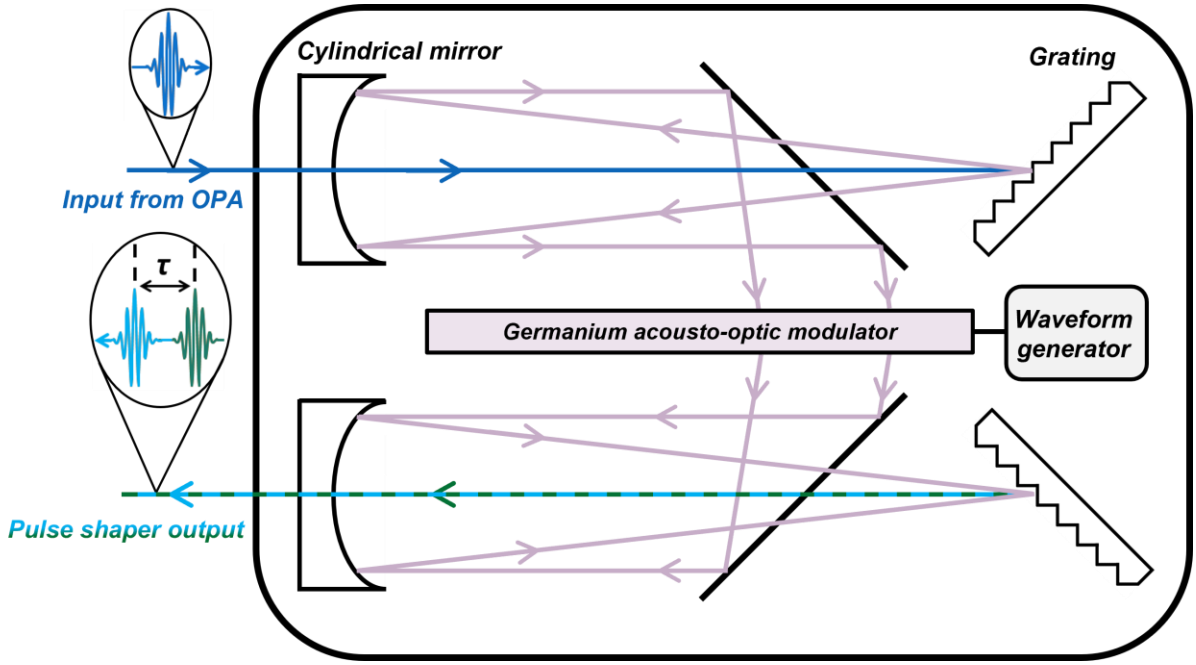

Figure 37 *Schematic representation of an IR pulse shaper.*

Inside the pulse shaper the pump pulse is directed onto diffraction grating, causing its components to be spatially separated according to their frequencies. The dispersed beam is collimated with a cylindrical mirror and directed into the germanium acousto-optic modulator (Ge AOM). The waveform generator applies an acoustic wave to the AOM, which propagates along its length. The speed at which the pump pulse moves across the AOM is such that the acoustic wave appears static, enabling it to act as modulating grating. Light leaving the AOM is focussed on a second grating which Fourier transforms it back into the time domain, and collimated with a second cylindrical mirror before leaving the pulse shaper. By programming the acoustic waveforms applied to the AOM, pump light of specified frequency, phase and amplitude is deflected (**Figure 38**). In this manner, the pulse shaper produces a series of collinear pump pulse pairs separated by the coherence time (τ). The value of τ was scanned in increments of 30 fs from 0 fs to 6 ps, and four-frame phase cycling to minimise the impact of pump light scattered onto the detector. With phase cycling, additional data points are collected for each value of τ in which the relative phase between

pump pulses is varied by a constant factor (here π/4). The background noise is independent of phase, whereas the desired information present in the signal will be out phase in the additional data points, so subtraction of the additional data collected with different phase removes artefacts including the scattering of pump light into the signal field.[111,119,120]

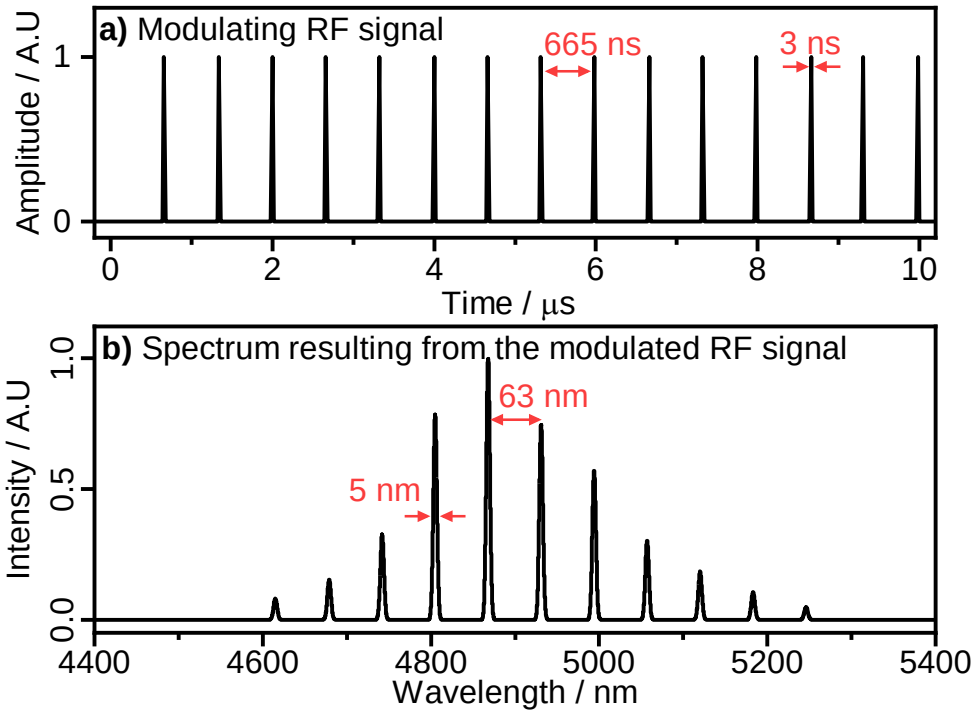

Figure 38 *Example of pulse shaping showing* ***(a)*** *the modulating waveform and* ***(b)*** *the spectrum following modulation.*

The pump and probe beams are focussed in the sample such that residual pump light is directed into a beam stop, and residual probe light onto a grating in a monochromator for subsequent detection with a pair of liquid N_2 cooled 128-element Mercury-Cadmium-Telluride (MCT) array detectors (resolution ~2.5 cm^{-1}, detector 1 centred at 1945 cm^{-1} and detector 2 at 2070 cm^{-1}). Spectra were recorded in the time-domain in so much that the pulse shaper scans the value of τ in regular increments, and for each value of τ the detector records a frequency-domain probe spectrum. The pump frequency axis is recovered by Fourier transforming the probe spectra with respect to τ. The pulse shaper also

modulates the pump pulse train at half the repetition rate of the laser. This means that half of the probe spectra are recorded in the absence of a pump pulse, these are subtracted from those recorded in the presence of a pump pulse to give self-heterodyned spectra. Self-heterodyned detection refers to the collection of information encoded in the frequency and/or phase of light via comparison with a reference beam, termed the local oscillator.

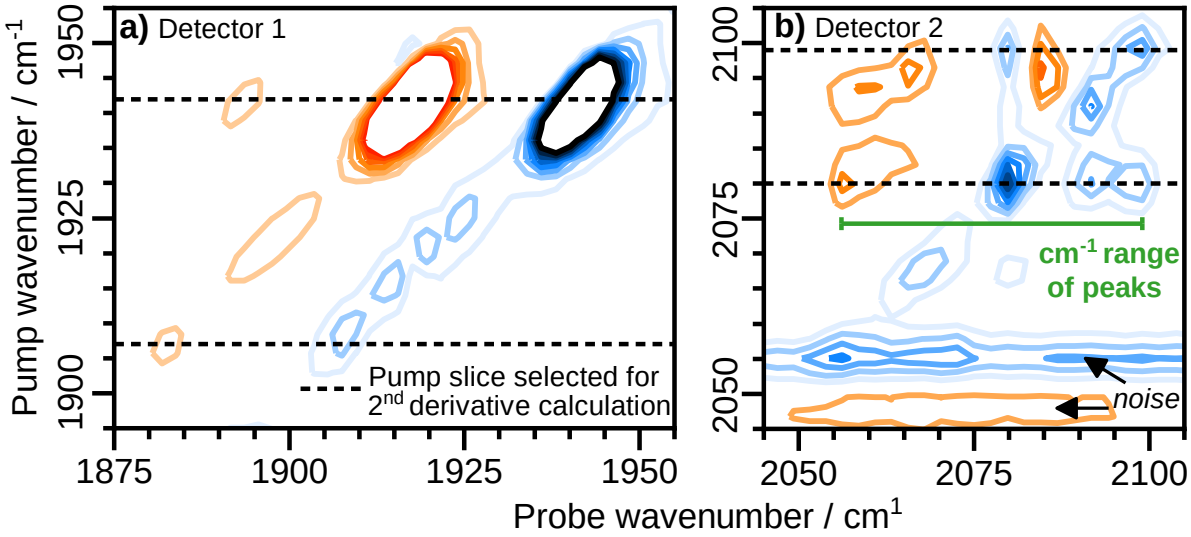

Figure 39 *2D-IR plots showing the diagonal regions of data collected for oxidised EcHyd-1 with* ***(a)*** *detector 1, and* ***(b)*** *detector 2. Dashed black lines indicate the pump slices selected for 2nd derivative calculation in order to determine baseline fitting ranges.*

v) 2D-IR data processing

Fourier transformation of time domain data and subsequent generation of 2D-IR spectra is carried out using a LabView software written by Dr. Gregory Greetham, this software also phases the data and applies window (apodisation) functions. Baseline subtraction of 2D-IR data was carried out using Origin (OriginLab 2018, 2019b and 2022).

The data processing scheme is as follows:

i) In LabView, data from the reference detector was subtracted from that collected with detectors 1 and 2, and the data was exported for subsequent processing in Origin.

ii) 2D-IR contour plots were examined to identify pump slices that contain peaks encompassing the entire probe wavenumber range in which peaks appear, as shown in **Figure 39**.

iii) For each detector the 2nd derivative spectra of the selected pump slices were calculated (**Figure 40(a)**, purple dotted lines) and used to define a range of data points in which peaks are not present to use as a baseline fit range (**Figure 40(a)**, red dotted lines).

iv) A 6th order polynomial baseline (**Figure 40(b)**, blue dashed lines) was fitted to the baseline fit range and subtracted from the corresponding pump slices (**Figure 40(c)**, grey lines).

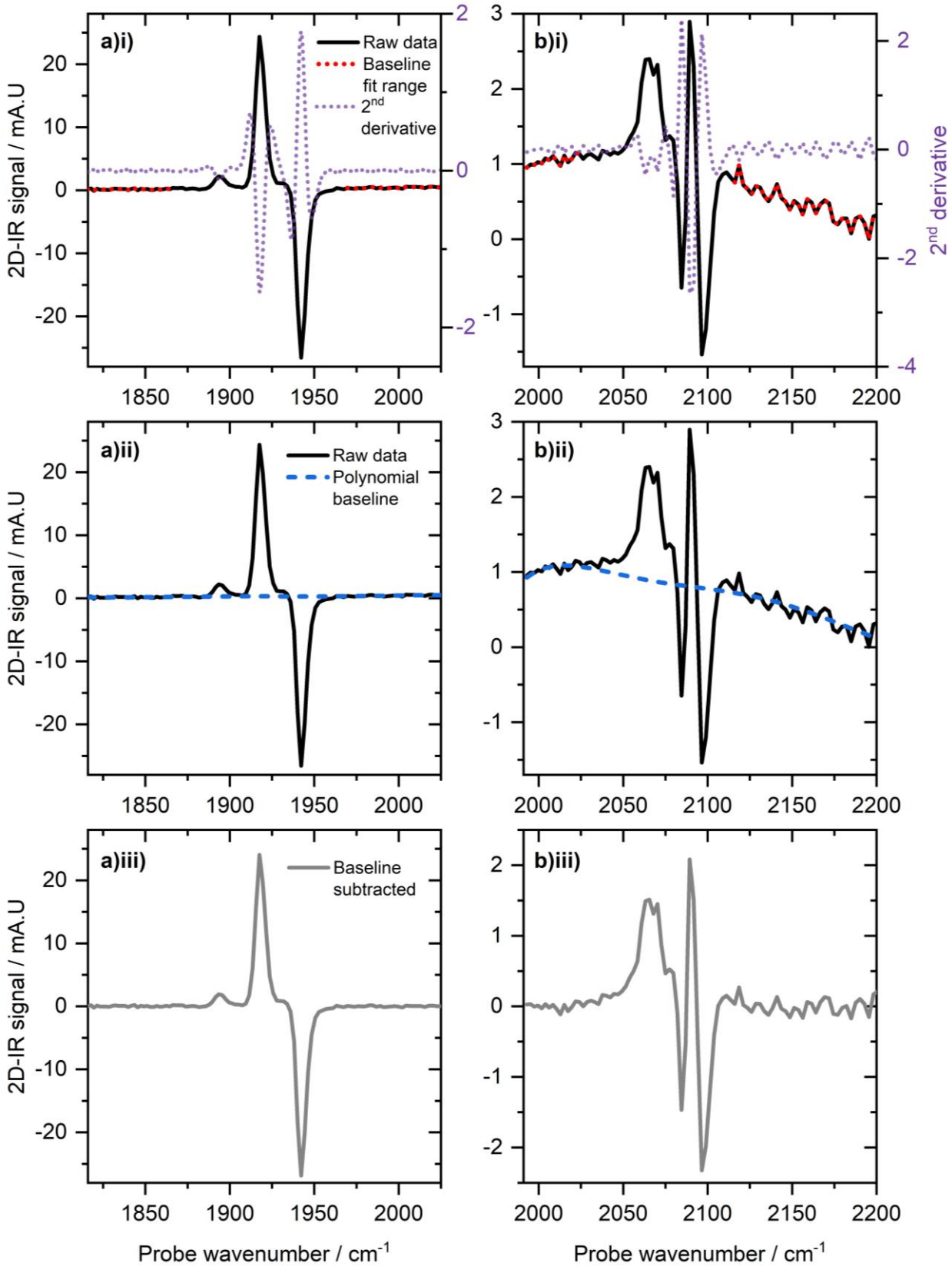

Figure 40 *2D-IR data processing, showing the determination of baseline fit ranges* ***(i)****, fitting* ***(ii)*** *and subtraction* ***(iii)*** *of a polynomial baseline from pump slices collected with detector 1* ***(a)*** *and 2* ***(b)****.*

It is apparent that for some data sets (namely the diagonal region of early T_w detector 1 data) a simpler baseline function would give comparable results. However, the curvature of the background as well as the magnitude of the noise are larger in data collected at later T_w and for off-diagonal regions. For the purposes of comparability the same baseline fitting range and order of polynomial baseline was used for each sample and T_w value. The full 2D-IR spectrum before and after baseline subtraction can be seen in **Figure 41**.

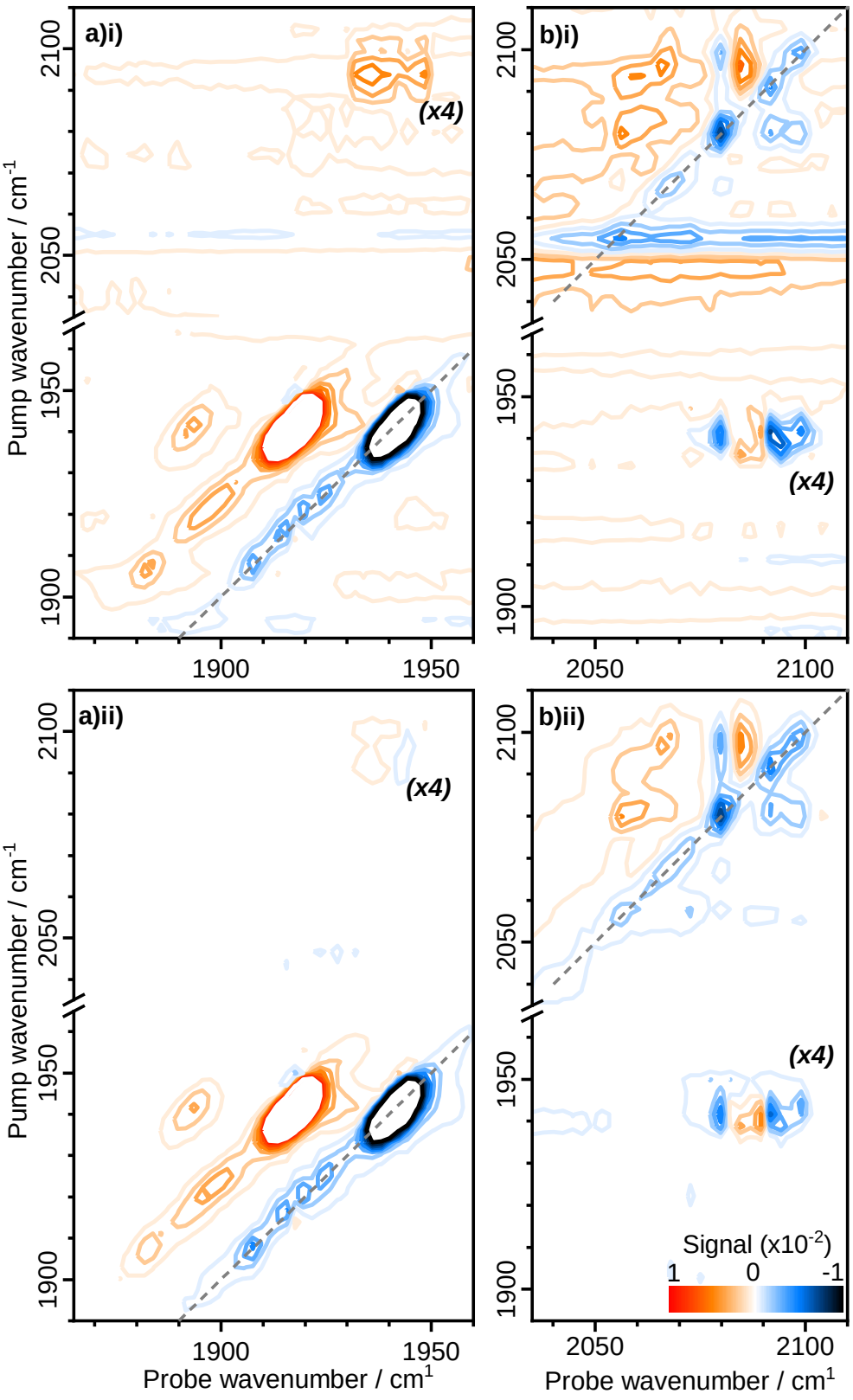

Figure 41 *Early T_w 2D-IR data collected with detector 1* ***(a)*** *and 2* ***(b)****, before* ***(i)*** *and after* ***(ii)*** *subtraction of a polynomial baseline. Signal intensity is indicated by the colour of the contours and signals in off-diagonal regions have been scaled by a factor of four.*

3.2.3 Pump-probe

Ultrafast pump-probe IR spectra were also collected using the ULTRA laser system[153] by setting the pulse shaper to the pump-probe mode, in which the first two excitation fields ($\vec{k}_1$ and $\vec{k}_2$) are degenerate and temporally overlapped and spectra are collected at predetermined values of T_w in a randomised ordering. [111] Mid-IR pulses with a central frequency of 2000 cm^{-1}, bandwidth > 300 cm^{-1}, 50 fs pulse duration and 10 kHz repetition rate were used in all cases. Pump-probe spectra were recorded by scanning the pump-probe delay time (T_w) from -20 to 54 ps in increments of 250 fs. The signal was acquired by dispersing the signal with a spectrograph followed by detection with liquid nitrogen cooled 128-element Mercury-Cadmium-Telluride (MCT) detectors.

The data processing scheme is as follows:

i) In LabView, data from the reference detector was subtracted from that collected with detectors 1 and 2, and the data was exported for subsequent processing in Origin (solid black lines in **Figure 42(i/ii)**).

ii) Early T_w pump-probe spectra were selected (for each detector) and their second derivatives calculated (purple dotted lines in **Figure 42(i)**), this was used to define a range of data points in which peaks are not present to use as a baseline fitting range (red dotted line in **Figure 42(i)**).

iii) For each T_w (with each detector) a 6^{th} order polynomial function (blue dashed lines in **Figure 42(ii)**) was fitted to the baseline fit range, and the resulting baseline subtracted from the raw data to produce the baseline subtracted spectra (solid grey lines in **Figure 42(iii)**).

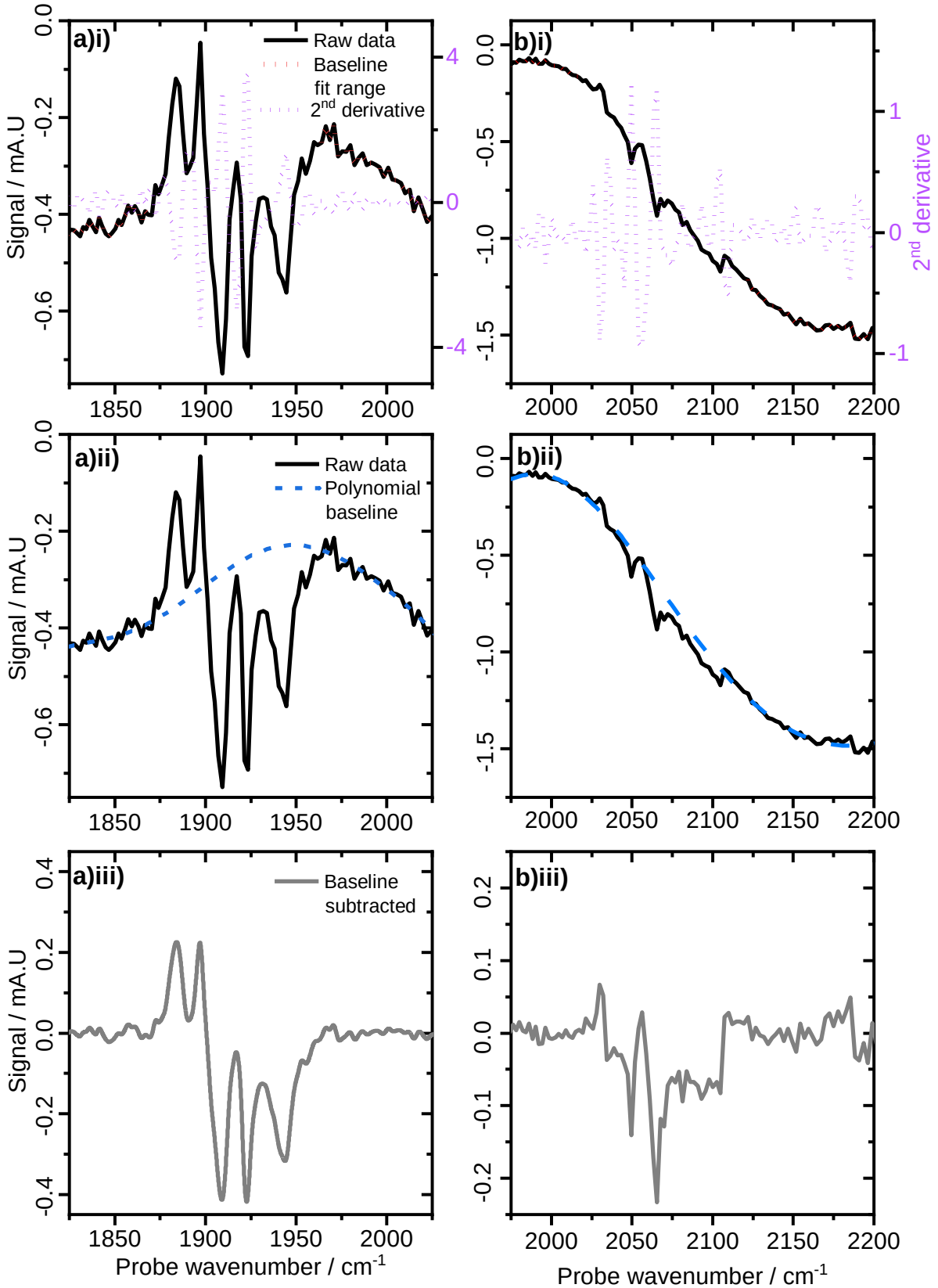

Figure 42 *Pump-probe data processing, showing the determination of baseline fit ranges* ***(i)****, fitting* ***(ii)*** *and subtraction* ***(iii)*** *of a polynomial baseline from early T_w pump-probe slices collected with detector 1* ***(a)*** *and 2* ***(b)****.*

A comparison of raw pump-probe spectra with spectra following polynomial baseline subtraction can be seen below in **Figure 43**.

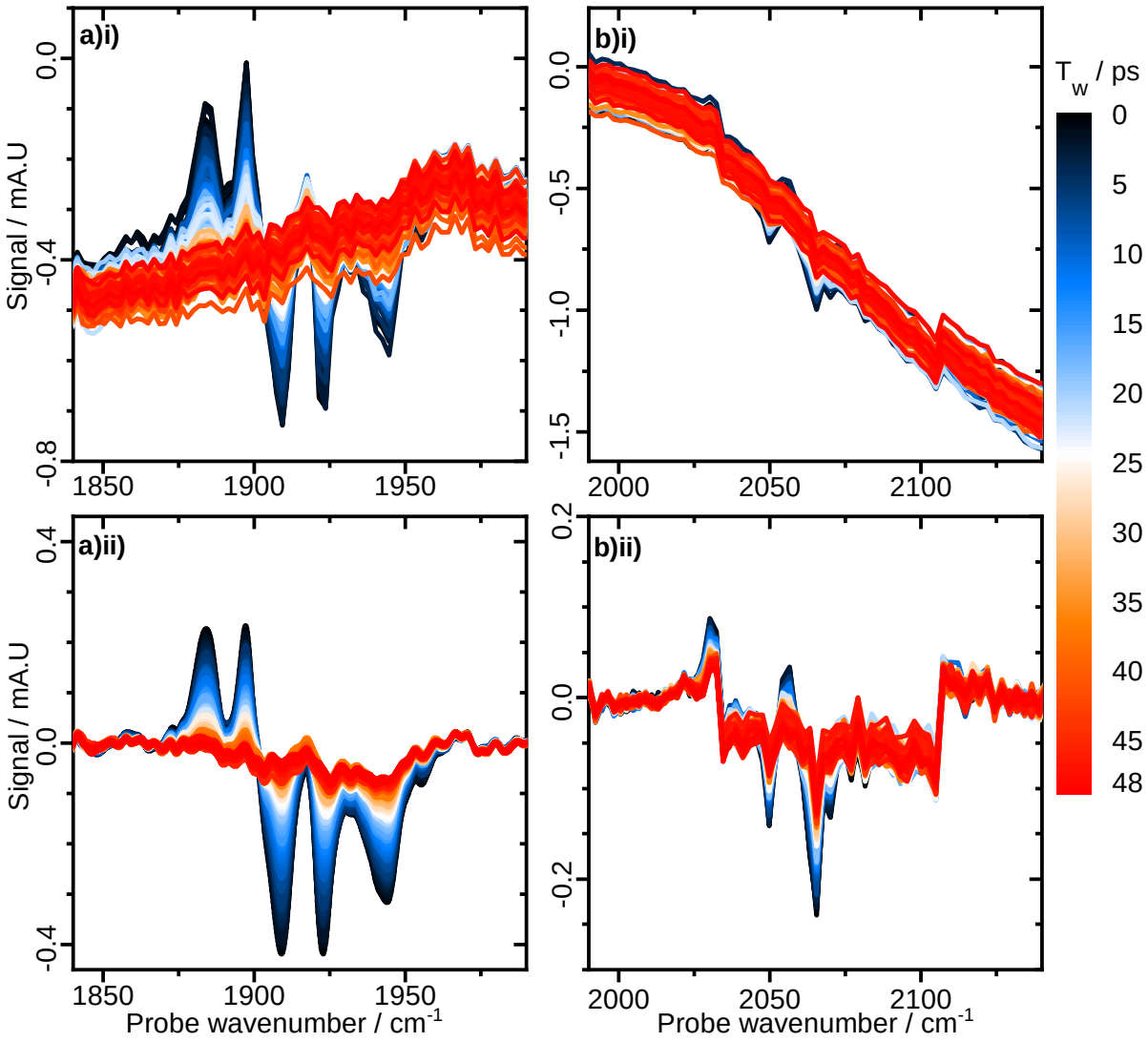

Figure 43 *Pump-probe spectra collected with detector 1* ***(a)*** *and 2* ***(b)****, before* ***(i)*** *and after* ***(ii)*** *polynomial baseline subtraction, coloured by* T_w *(colour bar).*

4 Pump-probe and 2D-IR spectroscopy of as-isolated *Re*RH

For this chapter spectroscopy measurements were performed at the Rutherford Appleton laboratories with Dr. Marius Horch of the Freie Universität Berlin, using enzyme samples prepared by Dr. Janna Schoknecht of the Technische Universität Berlin via established methods.[98,154] This work formed the basis for a publication.[154] All of the data presented in this chapter has been processed from the raw files solely by me. Additionally, all simulations and data analysis have been carried out personally, this enabled the extraction of more detailed information relative to the published paper of which I am a co-author.[154]

4.1 Abstract

Understanding the factors that make NiFe hydrogenases effective H_2-converting enzymes could lead to the development of novel catalysts for sustainable energy approaches. The active site CO and CN^- ligands are ideal IR reporters for local molecular structure, however there is limited structural and dynamic information that can be provided by conventional IR absorption techniques. This study presents the first application of ultrafast multidimensional IR spectroscopy techniques to the study of a NiFe hydrogenase, the model O_2-tolerant regulatory hydrogenase from *Ralstonia eutropha* (ReRH) in the on-cycle, catalytically active H_2-accepting Ni_a-S active site state. With 2D-IR spectroscopy we quantify the anharmonicities of the vibrations and identify that the CO stretching mode is well approximated by a Morse anharmonic potential, enabling the determination of fundamental bond properties including bond dissociation energy, harmonic frequency and curvature of the potential. Additionally we identify strong anharmonic coupling between ν_{CN} modes as well as weak coupling between ν_{CO} and ν_{CN} modes. With IR pump-probe spectroscopy

we observe that the ν_{CO} and ν_{CN} vibrational relaxation dynamics are rapid and also influenced by the surrounding protein architecture, this could be important for the dissipation of energy between rapid reaction steps. Vibrational quantum beats observed in the decay of ν_{CN} signals could be useful for deconvoluting the overlapping signals produced by samples containing complex mixtures of redox states.

4.2 Introduction

The regulatory hydrogenase from *Ralstonia eutropha* (*Re*RH) is a cytosolic H_2-uptake (i.e., group 2) NiFe-hydrogenase that, in its physiological context, performs a sensory role for its parent bacterium.[73,98,155,156] *Re*RH is composed of three subunits HoxB, HoxC and HoxJ with stoichiometry Hox($B_2C_2J_4$).[157] HoxC is the catalytically active large subunit that contains the NiFe active site, HoxB is the small subunit that ligates a trio of [4Fe-4S] clusters and HoxJ is a histidine kinase. H_2 oxidation causes electrons to be transmitted from the NiFe active site, via the FeS clusters, to the histidine kinase subunit.[157–159] HoxJ then acts as a molecular switch and induces a signalling cascade that brings about the upregulation of genes involved in the biosynthesis of energy converting NiFe hydrogenases.[5,13] The poor activity of *Re*RH towards H_2-oxidation and –evolution may be an adaptation to enable the sensing of high partial pressures of H_2.[5] *Re*RH has served as a convenient model system for EPR,[73] IR[96] and resonance Raman spectroscopy[98] studies because of the relative ease with which samples can be trapped in an almost pure redox state. As-isolated samples contain enzyme in the Ni_a-S state with a smaller minority in the Ni_a-C state (***Figure 44***),[160] reduction with H_2 collapses molecules in the Ni_a-S in to the Ni_a-C state,[73] and illumination at cryogenic temperatures converts Ni_a-C in to the Ni_a-L state.[160] The absence of oxidised (Ni_r- or Ni_u-) states of *Re*RH in as-isolated samples is considered to be a consequence of its oxygen tolerance.[161]

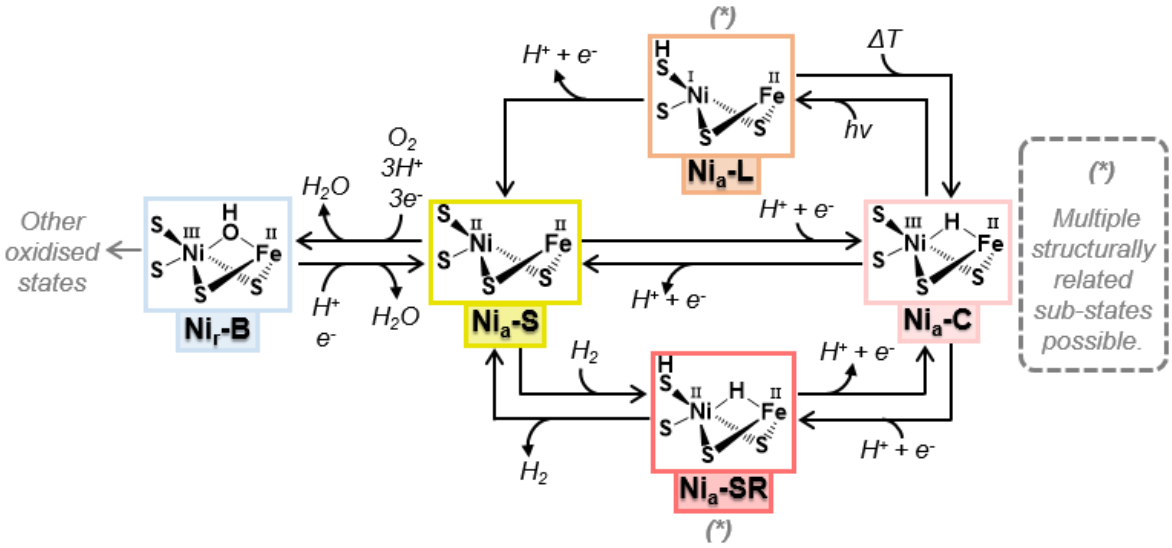

Figure 44 *NiFe hydrogenase catalytic cycle with truncated structures of the bimetallic active site.*

The vast majority of IR studies on NiFe hydrogenases have used linear absorption techniques to investigate the wavenumbers at which transitions appear and the macroscopic conditions that govern the interconversion of redox states (atmosphere, applied potential, temperature, pH), these studies provide only limited time-resolved structural information for the individual redox states.[11] Here we use ultrafast pump-probe and two-dimensional IR spectroscopy to probe *Re*RH in the biologically relevant H_2-accepting Ni_a-S state and investigate a number of previously unexplored observables that are not available to other techniques. Employing the sensitivity and resolution of pump-probe and 2D-IR spectroscopy we characterise a detailed vibrational signature for the ν_{CO} and ν_{CN} modes of the Ni_a-S redox state of *Re*RH, providing novel insights into the CO bond properties and the dynamic interactions between the CO/CN ligands and the surrounding protein architecture.

4.3 Results and discussion

4.3.1 Peak assignments - FT-IR and 2D-IR spectrum diagonal

The overlay of the FT-IR spectrum of as-isolated *Re*RH and an inverted projection of the 2D-IR spectrum diagonal is shown in **Figure 45(a)**. The ν_{CO} region (1850-1975 cm^{-1}) of the FT-IR spectrum (black trace in **Figure 45(a)**) contains three signals, the main signal is at 1943 cm^{-1} and has an absorbance of approximately 1.5 mO.D, a pair of minor signals with absorbance less than 0.3 mO.D are also present at 1934 cm^{-1} and 1960 cm^{-1}.[98,156,161] The ν_{CO} signals at 1934 cm^{-1} and 1943 cm^{-1} are reproduced in the projection of the 2D-IR spectrum diagonal (green trace in **Figure 45(a)**), the 1960 cm^{-1} signal is apparent in the 2D-IR spectrum contour plot (**Figure 45(b)**) but not in the projection of the diagonal. The ν_{CN} region (2025-2100 cm^{-1}) of the FT-IR spectrum contains a pair of signals with 0.6 mO.D and 0.9 mO.D absorbance at 2071 cm^{-1} and 2080 cm^{-1} (respectively), these signals are reproduced in the projection of the 2D-IR diagonal. The signals at 1943 cm^{-1}, 2071 cm^{-1} and 2080 cm^{-1} are consistent with assignment to the CO and the two CN stretching modes of *Re*RH in the Ni_a-S state. [98,156,161] The ν_{CO} signal at 1960 cm^{-1} corresponds to a small minority of *Re*RH molecules present in the Ni_a-C state, and the ν_{CO} signal at 1934 cm^{-1} has been tentatively assigned to the Ni_a-SR_{II} state, it is typical to find both of these minor signals in the IR absorbance spectra of as-isolated *Re*RH. [96,98,156,161]

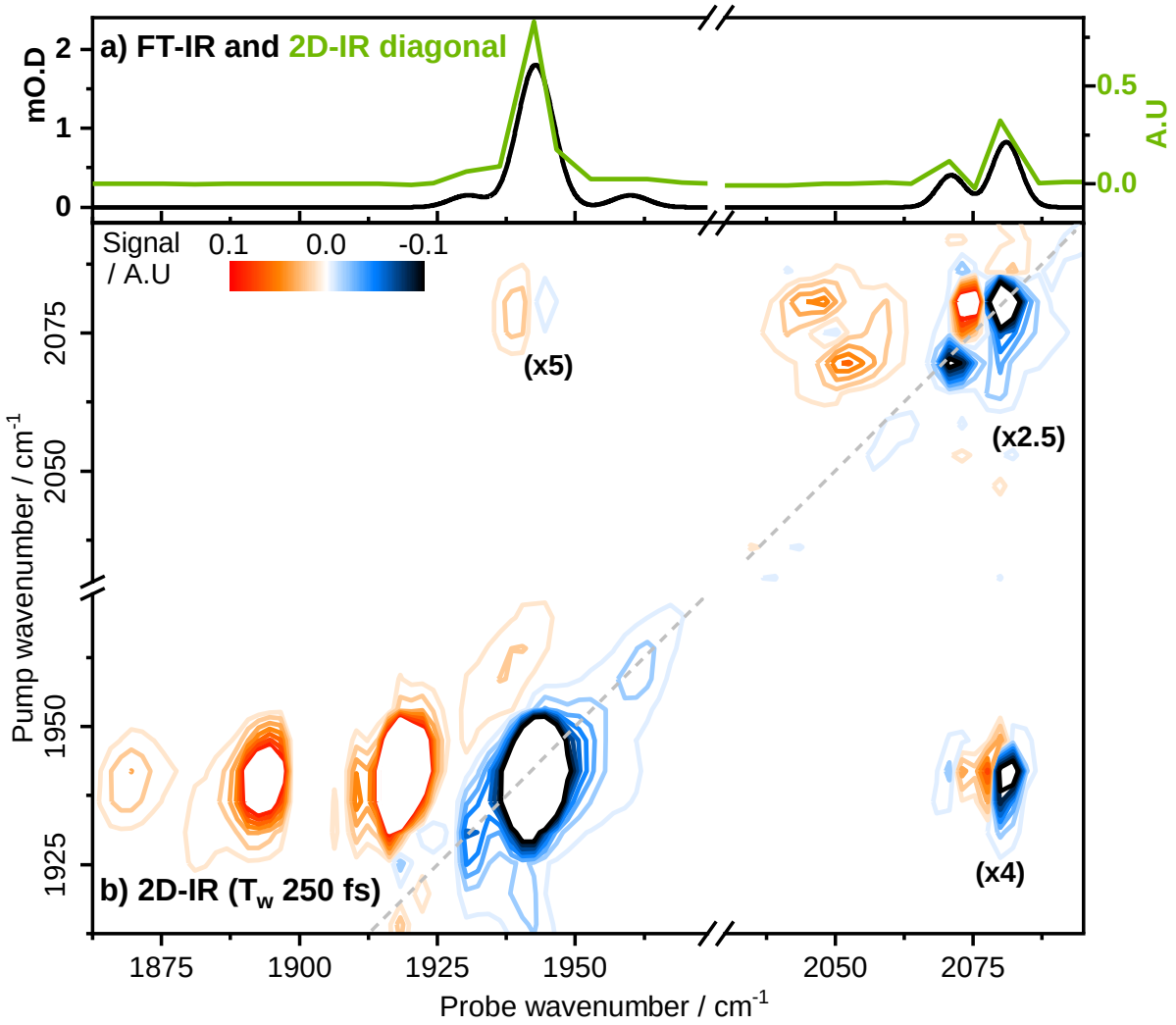

Figure 45 (a) *IR-absorption spectrum (from fitting) of as-isolated ReRH and inverted projection of the 2D-IR spectrum diagonal, shown as black and green traces respectively.* ***(b)*** *2D-IR spectrum of as-isolated ReRH recorded at a waiting time (T_w) of 250 fs. The dashed lines indicate the spectrum diagonal. Numbers in brackets indicate the scaling factors of the three quadrants of the 2D-IR spectrum containing peaks due to ν_{CN} modes in relation to the ν_{CO} region of the spectrum (1900 - 1950 cm^{-1}), which contains the most intense peaks.*

Peaks in the IR absorbance spectrum and on the 2D-IR diagonal correspond to n=0-1 transitions. The major diagonal peak in the ν_{CO} region, at 1943 cm^{-1}, is not connected to either of the minor ν_{CO} peaks (at 1934 and 1960 cm^{-1}) by off-diagonal peaks below (or above) the spectrum diagonal. The absence of such signals indicates that these ν_{CO} peaks are not vibrationally coupled and in fact there is no evidence for exchange between them for values of T_w up to 50 ps.

4.3.2 2D-IR peak assignments - ν_{CO} region

Figure 46 shows a magnified view of the *Re*RH 2D-IR spectra for pump wavenumbers corresponding to ν_{CO} signals at early and late values of T_w (250 fs and 15 ps, respectively).

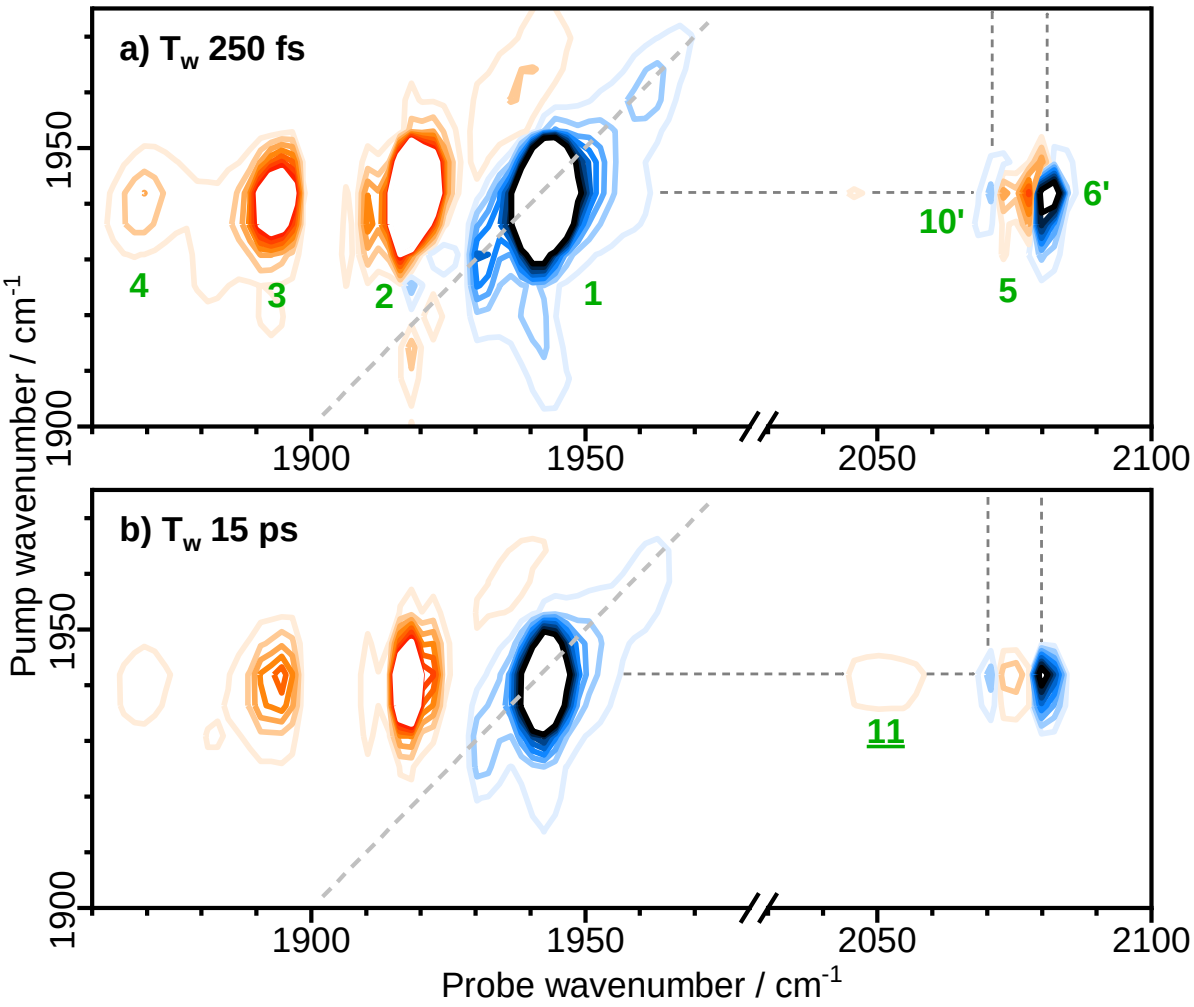

Figure 46 *As-isolated ReRH 2D-IR spectra for the pump wavenumber range coinciding with ν_{CO} bands at **(a)** 250 fs and **(b)** 15 ps pump-probe delay times (T_w). The scaling of bands is the same as in **Figure 45**. Green numbers refer to peak assignments (see **Figure 52**), numbers with apostrophes indicate ground state absorption signals caused by coupling, and underlined numbers indicate excited state absorption signals caused by energy transfer.*

At a waiting time of 250 fs the 1943 cm^{-1} peak (labelled **1** in **Figure 46(a)**) in the ν_{CO} region is accompanied by a trio of positive peaks (labelled **2**, **3** and **4**) that are each shifted downwards along the probe wavenumber axis by 25 cm^{-1}. In the 2D-IR experiment the interaction of the pump pulse with the sample populates

higher vibrational states, enabling the probe pulse to excite transitions that are not normally available in IR absorption experiments at room temperature, as such peaks **2-4** are assigned to v=1-2, v=2-3 and v=3-4 transitions, respectively. The diagonal ground state absorption signal at 1960 cm^{-1} (ascribed to the small minority of Ni_a-C present in the sample) is also accompanied by a positive v=1-2 peak that is downshifted by 22 cm^{-1} to a probe wavenumber of 1938 cm^{-1}. For a pump frequency of 1942 cm^{-1} an additional set of off-diagonal peaks can be observed in the ν_{CN} region of the spectrum (2030-2100 cm^{-1}) which indicate coupling between the ν_{CO} and ν_{CN} modes, as such the $|\nu_{CO}\nu_{CN1}\nu_{CN2}\rangle$ notation is used for describing transitions where ν_{CN1} and ν_{CN2} refer to the higher and lower wavenumber ν_{CN} modes respectively. Using this notation, peaks **1-4** correspond to: $|000\rangle$-$|100\rangle$, $|100\rangle$-$|200\rangle$, $|200\rangle$-$|300\rangle$, $|300\rangle$-$|400\rangle$. At a pump frequency of 1942 cm^{-1} there are four peaks visible in the ν_{CN} region ranging between 2050 cm^{-1} and 2080 cm^{-1} (labelled **10'**, **5**, **6'**,and **11** in **Figure 46**) along the probe wavenumber axis. The most intense of these peaks is a negative peak, **6'**, which has frequency coordinates (pump, probe) of (1942 cm^{-1}, 2080 cm^{-1}). The pump frequency of **6'** matches that of diagonal peak **1** (horizontal dashed line) and its probe frequency matches that of a diagonal peak in the ν_{CN} region (i.e., ν_{CN1} indicated by a vertical dashed line). The same is true of the remaining negative off-diagonal peak, **10'**, although its probe frequency matches that of the other diagonal peak in the ν_{CN} region (ν_{CN2}). The presence of these connecting off-diagonal peaks in early T_w spectra (**Figure 46(a)**) indicates that the CO stretching mode is coupled to both of the CN stretching modes. The positive peak labelled **5** with coordinates (1942 cm^{-1}, 2078 cm^{-1}) in **Figure 46** is assigned to a transition between the n=1 state of the ν_{CO} mode ($|100\rangle$), which is populated by the pump pulse, and a two quantum combination state with one quantum of energy in both ν_{CO} and ν_{CN1} modes (i.e., $|110\rangle$). The difference in wavenumber between a

combination band and its associated ground state absorption signal gives the mixed mode anharmonicity, this quantity is proportional to the coupling strength. Peaks **5** and **6'** exhibit considerable overlap indicating that the coupling between ν_{CO} and ν_{CN1} modes is weak, it is likely that peak **10'** is also accompanied by a combination band that is obscured by overlap. **Figure 47** shows the result of fitting the off-diagonal region (2050-2100 cm^{-1}) of the 1942 cm^{-1} pump slice from the T_w 250 fs 2D-IR spectrum shown in **Figure 46(a)**, for this fitting the positions and widths of the ground state absorption signals were taken from the FT-IR spectrum and the combination bands were permitted to have up to 2 cm^{-1} greater width than their associated ground state absorption signals.

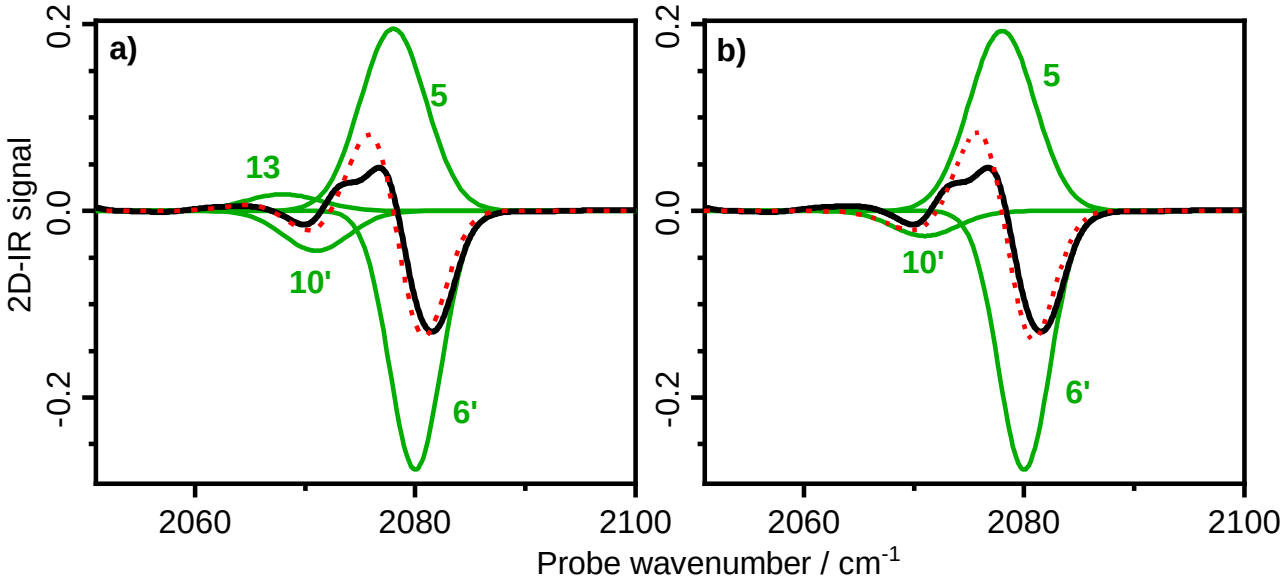

Figure 47 *Fitting of the off-diagonal region of the 1942 cm^{-1} pump-slice from the 2D-IR spectrum recorded with a T_w of 250 fs, with the fit **(a)** including and **(b)** not including the combination band **13**. The solid black line shows the experimental data, solid green lines indicate fitted peaks, and the dashed red line corresponds to the cumulative fitting.*

Fitting of the off-diagonal peaks in this manner corroborates the presence of an obscured combination band (labelled peak **13** in **Figure 47(a)**) and shows the mixed mode anharmonicity between ν_{CO} and both ν_{CN} modes to be less than 2 cm^{-1}, indicating very weak coupling between these vibrations.

In the spectrum recorded with a waiting time of 15 ps, shown in **Figure 46(b)**, an additional off-diagonal peak labelled 11 is present, it has (pump, probe) coordinates (1942 cm^{-1}, 2053 cm^{-1}). The emergence of peak 11 at a later T_w indicates that it is caused by energy transfer; during the delay time population transfer from the pumped n=1 level of the v_{CO} mode to the n=1 level of a v_{CN} mode occurs, this is followed by the probe pulse exciting the n=1-2 transition of the v_{CN} mode. It is not apparent from **Figure 46** whether peak 11 is associated with v_{CN1} or v_{CN2} but it is useful in assigning the region of the spectrum in which pump frequencies coincide with v_{CN} bands, this is shown in **Figure 49** and discussed in detail in the following section (4.3.3).

The transition energies for peaks 1-4 are well represented by a Morse anharmonic potential function (**Figure 48**), which is a good approximation for diatomic molecules with vibrational modes that are highly localised (i.e., uncoupled or weakly coupled to other modes) and have uniformly spaced energy levels (i.e., constant anharmonicity). Fitting the transition energies to a Morse potential enabled the extraction of fundamental bond properties for the CO ligand, these are summarised in **Table 2**, a more detailed procedure for how these quantities are obtained can be found in the appendix.

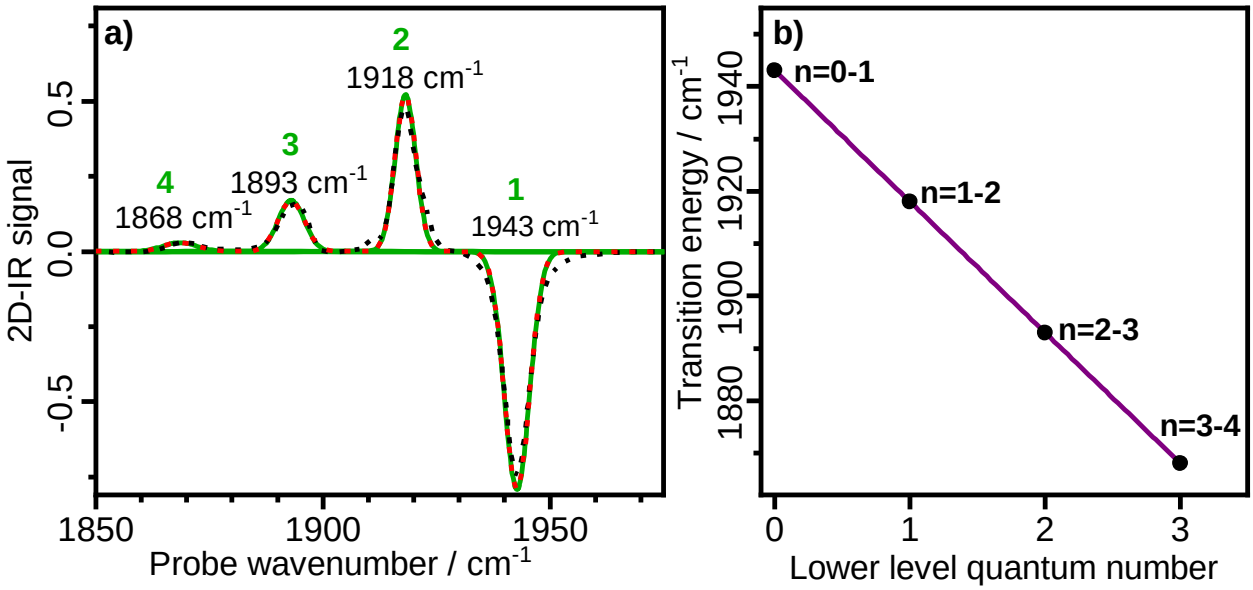

Figure 48 (a) *Fitting the 1942 cm^{-1} pump slice (from the T_w 250 fs 2D-IR spectrum) to determine transition energies for the ν_{CO} mode. Experimental data is shown as a dashed black line, solid green lines indicate fitting of individual peaks and the dashed red line indicates the cumulative fitting.* ***(b)*** *Fitting a function representing the energy level separations of a Morse potential (solid purple line) to experimentally determined transition energies (black dots) for the ν_{CO} mode.*

At 1967 cm^{-1} the harmonic frequency (**Table 2**) is significantly higher than the 1943 cm^{-1} observed for the fundamental transition. The harmonic frequency is a parameter that is typically calculated in theoretical studies simulating the NiFe hydrogenase active site. To date no theoretical studies have accounted for such a large disparity between fundamental and harmonic frequencies, as such this observation could have broad implications for future *in silico* studies.[154]

Table 2 *Bond properties for the CO ligand determined via fitting transition energies to a Morse potential.*

Fundamental frequency / cm^{-1}	Harmonic frequency / cm^{-1}	Dissociation energy / kJ mol^{-1}	Force constant / N m^{-1}	Anharmonicity constant (x10^{-3})
1943	1967	941	1563	6.18

Comparing the Morse fitting derived CO bond parameters with examples from the literature is problematic as i) there is no pump-probe/2D-IR literature data

available for other hydrogenases, and ii) the data available for small molecule hydrogenase mimics are unsuitable as the molecules feature multiple CO ligands, with their spectra indicating strong coupling and no excitation beyond the n=2 level.[123,127,162–164]

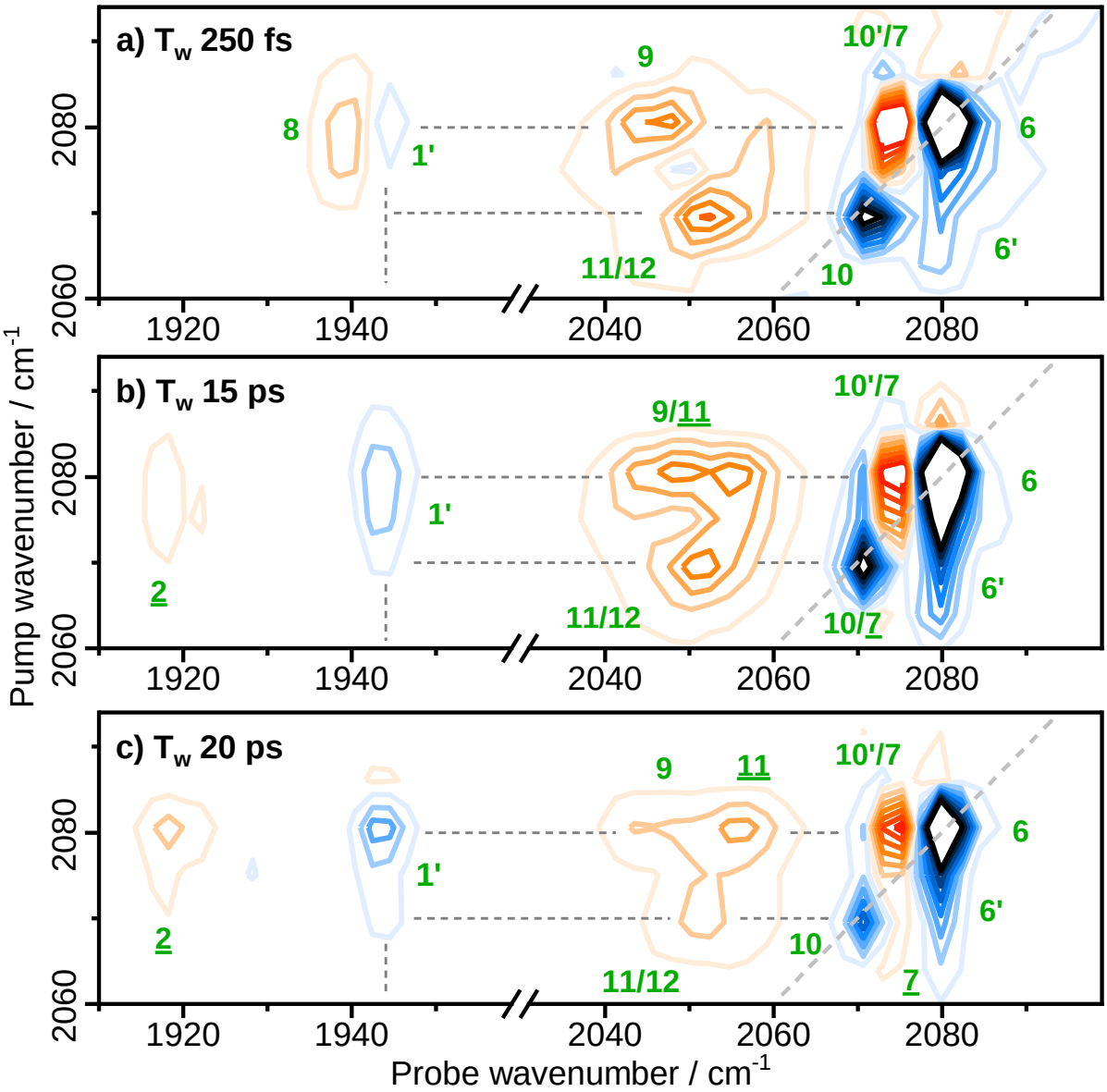

Figure 49 *As-isolated ReRH 2D-IR spectra for the pump wavenumber range coinciding with ν_{CN} bands at* ***(a)*** *250 fs and* ***(b)*** *15 ps pump-probe delay times (T_w). The scaling of bands is the same as in* ***Figure 45****. Green numbers refer to peak assignments.*

4.3.3 2D-IR peak assignments - ν_{CN} region

For pump wavenumbers coinciding with ν_{CN} peaks (**Figure 49**) there are two major peaks on the spectrum diagonal, peak **10** at 2071 cm^{-1} and peak **6** at 2080 cm^{-1}, these are assigned to the $|000\rangle$-$|001\rangle$ and $|000\rangle$-$|010\rangle$ transitions respectively.

First focussing on the higher wavenumber peak (**6**) in the T_w 250 fs spectrum (**Figure 49(a)**), at a pump wavenumber of 2080 cm^{-1} (upper horizontal line) there are five peaks in the off-diagonal region, these are labelled **7**, **10'**, **9**, **1'** and **8**. The positive peak **7** is assigned to the $|010\rangle$-$|020\rangle$ transition, this assignment is corroborated by the emergence of energy transfer peak **7** in later T_w spectra when pumping at 2070 cm^{-1} (**Figure 49(c)**). Overlap causes peak **7** to almost entirely cancel out the negative coupling peak **10'** ($|000\rangle$-$|001\rangle$), however fitting of relevant pump slices (**Figure 51(iii)**) indicates that **7** is centered at 2072 cm^{-1} which gives a single mode anharmonic shift of 8 cm^{-1}. Positive peak **9** at 2047 cm^{-1} is assigned to the combination transition $|010\rangle$-$|011\rangle$ which gives a mixed mode anharmonic shift of 24 cm^{-1}, indicating that the ν_{CN1} and ν_{CN2} modes are strongly coupled. The negative peak labelled **1'** at 1943 cm^{-1} indicates that the ν_{CN1} and ν_{CO} modes are coupled. Positive peak **8** is assigned to the $|010\rangle$-$|110\rangle$ combination transition. Peak **8** overlaps considerably with peak **1'**, however fitting the spectrum in this region (**Figure 50(a)(iii)**) shows that it is centered at 1941 cm^{-1} giving a mixed mode anharmonicity of 2 cm^{-1}, this matches the value obtained when pumping the ν_{CO} mode at 1942 cm^{-1} (**Figure 47**). In the spectra recorded at a T_w of 15 ps and 20 ps, combination band **8** is no longer visible and the energy transfer peaks **11** and **2** grow in. Peaks **11** and **2** correspond to the $|001\rangle$-$|002\rangle$ and $|100\rangle$-$|200\rangle$ transitions (respectively), and are caused by

energy transfer during the delay time from the $|010\rangle$ level to the $|001\rangle$ and $|100\rangle$ levels (respectively).

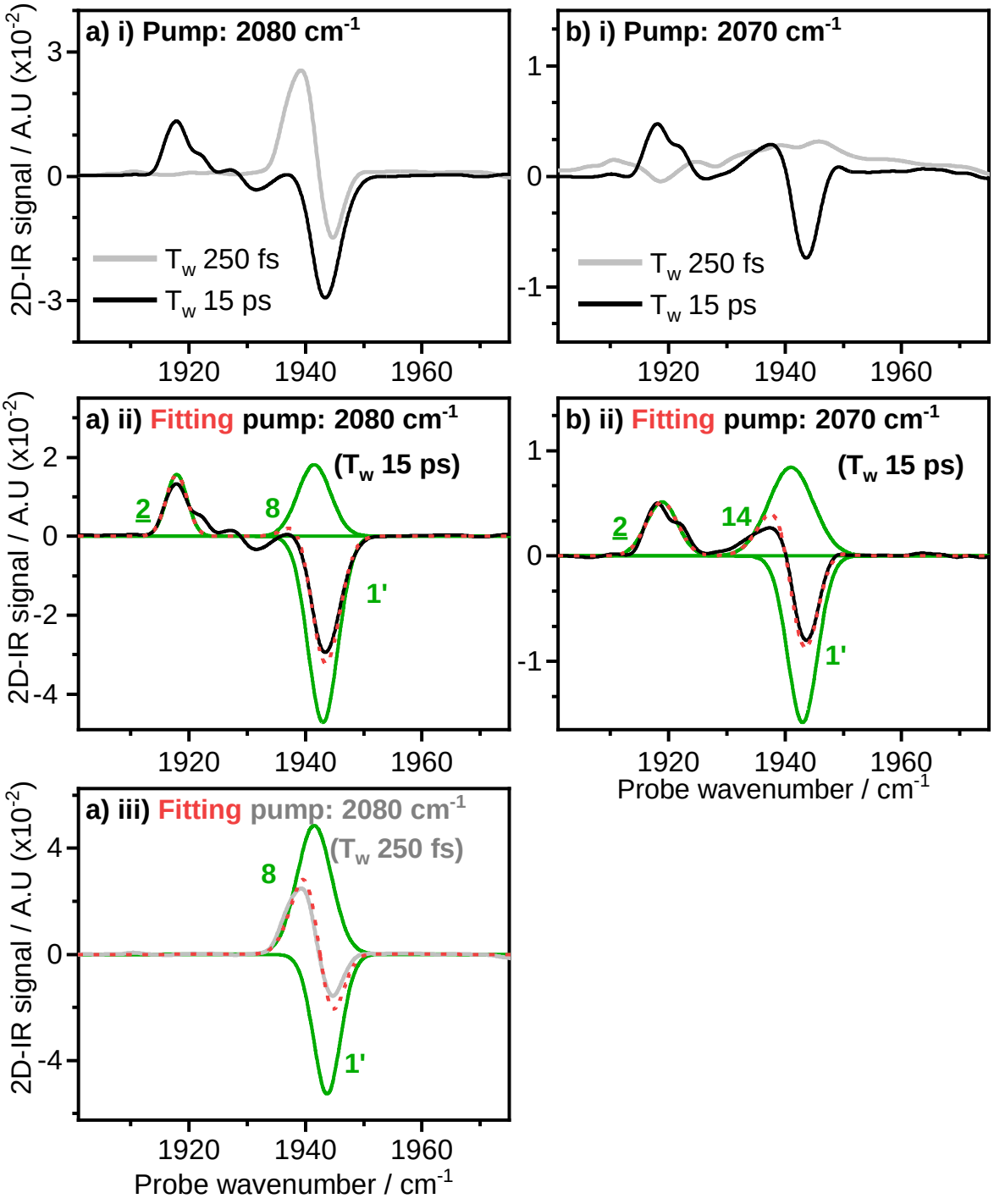

Figure 50 *Probe spectra for 2D-IR slices with pump frequencies of* ***(a)*** *2080 cm^{-1} and* ***(b)*** *2070 cm^{-1}, showing* ***(i)*** *experimental data and fitting of the* ***(ii)*** *T_w 15 ps and* ***(iii)*** *T_w 250 fs data. Experimental data for T_w 15 ps and 250 fs are shown as solid black and grey lines respectively, fitting of individual peaks are shown as solid green lines and the cumulative fitting as dashed red lines.*

Focussing on the lower wavenumber peak (**10**) in the T_w 250 fs spectrum (**Figure 49(a)**), at a pump wavenumber of 2070 cm^{-1} (lower horizontal line) there are three peaks in the off-diagonal region, these are labelled **6'**, **11** and **12**. The negative peak **6'** is assigned to the $|000\rangle$-$|010\rangle$ transition, and is equivalent to peak **10'** in indicating that the ν_{CN} modes are coupled. Peak **11** is the $|001\rangle$-$|002\rangle$ excited state absorption and peak **12** the $|001\rangle$-$|011\rangle$ combination transition. These peaks overlap considerably, however the position of **11** was determined from the energy transfer bands (**11**) present in later T_w spectra when pumping at 2080 cm^{-1} (**Figure 49(b-c)**) and 1942 cm^{-1} (**Figure 46(b)**), showing it to be centered at 2053 cm^{-1} giving a single mode anharmonicity of 18 cm^{-1} for ν_{CN2} mode. This information was used to aid in the fitting of relevant pump slices (**Figure 51(iv)**) to determine the position of peak **12**. Crucially the positions of combination transitions **9** and **12** both give the same value of 24 cm^{-1} for the mixed mode anharmonicity. **Figure 51(ii)** shows simulations of the CN-pump CN-probe region of the 2D-IR spectra using 2D-Gaussian functions (Equation (21) in Section 2.3.4) and parameters derived from fitting pump slices (positions of fundamental transitions, anharmonicities and widths), these simulations corroborate the peak assignments.

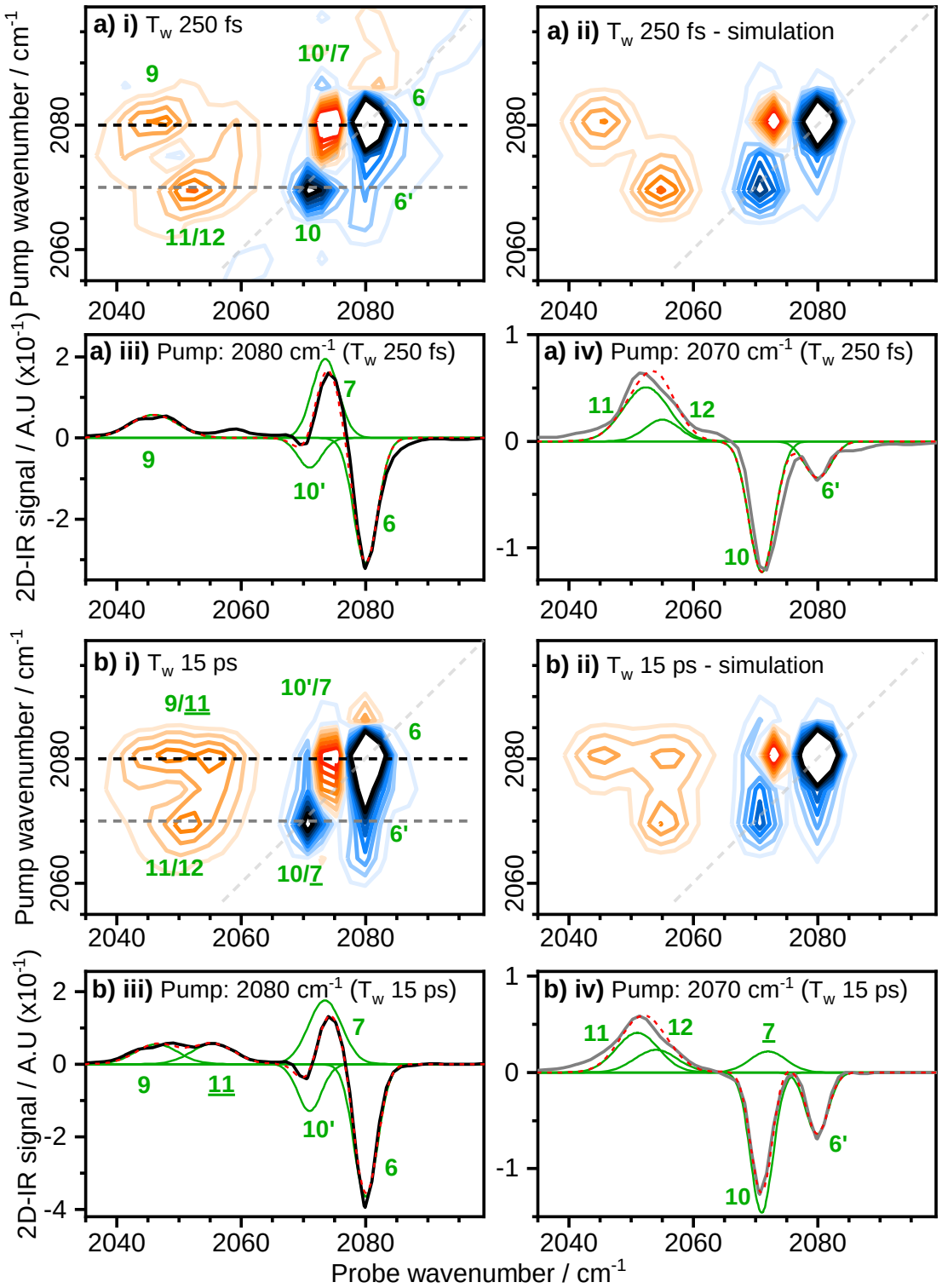

Figure 51 *As-isolated ReRH data showing 2D-IR* ***(i)*** *experimental and* ***(ii)*** *simulated spectra (magnification of the CN-pump CN-probe region) and fitted probe spectra for pump frequencies of* ***(iii)*** *2080 cm^{-1} and* ***(iv)*** *2070 cm^{-1} for T_w values of* ***(a)*** *250 fs and* ***(b)*** *15 ps. Numbers in green indicate peak assignments, solid black and grey lines correspond to experimental data (pump: 2080 cm^{-1} and 2070 cm^{-1}, respectively), solid green lines indicate fitted peaks, and dashed red line correspond to the cumulative fitting.*

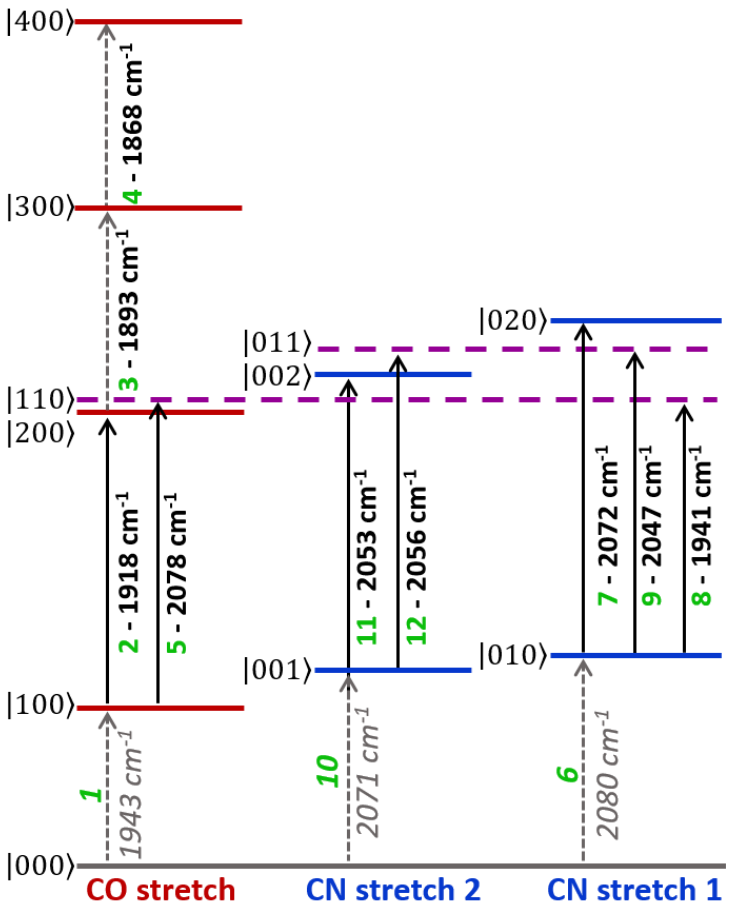

Figure 52 *Energy level diagram showing vibrational energy levels* $|v_{CO}v_{CN1}v_{CN2}\rangle$ *and transition wavenumbers of the* ν_{CO} *and* ν_{CN} *vibrational manifold, as detected for the active site state of ReRH with a* ν_{CO} *fundamental frequency of 1943 cm*$^{-1}$ *(*Ni_a*-S). Transitions are labelled with green numbers used to identify peak assignments in the 2D-IR spectra (see text).*

While the ν_{CO} mode is well approximated by a Morse anharmonic potential, the ν_{CN} modes have some unusual properties. The single mode anharmonicities for the ν_{CN} modes are markedly different, with 18 cm^{-1} for the ν_{CN2} mode and 8 cm^{-1} for the significantly less anharmonic ν_{CN1} mode (**Figure 52**). Examination of crystal structural data (**Figure 53**) shows that the H-bonding environments of the CN^- ligands are distinct and conserved, with one CN^- ligand H-bonded by an arginine and the other by a serine/threonine residue.

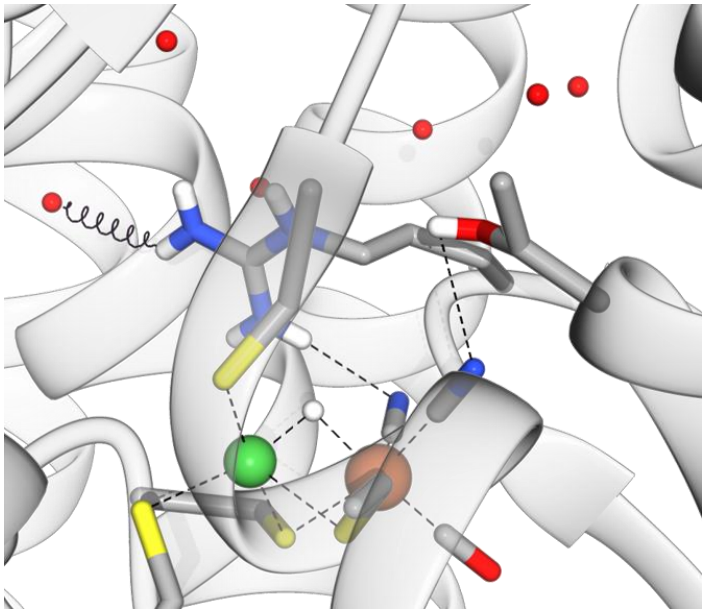

Figure 53 *Crystal structure data showing the active site environment of <u>Ec</u>Hyd-1 (PDB: 6FPW[15]) and structurally conserved water molecules in the vicinity of the R509 residue in the second coordination sphere. The protein is shown as white ribbon, with selected side chains/groups in ball and stick form, coloured by heteroatom (blue = N, red = O, yellow = S, green = Ni and orange = Fe). The black spring line indicates a possible H-bonding contact between the arginine head group and a conserved water molecule.*

While no crystal structure data is available for *Re*RH, sequence alignment analysis by *Kleihues et al*[159] has highlighted the conserved nature of arginine and serine/threonine residues that can be seen to act as H-bonding motifs to CN^- ligands in crystal structures of other NiFe-hydrogenases (**Figure 53** and **Figure 54**). CN^- ligands have been shown to be most strongly influenced by the internal electric field established between charged N^- and central metal ion (here Fe^{2+}).[165] Given that the threonine side chain is neutral while that of arginine is cationic, it would be expected that protein structural fluctuations would impact the charges on the CN^- ligands and by extension the ν_{CN} modes. It follows that perturbations at the arginine would have a greater impact on the ν_{CN} modes and perhaps account for the large disparity in single mode anharmonicities. While the active site excludes water molecules (other than the bridging water molecule present in some states), a number of structurally conserved water

molecules are present in the second coordination sphere in the vicinity of the R509 residue (**Figure 53**).[77] These water molecules could modulate the interaction of the arginine residue with the active site cyanide ligands, in this case a perturbation of the ν_{CN} mode anharmonicities would be expected in the spectra of D_2O exchanged hydrogenase samples.

```
371 -LARVVPLMEDWLQSLEIG------APYWASAHLPDQGAGVGLTEAARGS    413
     ..::....:..:.:|:.|      ...|..|..|.:..|||.|||.||:
462 AAGKLQYFFDKLMTNLKNGNLATASTEKWEPATWPTECRGVGFTEAPRGA    511

414 LGHWVSVRDGRIDNYQIVAPTSWNFSPRDIAGQPGAVEKALEGAPVLQGE    463
    ||||.::|||:||.||.|.||:||.||||..||.||.|.||....:...|
512 LGHWAAIRDGKIDLYQCVVPTTWNASPRDPKGQIGAYEAALMNTKMAIPE    561
```

Figure 54 *Alignment of the amino acid sequences of the large subunits of ReRH (top rows) and EcHyd-1 (bottom rows), residues that form H-bonds with the CN^- ligands are highlighted in green.*

However, from these results alone it is not possible to definitively determine whether these properties are intrinsic to the NiFe hydrogenase active site architecture, *Re*RH, the Ni_a-S state, the $Fe(CO)(CN)_2$ moiety or a combination of contributing factors.

4.3.4 Vibrational relaxation dynamics

Figure 55 shows broadband IR_{pump}-IR_{probe} spectra of as-isolated *Re*RH as a function of T_w. In the ν_{CO} region of the spectrum (1850-1970 cm^{-1}) peaks corresponding to transitions of the ν_{CO} mode up to the v=4 level are apparent (peaks **1-4**). In the ν_{CN} region of the spectrum (2030-2100 cm^{-1}) the fundamental transitions (peak **6** and **10**, i.e., $|000\rangle$-$|010\rangle$ and $|000\rangle$-$|001\rangle$) and the excited state absorption (peak **7**, $|010\rangle$-$|020\rangle$) of the ν_{CN1} mode are also clear, however the remaining ν_{CN} peaks (**9**, **11** and **12**) overlap considerably and are better identified in the 2D-IR spectra (**Figure 49** and **Figure 51**).

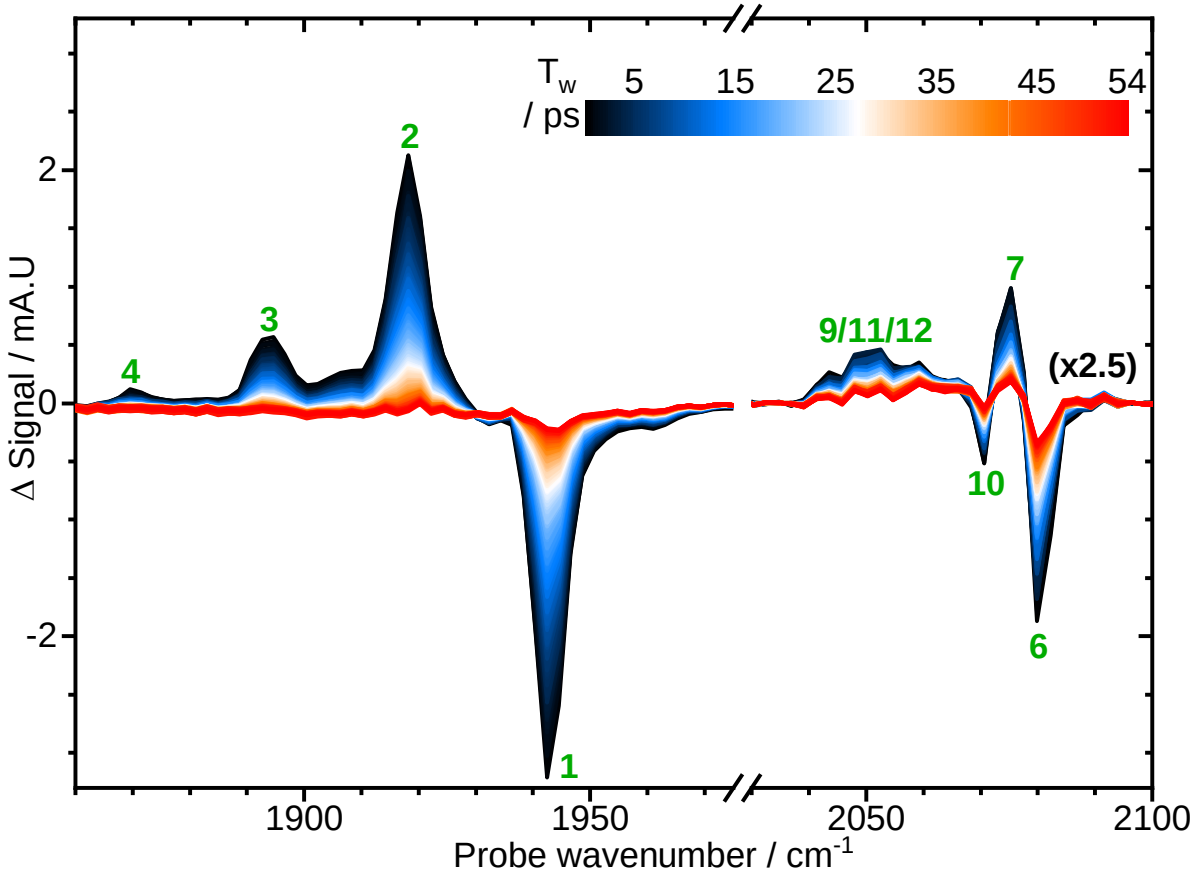

Figure 55 *IR_{pump}– IR_{probe} spectra of as-isolated ReRH in the ν_{CO} region of the spectrum, coloured by pump-probe delay time (T_w).*

By fitting the decay in peak intensity with advancing T_w to monoexponential functions, as shown in **Figure 56**, the vibrational relaxation dynamics of ν_{CO} and ν_{CN} modes of *Re*RH were determined.

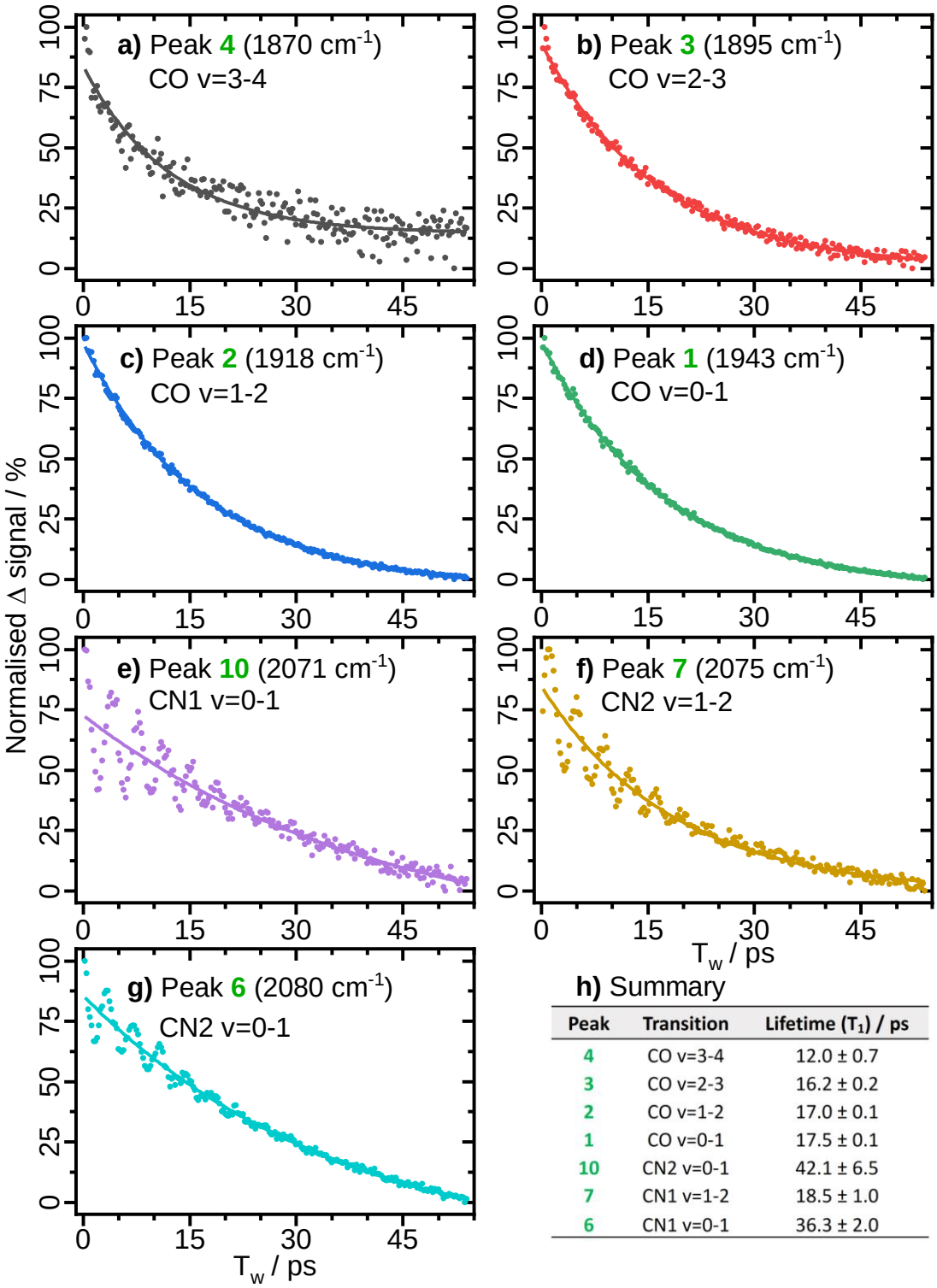

Peak	Transition	Lifetime (T_1) / ps
4	CO v=3-4	12.0 ± 0.7
3	CO v=2-3	16.2 ± 0.2
2	CO v=1-2	17.0 ± 0.1
1	CO v=0-1	17.5 ± 0.1
10	CN2 v=0-1	42.1 ± 6.5
7	CN1 v=1-2	18.5 ± 1.0
6	CN1 v=0-1	36.3 ± 2.0

Figure 56 (a-g) *Plots of pump-probe band intensity versus T_w (coloured circles) and fitted monoexponential functions (solid lines).* ***(h)*** *Tabulated summary of T_1 decay times.*

The vibrational lifetimes (T_1) for transitions up to the v=3 level of the ν_{CO} mode (i.e., peaks **1-3**) are highly consistent with values of 16.2-17.5 ps, whereas peak

4 has a T_1 of 12.0±0.7 ps, this deviation could be attributed to the greater influence of noise on smaller signals. The fundamental transitions of the ν_{CN} modes have similar T_1 values, with 36.3±2.0 ps for **6** and 42.1±6.5 ps for **10**. With a T_1 of 18.5±1.0 the lifetime of the v=1-2 transition of the ν_{CN1} mode (peak **7**) is significantly shorter than the fundamental transitions of either ν_{CN} mode. Energy transfer between ν_{CN} modes is apparent in the 2D-IR spectra recorded with a T_w of 15-20 ps (**Figure 49(b-c)**), so the low apparent T_1 of peak **7** is most probably a consequence of overlap.

Figure 57 shows a comparison of the T_1 times for the ν_{CO} mode of *Re*RH with a trio of hydrogenase active site mimics (molecules **1-3**) and a CO-releasing molecule (CORM) dissolved in a variety of solvents. The T_1 for the ν_{CO} mode of *Re*RH is significantly faster than that reported for small molecule mimics dissolved in hydrophobic or non-interacting solvents (37-158 ps) but slower than that of the CORM in H_2O (3.1 ps).[123,124,166,167] The rapid relaxation of the CORM in H_2O is attributed to spectral overlap of the ν_{CO} mode with the broad bend-libration combination band of water (centred at 2130 cm^{-1}). Since crystal structure data shows that the NiFe hydrogenase active site excludes water molecules (**Figure 53**) it can be assumed that the relaxation of the *Re*RH ν_{CO} mode is facilitated by anharmonic coupling with the Fe-ion (via σ- or π-interactions) in line with the mechanism that has been proposed for the similarly fast relaxing ν_{CO} mode of CO-bound heme proteins and metalloporphyrins.[122,168–170] Conversely, a more complex relaxation pathway involving the structurally conserved water molecules present in the second coordination sphere could account for the efficient relaxation of the ν_{CO} mode, however this would be expected to cause even faster relaxation akin to that observed in the CORM. Compounds **1** and **2** are very similar in structure, with the only difference being that compound **1** substitutes a CO for a CN^- ligand at each of the metal centres

(**Figure 57**). This substitution has a profound impact on the T_1 of the ν_{CO} mode, with values of 37 ps for compound **1** and 158 ps for compound **2** (dissolved in DCM) it is evident that CN^- ligands

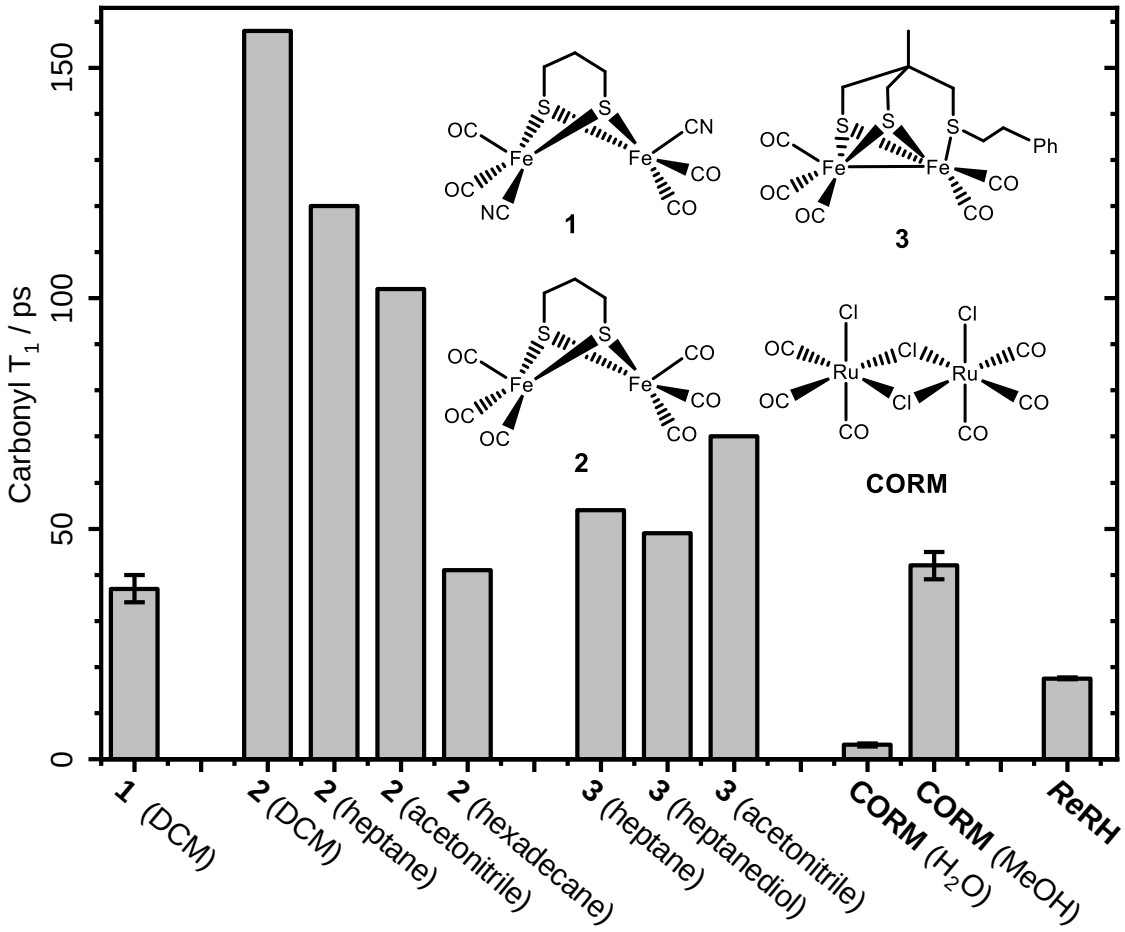

Figure 57 *Comparison of the T_1 times of the ν_{CO} mode of ReRH in the Ni_a-S state with a selection of hydrogenase active site mimics (**1-3**) and a CO-releasing molecule (CORM) dissolved in different solvents (indicated in brackets).*[123,124,166,167]

substantially facilitate relaxation of the ν_{CO} mode.[123,124,166,167] DFT studies on FeFe hydrogenase active site mimics have demonstrated significant anharmonic coupling between ν_{CO}/ν_{CN} modes and low frequency $Fe(CO)(CN)_2$ metal-ligand modes.[95,98,99,124] This raises the possibility that the short ν_{CO} lifetime could be a consequence of through-bond energy redistribution towards the protein matrix assisted via coupling to the H-bonded ν_{CN} modes.[154] The rapid relaxation of the ν_{CO} mode of *Re*RH could be of functional importance in the context of enzyme

molecules transitioning between catalytic states separated by low activation energy barriers in a vibrationally hot state, where the efficient dissipation of energy away from the active site prevents barrier recrossing and the reversion to the previous redox state. This could represent a mechanism by which hydrogenases ensure that the directionality of their catalysis is controlled by environmental conditions and not stalled by random barrier recrossing events.

An oscillatory pattern can be seen in the decay profiles for the ν_{CN} modes (**Figure 56(e-g)**), this modulation becomes more pronounced following subtraction of an exponentially damped sine function, as shown below in **Figure 58(a)**.

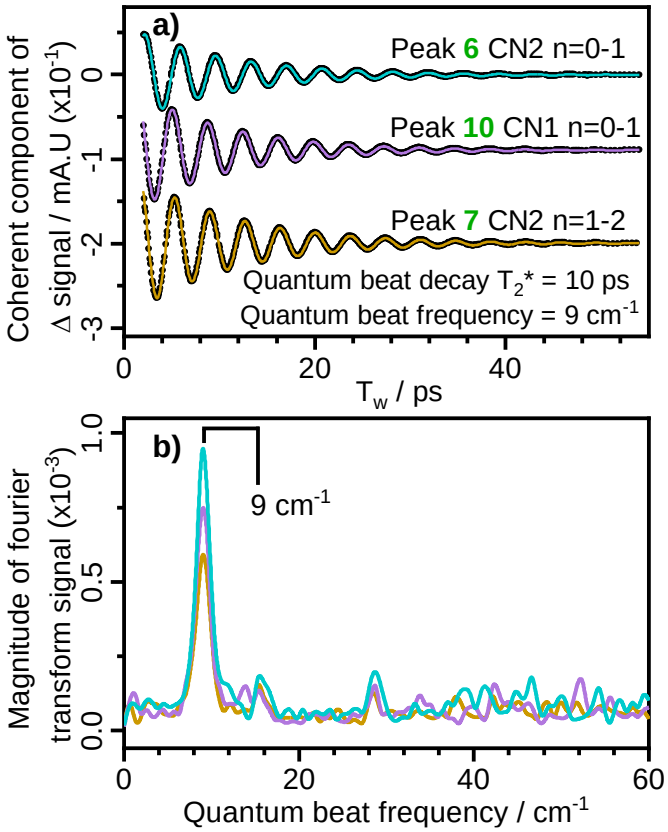

Figure 58 (a) *Quantum beat patterns observed in the kinetic data of the ν_{CN} modes (**Figure 56(e-g)**). Kinetic data with a monoexponential background subtracted are shown as black dots, and fitted monoexponentially damped sine functions as coloured lines.* ***(b)*** *Fourier transformation of the time traces shown in the top panel.*

The oscillatory modulation of ν_{CN} signal decay, termed a quantum beat, is caused by the coherent excitation of the ν_{CN} modes resulting in a superposition state of their n=1 levels.[171,172] Since the coherent superposition state decays faster than the associated excited states, the corresponding time constants (10 ps) obtained via fitting can be assigned to the pure dephasing time, T_2^*. The 9 cm^{-1} frequency of the quantum beat corresponds to the wavenumber separation of the ν_{CN} mode fundamental transitions (at 2071 cm^{-1} and 2080 cm^{-1}).[171,172] . The frequency of the quantum beat can be more easily observed in a plot of the Fourier transformation of the coherent decay profile (**Figure 58(b)**). The presence of a quantum beat indicates that the associated vibrational modes share a ground state, which corroborates the anharmonic coupling between ν_{CN} modes observed in the 2D-IR spectra.[171,172] This is a particularly useful observable as it could allow for the deconvolution of closely spaced ν_{CN} signals produced by hydrogenase samples containing complex mixtures of active site states.

4.3.5 Structural dynamics – 2D-IR diagonal lineshapes

As introduced in 2.3.4 the fluctuations in the local environment of a ligand can produce a range of structural microenvironments, each having a discrete vibrational frequency, this causes inhomogeneous broadening of the corresponding band. Inhomogeneously broadened bands are lengthened along the 2D-IR spectrum diagonal, whereas homogeneous broadening affects the antidiagonal width. If the structural dynamics that cause inhomogeneous broadening are faster than the relaxation time of the vibrational mode, then the 2D lineshape of the band becomes more circular with advancing T_w. This effect is termed spectral diffusion and is caused by the dynamic fluctuations in the

structure of the local environment allowing the pump vibrational mode to sample all available microenvironments before the arrival of the probe pulse.

Peaks in the 2D-IR spectra are elongated along the pump axis (see **Figure 46** and **Figure 47**), including those recorded at the earliest delay times (T_w 250 fs). To some extent this is caused by the resolution along the pump axis being lower than that along the probe axis (5.5 cm^{-1} and 2.1 cm^{-1} respectively). The absence of diagonal elongation of peaks indicates that no significant spectral diffusion is occurring. Analysis of the coherence time dependence of the ν_{CO} ground state absorption signal gives a 3 ps coherence decay time (**Figure 59**). The population relaxation time is considerably longer (T_1=18 ps, **Figure 56(d)**) so the coherence decay can be considered to be the pure dephasing time (T_2*) within the homogeneous limit.

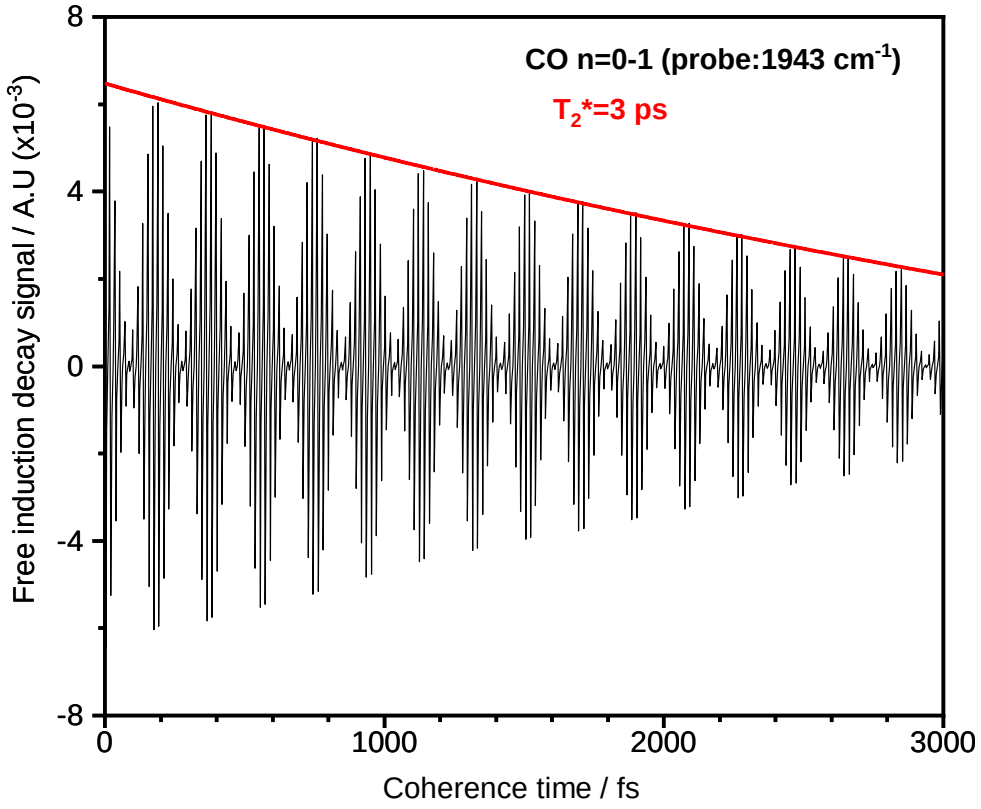

Figure 59 *Plot of the ν_{CO} ground state absorption 2D-IR signal as a function of coherence time (τ), with fitted monoexponential decay curve (black and red lines, respectively).*

This would give a homogeneous linewidth of 3.5 cm^{-1} which is significantly less than the 6.5 cm^{-1} obtained from fitting 2D-IR pump slices (**Figure 48(a)**). Similarly, the 10 ps T_2* obtained for the ν_{CN} modes (**Figure 58(a)**) gives a homogeneous width of 1 cm^{-1}, whereas fitting pump slices shows the signals to have widths of approximately 5.5 cm^{-1} (**Figure 51(iii-iv)**). These disparities indicate limited inhomogeneous broadening, likely a consequence of conformational constraints imposed by the surrounding protein architecture.

4.4 Conclusions

This account represents the first pump-probe and 2D-IR spectroscopic measurements on a NiFe hydrogenase and demonstrates that these techniques can provide a wealth of structurally and catalytically relevant insight, serving as a useful adjunct to well established techniques (X-ray crystallography, functional assays, FT-IR and EPR spectroscopy etc.) to further the understanding of hydrogenase catalysis. This work provides a detailed vibrational signature for the ν_{CO} and ν_{CN} modes of *Re*RH in the Ni_a-S state, forming a useful benchmark to facilitate the analysis of other active site states and hydrogenases with theoretical approaches, non-linear and conventional IR spectroscopies alike. With 2D-IR spectroscopy weak coupling between ν_{CO} and ν_{CN} modes has been observed as well as strong coupling between ν_{CN} modes. While coupling has previously been inferred from the FT-IR spectra of isotopically labelled enzyme,[88] this work represents the first direct observation and quantification of coupling. The importance of the protein matrix in tuning the chemistry at the NiFe active site has been highlighted by i) the detection of distinct differences in ν_{CN} single mode anharmonicities perhaps caused by asymmetric H-bonding environments, ii) the absence of spectral diffusion indicating protein structural constraints, and iii) the observation of efficient energy dissipation away from the ν_{CO}/ν_{CN} modes demonstrating a potential role for the protein matrix in

maintaining the directionality of catalysis. Additionally, the derivation of CO bond parameters from Morse fitting has the potential to facilitate theoretical studies and, as more hydrogenases and active site states are characterized, provide a more detailed picture of the role of CO-bonding in H_2-conversion.

5 Infrared spectroscopy of the oxidised states of *Ec*Hyd-1

Pump-probe and 2D-IR spectroscopy measurements were performed at the Rutherford Appleton laboratories with Dr. Barbara Procacci (University of York), and for as-isolated samples with Dr. Marius Horch (Freie Universität Berlin). Synthesis and 2D-IR data acquisition for the Fe-site mimic (**M1**) were done by Barabara Procacci. Cryo-EM measurements were performed with Chris Furlan (University of York) who also did the corresponding data analysis. Solomon Wrathall prepared *Ec*Hyd-1 samples, did IR and biochemical characterisation of *Ec*Hyd-1 samples, and data processing for 2D-IR spectra of **M1**. This work formed the basis for two publications, one of which has been accepted but not yet published (in PCCP), the other is still being worked on.

5.1 Abstract

The dynamic influence of the protein scaffold on the $Fe(CO)(CN)_2$ moiety present in the active site of *Escherichia coli* Hydrogenase-1 (*Ec*Hyd-1) is revealed using ultrafast pump-probe and two-dimensional infrared (2D-IR) spectroscopy. Measurements on samples of as-isolated and oxidized *Ec*Hyd-1 characterised the Ni_r-B state, in addition to the previously unreported Ni_r-$S_{I/II}$ and Ni_u-S states, with explicit assignment of carbonyl (ν_{CO}) and cyanide (ν_{CN}) stretching bands to each state enabled by 2D-IR. Transitions of the carbonyl stretching mode are found to be well described by a Morse anharmonic potential, and weakly coupled to the cyanide stretching vibrations. In contrast, the two CN stretching modes exhibit strong coupling, leading to the observation of formally forbidden vibrational transitions in the 2D-IR spectra. The vibrational parameters for the ν_{CO} and ν_{CN} stretching modes of the enzyme active site are compared with those of the Fe-site mimic $K[CpFe(CO)(CN)_2]$ in a variety of solvent systems, leading to

the conclusion that the protein scaffold creates a unique biomolecular environment for the NiFe site that cannot be represented by analogy to simple models of solvation.

5.2 Introduction

NiFe hydrogenases are attractive for sustainable energy conversion approaches as they are effective H_2-conversion catalysts that contain only earth-abundant base metals and operate under aqueous conditions.[11] *Ec*Hyd-1 is a membrane bound NiFe-hydrogenase with a catalytic bias towards H_2-oxidation rather than H_2-evolution. Able to sustain H_2-oxidation activity in the presence of inhibitory O_2, *Ec*Hyd-1 is designated an O_2-tolerant group 1 hydrogenase.[17] Achieving H_2-oxidation rates of up to 65 s^{-1}, the catalytic activity of *Ec*Hyd-1 exceeds that reported for small molecule mimics of the NiFe hydrogenase active site. [11,173,174] This implicates the protein architecture in tuning the active site chemistry and highlights the importance of attaining a deeper understanding of this modulation for the rational design of effective H_2-conversion catalysts.[81,94,175,176] Small molecules that exhibit comparable or superior activity to that of hydrogenases invariably feature either a second coordination sphere surrounding the metal ions, or are synthetic cofactors implanted within a protein matrix.[177-192] The implementation of hydrogenase-inspired catalysts is impeded by an incomplete understanding of the mechanisms by which H_2-activation and –evolution occur.[173,193,194] Experimental techniques that quantify the influence of the protein scaffold and explore the structure and bonding at the NiFe active site will provide useful insight for identifying the crucial factors that govern enzymatic H_2-conversion.

NiFe hydrogenase molecules transition through a number of active site substates during the course of H_2-conversion, inhibition by O_2/CO and

reactivation. The NiFe hydrogenase active site features an Fe-bound CO and a pair of CN^- ligands, being π-acidic ligands their ν_{CO} and ν_{CN} stretching modes are sensitive to redox structural changes at the bimetallic active site.[11,79,195]

IR spectroscopy has been widely employed to identify the active site states present in samples of NiFe hydrogenases by using the state specific frequencies of the ν_{CO} and ν_{CN} modes as fingerprints, however conventional IR absorption experiments provide only limited time-resolved information and a dynamic picture of the active site architecture has yet to emerge.[27,66,86,87,93,108,196] The CN^- ligands each form H-bonds with the side chains of residues (Arg and Thr/Ser) present in the active site pocket, experiments that probe the structural dynamics of the CN^- ligands could thus contribute to understanding how the active site chemistry is tuned by the surrounding protein scaffold. Developing a richer understanding of the factors influencing the active site chemistry is crucial for identifying the key determinants of efficient enzymatic H_2-cycling and applying them to synthetic systems.

Ultrafast pump-probe and 2D-IR spectroscopy have been used to investigate the Ni_a-S site state of *Ralstonia Eutropha* regulatory hydrogenase (*Re*RH).[154] These non-linear spectroscopy methods employ sequences of ultrashort duration IR laser pulses to explore transient vibrational phenomena. In pump-probe spectroscopy the efficiency with which energy is dissipated away from an excited vibrational mode is analysed via the rate of signal decay. In 2D-IR spectroscopy a two-dimensional map is generated that correlates the excitation (pump) and detection (probe) frequencies, and describes the interrelation of coupled vibrational modes.[111,116,118,197–199] The use of multiple laser pulses enables the accession of vibrational levels above v=1 which provides

information about the shape of the vibrational potential energy surface. By varying the polarisation of laser pulses, information pertaining to the relative orientation of coupled vibrations can be extracted. The sub-picosecond time resolution of pump-probe and 2D-IR spectroscopy allows for the structural and vibrational dynamics to be analysed on a timescale far shorter than that of the turnover frequency, providing bond specific insight relating to the rapid changes and interactions that occur during chemical processes.

In application to *Re*RH, a detailed description of the potential energy surface of the ν_{CO} mode and its associated relaxation dynamics was generated. Observation of off-diagonal peaks in 2D-IR spectra provided the first direct evidence of coupling between ν_{CO}/ν_{CN} modes, with indications of strong coupling between ν_{CN} modes and weak coupling between ν_{CO} and ν_{CN} modes. Additionally, an unexpectedly large disparity in the single mode anharmonicities of the ν_{CN} modes was identified, perhaps highlighting the importance of the asymmetric H-bonding environments of CN^- ligands. A quantum beat pattern seen in the decay of ν_{CN} signals was found to oscillate with a frequency equal to the separation in wavenumber between the coupled ν_{CN} modes, a phenomenon that could prove useful for the deconvolution of ν_{CN} signals from samples containing complex mixtures of active site states.

Here this approach is extended to the study of *Ec*Hyd-1 in a variety of active site states, including the previously unreported Ni_r-$S_{I/II}$ and Ni_u-S states. Making use of the sensitivity and peak resolution of 2D-IR to investigate both the ν_{CO} and ν_{CN} regions of the spectrum in detail while off-diagonal peaks enable pairs of ν_{CN} modes to be linked definitively with their ν_{CO} counterparts.[93,200] By probing vibrational energy levels up to and including two-quantum excited states as well

as their vibrational and structural dynamics, the spectroscopy of the ν_{CO} and ν_{CN} modes is characterised with comparison to that of Fe-site mimic $K[CpFe(CO)(CN)_2]$ in a selection of solvent systems of varying polarity. The results are discussed in terms of the role played by the protein scaffold in modulating the environment of the active site and how these techniques can be employed to investigate differences in active site states of hydrogenase enzymes to inform the development of novel H_2 production catalysts and further our understanding of catalysis by NiFe-hydrogenases.

5.3 Results and discussion

5.3.1 Biochemical characterisation of EcHyd-1 samples

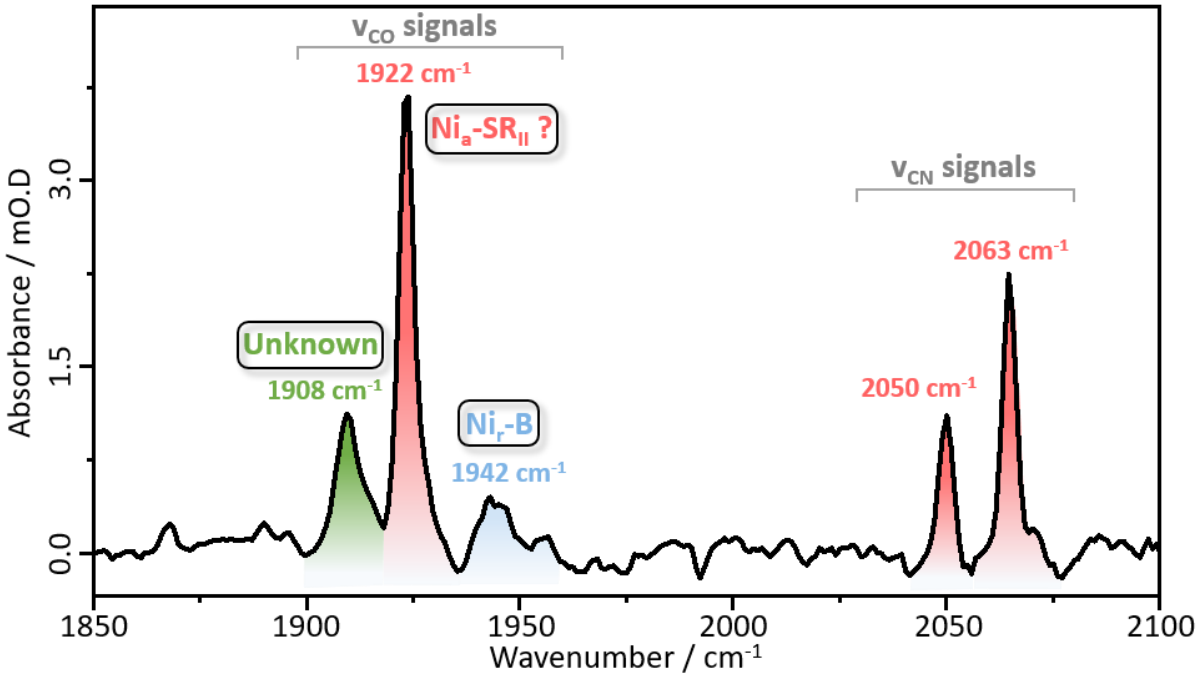

Figure 60 *FT-IR spectrum of as isolated EcHyd-1. Peaks are coloured by redox structural state, with these assignments based on literature wavenumbers.*[27,85,93]

An FT-IR spectrum obtained for an as-isolated sample of *Ec*Hyd-1 is shown above in **Figure 60**. This spectrum contains three ν_{CO} signals centred at 1908 cm^{-1}, 1922 cm^{-1} and 1942 cm^{-1} and a pair of ν_{CN} signals at 2050 cm^{-1} and 2063 cm^{-1}. These signals are consistently present in different purifications (**Figure 69** and **Figure 93**). The ν_{CO} signal at 1942 cm^{-1} is consistent with assignment to the Ni$_r$-B state.[27,85,93] No active site state of *Ec*Hyd-1 has been reported with a ν_{CO} signal at 1908 cm^{-1}. The signals at 1922 cm^{-1}, 2050 cm^{-1} and 2063 cm^{-1} match those reported for the Ni$_a$-SR$_{II}$ state,[27,85,93] however the observation of this state in an aerobically purified sample of *Ec*Hyd-1 is improbable as this is the most reduced state and so is formed only under reducing conditions. As such, it was necessary to perform a thorough biochemical characterisation of *Ec*Hyd-1 samples in order to identify the unknown state (with ν_{CO} at 1908 cm^{-1}), and determine whether the apparent Ni$_a$-SR$_{II}$ signals are caused by another unidentified state

coincidentally producing signals at the same wavenumbers as reported for Ni_a-SR_{II}.

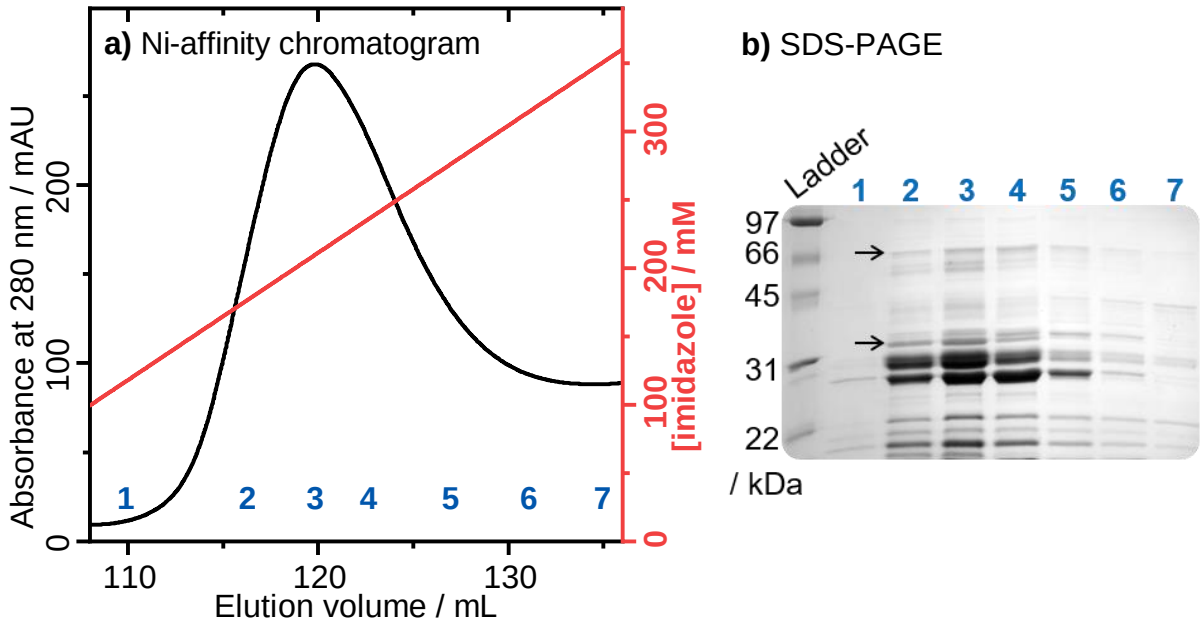

Figure 61 (a) *Ni-affinity chromatogram showing the 280 nm absorbance (black trace) and imidazole concentration (red trace) of elutants.* ***(b)*** *SDS-PAGE of Ni-affinity fractions (**1-7**), black arrows indicate bands of masses consistent with large and small subunits of Ec*Hyd-1.

Purification of lysate via Ni-affinity chromatography (**Figure 61(a)**) produces a 280 nm absorbance profile with a sigmoidal peak that is centred at an elution volume of 120 mL (215 mM imidazole), the peak exhibits tailing at elution volumes greater than 127 mL (275 mM imidazole). Analysis of eluting fractions with SDS-PAGE (**Figure 61(b)**) demonstrates that proteins of masses consistent *Ec*Hyd-1 subunits (36.4 kDa and 66.3 kDa) elute in the sigmoidal peak (lanes **2-4**) and to a lesser extent the tailing fractions (lanes **5-7**). The large number of bands visible in the SDS-PAGE indicate the presence of a number of non-target Ni-binding proteins, this necessitated additional purification by size-exclusion chromatography to ensure that sample concentration of *Ec*Hyd-1 was not limited by impurity content.

Protein eluting from a Ni-affinity column (elution volume > 115 mL in **Figure 61(a)**) that was assessed via SDS-PAGE (**Figure 61(b)**) to contain proteins of masses consistent with *Ec*Hyd-1 subunits was further purified by size exclusion chromatography (SEC), as shown below in **Figure 62(a)**. Protein eluted in three

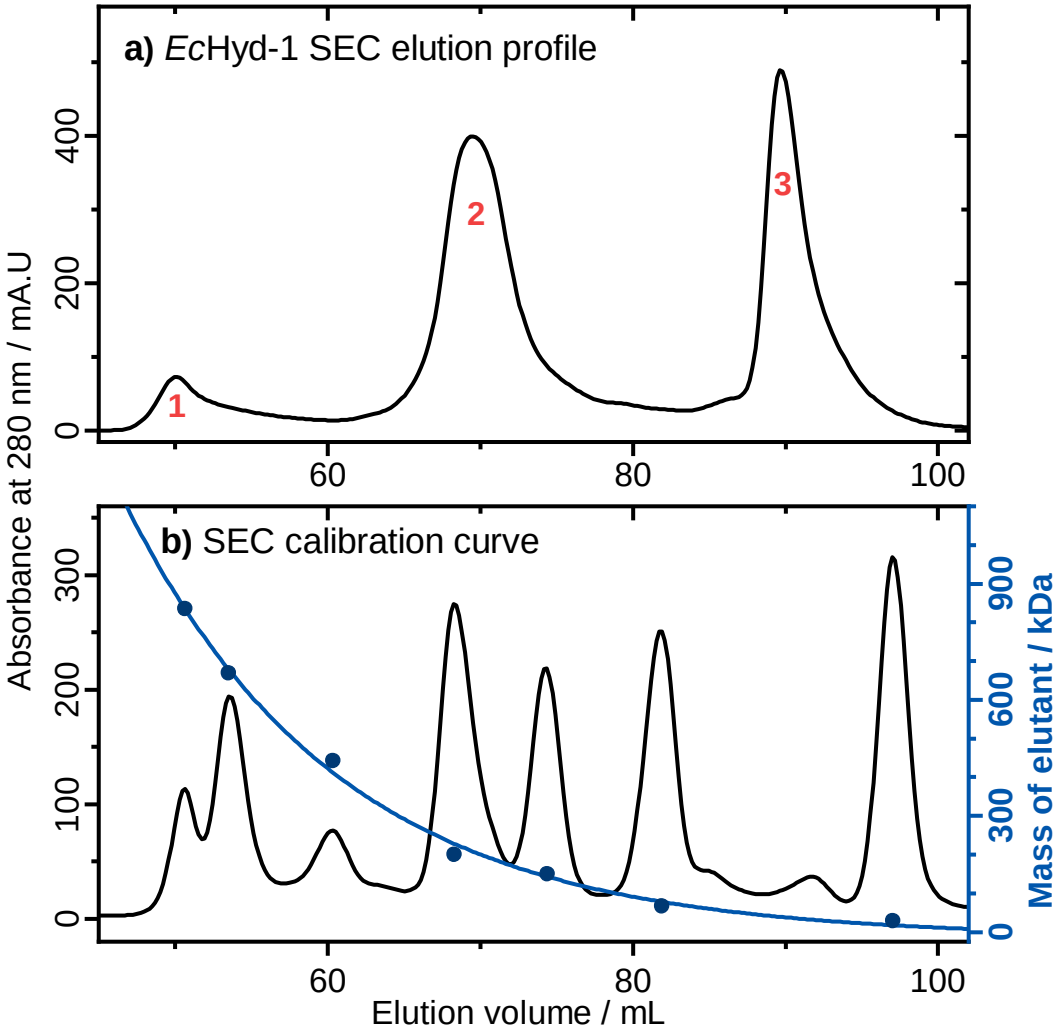

Figure 62 *Size exclusion chromatography (SEC) for* ***(a)*** *an EcHyd-1 sample following purification by Ni-affinity chromatography, and* ***(b)*** *a calibration sample (black traces), with masses of calibrant proteins (blue circles) fitted to a monoexponential function (blue trace).*

peaks, labelled **1**-**3** (**Figure 62(a)**), at volumes of 50 mL, 70 mL and 89 mL, respectively. The masses of proteins eluting in peaks **1**-**3** was estimated by running a calibration sample (black trace in **Figure 62(b)**), comprising proteins of known masses, and fitting the elution volumes/masses to a monoexponential function (blue trace in **Figure 62(b)**). Via this method protein eluting in peaks **1**,

2 and 3 were estimated to have masses of 868 kDa, 207 kDa and 39 kDa, respectively.

The constituents of SEC peaks 1-3 were further analysed using native PAGE with protein bands visualised using a standard Coomassie stain (**Figure 63(a)**) as well as a PMS/NBT activity stain (**Figure 63(b)**) in which only the bands that contain H_2-oxidising protein are visualised.

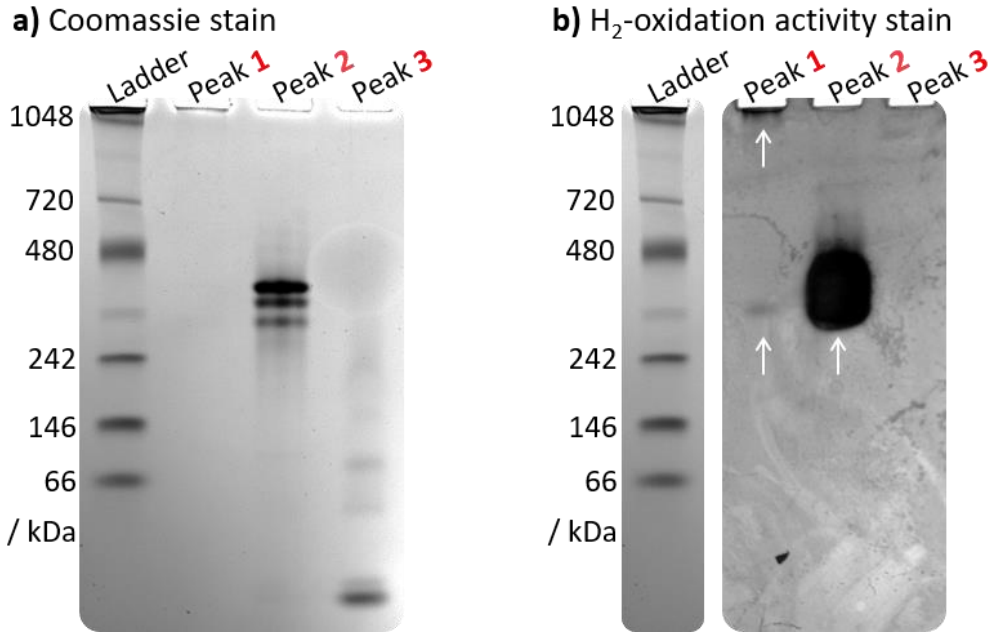

Figure 63 *Native PAGE of protein samples from SEC peaks (1-3) visualised with* ***(a)*** *standard Coomassie (G-250) protein stain and* ***(b)*** *phenazine methosulfate/nitroblue tetrazolium (PMS/NBT) H_2-oxidation activity stain. White arrows indicate bands containing H_2-oxidising protein.*

For the standard Coomassie stain, peak 1 gave a single band that did not move out of the well (approximately 1048 kDa), for peak 2 a triplet of closely spaced bands in the 242-480 kDa range are visible, for peak 3 there are two feint bands and one stronger band with masses less than 66 kDa. Use of an H_2-oxdiation activity stain showed that the (Coomassie visualised) bands in peaks 1 and 2 both contain H_2-oxdising protein. The most likely assignments for peak 3 are the naturally occurring *E. coli* Ni-binding proteins, i.e. cAMP receptor protein (CRP), Cu-Zn superoxide dismutase (CuZn-SOD), and the peptidyl-prolyl cis/trans

isomerase sensitive to lysis D (SlyD) which form dimers of masses 47, 35 and 42 kDa (respectively).[201–203] For peak **1** the activity stain revealed an additional very feint band in the 242-480 kDa range that is not visible using the Coomassie stain, it is unclear whether this band is caused by better staining ability of the activity stain or permeation of protein from the much stronger band present in the adjacent peak **2** lane. These experiments show that the band with maximal H_2 oxidation activity runs at a mass in the 242-280 kDa range which is consistent with a dimer of heterodimers of large (HyaB) and small (HyaA) subunits of *Ec*Hyd-1, i.e. $(HyaAHyaB)_2$, which should have a mass of 205 kDa. Some disparity between the protein mass estimated via SEC and PAGE is to be expected, as in SEC the chromatographic separation depends on the volume of the elutants whereas in PAGE it depends on charge to volume ratio.

UV/vis-spectroscopy was used to analyse protein eluting in SEC peaks **1**-**3**, this is shown in **Figure 64**. SEC peaks **2** and **3** exhibit UV/vis profiles typical of protein samples, with strong absorption at 280 nm and no- or tailing absorption at longer wavelengths. For peak **1** an additional band is visible at approximately 416 nm, a Soret band characteristic of an oxidised heme group.[32,204] UV/vis-spectra of H_2-reduced aliquots of peak **1** (**Figure 64(b-c)**) results in a shoulder at 432 nm to grow in to the Soret band, as well as a less intense α-band 562 nm, indicating partial reduction of the heme group.[32,204] This is especially apparent in the difference spectrum shown in **Figure 64(d)**. As cytochrome subunits cannot be directly reduced by H_2 exposure, this indicates that peak **1** contains a proportion of active *Ec*Hyd-1 molecules isolated in complex with their physiological partner, the *b*-type cytochrome HyaC subunits.

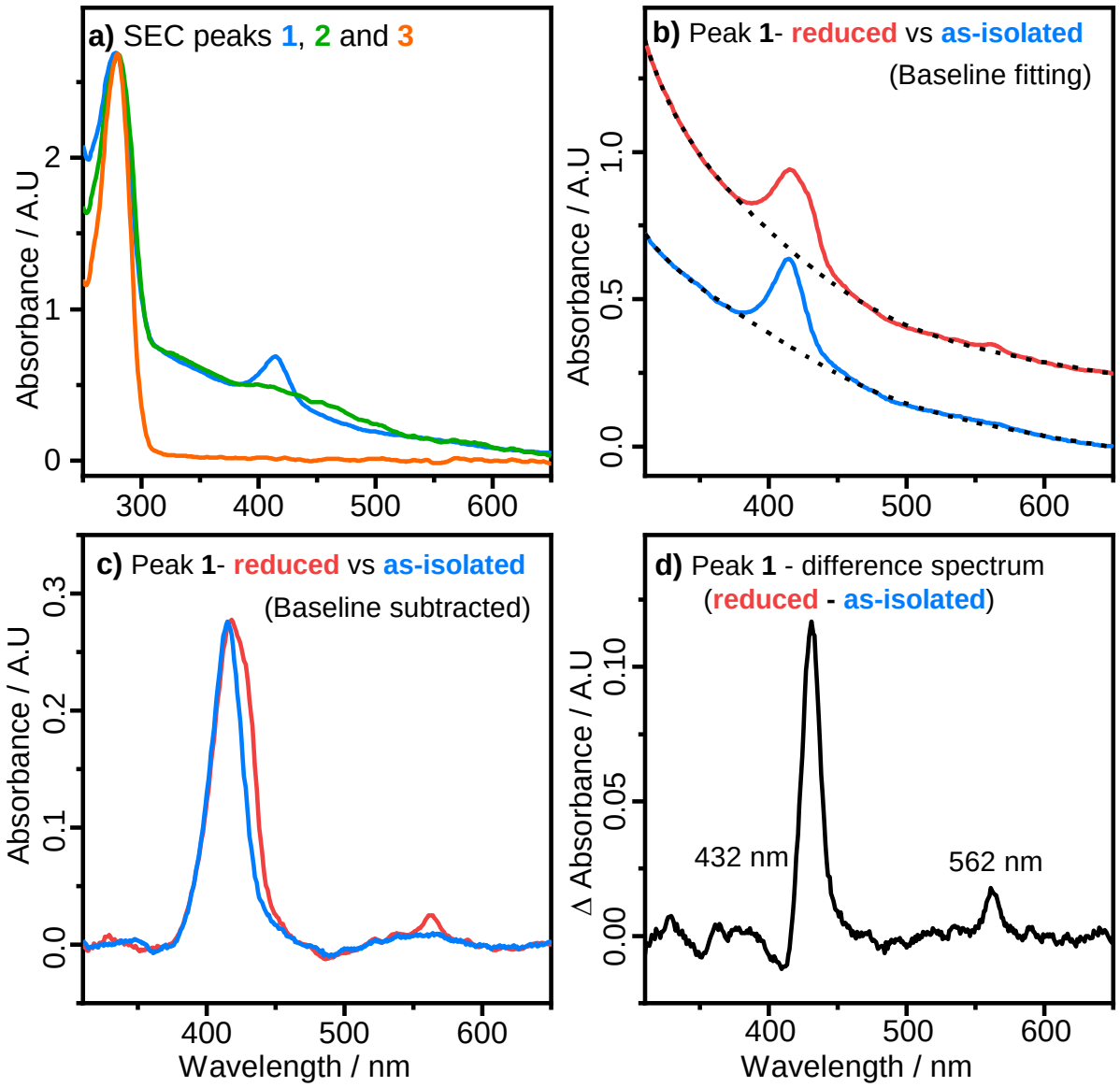

Figure 64 *UV-vis spectra of* ***(a)*** *aliquots of protein eluting in SEC peaks (****1-3*** *in Figure 62(a)), enlarged view of the cytochrome region of peak* ***1*** *aliquots in as-isolated (blue trace) and H_2-reduced (red trace) states showing* ***(b)*** *polynomial baseline (dashed black trace) fitting,* ***(c)*** *following baseline subtraction and* ***(d)*** *as a difference spectrum (solid black trace, as-isolated subtracted from H_2-reduced spectrum).*

Subsequent biochemical analysis was performed on protein eluting in SEC peak **2**, as attempts to concentrate peak **1** aliquots to levels appropriate for IR measurements invariably resulted in precipitation.

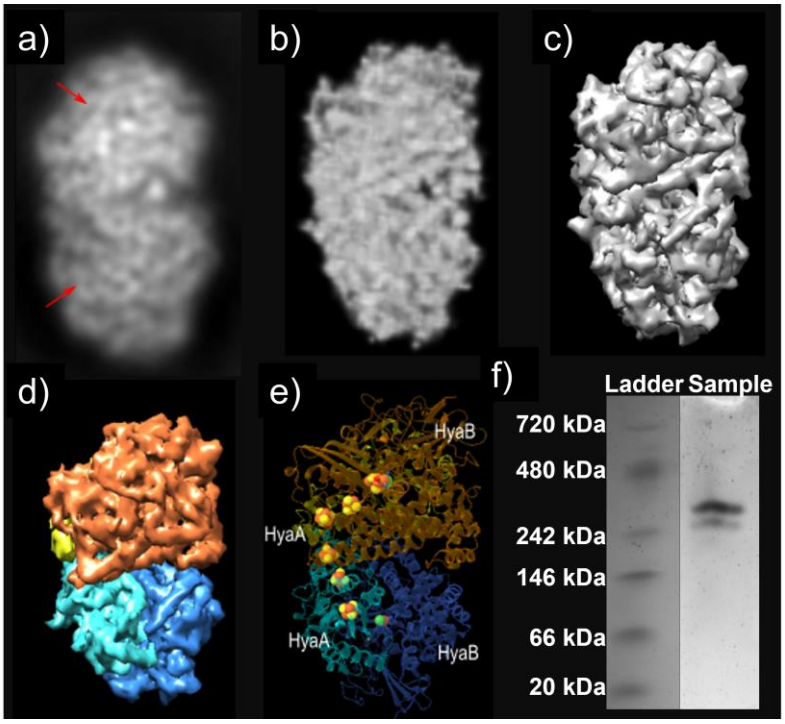

Figure 65 (a) *EcHyd-1 2D class obtained from the cryo-EM data using RELION 3.1 with red arrows indicating each heterodimer,* ***(b)*** *solid map created using existing crystallographic structures showing the similarity to the 2D experimental class,* ***(c)*** *3D display of the solid map in panel b,* ***(d)*** *panel c but with coloured subunits,* ***(e)*** *ribbon structure used to create the maps shown in panels b, c, d* ***(f)*** *Native PAGE of the EcHyd-1 sample used for cryo-EM measurements.*

Cryo-EM analysis of protein eluting in peak **2** is shown in **Figure 65**. While the orientational bias of particles on the cryo-EM grids prevented attainment of a high-resolution structure, the resolution was sufficient to confirm that the arrangement of subunits matches that of previously-reported X-ray crystallographic data for the $(HyaAHyaB)_2$ dimer-of-dimers.[32]

The activation kinetics for samples of as-isolated and subsequently O_2-inhibited *Ec*Hyd-1 were investigated using cyclic voltammetry (CV) and chronoamperometry (CA) experiments, this is shown in **Figure 66** and **Figure 67**, respectively.

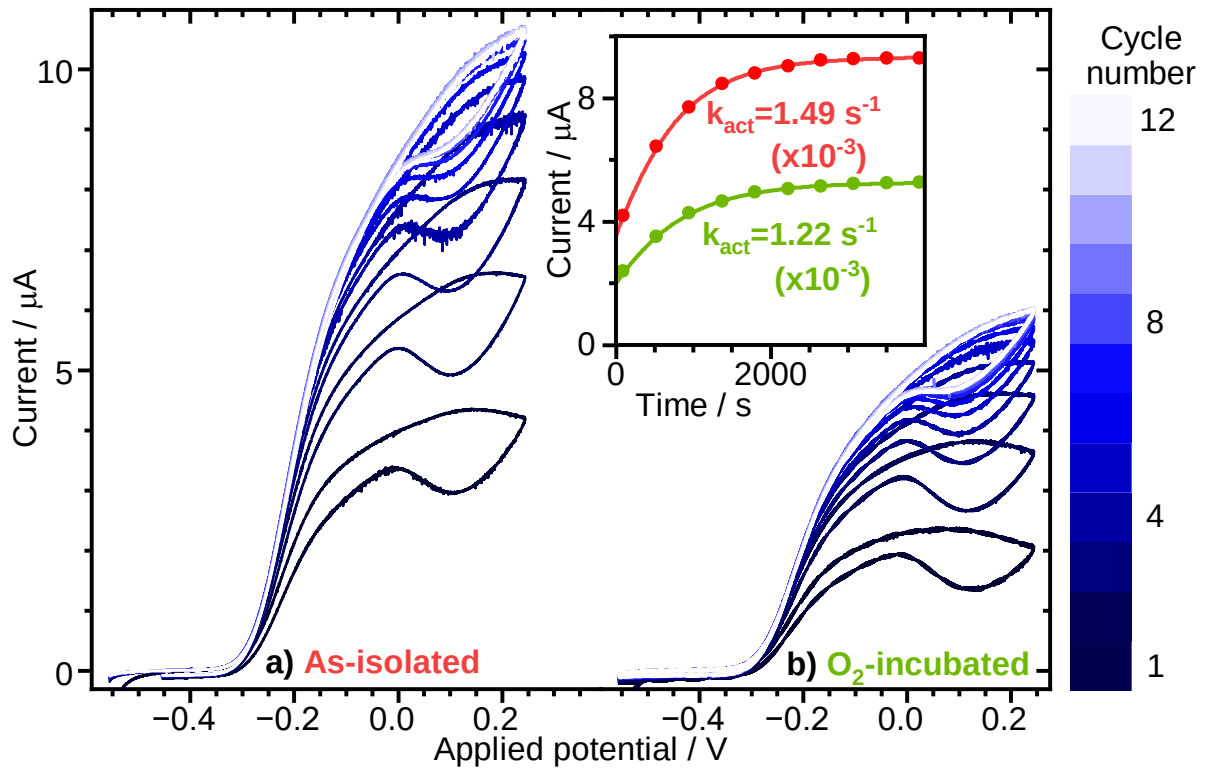

Figure 66 *Cyclic voltammograms showing the activation of* ***(a)*** *as-isolated and* ***(b)*** *subsequently O_2-incubated EcHyd-1 samples. Traces are coloured by cycle number as indicated by the scale bar on the right. Inset current/time plot shows the activation rate (k_{act}) at 60 mV vs SHE. Voltammograms were recorded with a 5 mV s^{-1} scan rate, using a 0.03 cm^2 PGE working electrodes rotating at 3000 rpm under a 1 cm^3 s^{-1} flow of 100% H_2 gas. The electrochemical cell was filled with mixed buffer comprising 100 mM NaCl and 15 mM MES, CHES, TAPS, HEPES and Na acetate at pH 7.6.*

In CV experiments as-isolated enzyme was applied to the working electrode under atmospheric conditions before porting the electrode in to an anaerobic glovebox where it was fixed to an electrochemical cell that had been pre-equilibrated with an atmosphere of 100% H_2. CV cycles were run until successive cycles caused no increase in oxidative (positive) current, indicating that all adsorbed enzyme molecules had been converted to full active form, this typically occurred after around seven cycles (**Figure 66(a)**). The electrode was then removed from the anaerobic glovebox and the adsorbed *Ec*Hyd-1 inhibited by exposure to an atmosphere of 100% O_2 before porting the electrode back in to the glovebox and repeating the CV experiment (**Figure 66(b)**). At 10.8 µA, the

maximum current observed for the as-isolated sample in **Figure 66** is significantly more than the 6 µA seen following O_2-incubation, it is not clear to what extent this is caused by degradation of the enzyme or desorption from the electrode. The activation rate of *Ec*Hyd-1 at 60 mV was explored by extracting current/time data from the forward sweep of CV plots and fitting to exponential functions, as shown by the inset in **Figure 66**. Activation rates of 1.49 $x10^{-3}$ s^{-1} and 1.22 $x10^{-3}$ s^{-1} were determined for as-isolated and O_2-inhibited *Ec*Hyd-1 samples, respectively. These $k_{activation}$ rates are similar to literature reports for *Ec*Hyd-1 ($2x10^{-3}$ s^{-1} at pH 6) and are an order of magnitude faster than that reported for O_2-sensitive NiFe hydrogenases.[17,116]

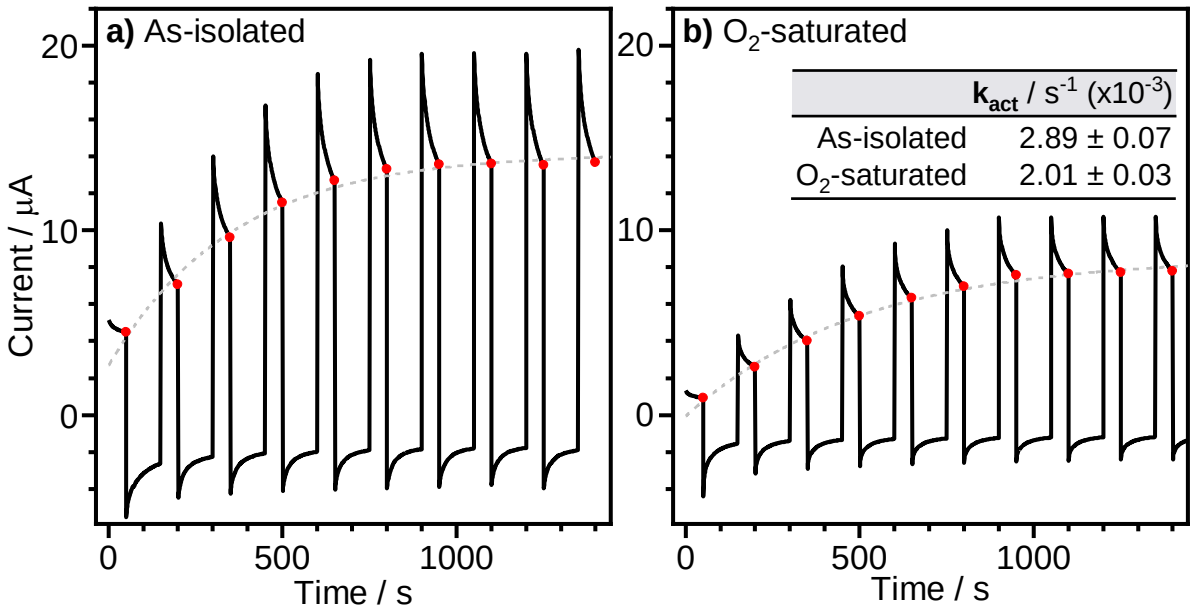

Figure 67 *Chronoamperometry traces showing the activation* ***(a)*** *as-isolated and (b) subsequently O_2-saturated EcHyd-1 samples. Chronoamperometry traces are shown as solid black lines, fitted monoexponential function is indicated by dashed grey lines and data points used for fitting as red circles. For these experiments the applied potential was cycled between +60 mV (for 50 s) and –200 mV (for 100 s).*

The activation kinetics were also monitored via chronoamperometry, as shown in **Figure 67**. These experiments used the same methodology as the CV

experiments, except the applied potential was cycled between +60 mV (for 50 s) and -200 mV (for 100s), rather than incrementally scanning the applied potential in a cyclic manner. In chronoamperometry experiments it is conventional to fix the applied potential at a single value, however (for undetermined reasons) this resulted in the current/time trace having an exponential decay profile rather than the expected exponential growth profile. Fitting the oxidative current (**Figure 67**) gave activation rates of 2.89 ± 0.07 s^{-1} ($x10^{-3}$) and 2.01 ± 0.01 s^{-1} ($x10^{-3}$) for as-isolated and subsequently O_2-saturated *Ec*Hyd-1 samples, respectively. These values are 58% and 39% greater than that obtained via CV experiments for as-isolated and O_2-inhibited samples respectively. The lower $k_{activation}$ rates obtained via CV experiments likely reflect the oxidative inactivation of enzyme at the most positive potentials during the forward sweep.

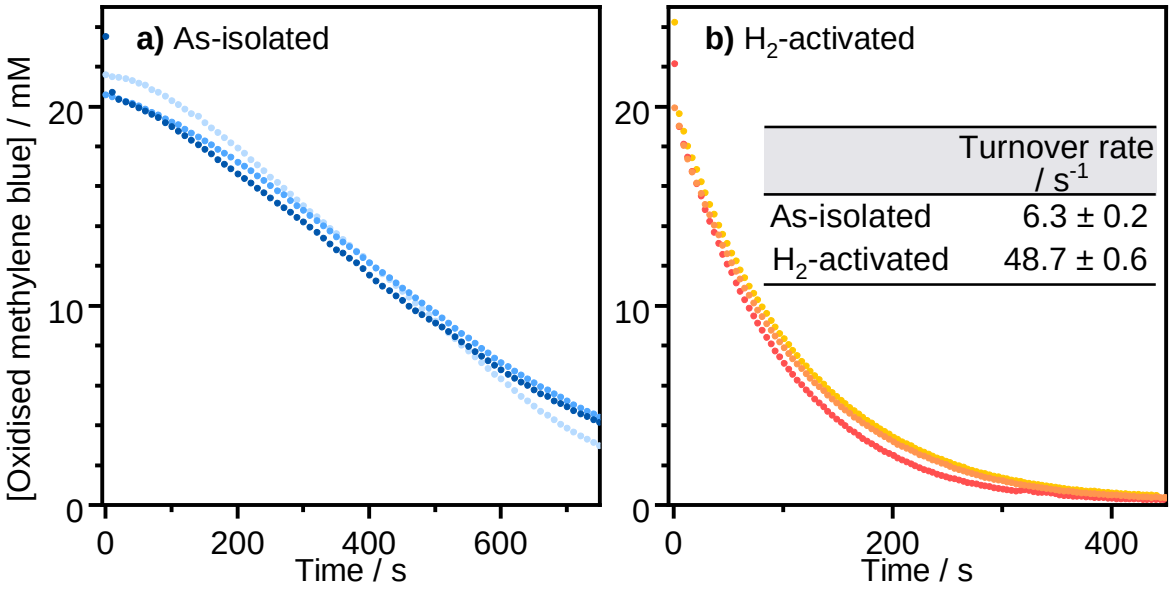

Figure 68 *Solution activity assay data, showing the H_2-oxidation activity of EcHyd-1 determined via the reduction of methylene blue (MB^+), monitored spectrophotometrically. Data are shown for* ***(a)*** *as-isolated enzyme (blue) and* ***(b)*** *for samples that had been pre-activated by exposure to a 100% H_2-atmosphere for 2 h (yellow-red). The inset table shows turnover rates, each representing the average of three repeats ± the standard error.*

The maximum H_2-oxidation activity of as-isolated and H_2-activated samples of *Ec*Hyd-1 was explored using a methylene blue assay, as shown in **Figure 68**. In this assay the hydrogenase catalysed oxidation of H_2-releases electrons, these electrons reduce methylene blue leading to decolourisation of the solution, which is monitored spectrophotometrically. Using the total protein concentration determined via Bradford assay as a proxy for *Ec*Hyd-1 concentration, a turnover rate of 6.3 ± 0.2 s^{-1} is determined for as-isolated *Ec*Hyd-1 and 48.7 ± 0.6 s^{-1} for samples that had been pre-activated with H_2 (at pH 7.6). These values are comparable to previous measurements reported for H_2-activated *Ec*Hyd-1 at acidic pH values: approximately 65 s^{-1} at pH 6.0, and 21 ± 4 s^{-1} at pH 4.5.[11,193] These biochemical characterisation techniques demonstrated that *Ec*Hyd-1 was produced in a correctly folded state, exhibiting activity levels typical of an as-isolated sample rather than the high level of activity that would be expected of a sample comprising a majority of enzyme in the Ni_a-SR_{II} state.

5.3.2 FT-IR Spectroscopy

FT-IR spectroscopy was used in gas cycling experiments to explore the changes in active site states present in *Ec*Hyd-1 samples brought about by exposure to differing gas atmospheres and exposure orderings. ***Figure 69*****(b)** shows the FT-IR spectra of **i)** as-isolated, **ii)** H_2-reduced and **iii)** H_2-reduced and subsequently O_2-inhibited *Ec*Hyd-1. ***Figure 69*****(c)** shows the FT-IR spectra of **i)** as-isolated, **ii)** O_2-inhibited and **iii)** O_2-inhibited and subsequently H_2-reduced *Ec*Hyd-1. In the FT-IR spectra of as-isolated *Ec*Hyd-1 (***Figure 69*****(b)(i)**, **(c)(i)** and **Figure 93**) a trio of signals can be seen in the ν_{CO} region at 1908 cm^{-1}, 1922 cm^{-1} and 1942 cm^{-1}. These ν_{CO} signals, along with a pair of ν_{CN} signals at 2050 and 2063 cm^{-1} (**Figure**

93), are consistently present in the IR spectra of as-isolated *Ec*Hyd-1 across different cell growth and purification processes. In line with previous IR absorption studies the ν_{CO} signal at 1942 cm^{-1} is assigned to the Ni_r-B state. To date there are no literature reports of an *Ec*Hyd-1 state with a ν_{CO} signal at 1908 cm^{-1}. The Ni_a-SR states have been reported to produce ν_{CO} signals at 1922 cm^{-1}

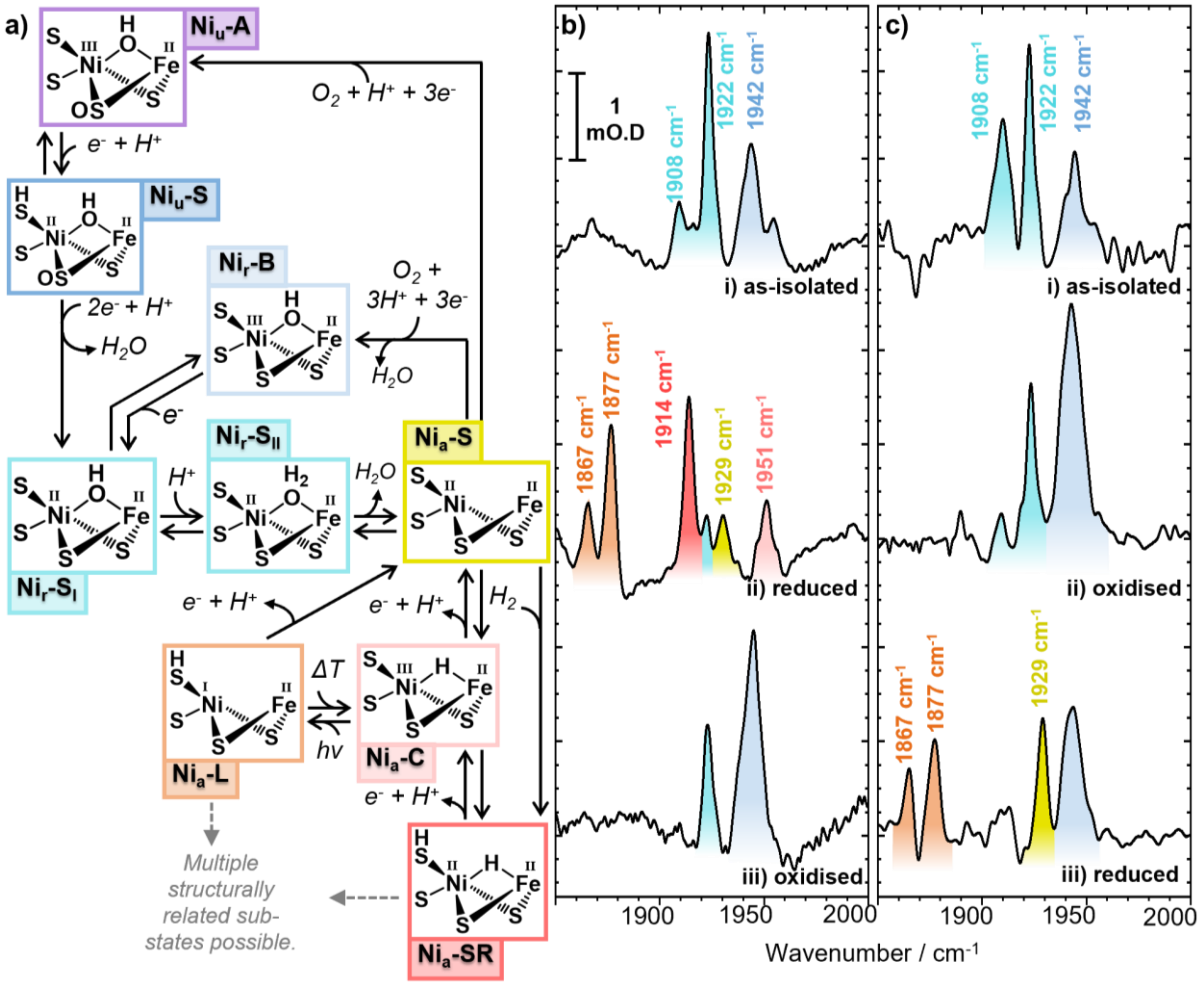

Figure 69 **(a)** *Catalytic cycle for EcHyd-1 with truncated structures of the bimetallic active site. FT-IR spectra of EcHyd-1 showing the ν_{CO} region of the spectrum, enzyme samples were exposed to differing gas atmospheres* ***(i-iii)*** *and exposure orderings* ***(b-c)****. In* ***(b)*** *the as-isolated EcHyd-1 sample* ***(i)*** *was H_2-reduced* ***(ii)*** *and subsequently O_2-oxidised* ***(iii)****. In* ***(c)*** *the as-isolated EcHyd-1 sample* ***(i)*** *was O_2-oxidised* ***(ii)*** *and subsequently H_2-reduced* ***(iii)****. The states assigned to peaks in* ***(b-c)*** *are indicated by the peak/label colours which are consistent with those used in* ***(a)****.*

and 1914 cm^{-1}, along with ν_{CN} signals at 2050 cm^{-1} and 2067 cm^{-1}.[93] The 1922/2050/2063 cm^{-1} signals seen here would seem to coincide with a Ni_a-SR state, however observation of a Ni_a-SR state is both unexpected for an as-isolated sample and inconsistent with the activity measurements reported in **5.3.1**.[15,17,32,205] As shown in **Figure 69(b)(i)→(ii)**, reduction of an as-isolated sample with 100% H_2 causes complete loss of the Ni_r-B and the 1908 cm^{-1} signal, almost complete loss of the 1922 cm^{-1} signal, along with the formation of additional ν_{CO} signals that are consistent with assignment to the Ni_a-L (1867 cm^{-1} and 1877 cm^{-1}), Ni_a-SR_{II} (1914 cm^{-1}), Ni_a-S (1929 cm^{-1}) and Ni_a-C (1951 cm^{-1}) states. Upon subsequent O_2-saturation of the H_2-reduced sample (**Figure 69(b)(ii)→(iii)**) the Ni_a-X states are lost, the Ni_r-B signal reforms, and the 1922 cm^{-1} signal increases in intensity. This sequence of state interconversions shows that the 1908 cm^{-1} and 1922 cm^{-1} signals correspond to states that are more oxidised than the Ni_a-X states.

As shown in **Figure 69(c)(i)→(ii)**, oxidation of an as-isolated sample with 100% O_2 causes the 1908 cm^{-1} and 1922 cm^{-1} signals to diminish along with concomitant growth of the Ni_r-B signal. This shows that the Ni_r-B state is more oxidised than the states to which the 1908 cm^{-1} and 1922 cm^{-1} signals belong. Subsequent H_2-incubation of the O_2-oxidised sample (**Figure 69(c)(ii)→(iii)**) causes the Ni_r-B signal to decrease in intensity, complete loss of 1908 cm^{-1} and 1922 cm^{-1} signals, along with formation of Ni_a-L and Ni_a-S signals. The presence of Ni_r-B in **Figure 69(c)(iii)** is likely caused by incomplete reduction and this signal is expected to diminish with continued H_2-exposure. The series of state interconversions described above, along with the activity measurements in section **5.3.1**, support the assignment of the 1908 cm^{-1} and 1922 cm^{-1} signals to intermediate states between the Ni_a-S and Ni_r-B/Ni_u-X states, perhaps

assignable to the Ni_r-$S_{I/II}$ states. It bears noting that any novel state assignments based only on the data shown in **Figure 69** must be tentative, because in panels **(b)(iii)** and **(c)(iii)** it is evident that the samples were not completely oxidised and reduced, respectively. Total conversion of Ni_r-$S_{I/II}$ to Ni_r-B signals under oxidising conditions (**Figure 69(b)(ii)→(iii)**) is necessary for validating the assignment of Ni_r-$S_{I/II}$ signals. Similarly, total conversion of Ni_r-B to Ni_a-X signals under reducing conditions (**Figure 69(c)(ii)→(iii)**) is necessary for validating the assignment of the Ni_r-B signal as otherwise it is possible that the signals may represent inactivated enzyme that coincidentally produces a ν_{CO} signal at the same wavenumber as the Ni_r-B state.

The ν_{CN} signals associated with the 1908 cm^{-1} and 1922 cm^{-1} ν_{CO} signals were identified by analysis of 2D-IR spectra (see **5.3.3**). Signals at 2059/2070 cm^{-1} were found to correspond to the 1908 cm^{-1} ν_{CO} signal, and 2050/2063 cm^{-1} ν_{CN} mode signals corresponding to the 1922 cm^{-1}. **Figure 70** shows a comparison of the wavenumbers reported for ν_{CO} and ν_{CN} modes of a range of NiFe-hydrogenases, relative to Ni_r-B signals from the same enzyme. This comparison shows that the signals reported here as belonging to the Ni_r-S states of *Ec*Hyd-1 have wavenumbers consistent with literature reports for other enzymes. As the Ni_a-C state is the state typically reported as having the highest ν_{CO} frequency it would ostensibly be a more appropriate reference point than the Ni_r-B state, however the *Ec*Hyd-1 $\nu_{CN1/2}$ mode frequencies for the Ni_a-C state have not been identified. An alternate version of **Figure 70** using Ni_a-C signals as a reference point is shown in **Appendix Figure 107**, the $\nu_{CN1/2}$ wavenumbers for the Ni_a-C state of *Ec*Hyd-1 were estimated based on values reported for *Re*MBH. Irrespective of which state is used as a reference point, the ν_{CO}/ν_{CN1}/ν_{CN2} wavenumbers reported here appear to be consistent with assignment to the Ni_r-

$S_{I/II}$ states. While the hydrogenases selected for the wavenumber analysis shown here (in **Figure 70** and **Figure 107**) have all been robustly characterised, it is worth noting that this sort of data analysis is not appropriate for all hydrogenase data present in the literature because there can be a degree of uncertainty in the reported state assignments (particularly in early hydrogenase literature).

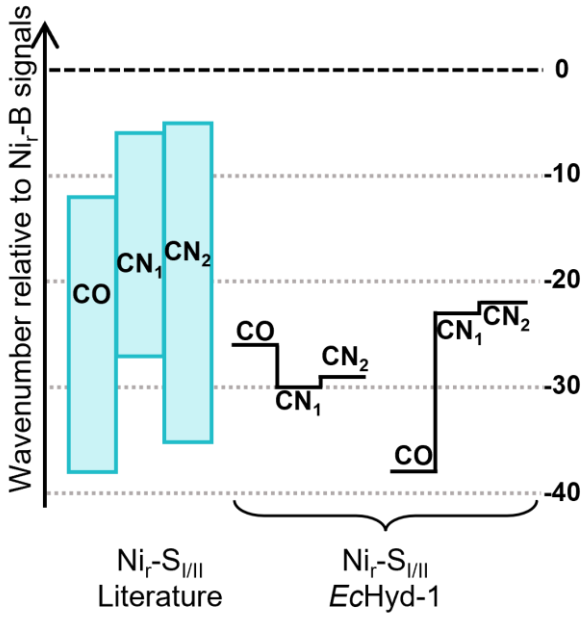

Figure 70 *Diagram showing the wavenumbers reported for CO, CN_1 and CN_2 stretching modes of NiFe-hydrogenases (DvMF, AvMBH, DgMBH and ReMBH) in the Ni$_r$-S states (blue) relative to Ni$_r$-B signals from the same enzyme.*[24,66,206,207]

Since the Ni$_r$-S$_I$ state bears a μ-$^-$OH ligand which is protonated to form a μ-OH$_2$ ligand in the Ni$_r$-S$_{II}$ state (**Figure 69(a)**), an increase in pH should increase the population of the Ni$_r$-S$_I$ state relative to the Ni$_r$-S$_{II}$ state. **Figure 71** shows a comparison of the FT-IR spectra of as-isolated *Ec*Hyd-1 at pH 7.6 and following buffer exchange to pH 9.0 and pH 3.0.

Increasing the pH from 7.6 to 9.0 (**Figure 71(a)→(b)**) caused a decrease in the amplitudes of the Ni$_r$-S ν_{CO} signals at 1908 cm^{-1} and 1922 cm^{-1} from 0.6 mO.D to 0.3 mO.D and from 2.4 mO.D to 2.0 mO.D, respectively, in addition to an

increase in the Ni_r-B ν_{CO} signal at 1942 cm^{-1} from 1.2 mO.D to 1.4 mO.D. Decreasing the pH from 7.6 to 3.0 (**Figure 71(a)→(c)**) resulted in the complete loss of the 1908 cm^{-1} Ni_r-S signal, as well as reduction of the 1922 cm^{-1} Ni_r-S and 1942 cm^{-1} Ni_r-B signals to 0.5 mO.D and 1 mO.D, respectively. For ***Figure 71*(c)**,

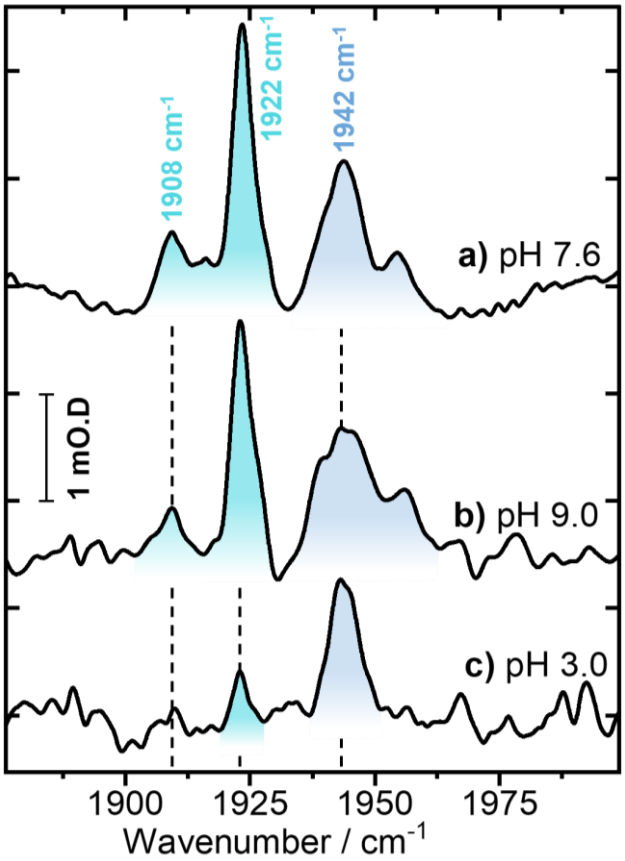

Figure 71 *FT-IR spectra of as-isolated (aerobically purified) EcHyd-1 at* ***(a)*** *pH 7.6, and following buffer exchange from pH 7.6 to* ***(b)*** *pH 9.0 and* ***(c)*** *pH 3.0.*

the loss of signal intensity across all of the states is likely a consequence of the enzyme's instability at this pH. Transitioning from pH 7.6 to pH 9.0 the increase in the proportion of the 1922 cm^{-1} ν_{CO} signal relative to the 1908 cm^{-1} signal would seem to identify the 1922 cm^{-1} signal as belonging to the Ni_r-S_I state, however definitive assignment requires the observation of a relative increase in the 1908 cm^{-1} signal at more acidic pH values which is not possible from this data considering the degradation observed in the pH 3.0 spectrum. As such, in the

following analysis no definitive assignment of Ni_r-$S_{I/II}$ states is made and they are instead differentiated by their ν_{CO} frequencies.

5.3.3 As-isolated EcHyd-1 FT-IR spectrum and 2D-IR spectrum diagonal

The FT-IR spectrum of as-isolated *Ec*Hyd-1 overlaid with an inverted projection of the 2D-IR spectrum diagonal are shown in **Figure 72(a)**. The ν_{CO} region (1850-1975 cm^{-1}) of the FT-IR spectrum (black trace in **Figure 72(a)**) contains three

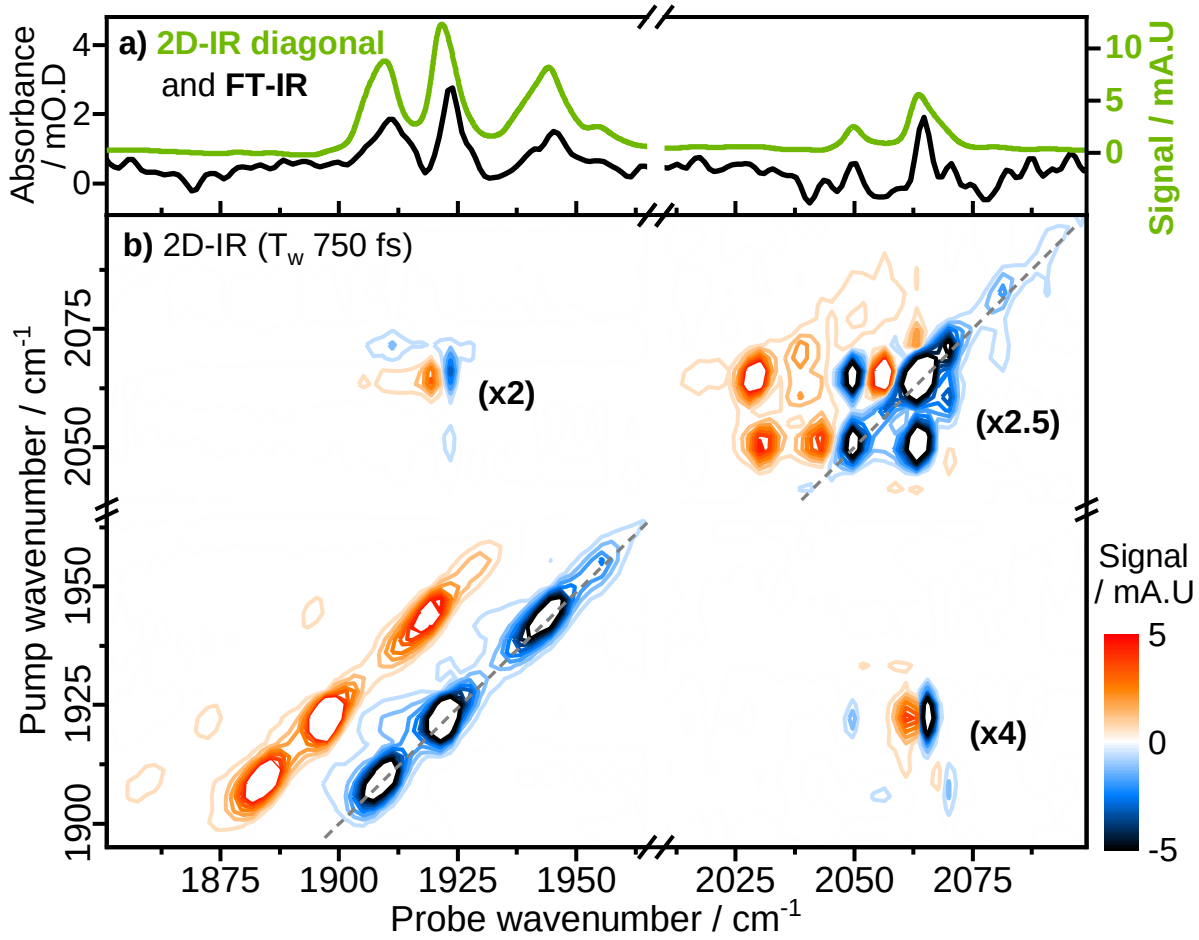

Figure 72 (a) *IR absorption spectrum of as-isolated EcHyd-1 (black trace) and projection of the 2D-IR spectrum diagonal (green). The negative signals of the diagonal have been inverted for comparison with the IR absorption spectrum.* ***(b)*** *2D-IR spectrum of as-isolated EcHyd-1 recorded at a waiting time (T_w) of 750 fs. The dashed line indicates the spectrum diagonal. Numbers in brackets indicate the magnification of the three quadrants of the 2D-IR spectrum containing peaks due to ν_{CN} modes in relation to the ν_{CO} region of the spectrum (1900-1950 cm^{-1}), which contains the most intense peaks.*

signals at 1942 cm^{-1}, 1922 cm^{-1} and 1908 cm^{-1}. These signals are reproduced in the projection of the 2D-IR spectrum diagonal (green trace in **Figure 72(a)**) and are assigned to the ground state absorption (v=0-1) transitions of the Ni_r-B, and the two Ni_r-S states, respectively. In the 2D-IR spectrum diagonal a shoulder can be seen towards the high frequency side of the 1942 cm^{-1} peak (around 1955 cm^{-1}), this is discussed in more detail in the spectra of oxidised *Ec*Hyd-1 (section 5.3.7). The ν_{CN} region (2010-2100 cm^{-1}) of the FT-IR spectrum contains two signals at 2050 cm^{-1} and 2063 cm^{-1}, these are also reproduced in the projection of the 2D-IR spectrum diagonal and are assigned to ground state absorption transitions of the ν_{CN} modes.

5.3.4 2D-IR spectroscopy of as-isolated EcHyd-1 – assigning the major peaks in the ν_{CO} pump region

Figure 73 shows a magnified view of the *Ec*Hyd-1 2D-IR spectra for pump wavenumbers corresponding to ν_{CO} signals recorded with a range of T_w values (750 fs, 15 ps and 45 ps).

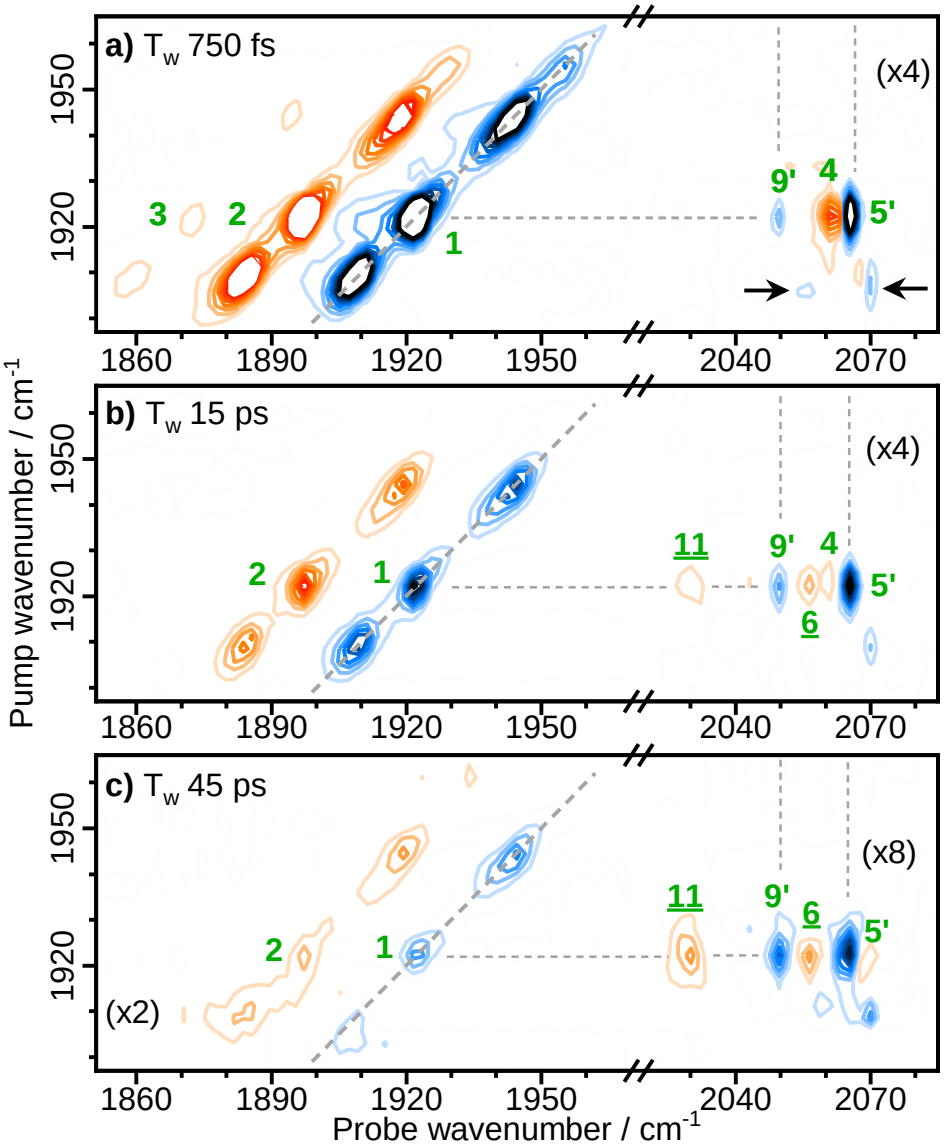

Figure 73 *Magnification of the 2D-IR spectra of EcHyd-1 for pump frequencies coinciding with ν_{CO} bands, showing spectra recorded with T_w values of **(a)** 750 fs, **(b)** 15 ps and **(c)** 45 ps. Green numbers refer to peak assignments. Numbers in brackets indicate the magnification of signals in quadrants of the 2D-IR spectra.*

The negative ν_{CO} peaks on the spectrum diagonal at 1908 cm^{-1}, 1922 cm^{-1} and 1942 cm^{-1} (blue in **Figure 73**) are not linked by peaks below the spectrum diagonal, this indicates that there is no vibrational coupling or energy transfer between ν_{CO} modes, as would be expected for ν_{CO} modes of a single molecular unit.[208] The absence of coupling and energy transfer between ν_{CO} modes is consistent with their assignment to distinct active site states of *Ec*Hyd-1.[93] The following peak assignments for transitions of *Ec*Hyd-1 states are highly consistent with those of *Re*RH in the previous chapter, despite the enzymes being distinctly different in terms of states, physiological functions, parent organisms and activity profiles. This raises the possibility that the overall structural similarities observed in the active site regions of NiFe hydrogenases are more important determinants of the $\nu_{CO}/\nu_{CN1}/\nu_{CN2}$ mode properties than the physiological context of the enzyme of the redox state specific variations in structure.

The three dominant on-diagonal ν_{CO} peaks (at 1908 cm^{-1}, 1922 and 1942 cm^{-1}) are each accompanied by a positive peak shifted to lower probe wavenumber by 25 cm^{-1}. In the T_w 750 fs spectrum (**Figure 73(a)**) they are also accompanied by an additional much weaker positive peak that is downshifted by a further 25 cm^{-1} along the probe axis. The assignment of these peaks is discussed in terms of the most intense set of signals, i.e., that with an on-diagonal v=0-1 peak at 1922 cm^{-1} (labelled **1** in **Figure 73**). In the 2D-IR experiment the interaction of the pump pulse with the sample populates higher vibrational states, enabling the probe pulse to excite transitions that are not normally available in IR absorption experiments at room temperature, as such peaks **2** and **3** are assigned to v=1-2 and v=2-3 transitions, respectively.

For a pump frequency of 1922 cm^{-1} (horizontal dashed line, **Figure 73**) an additional set of off-diagonal peaks (labelled **9'**, **4**, **5'**, **6** and **11**) can be seen in the ν_{CN} region of the spectrum indicating coupling between ν_{CO} and ν_{CN} modes. As such the $|\nu_{CO}\nu_{CN1}\nu_{CN2}\rangle$ notation is used for describing transitions where ν_{CN1} and ν_{CN2} refer to the higher and lower wavenumber ν_{CN} modes respectively, all peak assignments are consistent with the energy level diagram shown in **Figure 74**. Using the $|\nu_{CO}\nu_{CN1}\nu_{CN2}\rangle$ notation, peaks **1-3** correspond to: $|000\rangle$-$|100\rangle, |100\rangle$-$|200\rangle, |200\rangle$-$|300\rangle$. For a pump frequency of 1922 cm^{-1} in the T_w 750 fs spectrum (**Figure 73(a)**) there are four off-diagonal peaks in the ν_{CN} region of the spectrum. The most intense of these peaks is a negative peak, **5'**, which has frequency coordinates (pump, probe) of (1922cm^{-1}, 2063 cm^{-1}). The pump frequency of **5'** matches that of diagonal peak **1** (horizontal dashed line) and its probe frequency matches that of a diagonal peak in the ν_{CN} region (i.e., ν_{CN1} indicated by a vertical dashed line). The same is true of the remaining negative off diagonal peak, **9'** at coordinates (1922 cm^{-1}, 2050 cm^{-1}), although its probe frequency matches that of the other diagonal peak in the ν_{CN} region (ν_{CN2}). The presence of these connecting off-diagonal peaks in early T_w spectra (**Figure 73(a)**) indicates that the ν_{CO} mode is coupled to both of the ν_{CN} stretching modes, validating that they are produced by enzyme in the same active site state.[209] Ground state absorption (v=0-1) signals caused by coupling are indicated by a number with a prime (here **9'** and **5'**) to differentiate them from their on-diagonal counterparts.

The positive peak labelled **4** with coordinates (1922 cm^{-1}, 2061 cm^{-1}) in **Figure 73** is assigned to a transition between the v=1 state of the ν_{CO} mode ($|100\rangle$), which is populated by the pump pulse, and a two quantum combination state with one quantum of energy in both ν_{CO} and ν_{CN2} modes (i.e., $|101\rangle$). The difference in

wavenumber between a combination band and its associated ground state absorption signal gives the mixed mode anharmonicity, this quantity is proportional to the coupling strength. Peaks **4** and **5'** exhibit considerable overlap indicating that the coupling between ν_{CO} and ν_{CN1} modes is weak, it is likely that peak **9'** is also accompanied by a combination that is obscured by overlap.

Careful examination of **Figure 73** reveals a second set of off-diagonal peaks (black arrows in **Figure 73(a)**) that link the ν_{CO} mode at 1908 cm^{-1} to ν_{CN} signals on the diagonal at 2059 cm^{-1} and 2070 cm^{-1}. The intensity of these peaks is too low to clearly resolve their associated positive peaks, although they do indicate the ν_{CN} modes to which the 1908 cm^{-1} ν_{CO} mode is coupled.

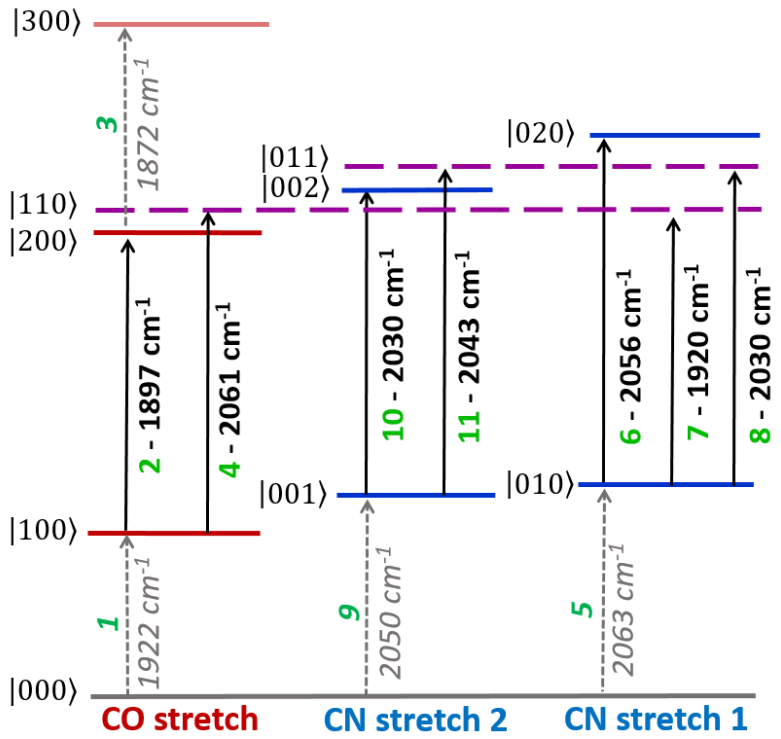

Figure 74 *Energy level diagram showing vibrational energy levels* $|v_{CO}v_{CN1}v_{CN2}\rangle$ *and transition wavenumbers of the* ν_{CO} *and* ν_{CN} *vibrational manifold, as detected for the active site state of EcHyd-1 with a* ν_{CO} *fundamental frequency of 1922* cm^{-1}*. Transitions are labelled with green numbers used to identify peak assignments in the 2D-IR spectra (see text).*

In the spectra recorded with T_w values of 15 ps and 45 ps, shown in **Figure 73(b-c)**, a pair of additional off-diagonal peaks labelled 6 and 11 can be seen at (pump, probe) coordinates (1922 cm^{-1}, 2056 cm^{-1}) and (1922 cm^{-1}, 2043 cm^{-1}), respectively. The emergence of these peaks at later T_w values indicates that they are caused by energy transfer; during the delay time population transfer from the pumped v=1 level of the ν_{CO} mode to the v=1 level of the ν_{CN} modes occurs, this is followed by the probe pulse exciting the v=1-2 transitions of the ν_{CN} modes. It is not apparent from **Figure 73** which of the ν_{CN} modes each of the energy transfer peaks is associated with, however this was determined by analysis of the ν_{CN}-pump region of the spectrum as outlined in the following section. Excited state absorption (v=1-2) signals caused by energy transfer are indicated by an underlined number (here 6 and 11) to differentiate them from their counterparts in the diagonal region.

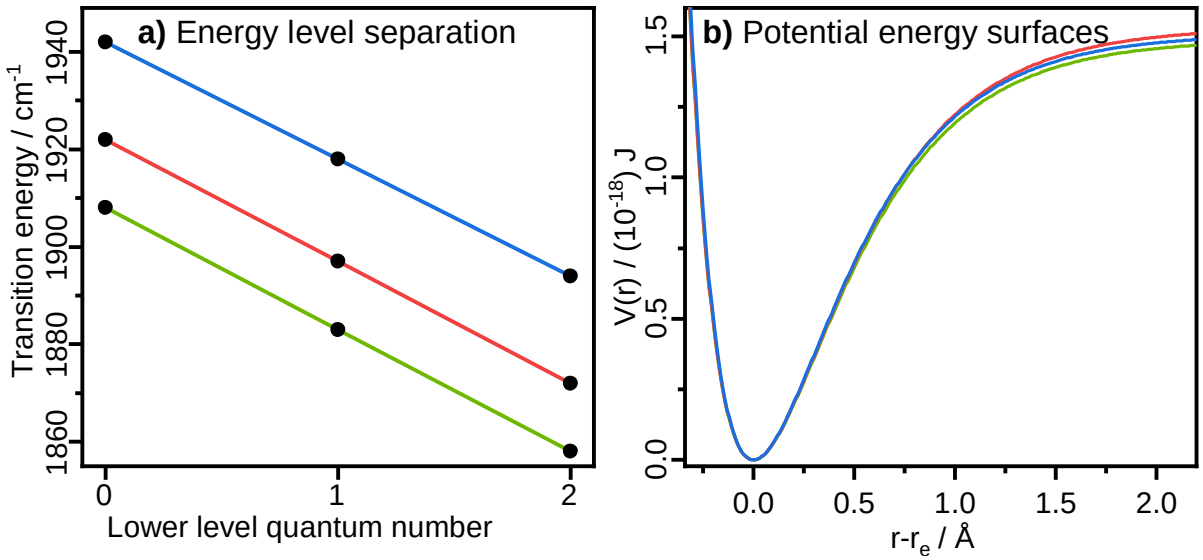

Figure 75 *Morse anharmonic potential data for the ν_{CO} modes of the Ni_r-B (blue line) and Ni_r-$S_{I/II}$ (red and green lines) states of EcHyd-1, showing* ***(a)*** *fitting of functions representing the energy level separations of a Morse potential to experimentally determined transition energies (black dots) and* ***(b)*** *Morse potential energy curves.*

Like in the *Re*RH data, the Morse anharmonic potential was found to be a good approximation for the ν_{CO} modes of *Ec*Hyd-1 active site states, owing to their uniform separation of energy levels and weak coupling to the ν_{CN} modes. ***Figure 75*** shows the fitting of transition energies and plots of the potential energy surfaces for the ν_{CO} modes of the Ni_r-B and Ni_r-$S_{I/II}$ states, the derived CO-bonding parameters are summarised in **Table 3**.

Table 3 *Morse fitting parameters determined for the ν_{CO} mode of the three active site states of EcHyd-1 and the single one from ReRH (*).*

Redox state	Fundamental frequency / cm^{-1}	Harmonic frequency / cm^{-1}	Dissociation energy / kJ mol^{-1}	Force constant / N m^{-1}	Anharmonicity constant ($x10^{-3}$)
Ni_r-$S_{I/II}$	1908	1934	897	1512	6.45
Ni_r-$S_{I/II}$	1922	1946	922	1531	6.31
Ni_r-B	1942	1970	908	1569	6.49
Ni_a-S (*)	1943	1967	941	1563	6.18

The CO-bonding parameters are highly consistent between redox states of *Ec*Hyd-1 and *Re*RH with less than 5% variation observed for all parameters, which is notable for distinct states of enzymes with different functions. This similarity raises the possibility that the CO ligand provides a static contribution to bonding at the NiFe site irrespective of redox state, and supports the notion (based on the observed lack of spectral diffusion, see 5.3.10) that the surrounding protein architecture forms a restricted environment. Of relevance for *in silico* studies, the harmonic frequency is significantly larger than the fundamental frequency by a value approximately equal to the anharmonicity (± 1-4 cm^{-1}).[154]

5.3.5 2D-IR spectroscopy of as-isolated EcHyd-1 – assigning the major peaks in the ν_{CN} pump region

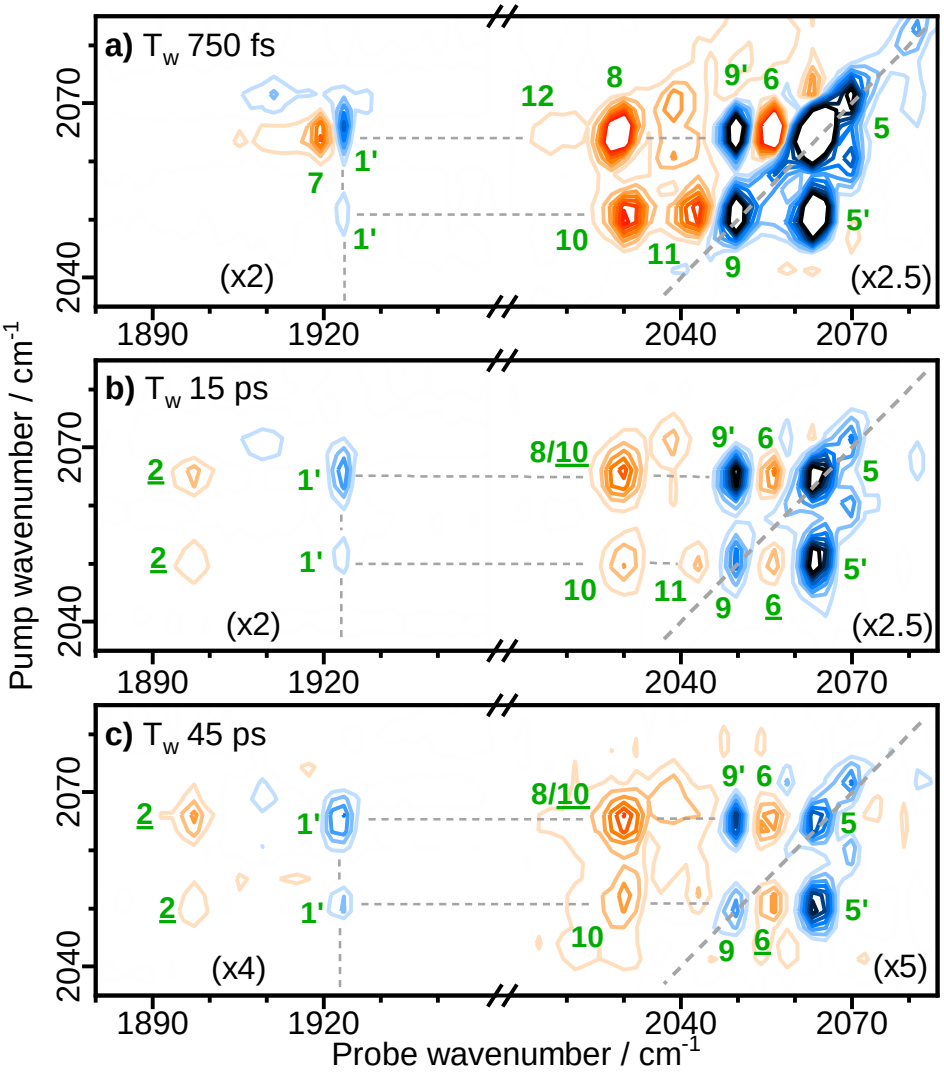

Figure 76 *Magnification of the 2D-IR spectra of EcHyd-1 for pump frequencies coinciding with ν_{CN} bands, showing spectra recorded with T_w values of **(a)** 750 fs, **(b)** 15 ps and **(c)** 45 ps. Green numbers refer to peak assignments. Numbers in brackets indicate the magnification of signals in quadrants of the 2D-IR spectra.*

The 2D-IR spectra of as-isolated *Ec*Hyd-1 at pump frequencies corresponding to ν_{CN} peaks at a range of waiting times are shown in **Figure 76**. There are two major peaks on the spectrum diagonal, peak **9** at 2050 cm^{-1} and peak **5** at 2063 cm^{-1}, these are assigned to the $|000\rangle$-$|001\rangle$ and $|000\rangle$-$|010\rangle$ transitions (i.e., ν_{CN1} and ν_{CN2} modes), respectively. Two additional diagonal peaks are present at 2059

cm^{-1} and 2070 cm^{-1}, the 2059 cm^{-1} peak is significantly obscured by overlap with **5**, where it is visible as a shoulder. These peaks, along with their off diagonal counterparts are discussed in more detail in section 5.3.6.

First focussing on the higher wavenumber peak (**5**) in the T_w 750 fs spectrum (**Figure 76(a)**), at a pump wavenumber of 2066 cm^{-1} (upper horizontal line) there are six peaks in the off-diagonal region, these are labelled **6**, **9'**, **8**, **12**, **1'** and **4**. The positive peak **6** is assigned to the $|010\rangle$-$|020\rangle$ transition, this assignment is corroborated by the emergence of energy transfer peak **6** in later T_w spectra when pumping at 2050 cm^{-1} (lower horizontal lines in **Figure 76(b-c)**). The probe wavenumber of **6** (2056 cm^{-1}) relative to its on-diagonal counterpart **5** gives a single mode anharmonic shift of 7 cm^{-1}. Negative peak **9'** at 2050 cm^{-1} is assigned to the $|000\rangle$-$|001\rangle$ transition and indicates coupling between ν_{CN} modes. Positive peak **8** at 2030 cm^{-1} is assigned to the combination transition $|010\rangle$-$|011\rangle$, the separation of **8** relative to **6'** gives a mixed mode anharmonic shift of 20 cm^{-1} indicating that the ν_{CN} modes are strongly coupled. The negative peak labelled **1'** at 1922 cm^{-1} indicates that the ν_{CN1} and ν_{CO} modes are coupled. Positive peak **7** is assigned to the $|010\rangle$-$|110\rangle$ combination transition. Peak **7** overlaps considerably with peak **1'**, however fitting the spectrum in this region shows that it is centered at 1920 cm^{-1} giving a mixed mode anharmonicity of 2 cm^{-1}, this matches the value obtained when pumping the ν_{CO} mode at 1922 cm^{-1} (appendix **Figure 95**). In the spectra recorded at a T_w of 15 ps and 45 ps, energy transfer peaks **2** and **10** can be seen at 1897 cm^{-1} and 2030 cm^{-1}, respectively. Peaks **10** and **2** correspond to the $|001\rangle$-$|002\rangle$ and $|100\rangle$-$|200\rangle$ transitions (respectively), and are caused by energy transfer during the delay time from the $|010\rangle$ level to the $|001\rangle$ and $|100\rangle$ levels, respectively. Peaks **10** and **8** occur at the same wavenumber, however **10** can be identified as a distinct

peak caused by energy transfer due to its persistence in later T_w spectra in contrast to the combination bands **4**, **7** and **11**.

Moving on to the lower wavenumber diagonal peak (**9**) in the T_w 750 fs spectrum (**Figure 76(a)**), for a pump wavenumber of 2050 cm^{-1} (lower horizontal line) there are four peaks in the off-diagonal region, these are labelled **5'**, **11**, **10** and **1'**. The negative peak **5'** is assigned to the $|000\rangle$-$|010\rangle$ transition, and is equivalent to peak **9'** in indicating that the v_{CN} modes are coupled. Peak **10** is the $|001\rangle$-$|002\rangle$ excited state absorption. The position of **10** (2030 cm^{-1}) relative to its on-diagonal counterpart **9** (2050 cm^{-1}) gives a single mode anharmonicity of 20 cm^{-1} which is significantly greater than the 7 cm^{-1} observed for the v_{CN1} mode. Peak **11** is assigned to the $|001\rangle$-$|011\rangle$ combination transition, and its position relative to **9'** reproduces the 20 cm^{-1} mixed mode anharmonicity obtained when pumping the higher frequency v_{CN1} mode (comparing **8** and **5'**). This assignment of peaks is corroborated by fitting pump slices as shown in appendix **Figure 94**, and implementing the parameters derived from fitting to simulate the major set of peaks, as shown in **Figure 77(a)(ii)** and **(b)(ii)**. The positions of peaks **12** and **13** in **Figure 77(a)(ii)** are consistent with assignment to the forbidden transitions $|001\rangle$-$|020\rangle$ and $|010\rangle$-$|002\rangle$, respectively

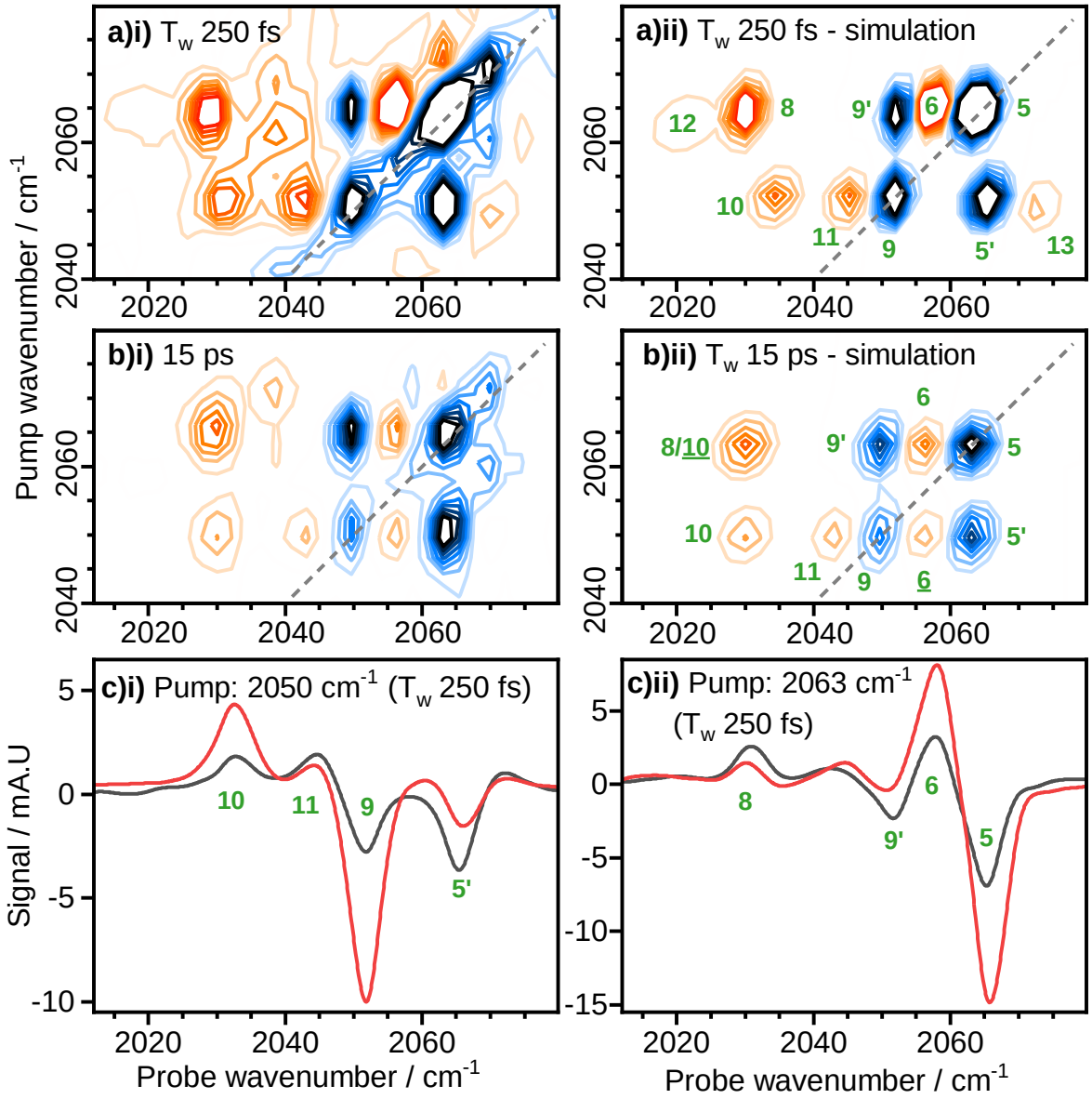

Figure 77 *Magnification of the 2D-IR spectra of EcHyd-1 for pump frequencies coinciding with ν_{CN} bands, showing spectra recorded with T_w values of **(a)** 250 fs and **(b)** 15 ps, showing **(i)** experimental spectra and **(ii)** simulated spectra for the major pair of coupled CN modes. Probe spectra **(c)** for pump frequencies of **(i)** 2050 cm^{-1} and **(ii)** 2063 cm^{-1}, extracted from T_w 250 fs 2D-IR spectra recorded with parallel (red traces) and perpendicular (black traces) polarization conditions. Numbers in green correspond to the assignment of peaks.*

The previously examined 2D-IR spectra were all recorded with perpendicular pump-probe polarisation geometry, additional insight is provided by their comparison with spectra recorded with parallel polarisation geometry (**Figure 78(a-b)**). The amplitudes of coupling peaks varies with the angle between their

respective transition dipole moments according to the functions shown in **Figure 78(c)**.

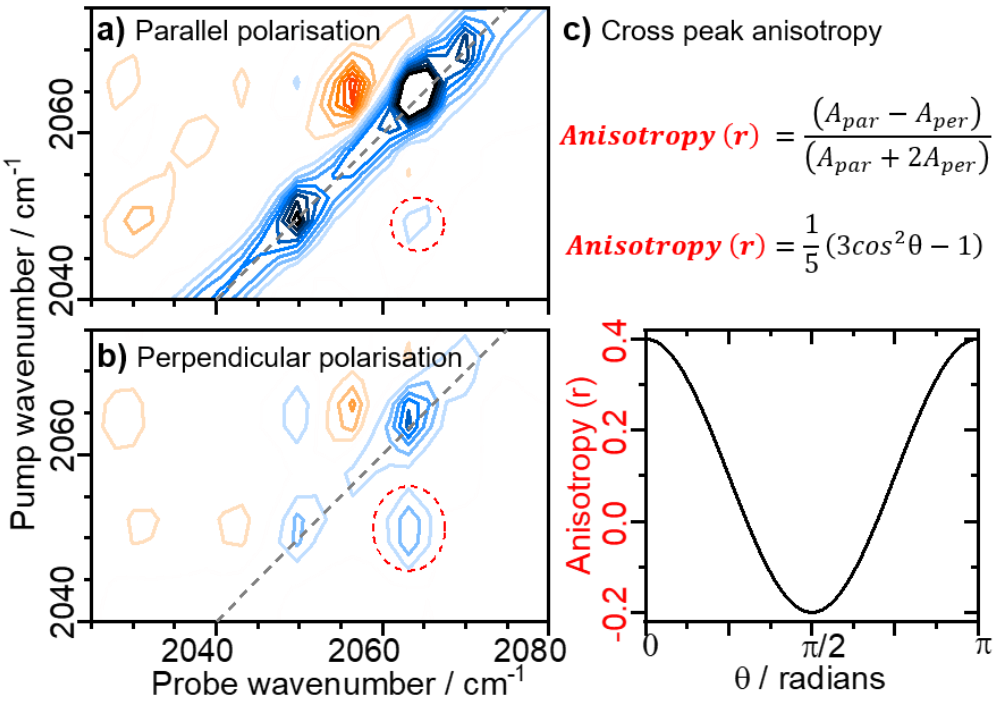

Figure 78 *2D-IR spectra of as-isolated EcHyd-1 recorded at a T_w of 250 fs with* ***(a)*** *perpendicular and* ***(b)*** *parallel polarisation geometries. The spectra show the ν_{CN}-pump, ν_{CN}-probe quadrant displayed with the same signal scaling. The amplitude of the peak, indicated by the red dashed circle, was used along with the displayed equations in* ***(c)*** *to determine the angle between the transition dipole moments of the coupled ν_{CN} modes.*[121]

The amplitudes of coupling peak **5'** (indicated by the red dashed circle, **Figure 78(a-b)**) produces an anisotropy value of -0.24, which is consistent with the ν_{CN} modes having orthogonal transition dipole moments (**Figure 78(c)**). This observation is consistent with crystal structure data, however this provides geometric information for a molecule in the solution phase. Assuming other hydrogenase crystal structures constitute accurate representations of their solution phase structure, the converse approach could be applied to the prediction of relative peak intensities from crystal structural data. Cross peak anisotropy calculations for other states was hindered by the overlapping of peaks (for both ν_{CN}/ν_{CN} and ν_{CO}/ν_{CN} coupling peaks).

5.3.6 2D-IR spectroscopy of as-isolated EcHyd-1 – assigning the minor peaks

The 2D-IR signals corresponding to the minority Ni_r-S state present in as-isolated *Ec*Hyd-1 samples (i.e., that with v=0-1 transitions for ν_{CO}, ν_{CN2} and ν_{CN1} modes at 1908 cm^{-1}, 2059 cm^{-1} and 2070 cm^{-1}, respectively) were assigned in a manner similar to that described for the major Ni_r-S state in the previous section. A magnified view of the 2D-IR spectrum (T_w 750 fs) with this assignment of peaks is shown below in ***Figure 79***, a full 2D-IR spectrum with assignment of peaks corresponding to this state can be found in the appendix in **Figure 96**.

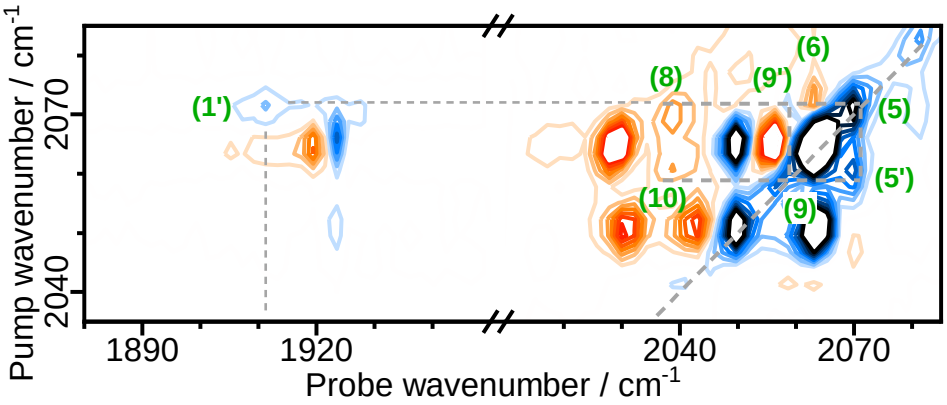

Figure 79 *Magnification of the 2D-IR spectrum (T_w 750 fs) of as-isolated EcHyd-1 for pump frequencies coinciding with ν_{CN} bands with peak assignment for the minor set (dashed lines) of coupled signals with v=0-1 transitions of ν_{CO}, ν_{CN2} and ν_{CN1} at 1908 cm^{-1}, 2059 cm^{-1} and 2070 cm^{-1}, respectively.*

An energy level scheme for the minority Ni_r-S state can be seen below in **Figure 80**. Values for the mixed mode and single mode anharmonicities are summarised in **Table 4**, these values are consistent with those observed for the majority Ni_r-S state, as would be expected from closely related redox states.

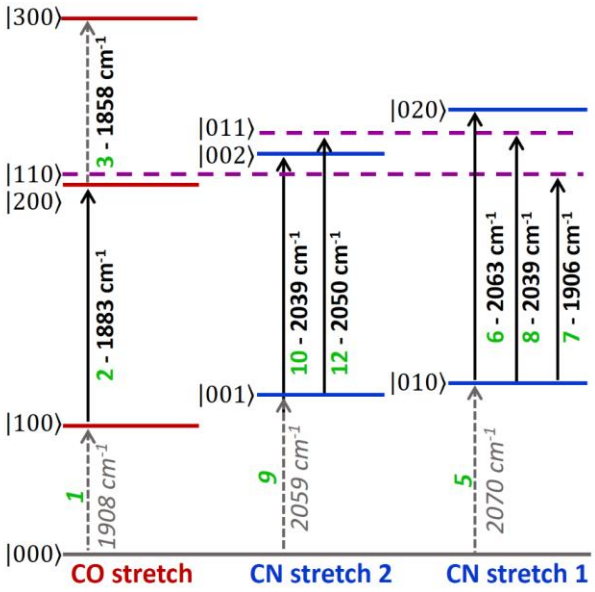

Figure 80 *Energy level diagram showing vibrational energy levels $|v_{CO}v_{CN1}v_{CN2}\rangle$ and transition wavenumbers of the v_{CO} and v_{CN} vibrational manifold, as detected for the active site state of EcHyd-1 with a v_{CO} fundamental frequency of 1908 cm^{-1}. Transitions are labelled with green numbers used to identify peak assignments in the 2D-IR spectra (see text).*

5.3.7 2D-IR spectroscopy of oxidised EcHyd-1 – assignment of peaks

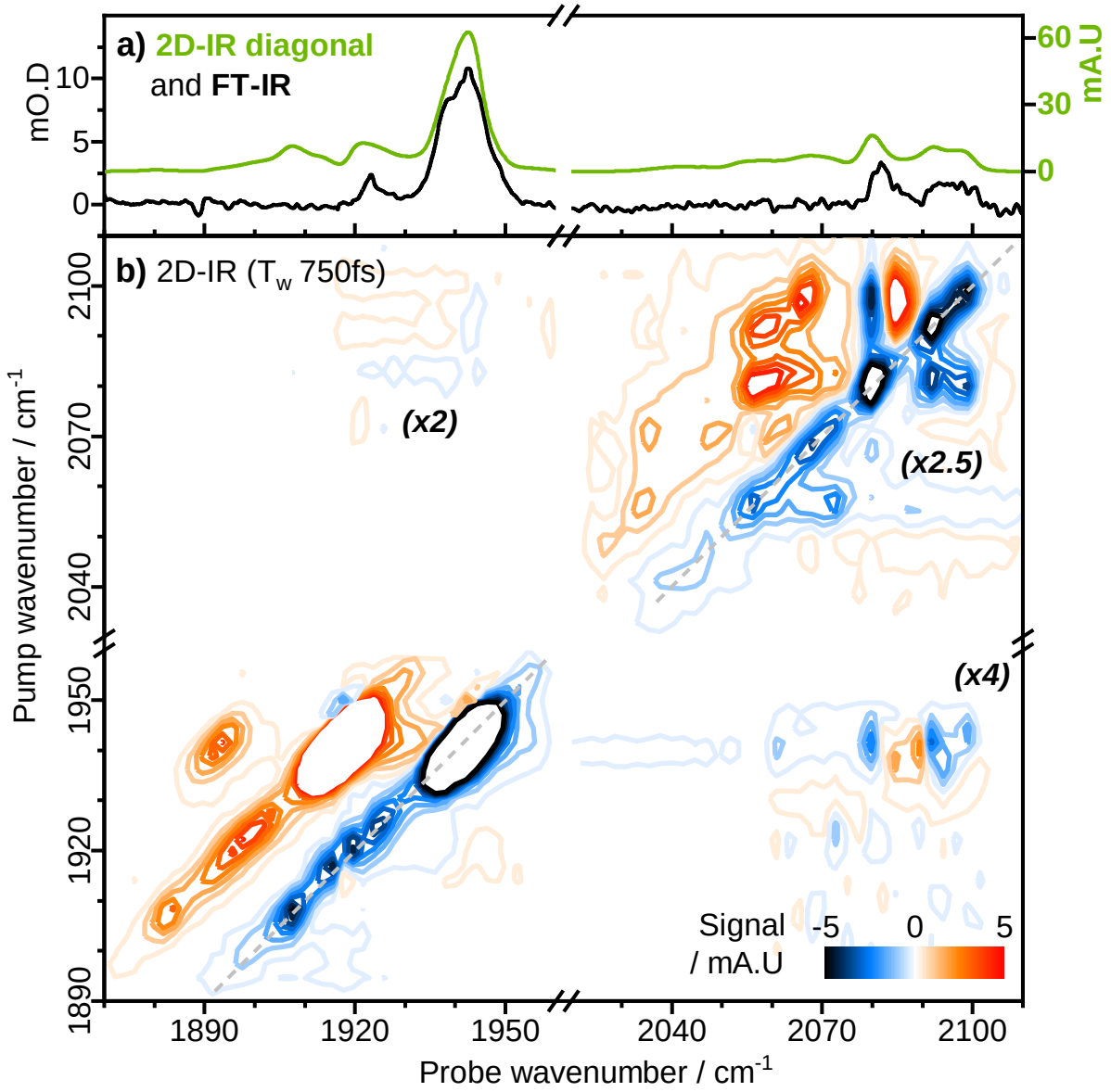

Figure 81 (a) *IR absorption spectrum of oxidised EcHyd-1 (black trace) and projection of the 2D-IR spectrum diagonal (green). The negative signals of the diagonal have been inverted for comparison with the IR absorption spectrum.* ***(b)*** *2D-IR spectrum of as-isolated EcHyd-1 recorded at a waiting time (T_w) of 750 fs. The dashed line indicates the spectrum diagonal. Numbers in brackets indicate the magnification of the three quadrants of the 2D-IR spectrum containing peaks due to ν_{CN} modes in relation to the ν_{CO} region of the spectrum (1900 - 1950 cm^{-1}), which contains the most intense peaks.*

The FT-IR spectrum of oxidised *Ec*Hyd-1 overlaid with an inverted projection of the 2D-IR spectrum diagonal are shown in **Figure 81(a)**. The ν_{CO} region (1850-

1975 cm^{-1}) of the FT-IR spectrum (black trace in **Figure 81(a)**) contains three signals at 1945 cm^{-1}, 1922 cm^{-1} and 1908 cm^{-1}. These signals are consistent with the gas cycling FT-IR experiments (***Figure 69*(c)(ii)** in section 5.3.1) and represent a sample for which the Ni_r-S states have been depleted and the Ni_r-B state enriched. Indications that the 1942 cm^{-1} ν_{CO} signal for the Ni_r-B state overlaps with the ν_{CO} of another state can be found in both the 2D-IR spectra of as-isolated *Ec*Hyd-1 (shoulder at 1955 cm^{-1}) and the FT-IR spectra (greater width of "Ni_r-B" relative to Ni_r-S signals). Analysis of the 2D-IR spectra of oxidised *Ec*Hyd-1 (**Figure 81(b)**) confirms the presence of an additional set of signals that overlap with those of the Ni_r-B state.

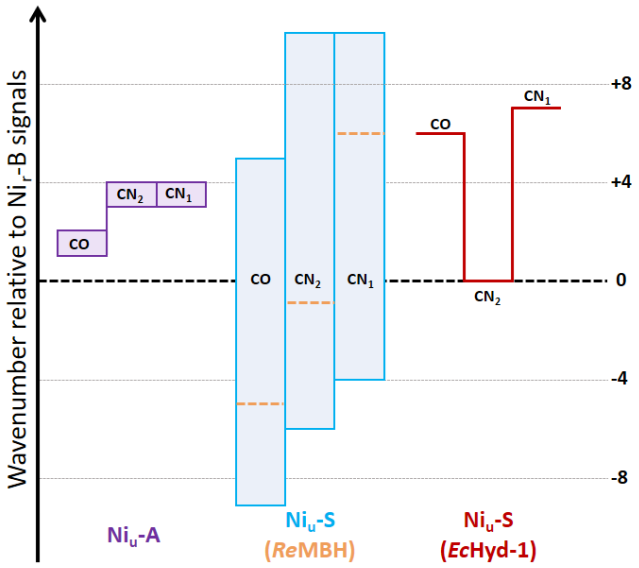

Figure 82 *Diagram showing the wavenumbers reported for CO, CN_1 and CN_2 stretching modes of NiFe-hydrogenases (DvMF, AvMBH, DgMBH and ReMBH) in the Ni_u-A (purple) and Ni_u-S states (blue) relative to Ni_r-B signals from the same enzyme.* [24,66,206,207]

The fundamental transitions for ν_{CO} , ν_{CN2} and ν_{CN1} modes are found at 1942 cm^{-1}, 2080 cm^{-1} and 2092 cm^{-1} for the Ni_r-B state, and 1948 cm^{-1}, 2080 cm^{-1} and 2098 cm^{-1} for the additional overlapping state. Given that the state with a ν_{CO} of

1948 cm^{-1} is enriched in oxidised samples it is reasonable to assign it to an 'unready' state, either Ni_u-A or Ni_u-S. However, comparison of the wavenumbers reported for ν_{CO} and ν_{CN} modes of a range of NiFe-hydrogenases in the Ni_u-A and Ni_u-S states, relative to Ni_r-B signals from the same enzyme (**Figure 82**) indicates that the new state observed here for *Ec*Hyd-1 is more consistent with assignment to the Ni_u-S state than the Ni_u-A state.

An enlarged view of the region of the T_w 750 fs 2D-IR spectrum for pump- and probe frequencies corresponding to ν_{CN} transitions is shown below in **Figure 83(a)**. Assigning transitions in this spectral region was complicated by the fundamental transitions of the ν_{CN1} modes of the Ni_u-S and Ni_r-B states occurring at the same frequency (2080 cm^{-1}), in addition to their ν_{CN2} modes (at 2092 cm^{-1} and 2098 cm^{-1}, respectively) being sufficiently close to overlap. However, using the pattern of anharmonicities observed in the *Re*RH and as-isolated *Ec*Hyd-1 data as a blueprint a feasible assignment of peaks was assembled and their frequencies corroborated by fitting pump slices **Figure 83(c-e)** and simulating the 2D-IR spectrum **Figure 83(b)**. This enabled the construction of energy level schemes for the Ni_r-B and Ni_u-S states of *Ec*Hyd-1, as shown in **Figure 84**.

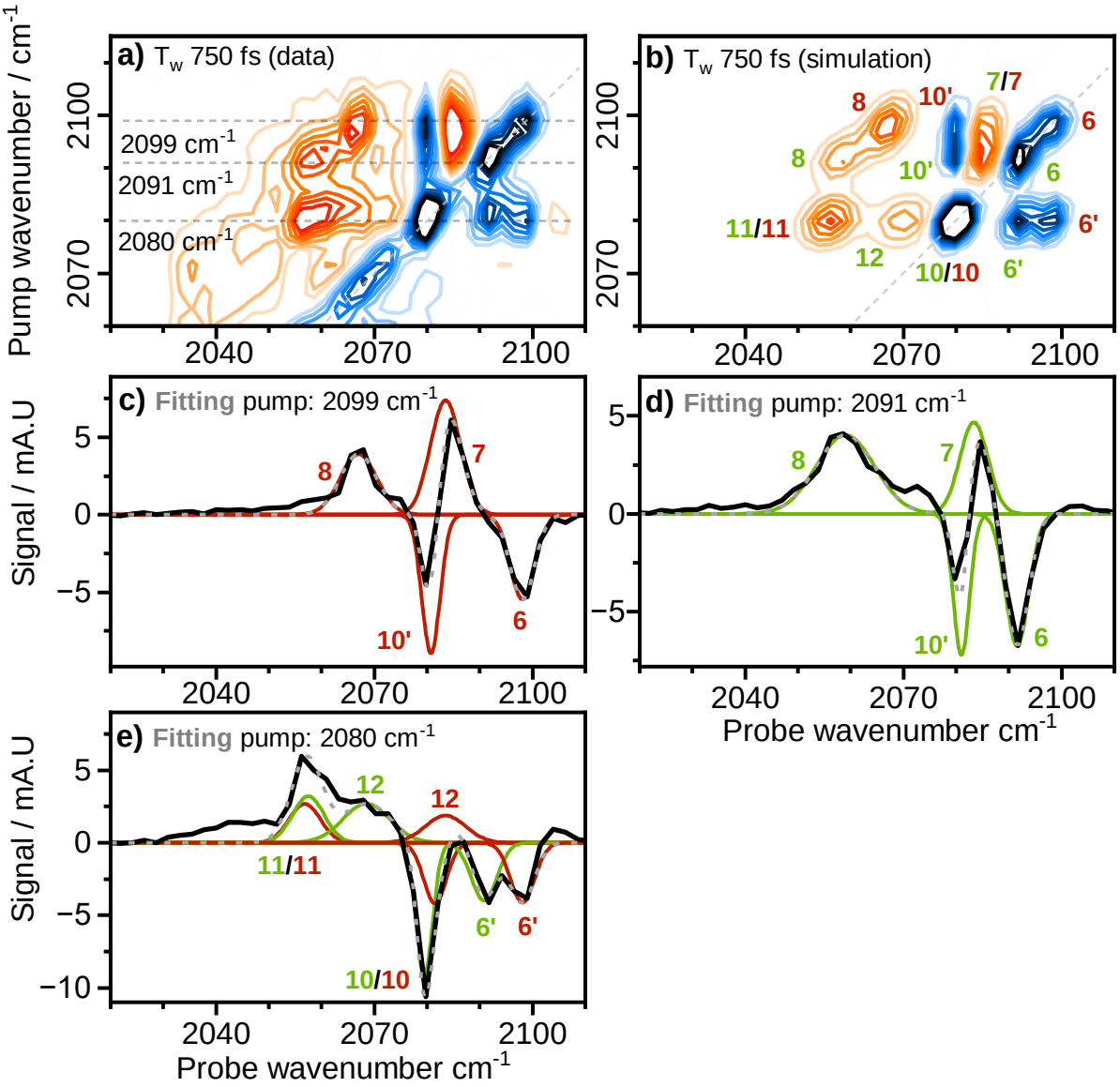

Figure 83 *Magnification of the 2D-IR spectra of EcHyd-1 for pump frequencies coinciding with ν_{CN} bands, showing the* ***(a)*** *T_w 750 fs experimental and* ***(b)*** *simulated spectra. Probe spectra for pump frequencies of* ***(c)*** *2098 cm^{-1},* ***(d)*** *2091 cm^{-1} and* ***(e)*** *2080 cm^{-1}, extracted from the T_w 750 fs 2D-IR spectrum. For* ***(c-e)*** *the experimental data is shown as solid black lines, fitting of individual peaks are shown as solid red and green lines, and the cumulative fitting as dashed grey lines. Green and red numbers are used to identify transitions of the Ni_r-B and Ni_u-S states respectively.*

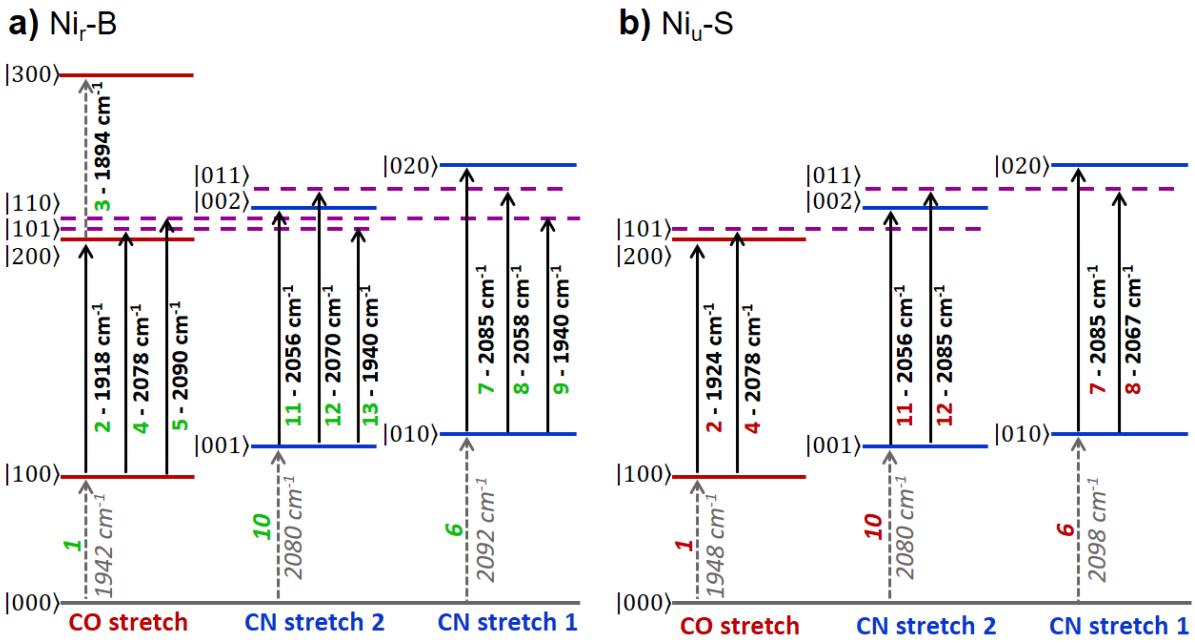

Figure 84 *Energy level diagram showing vibrational energy levels* $|v_{CO}v_{CN1}v_{CN2}\rangle$ *and transition wavenumbers of the* ν_{CO} *and* ν_{CN} *vibrational manifold, as detected for the* ***(a)*** *Ni$_r$-B and* ***(b)*** *Ni$_u$-S active site state of EcHyd-1. Transitions are labelled with green and red numbers used to identify peak assignments in the 2D-IR spectra (see text).*

5.3.8 2D-IR spectroscopy of a NiFe hydrogenase active site mimic

Having first identified the large disparity in ν_{CN} single mode anharmonicities in the *Re*RH data as a potential indicator of the protein scaffold tuning the chemistry at the NiFe centre, the observation of remarkably similar single (and mixed) mode anharmonicities for all detected states of *Ec*Hyd-1 raised two possibilities i) that these properties are intrinsic to the $Fe(CO)(CN)_2$ unit, or ii)

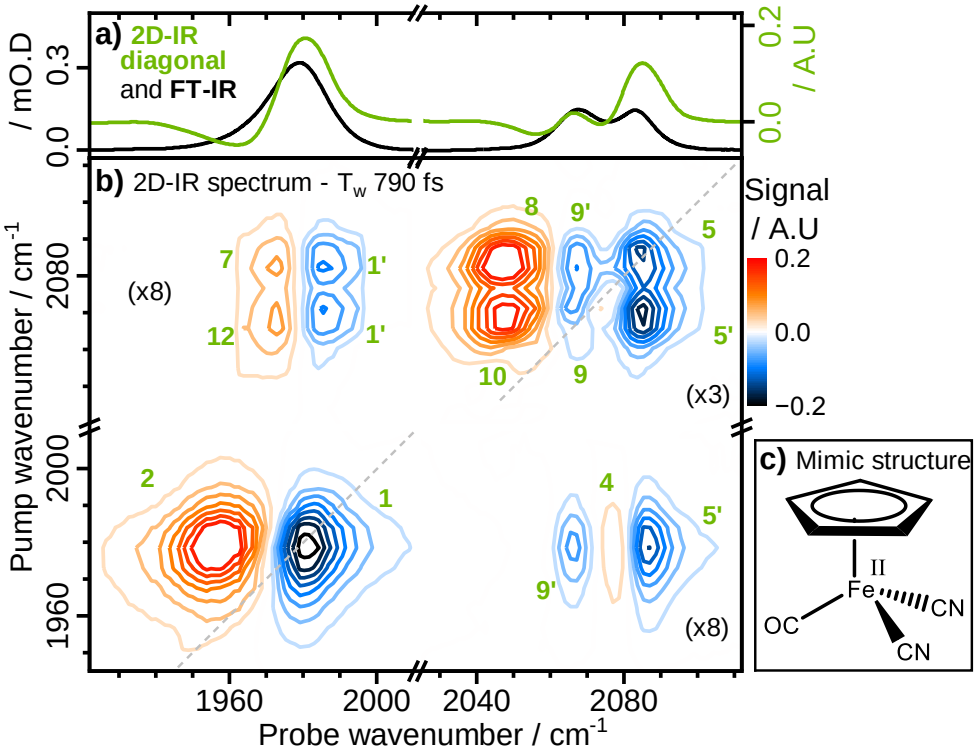

Figure 85 (a) *IR absorption spectrum of the mimic* ***M1*** *dissolved in water (black trace) and projection of the 2D-IR spectrum diagonal (green). The negative signals of the diagonal have been inverted for comparison with the IR absorption spectrum.* ***(b)*** *2D-IR spectrum of* ***M1*** *recorded at a waiting time (T_w) of 790 fs. The dashed line indicates the spectrum diagonal. Numbers in brackets indicate the magnification of the three quadrants of the 2D-IR spectrum containing peaks due to ν_{CN} modes in relation to the ν_{CO} region of the spectrum (1900 - 1950 cm^{-1}), which contains the most intense peaks.* ***(c)*** *Structure of* ***M1****.*

that the active site environment exerts a similar influence on the CN^- ligands irrespective of redox state/enzyme. To investigate the influence of the protein architecture on the spectroscopy of the Fe-bound carbonyl and cyanide ligands in the NiFe hydrogenase active, 2D-IR spectra were recorded of the iron site

model K[(η^5-C_5H_5)Fe(CO)$(CN)_2$] (referred to as **M1**) dissolved in a variety of solvents. An early T_w 2D-IR spectrum of **M1** is shown in **Figure 85(b)**.

The assignment of peaks followed the same procedure as that used for the spectra of *Ec*Hyd-1 and *Re*RH, comparing spectra recorded with differing T_w values and polarisation geometries to facilitate the assignment of transitions, in addition to fitting pump slices and simulating spectra to validate the assignments. An energy level scheme for **M1** dissolved in water can be seen in **Figure 86** as well as fitted slices and simulated spectra (for the ν_{CN} region) in **Figure 87**. The pattern of bands observed for **M1** are broadly similar to that seen

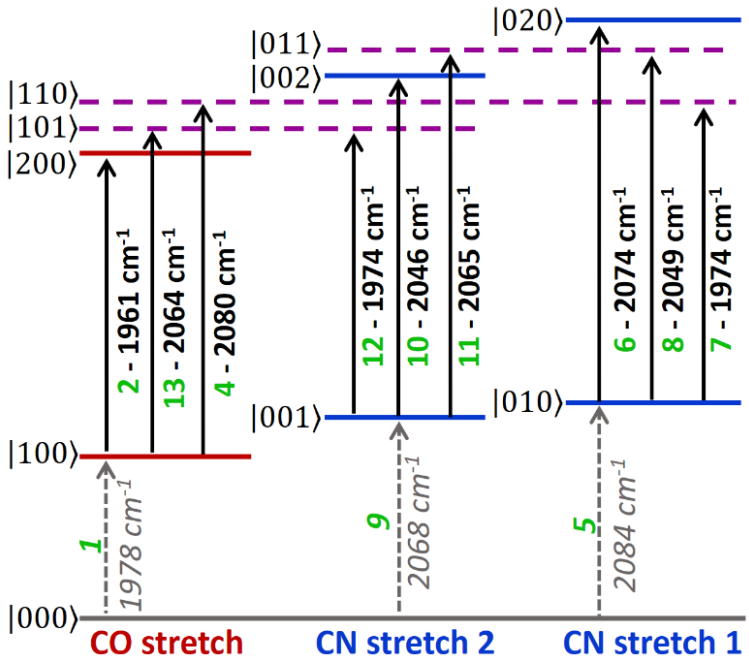

Figure 86 *Energy level diagram showing vibrational energy levels* $|v_{CO}v_{CN1}v_{CN2}\rangle$ *and transition wavenumbers of the* ν_{CO} *and* ν_{CN} *vibrational manifold, as detected for the mimic* ***M1*** *dissolved in water. Transitions are labelled with green numbers used to identify peak assignments in the 2D-IR spectra (see text).*

in the spectra of NiFe hydrogenase samples, although the bands are significantly broader. Cross peaks indicate weak coupling between ν_{CO} and ν_{CN} modes, as well as strong coupling between ν_{CN} modes. The separation of fundamental and

excited state absorption transitions provides the single mode anharmonicities, for **M1** in water these are broadly similar to that of the enzymes with values of 17 cm^{-1}, 22 cm^{-1} and 10 cm^{-1} for ν_{CO} , ν_{CN2} and ν_{CN1} modes, respectively.

The 2D-IR spectra (experimental and simulated) and fitted slices for **M1** dissolved in D_2O, MeOH, CH_3CN and DMSO can be found in the appendix (**Figure 99** to **Figure 104**). The anharmonicities of the vibrational modes of **M1** are shown in **Table 5** and are discussed in more detail in 5.3.9.

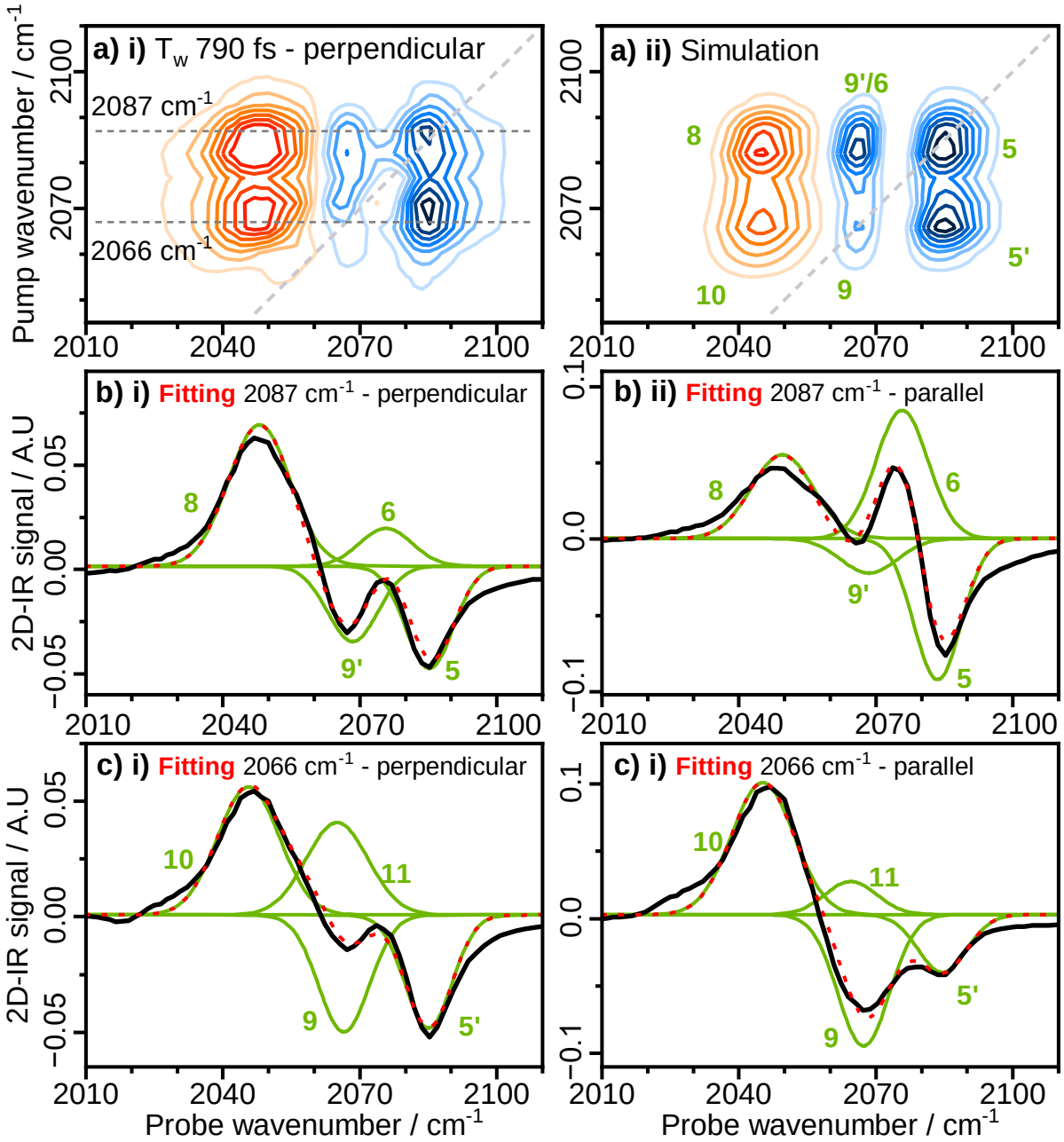

Figure 87 (a) *Magnification of the 2D-IR spectra of the mimic (dissolved in H_2O) for pump frequencies coinciding with ν_{CN} bands, showing the **(i)** T_w 750 fs experimental and **(ii)** simulated spectra (perpendicular polarization). Fitted probe spectra for pump frequencies of **(b)** 2087 cm^{-1} and **(c)** 2066 cm^{-1}, extracted from T_w 790 fs 2D-IR spectra collected with **(i)** perpendicular and **(ii)** parallel polarization geometries. For **(b)** and **(c)** the experimental data is shown as solid black lines, fitting of individual peaks are shown as solid green lines and the cumulative fitting as dashed red lines. Green numbers are used to identify transitions.*

5.3.9 Anharmonicities of ν_{CO} and ν_{CN} modes

Table 4 shows a comparison of the ν_{CO} and ν_{CN} mode anharmonicities of the different active states observed in samples of *Ec*Hyd-1 and *Re*RH. With the exception of the Ni_u-S state of *Ec*Hyd-1 these values are highly similar, having the same unusual pattern of a large single mode anharmonicity for the ν_{CN2} mode and a much smaller value for the harmonic ν_{CN1} mode, in addition to large ν_{CN1}/ν_{CN2} mixed mode anharmonicity. While coupling has previously been inferred from the IR absorption spectra of isotopically labelled hydrogenase,[88,154] these results demonstrate that coupling between ν_{CN} modes

Table 4 *Fundamental frequencies, single and mixed mode anharmonicities for the four redox states of EcHyd-1 and the single one from ReRH (*).*

Redox state	Fundamental (n=0-1) frequency / cm^{-1}			Anharmonicity / cm^{-1}					
				Single mode			Mixed mode		
	ν_{CO}	ν_{CN2}	ν_{CN1}	ν_{CO}	ν_{CN2}	ν_{CN1}	ν_{CO} / ν_{CN2}	ν_{CO} / ν_{CN1}	ν_{CN1} / ν_{CN2}
Ni_r-$S_{I/II}$	1908	2059	2070	25	20	7	2	2	20
Ni_r-$S_{I/II}$	1922	2050	2063	25	20	7	2	-	20
Ni_r-B	1942	2080	2092	24	24	7	2	-	22
Ni_u-S	1948	2080	2098	24	24	13	2	-	13
Ni_a-S (*)	1943	2071	2080	25	18	8	2	2	24

is very strong, which in the case of the majority Ni_r-S state the coupling is sufficiently strong to cause the breakdown of the harmonic oscillator selection rules (indicated by the presence of peaks **12** and **13** in **Figure 77**). This effect is caused by the higher order terms of the molecular response function and cannot be explained using a harmonic description of the potential energy surfaces of the CN^- bonds.[111,210–213] For the Ni_u-S state, the markedly higher single (ν_{CN1}) and lower mixed (ν_{CN1}/ν_{CN2}) mode anharmonicities may be attributable to the sulfoxygenated cysteine residue some believe is present in this active site state.

Table 5 *Fundamental frequencies, single and mixed mode anharmonicities for* ***M1*** *dissolved in a variety of solvents, listed in descending order of polarity.*

Solvent	Fundamental (n=0-1) frequency / cm^{-1}			Anharmonicity / cm^{-1}					
				Single mode			Mixed mode		
	ν_{CO}	ν_{CN2}	ν_{CN1}	ν_{CO}	ν_{CN2}	ν_{CN1}	ν_{CO} / ν_{CN2}	ν_{CO} / ν_{CN1}	ν_{CN1} / ν_{CN2}
H_2O	1978	2068	2084	17	22	10	3	3	19
D_2O	1977	2068	2084	17	21	12	4	4	21
MeOH	1972	2082	2095	19	19	16	4	4	21
CH_3CN	1954	2088	2096	23	23	18	-	5	21
DMSO	1943	2086	2094	24	23	19	-	5	21

For **M1** (**Table 5**) dissolved in polar solvents (H_2O and D_2O specifically) the pattern of anharmonicities is comparable to that seen in NiFe hydrogenase states, with a low single mode anharmonicity for the ν_{CN1} mode accompanied by high values for the ν_{CN2} mode and for the ν_{CN1}/ν_{CN2} mixed mode anharmonicity. The results for **M1** indicate that some of the observations on the spectroscopy of the NiFe hydrogenase samples can be attributed to the intrinsic properties of the $Fe(CO)(CN)_2$ moiety, i) the ν_{CN2} single mode anharmonicity is consistently ~20 cm^{-1}, ii) the ν_{CO}/ν_{CN} mixed mode anharmonicities are very low and iii) the ν_{CN1}/ν_{CN2} mixed mode anharmonicity is large. The latter two points indicate that weak ν_{CO}/ν_{CN} coupling and strong ν_{CN1}/ν_{CN2} coupling are intrinsic features of the moiety. Additionally, literature reports on complexes containing Fe ions with multiple CN^- ligands do not reproduce the strong coupling between ν_{CN} modes observed here.[124,214]

As shown in **Table 5**, the solvent polarity affects the fundamental transition frequencies, in less polar solvents the frequency of the ν_{CO} mode decreases and the ν_{CN} modes increase in such a way as to narrow the frequency separation between ν_{CN} modes. The effect of solvent polarity on anharmonicities is more subtle, with most of the parameters largely unchanged and only the ν_{CN1} single

mode anharmonicity significantly impacted by solvent polarity. As the solvent polarity decreases the ν_{CN1} single mode anharmonicity increases from 10 cm^{-1} in H_2O to 19 cm^{-1} in DMSO, with the separation in ν_{CN} single mode anharmonicities narrowing (from 12 cm^{-1} to 4 cm^{-1}) in a fashion similar to the fundamental frequency separation (which narrows from 21 cm^{-1} to 9 cm^{-1}). Comparing the values obtained for NiFe hydrogenase states (excluding Ni_u-S) with the trends observed for **M1**, demonstrates that the enzyme ν_{CN} modes have some properties consistent with **M1** in both the less and more polar solvents. The hydrogenase states exhibit i) lower ν_{CN1} single mode anharmonicities (7-8 cm^{-1}) than that of **M1** in even the most polar solvents, ii) separation in fundamental transition frequency (9-13 cm^{-1}) approaching that of **M1** in less polar solvents, iii) large separation in ν_{CN} mode anharmonicities (10-17 cm^{-1}) similar to that of **M1** in H_2O. These differences are summarised below in **Table 6**.

Table 6 *Comparison of selected ν_{CN} mode parameters for EcHyd-1, ReRH (*), and **M1**. Fundamental transition frequencies for the ν_{CO} modes are included to differentiate Ni_r-$S_{I/II}$ states. All values are quoted in cm^{-1}.*

	NiFe hydrogenase active site state:					M1 in solvent:				
	Ni_r-$S_{I/II}$	Ni_r-$S_{I/II}$	Ni_r-B	Ni_u-S	Ni_a-S (*)	H_2O	D_2O	MeOH	CH_3CN	DMSO
ν_{CO} n=0-1 frequency	1908	1922	1942	1948	1943	1978	1977	1972	1954	1943
ν_{CN1} single mode anharmonicity	7	7	7	13	8	10	12	16	18	19
Separation of (ν_{CN}) single mode anharmonicities	13	13	17	11	10	12	9	3	5	4
Separation of (ν_{CN}) n=0-1 transition frequencies	11	13	12	18	9	16	16	13	8	8

The observed variation in ν_{CN1} single mode anharmonicity and in the separation between ν_{CN} single mode anharmonicities suggests a degree of environmental sensitivity, however it bears noting that conclusions based on the contentious

sulfoxygenation state of the Ni_u-S state must be tempered by a degree of uncertainty. A recent theoretical study on the spectroscopy of **M1** (in H_2O) and the Ni_a-S state attributed the disparity between ν_{CN} mode anharmonicities to a Darling-Dennison resonance between their v=2 levels.[91] This phenomenon causes a splitting effect that lowers the anharmonicity of one mode and raises that of the mode by altering the energies of the v=2 levels. The authors found that removing this effect from their calculations resulted in the ν_{CN} modes having equivalent anharmonicities.[91] It is apparent from the **M1** data shown here (**Table 6**) that the disparity in ν_{CN} mode anharmonicities is solvent polarity dependent,

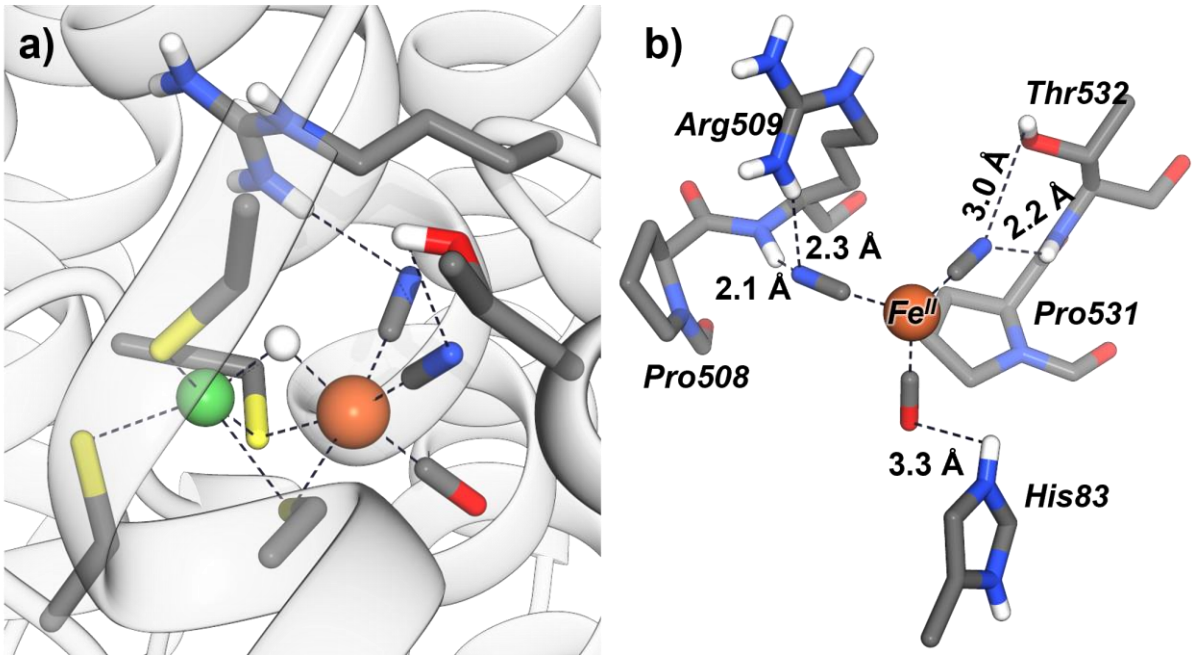

Figure 88 *Crystal structure data (PDB: 6FPW)[15] showing the* ***(a)*** *active site environment of H_2-reduced EcHyd-1 and (b) an enlarged view of the Fe(CO)(CN)$_2$ moiety. Secondary structure is shown as white ribbon, selected groups are shown in ball and stick form, coloured by atom.*

this raises the possibility that the polarity of the local environment of the CN^- ligands modulates the extent of the coincidence in energy of their v=2 levels. Indeed vibrations of CN^- ligands have been stated to have small changes in dipole moment and large changes in quadrupole moment.[165] It was determined

that the CN^- ligands are strongly influenced by the internal electric field established between the ligated metal ion and the charged N atom, this is termed an internal Stark Effect (ISE).[165] It follows that if the ν_{CN} modes are sensitive to through space electrostatic effects (i.e., an ISE) the perturbation of their potentials will be more significant in polar solvents, perhaps forming the basis for the splitting in their single mode anharmonicities.

The similarity in these parameters exhibited by **M1** in H_2O and by hydrogenase, in conjunction with the conserved H-bonds formed between Arg/Thr side chains and CN^- ligands (**Figure 88**) imply that these parameters are tuned by H-bonding. These results suggest that the spectroscopic differences between **M1** and the enzyme stem from the environment of the active site dictated by the protein scaffold. It is however important to note that, while the Cp ring enables **M1** to provide a good structural mimic of the $Fe(CO)(CN)_2$ unit, [215,216] **M1** does not replicate either the Ni or the terminal and bridging cysteine residues, which have been shown to strictly control the local geometry of the NiFe site, leading to asymmetry in the two cysteine bridges.[63,81,94,98] These differences could in principle influence the vibrational potentials of the cyanide ligands that lie trans to them.

5.3.10 Structural dynamics – 2D-IR diagonal lineshapes

Dynamic fluctuations in the environment of a ligand can give rise to a range of structural microenvironments, each with a discrete vibrational frequency, thereby causing inhomogeneous broadening of the corresponding IR band. In 2D-IR spectroscopy, homogeneous broadening affects the antidiagonal linewidth of bands whereas inhomogeneous broadening affects the diagonal linewidth. Inhomogeneously broadened bands are elongated along the diagonal.[111] If the dynamic fluctuations that give rise to inhomogeneous broadening occur on timescales that are similar (or shorter) than the vibrational relaxation time of the mode, then with advancing T_w the lineshape transitions from being elongated along the diagonal to more circular. This evolution in lineshape, termed spectral diffusion, is caused by the structural dynamics

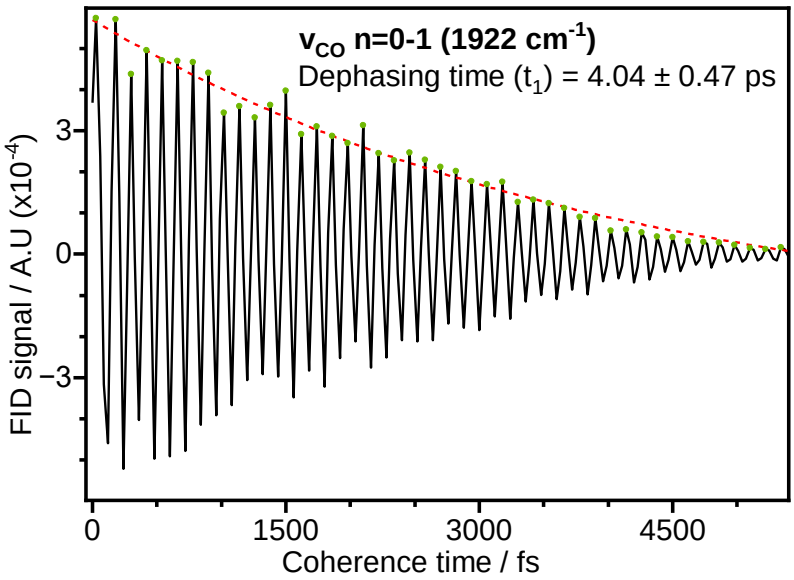

Figure 89 *Plot of the 1922 cm^{-1} ν_{CO} ground state absorption 2D-IR signal as a function of coherence time (τ), with fitted monoexponential decay curve (black and red lines, respectively), data points used for fitting are shown as green circles.*

enabling the pumped mode to sample all of its available microenvironments before the arrival of the probe pulse.[198] The timescale of local environmental

fluctuations can be evaluated from 2D-IR peaks via their ratio of diagonal to anitdiagonal linewidths. For all observed states of *Ec*Hyd-1 the ratio of diagonal to antidiagonal FWHM values are very similar, with values of 1.7, 1.6 and 1.5 for the fundamental transitions of the ν_{CO}, ν_{CN1} and ν_{CN2} modes, respectively (at T_w 250 fs). These ratios did not change in the T_w 15 ps spectra, which indicates that minimal structural dynamics occur within this timescale. Fitting the coherence decay of the 1922 cm^{-1} ground state absorption signal (**Figure 89**) gave a dephasing time of 4.04 ± 0.47 ps (i.e., 8 cm^{-1}), taking in to account the 5 cm^{-1} diagonal linewidth this corresponds to a homogeneous linewidth of 3 cm^{-1}. This homogeneous linewidth is consistent with the anitdiagonal linewidth obtained from the 2D-IR spectra and the observed ratio indicates very limited inhomogeneous broadening.

The spectral linewidths of ν_{CO} and ν_{CN} modes of **M1** are significantly broader than those of *Ec*Hyd-1 and *Re*RH. The fundamental ν_{CO} transition of **M1** (in water) has a diagonal linewidth of 20 cm^{-1} while the enzymes have linewidths of 5-12 cm^{-1}, the ν_{CN} transitions of **M1** have linewidths of 12 cm^{-1} and 14 cm^{-1} while those of the enzymes are 5 cm^{-1} irrespective of redox state. Transitions of **M1** undergo significant spectral diffusion as evidenced by the ratios of diagonal to antidiagonal linewidths increasing from 1.5, 1.2 and 1.5 (ν_{CO}, ν_{CN1} and ν_{CN2}) in T_w 125 fs spectra to unity in T_w 2 ps spectra, indicating the occurrence of rapid structural fluctuations in the local environment of CO and CN^- ligands. The rapid spectral diffusion of ν_{CO} and ν_{CN} modes in aqueous solutions is consistent with previous studies and reflects their dynamically evolving H-bonding environments.[217] At 0.96 ps, the dephasing time for the ν_{CO} mode of **M1** is significantly faster than the 4 ps observed for *Ec*Hyd-1. Faster dephasing contributes to the increased linewidth of **M1** relative to *Ec*Hyd-1. However, taking in to account the 20 cm^{-1} diagonal linewidth of **M1** produces a

homogeneous linewidth of 12 cm^{-1} which indicates a significant degree of inhomogeneous broadening.

The observations for the structural dynamics of *Ec*Hyd-1 are consistent with those from *Re*RH and imply two scenarios that are not mutually exclusive, the protein architecture around the NiFe active site i) forms a restricted environment with minimal structural fluctuations, and/or ii) structural fluctuations do not give rise to spectral diffusion.[154] Further clarification is not possible from these datasets and would require a protein scaffold with markedly different behaviour to the few picosecond spectral diffusion dynamics that are routinely observed for proteins.[126,218–223] Considering that the function of NiFe hydrogenases involves the manipulation of small substrates (i.e., H_2/H^+) and the exclusion of slightly larger molecules (e.g., the narrow gas-channels of O_2-tolerant hydrogenases restricting the access of O_2), such a rigid architecture may be the biological solution to these problems. Previous studies have postulated that structural rigidity may be important for the correct positioning of Arg509 (**Figure 88**) for participation in the FLP mechanism of H_2-activation, indeed such rigidity may also help explain the peculiar see-saw geometry observed for Ni-ion.[27,77,83,94] Alternatively, the observed lack of spectral diffusion could be caused by the H-bonding to the CN^- ligands being sufficiently weak (perhaps due to sub-optimal H-bonding geometry) that the ν_{CN} frequencies do not act as efficient reporters of protein fluctuations, with the ν_{CO} mode similarly decoupled. This scenario would have implications for the vibrational relaxation mechanism, indicating that energy dissipation occurs via the dimetallic unit rather than through the protein (or via a pathway that has yet to be elucidated).

5.3.11 Vibrational relaxation dynamics

The broadband IR pump-probe spectra of as-isolated and O_2-incubated *Ec*Hyd-1 are shown below in **Figure 90(a)** and **(b)**, respectively.

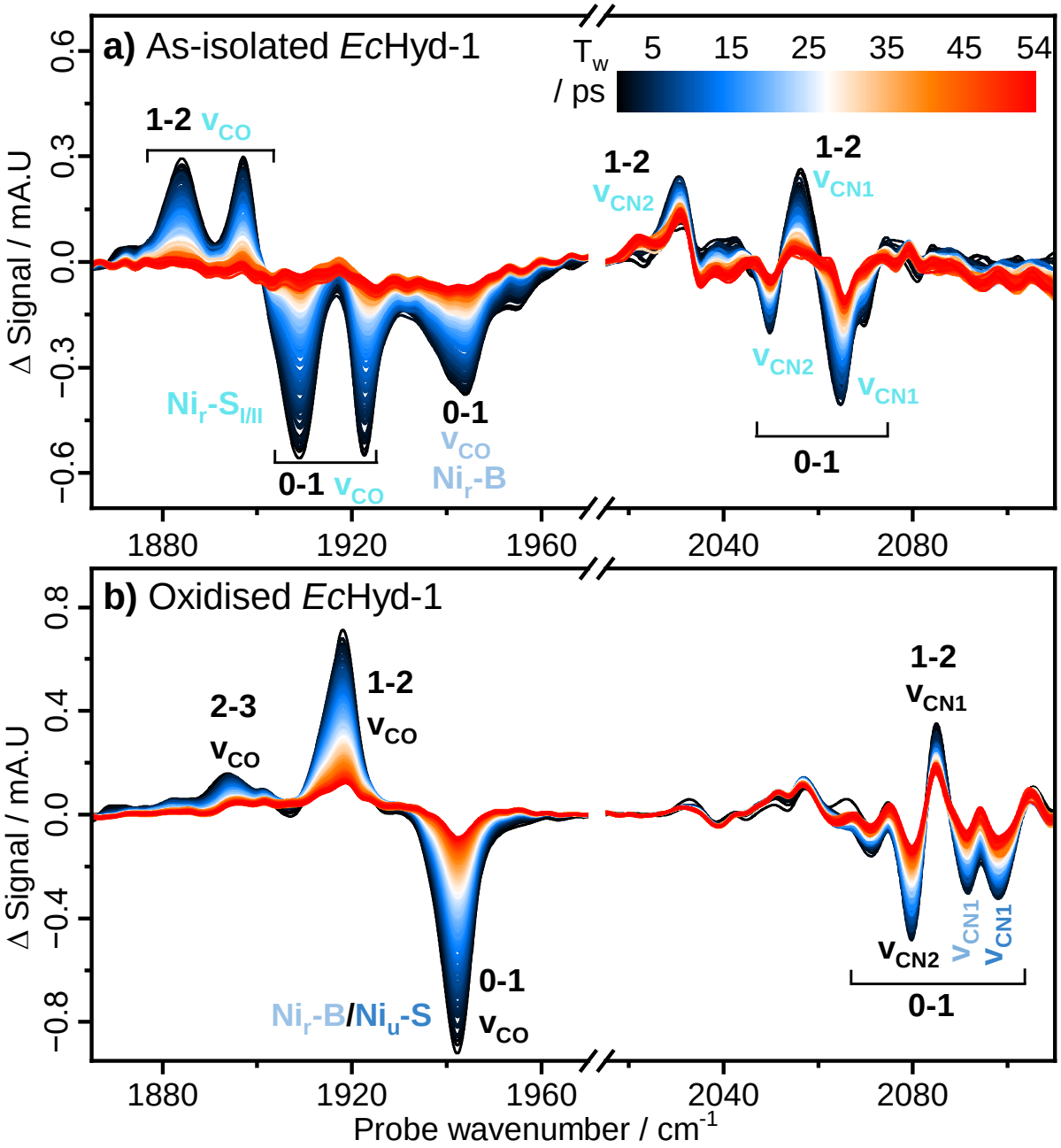

Figure 90 *IR_{pump}– IR_{probe} spectra of* ***(a)*** *as-isolated and* ***(b)*** *oxidised EcHyd-1. Traces are coloured by pump-probe delay time (T_w) and ν_{CN} signals are scaled by a factor of 2.5.*

In the pump-probe spectra of as-isolated *Ec*Hyd-1 (**Figure 90(a)**) three negative bands are visible in the ν_{CO} region (1870-1970 cm^{-1}), these are assigned to the

v=0-1 transitions of the Ni_r-$S_{I/II}$ and Ni_r-B states. A pair of positive peaks assigned to the v=1-2 transitions of the Ni_r-$S_{I/II}$ states are also present. In the ν_{CN} region (2020-2110 cm^{-1}) of **Figure 90(a)** a set of overlapping features assignable to the v=0-1 and v=1-2 transitions of the Ni_r-$S_{I/II}$ states can be seen. In the pump-probe spectra of oxidised *Ec*Hyd-1 (**Figure 90(b)**) three ν_{CO} peaks assigned to the v=0-1, v=1-2 and v=2-3 transitions of the overlapping Ni_r-B and Ni_u-S states are visible, similarly overlapping v=0-1 and v=1-2 transitions of the ν_{CN} modes are

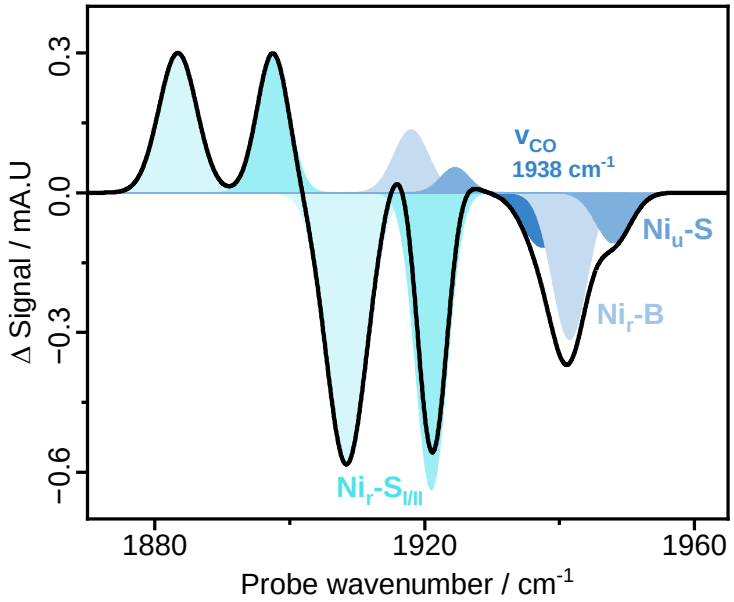

Figure 91 *Simulation of the ν_{CO} region of an early waiting time IR_{pump}– IR_{probe} spectrum of as-isolated EcHyd-1 (solid black line). Signals are coloured by active site state and their positions/widths are based on the fitting of 2D-IR spectrum slices. Second excited state absorption (v=2-3) transitions are omitted.*

also apparent. For NiFe hydrogenase samples comprising mixtures of active site states, the assignment of bands and the calculation of accurate decay times are complicated by the overlapping nature of the signals. This is demonstrated in **Figure 91** which shows a simulation of an early T_w pump-probe spectrum of as-isolated *Ec*Hyd-1 (i.e., from **Figure 90(a)**). This simulation demonstrates how the shape of the Ni_r-B v=0-1 transition is distorted by the presence of the same shoulder features observed in the corresponding 2D-IR spectra (**Figure 73(a)**), in

addition to showing how the intensity of the v=0-1 transition at 1922 cm^{-1} (Ni_r-$S_{I/II}$) is diminished by overlap with v=1-2 features.

Vibrational lifetimes (T_1) for the v=1 states were determined by fitting the time-dependence of the respective peak intensities to monoexponential functions, as shown in appendix **Figure 97** and **Figure 98**. Values ranging between 16 ± 3 ps and 25 ± 2 ps were obtained for the ν_{CO} mode, and values between 29 ± 2 ps and 39 ± 5 ps for the ν_{CN} modes of the four active site states. These vibrational lifetimes are consistent with peaks due to energy transfer between ν_{CN} modes, which are apparent in 2D-IR spectra at T_w values of 15 ps and later. Pump-probe spectra of as-isolated *Ec*Hyd-1 were also collected with a commercial spectrometer in-house (not shown here), and comparable rates were obtained for the 1922 cm^{-1} ground state absorption signal demonstrating that a national laser facility is not a necessity for such measurements.

Figure 92 shows an extension of **Figure 57** from 4.3.4, comparing the vibrational lifetimes (T_1) for the ν_{CO} modes of *Ec*Hyd-1 and *Re*RH with a trio of hydrogenase active site mimics (molecules **1-3**) and a CO-releasing molecule (CORM) dissolved in a variety of solvents. The enzyme T_1 values are consistently low for both different redox structural states and enzymes. This highlights the presence of an efficient and likely conserved pathway for the dissipation of energy away from the active site. As outlined in 4.3.4, such a pathway could be important for maintaining the directionality of catalysis.

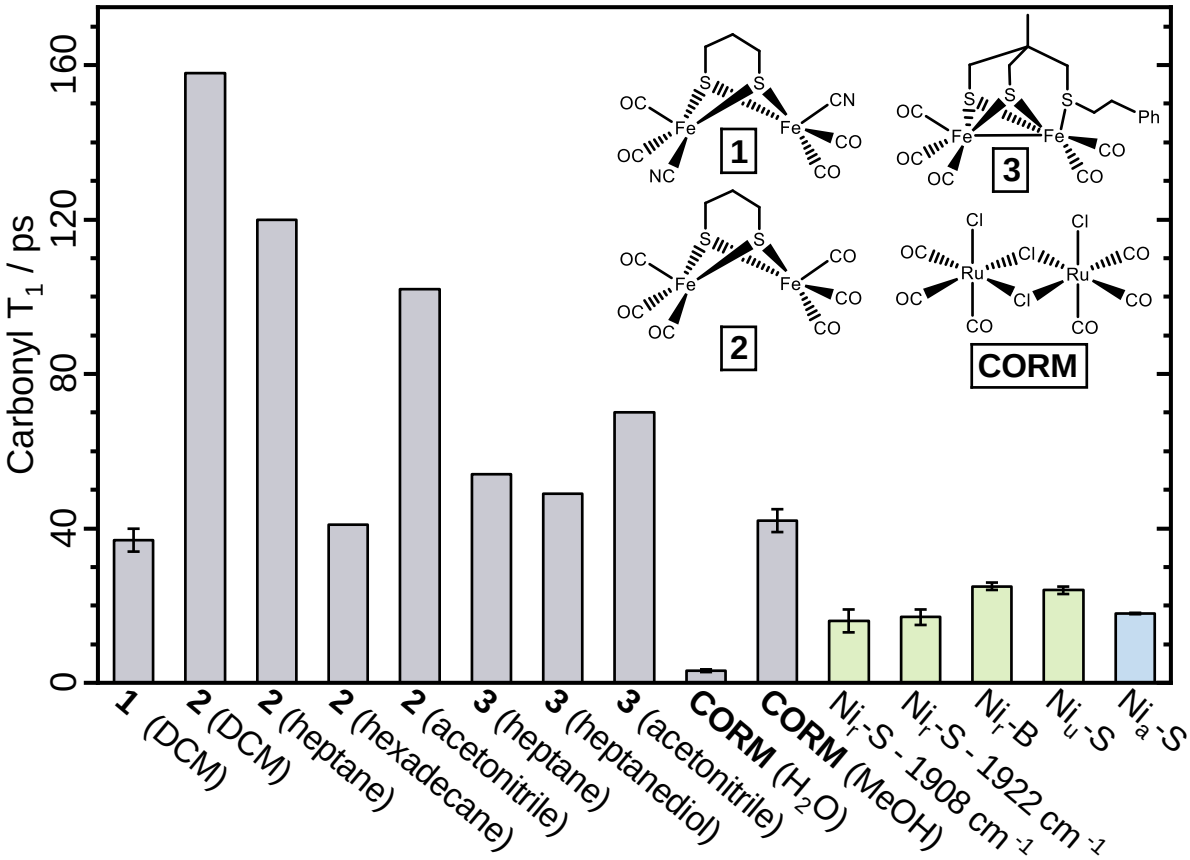

Figure 92 *Bar chart comparing the T_1 times of the ν_{CO} modes of <u>Ec</u>Hyd-1 (green bars), <u>Re</u>RH (blue bar), hydrogenase active site mimics (**1-3**) and a CO-releasing molecule (CORM) dissolved in different solvents (indicated in brackets).* [123,124,166,167]

5.4 Conclusions

These results demonstrate the successful application of pump-probe and 2D-IR spectroscopy to study the active site of *Ec*Hyd-1 in a number of states, including the previously unreported Ni_r-$S_{I/II}$ and Ni_u-S states. Via comparison of the enzyme results with those of the model compound **M1** in a variety of different solvents, the vibrational potential energy surfaces and dynamics of the $Fe(CO)(CN)_2$ moiety (and in particular the ν_{CN} modes) are revealed to be sensitive probes of local environment. The vibrational potentials of the ν_{CN} modes are determined to be strongly coupled with distinctly different single mode anharmonicities. The strong coupling between ν_{CN} modes and the weak coupling between ν_{CO} and ν_{CN} modes are found to be attributes of the $Fe(CO)(CN)_2$ unit, whilst the anharmonicity of the ν_{CN1} mode and its disparity with that of the ν_{CN2} mode are found to be effective probes of the local environment. Observations based on the anharmonicities of the ν_{CN} modes, in addition to the structural dynamics (of ν_{CO} and ν_{CN} modes), indicate that the protein scaffold creates a highly specialised environment by eliminating solvent from the active site and leading to dynamics that cannot be entirely replicated using solvent analogs. The indication is of a protein scaffold that interacts surprisingly weakly with the active site or which very tightly controls the local structure via cysteine links to the NiFe centre and asymmetric H-bonding arrangement between the protein scaffold and the CN^- ligands. The similarity in spectroscopic parameters observed for different active site states of *Ec*Hyd-1 and *Re*RH imply an evolutionarily selected active site environment that is crucial to the enzyme structure, while not necessarily to its function. Additionally these results demonstrate the necessity of including anharmonic effects for understanding the potential energy surfaces of the active site vibrational modes, its structure and dynamics. The need for incorporating secondary coordination spheres in

biomimetic hydrogen conversion catalysts is highlighted by the comparison of vibrational parameters for *Ec*Hyd-1 and **M1** in varying solvent systems, which demonstrate that not all of the parameters can be emulated using a simple solvent system. This work should provide valuable blueprint for the analysis of the physical properties of other NiFe hydrogenases and hydrogenase biomimetics.

6 Conclusion and outlook

This thesis has demonstrated the utility of pump-probe and 2D-IR spectroscopy in providing dynamic and structural insight that contributes to understanding the active site chemistry of NiFe hydrogenases and how it is tuned by the surrounding protein scaffold.

In chapter 4 the regulatory hydrogenase from *Ralstonia eutropha* served as an ideal starting point for the first pump-probe and 2D-IR study of a NiFe hydrogenase due to its isolation in an almost pure redox structural state. In these initial measurements the first direct evidence of strong coupling between ν_{CN} modes and weak coupling between ν_{CO} and ν_{CN} modes was obtained, this confirmed *Pierik et al*'s suppositions in early isotope labelling IR absorption studies.[88] Here the first indications that the protein scaffold tunes the active site chemistry were observed via i) the large disparity in ν_{CN} single mode anharmonicities, perhaps a result of the asymmetric H-bonding contacts of the CN^- ligands, ii) the absence of spectral diffusion indicating significant protein structural constraints and iii) the observation of efficient dissipation of energy away from the $Fe(CO)(CN)_2$ unit and its potential importance in maintaining the directionality of catalysis. This chapter provided a good starting point for the interpretation of the more complex spectra produced by hydrogenase samples comprising mixtures of active site states.

In chapter 5 the spectra of the as-isolated and oxidised states of *Ec*Hyd-1 were analysed. Here the facility of 2D-IR spectroscopy in assigning transitions originating from the same molecule, in tandem with thorough biochemical characterisation, enabled the identification of a trio of redox structural states not previously observed in *Ec*Hyd-1 (Ni_r-$S_{I/II}$ and Ni_u-S). Analysis of *Ec*Hyd-1 states

demonstrated that many of the derived properties (ν_{CO}/ν_{CN} single and mixed mode anharmonicities, CO bond properties, relaxation and structural dynamics) are highly similar to those in the previous chapter, despite the enzymes being distinctly different (in terms of redox state, physiological function, parent organism and activity profile). This lead to the notion that the active site environment is evolutionarily selected, with the protein scaffold creating a highly specialised environment around the CO and CN^- ligands. Analysis of the spectra of the Fe-site mimic **M1** demonstrated that strong coupling between ν_{CN} modes and weak coupling between ν_{CO} and ν_{CN} modes are intrinsic properties of the $Fe(CO)(CN)_2$ moiety. Additionally, the spectra of **M1** dissolved in different solvents highlighted how the polarity in the local environment of the CN^- ligands modulates the disparity in ν_{CN} mode anharmonicities and fundamental frequencies. The enzyme active site excludes solvent molecules but reproduces this effect likely via the conserved H-bonding contacts formed by the CN^- ligands (it bears noting that crystallographically conserved water molecules are present in the second coordination sphere in the vicinity of the H-bonding arginine residue). The deviation from the trend in ν_{CN} mode properties observed for the Ni_u-S state (lower ν_{CN1}/ν_{CN2} mixed mode anharmonicity and lower separation in ν_{CN} mode fundamental frequencies) could be a consequence of the sulfoxygenated bridging cysteine residue thought to be present in this state, this would indicate that the bridging cysteine residues have a role in the anharmonic coupling of ν_{CN} modes.

Overall this study would have benefitted from additional analysis techniques and approaches, namely the use of crystallography and EPR spectroscopy to validate the identification of the new states observed here for *Ec*Hyd-1 and also the observations based on cysteine sulfoxygenation. Additionally, pump-probe

and 2D-IR experiments featuring D_2O exchanged hydrogenase samples could prove highly useful for deconvoluting the influence of the H-bonding arginine residue and the second coordination sphere water molecules. Future work would seek to characterise the active Ni_a-X states (X=C, S, $SR_{II/III}$ and $L_{I/II/III}$) of *Ec*Hyd-1 with pump-probe and 2D-IR spectroscopy. Enzyme samples comprising these states could be produced via H_2-incubation, chemical reductants, pH alteration and/or application of a reducing potential. Additional insight relating to the interaction of the ν_{CO}/ν_{CN} modes with the bridging cysteine residues could be provided via two-colour experiments. The simplest implementation of this approach would be to centre the probe beam at an appropriate position (400-600 cm^{-1}) for detection of the Fe-μS and Fe-CO/CN vibrations. Alternatively, a Vis_{pump}-IR_{pump}-IR_{probe} methodology could be used to investigate the ν_{CO}/ν_{CN} modes of enzyme in a non-equilibrium state following visible excitation of the S→Fe ligand to metal charge transfer transition (488 nm or 568 nm), in a similar manner to that used in resonance Raman experiments. Similarly, the photoconversion of the Ni_a-C state to the Ni_a-L could be explored by using a 358 nm pump beam, this approach has been used successfully in transient IR absorbance studies to explore the coupling of proton and electron transfer steps during this transition.

7 Appendices

The Morse anharmonic potential (**Equation (24)**) describes the potential energy (V) of a diatomic molecule as a function of internuclear separation (r), equilibrium bond length (r_e), bond dissociation energy (D_e) and width of the potential (a).

$$V(r) = D_e\left(1 - e^{-a(r-r_e)}\right)^2 \qquad \textit{(24)}$$

Where the width of the potential (a) is related to potential well depth (D_e) and force constant (k) via **Equation (25)**:

$$a = \sqrt{\frac{k}{2D_e}} \qquad \textit{(25)}$$

Approximate energies for vibrational levels of a Morse potential are given by **Equation (26)**. Here v_0 is the harmonic frequency and n is the vibrational quantum number.

$$E_n = hv_0\left(v + \frac{1}{2}\right) - \frac{\left(hv_0\left(v + \frac{1}{2}\right)\right)^2}{4D_e} \qquad \textit{(26)}$$

The harmonic frequency (v_0) is related to the mass of the particles (μ), the dissociation energy and the curvature of the potential well (a) via:

$$v_0 = \frac{a}{2\pi}\sqrt{\frac{2D_e}{\mu}} \qquad \textbf{(27)}$$

Where μ is calculated from the masses of bonded atoms:

$$\mu = \frac{m_1 m_2}{m_1 + m_2} \qquad \textbf{(28)}$$

Equation (26) can be alternatively expressed to give the transition energy between adjacent vibrational energy levels as shown in **(29**:

$$E_{n+1} - E_n = hv_0 - \frac{(n+1)(hv_0)^2}{2D_e} \qquad \textit{(29)}$$

Rearranging **Equation (29)** gives **Equation (30)**:

$$v_{n+1} - v_n = -\frac{n\boldsymbol{hv_0^2}}{\boldsymbol{2D_e}} - \frac{\boldsymbol{hv_0^2}}{\boldsymbol{2D_e}} + \boldsymbol{v_0} \qquad \textit{(30)}$$

This equation can describe experimentally determined transition energies (v_{n+1}-v_n) as a linear function of the lower level quantum number (n), where the red portion of the equation is the gradient and the blue portion is the y-intercept. This expression is useful as it allows for direct determination of D_e and v_0 which enables calculation of a number of other constants. By combining **Equation (25)** and **Equation (27)** the width of the potential (a) and the bond stiffness (k) can be calculated. The zero point energy (E_0) is determined by substituting into **Equation (26)** where v=0. The bond dissociation energy (D_0) can be calculated from **Equation (31)**:

$$D_0 = D_e - E_0 \qquad \textit{(31)}$$

Combining **Equation (32)**, an alternate empirical expression for vibrational energy levels, with **Equation (26)** gives **Equation (33)**, which allows for calculation of the anharmonicity (χ) as a dimensionless constant.

$$E_n = hv_0\left(n + \frac{1}{2}\right) - hv_0\chi\left(n + \frac{1}{2}\right)^2 \qquad \textit{(32)}$$

$$\chi = \frac{hv_0}{4D_e} \qquad \textit{(33)}$$

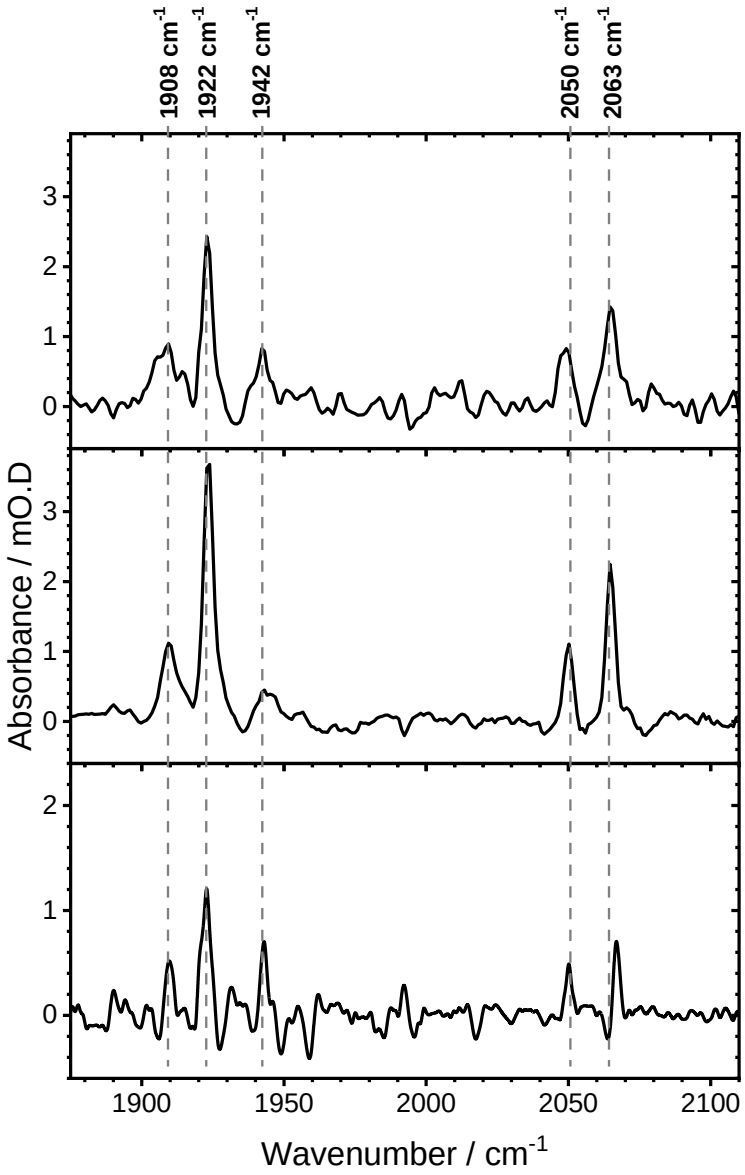

Figure 93 *FT-IR spectra of <u>Ec</u>Hyd-1 samples from three different cell growth and protein purification processes. The sample analysed in a) was also used in the H_2-oxidation activity assays.*

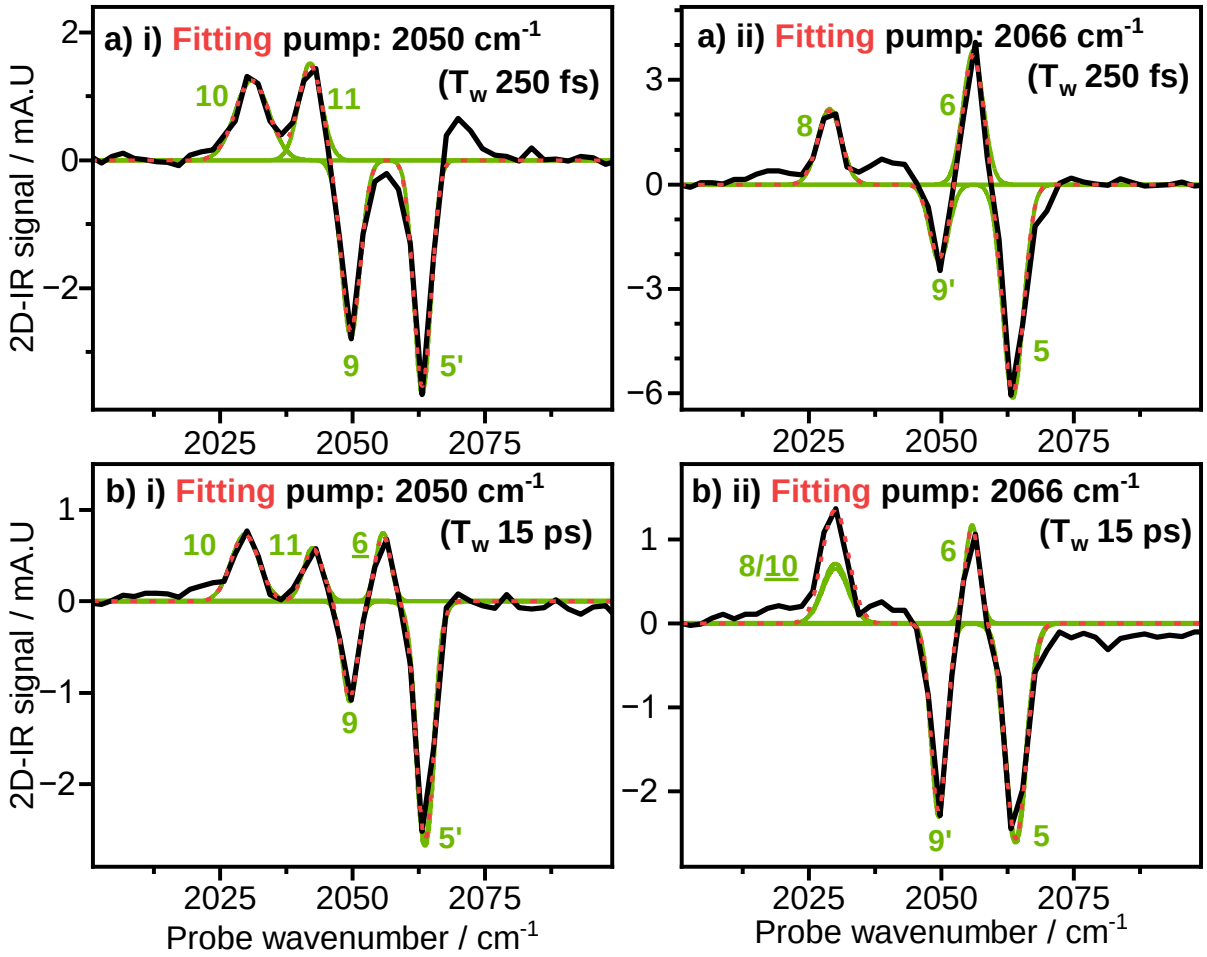

Figure 94 *As-isolated EcHyd-1 probe spectra for 2D-IR slices with pump frequencies of* ***(i)*** *2050 cm^{-1} and* ***(ii)*** *2066 cm^{-1} recorded with T_w values of* ***(a)*** *250 fs and* ***(b)*** *15 ps. Experimental data are shown as solid black lines, fitting of individual peaks are shown as solid green lines and the cumulative fitting as dashed red lines.*

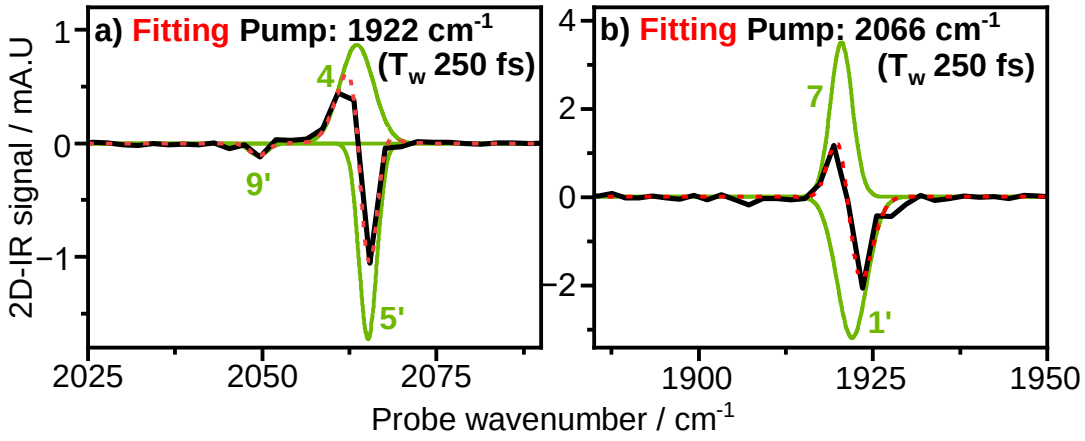

Figure 95 *As-isolated EcHyd-1 probe spectra for (T_w 250 fs) 2D-IR slices with pump frequencies of* ***(a)*** *1922 cm^{-1} and* ***(b)*** *2066 cm^{-1}. Experimental data are shown as solid black lines, fitting of individual peaks are shown as solid green lines and the cumulative fitting as dashed red lines.*

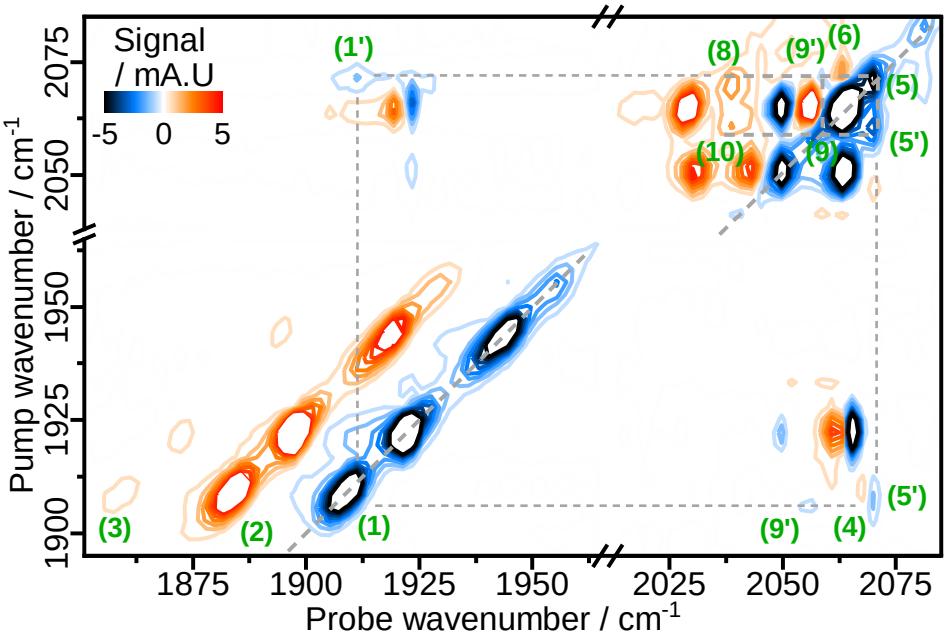

Figure 96 *2D-IR spectrum (T_w 750 fs) of EcHyd-1 with peak assignment for the minor set (dashed lines) of coupled signals with v=0-1 transitions of ν_{CO}, ν_{CN2} and ν_{CN1} at 1908 cm^{-1}, 2059 cm^{-1} and 2070 cm^{-1}, respectively.*

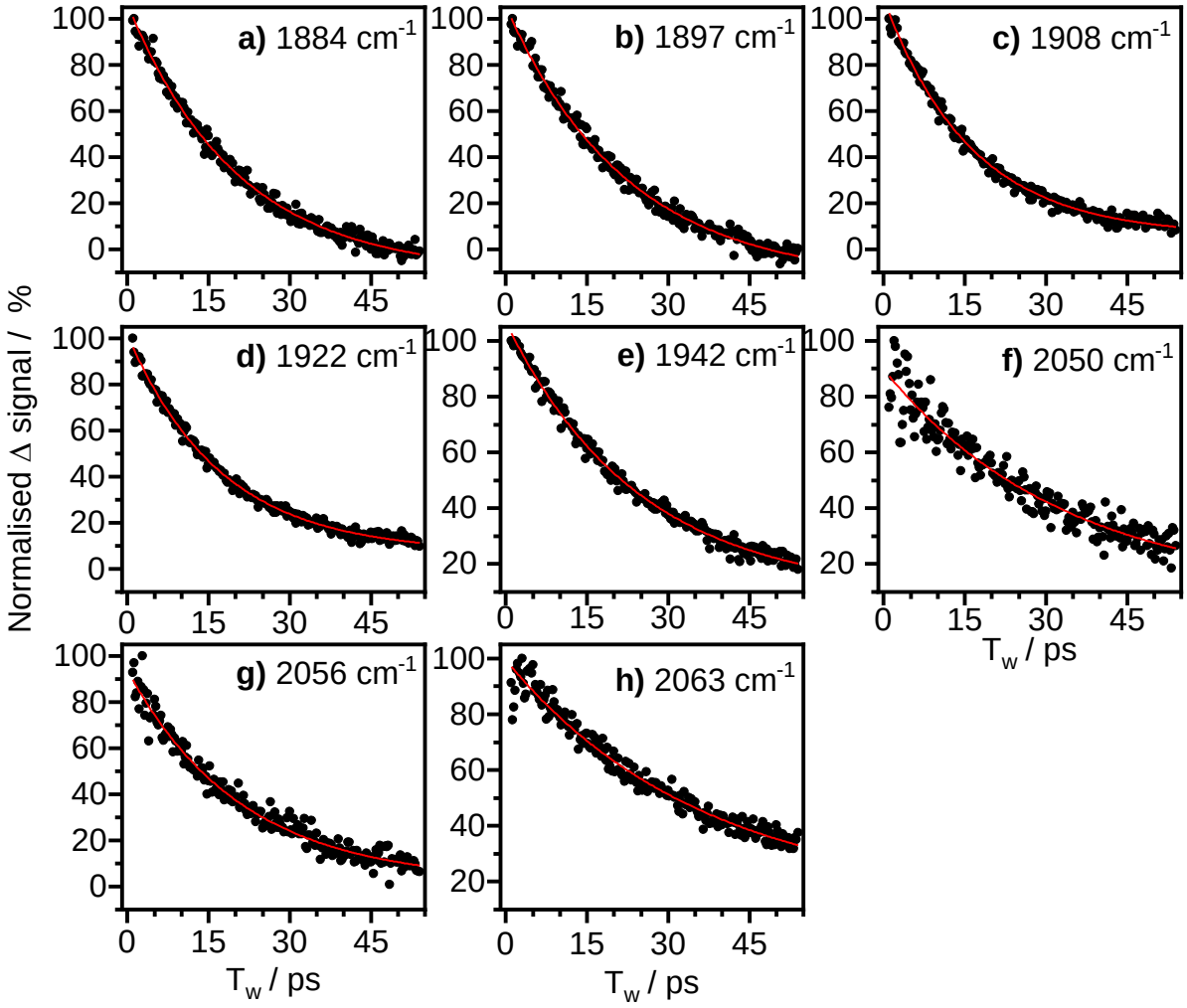

Figure 97 *As-isolated EcHyd-1: Plots of pump-probe band intensity versus T_w (black circles) and fitted monoexponential functions (solid red lines), for bands at various wavenumbers* ***(a-h)****.*

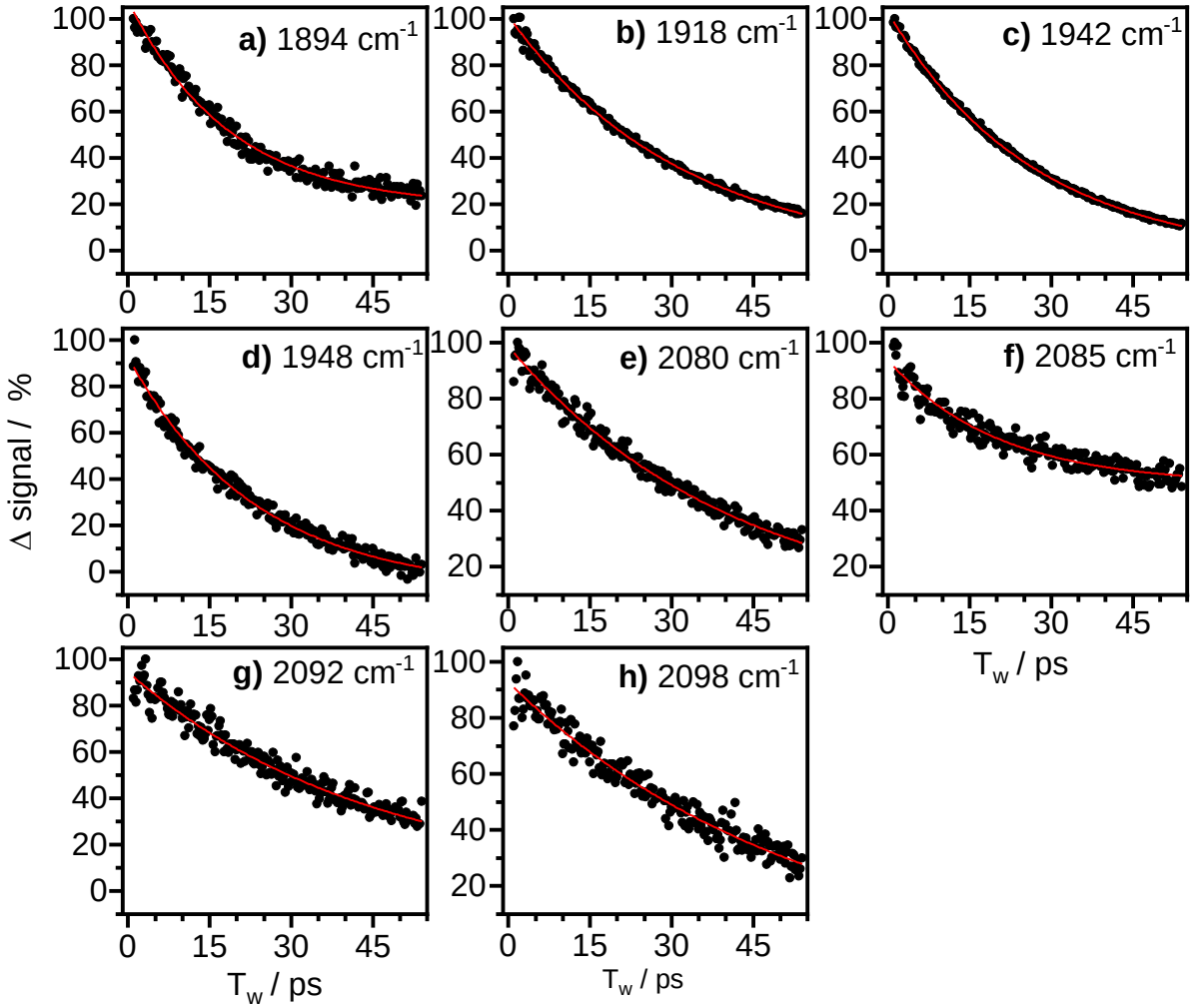

Figure 98 *Oxidised EcHyd-1: Plots of pump-probe band intensity versus T_w (black circles) and fitted monoexponential functions (solid red lines), for bands at various wavenumbers* ***(a-h)****.*

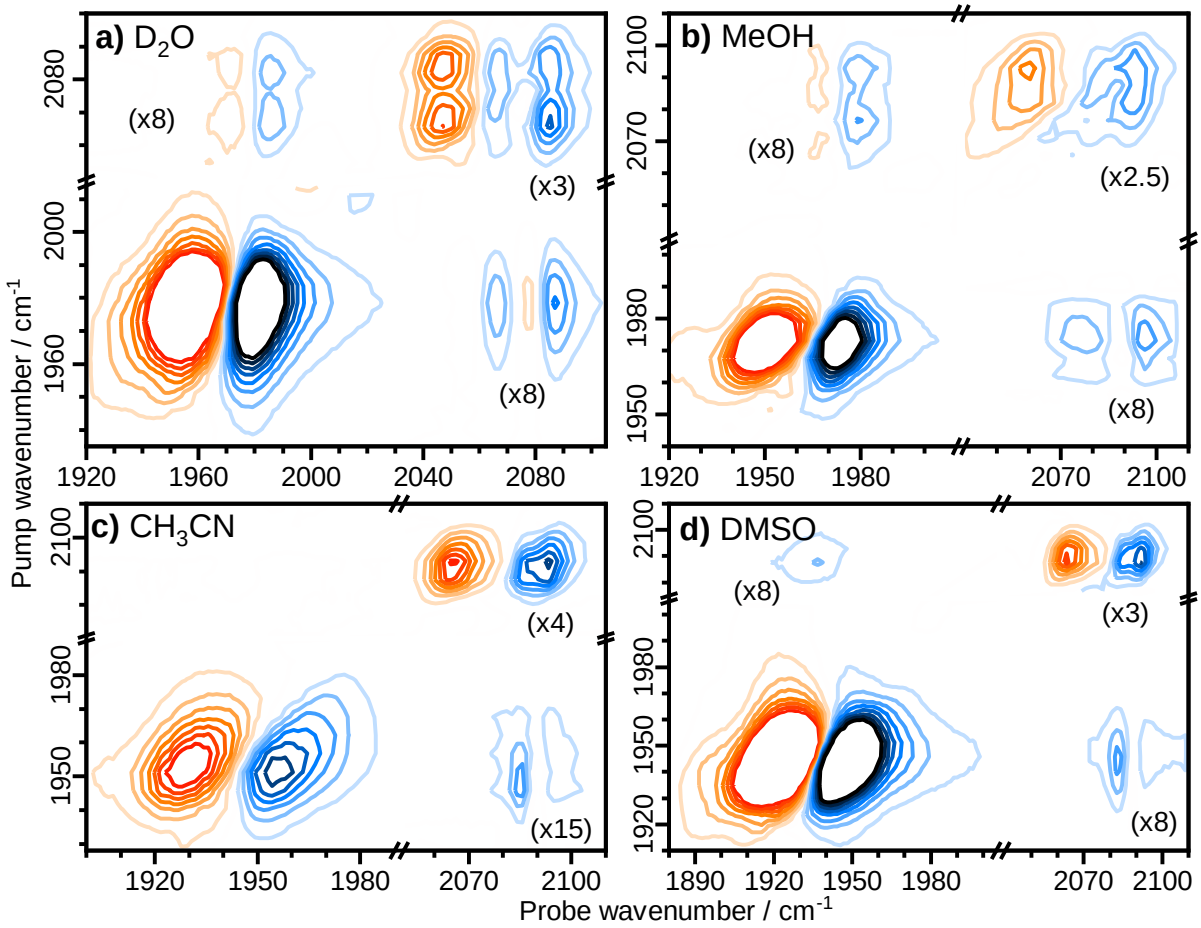

Figure 99 *T_w 790 fs 2D-IR spectra of **M1** dissolved in **(a)** D_2O, **(b)** MeOH, **(c)** CH_3CN and **(d)** DMSO. The dashed line indicates the spectrum diagonal. Numbers in brackets indicate the magnification of the three quadrants of the 2D-IR spectrum containing peaks due to ν_{CN} modes in relation to the ν_{CO} region of the spectrum (1900 - 2000 cm^{-1}).*

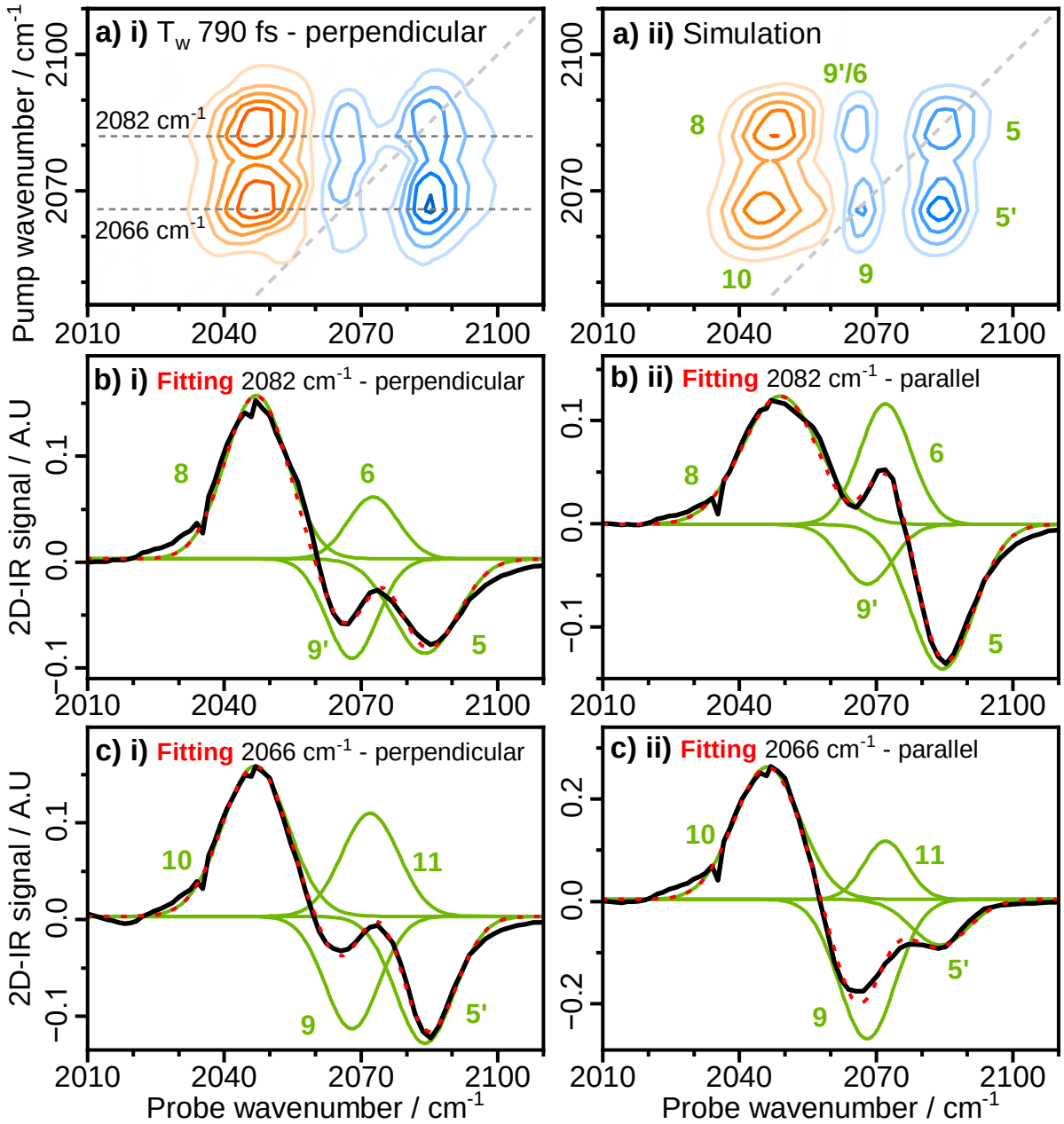

Figure 100 (a) *Magnification of the 2D-IR spectra of the mimic (dissolved in D_2O) for pump frequencies coinciding with ν_{CN} bands, showing the **(i)** T_w 790 fs experimental and **(ii)** simulated spectra, recorded with perpendicular polarization. Fitted probe spectra for pump frequencies of **(b)** 2087 cm^{-1} and **(c)** 2066 cm^{-1}, extracted from T_w 790 fs 2D-IR spectra collected with **(i)** perpendicular and **(ii)** parallel polarization geometries. For **(b)** and **(c)** the experimental data is shown as solid black lines, fitting of individual peaks are shown as solid green lines, and the cumulative fitting as dashed red lines. Green numbers are used to identify transitions.*

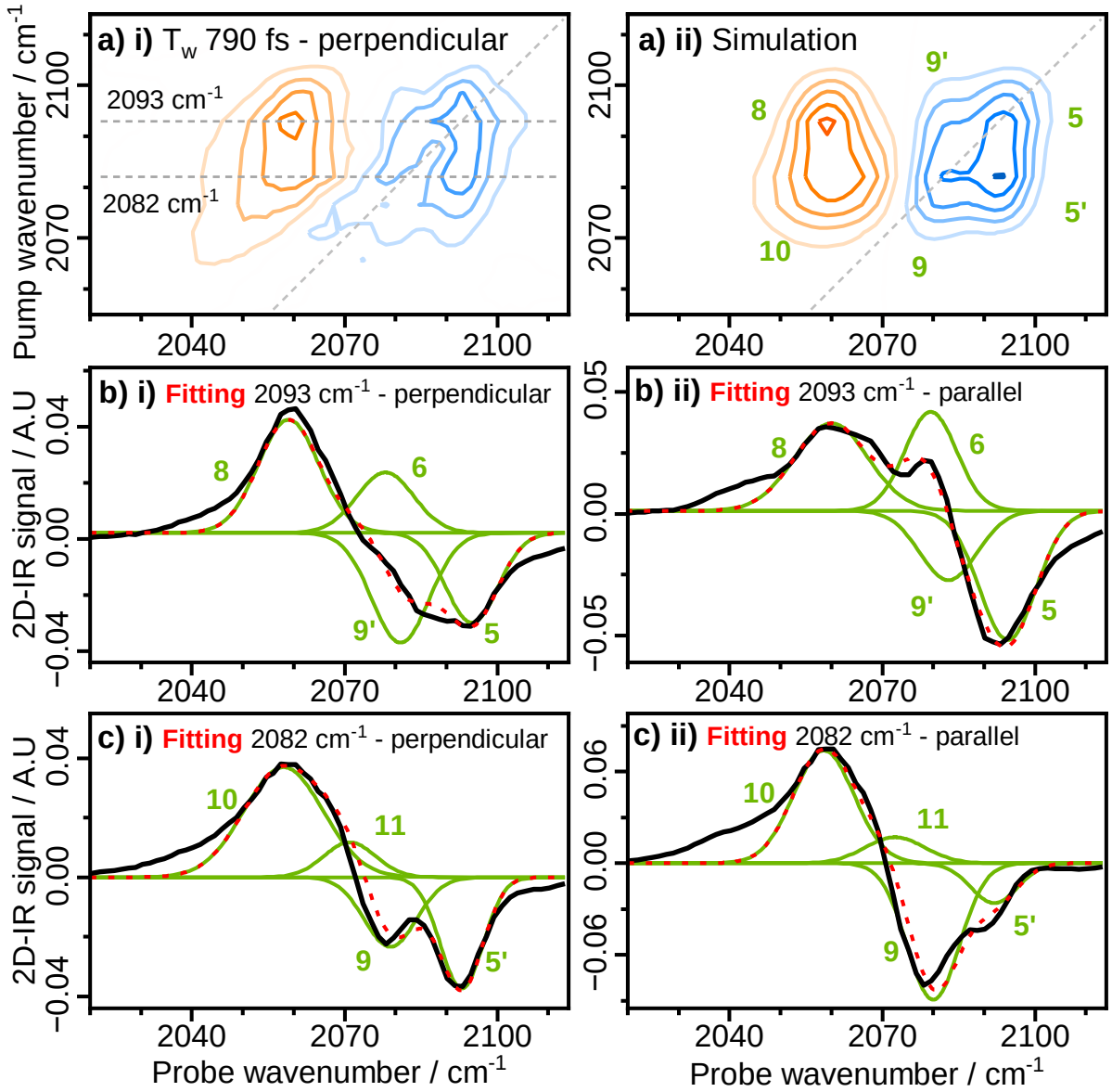

Figure 101 (a) *Magnification of the 2D-IR spectra of the mimic (dissolved in MeOH) for pump frequencies coinciding with ν_{CN} bands, showing the* ***(i)*** *T_w 790 fs experimental and* ***(ii)*** *simulated spectra, recorded with perpendicular polarization. Fitted probe spectra for pump frequencies of* ***(b)*** *2087 cm^{-1} and* ***(c)*** *2066 cm^{-1}, extracted from T_w 790 fs 2D-IR spectra collected with* ***(i)*** *perpendicular and* ***(ii)*** *parallel polarization geometries. For* ***(b)*** *and* ***(c)*** *the experimental data is shown as solid black lines, fitting of individual peaks are shown as solid green lines, and the cumulative fitting as dashed red lines. Green numbers are used to identify transitions.*

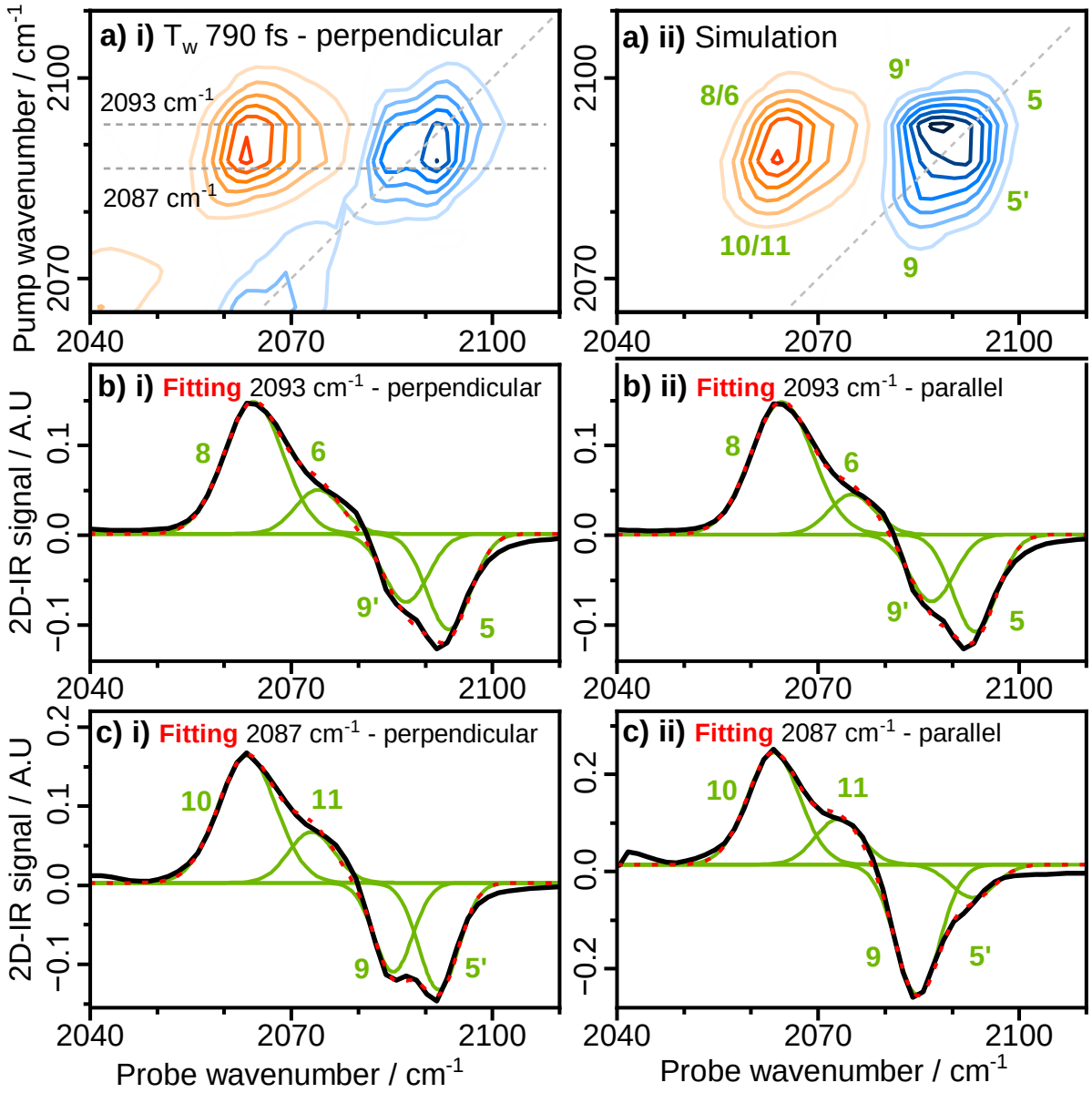

Figure 102 (a) *Magnification of the 2D-IR spectra of the mimic (dissolved in DMSO) for pump frequencies coinciding with ν_{CN} bands, showing the* ***(i)*** *T_w 790 fs experimental and* ***(ii)*** *simulated spectra, recorded with perpendicular polarization. Fitted probe spectra for pump frequencies of* ***(b)*** *2087 cm^{-1} and* ***(c)*** *2066 cm^{-1}, extracted from T_w 790 fs 2D-IR spectra collected with* ***(i)*** *perpendicular and* ***(ii)*** *parallel polarization geometries. For* ***(b)*** *and* ***(c)*** *the experimental data is shown as solid black lines, fitting of individual peaks are shown as solid green lines, and the cumulative fitting as dashed red lines. Green numbers are used to identify transitions.*

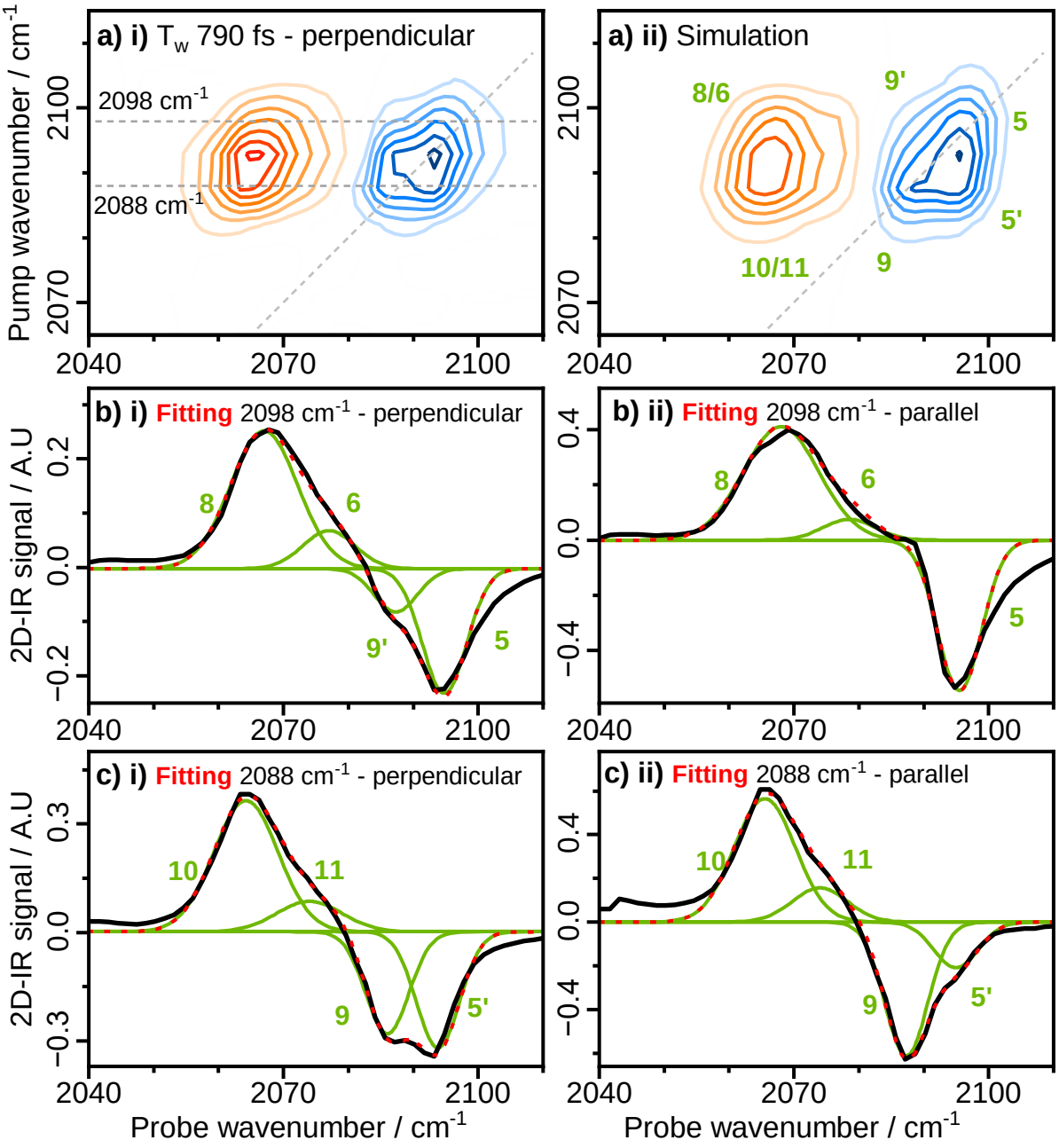

Figure 103 (a) *Magnification of the 2D-IR spectra of the mimic (dissolved in CH_3CN) for pump frequencies coinciding with ν_{CN} bands, showing the* ***(i)*** *T_w 790 fs experimental and* ***(ii)*** *simulated spectra, recorded with perpendicular polarization. Fitted probe spectra for pump frequencies of* ***(b)*** *2087 cm^{-1} and* ***(c)*** *2066 cm^{-1}, extracted from T_w 790 fs 2D-IR spectra collected with* ***(i)*** *perpendicular and* ***(ii)*** *parallel polarization geometries. For* ***(b)*** *and* ***(c)*** *the experimental data is shown as solid black lines, fitting of individual peaks are shown as solid green lines, and the cumulative fitting as dashed red lines. Green numbers are used to identify transitions.*

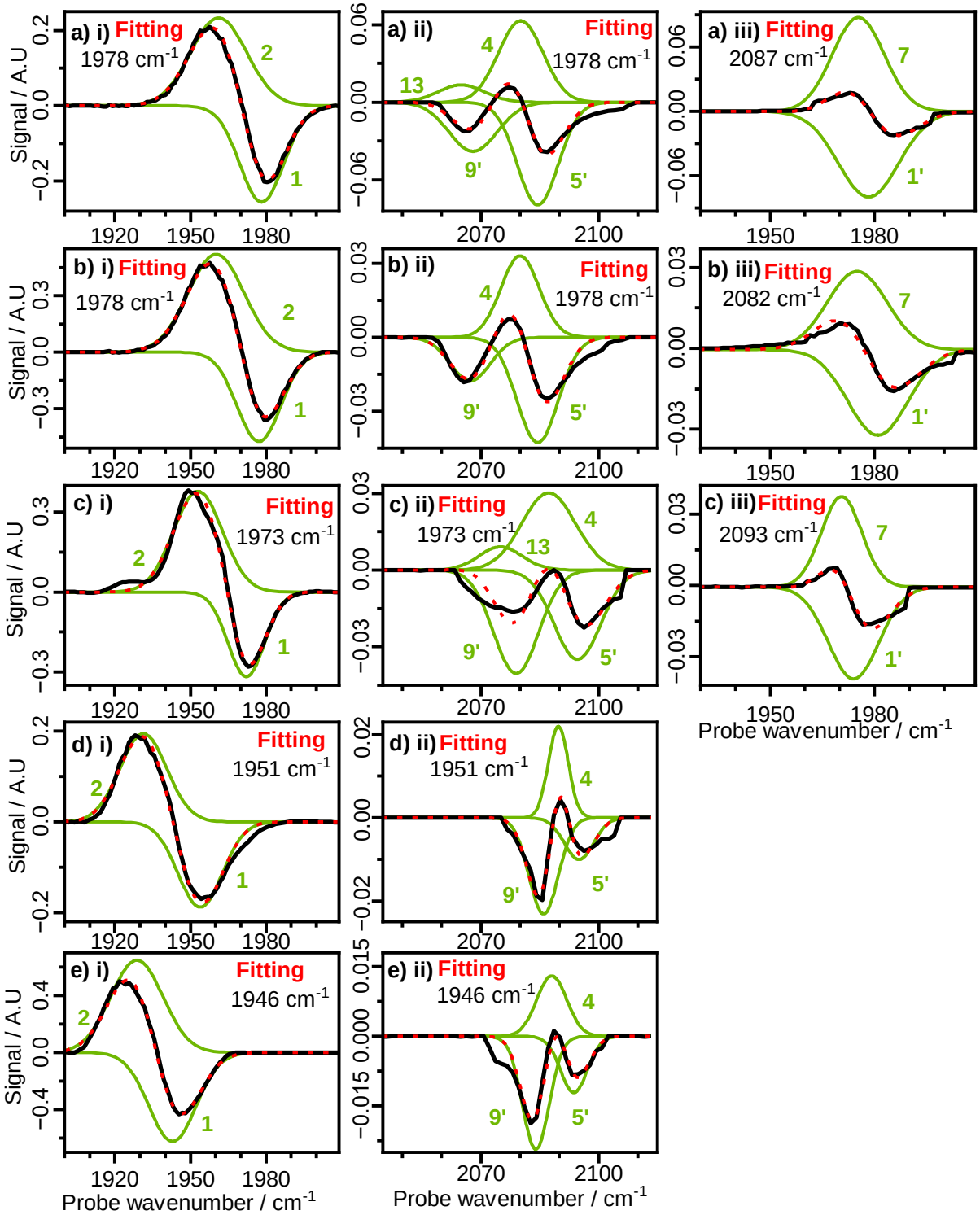

Figure 104 *Probe spectra extracted from T_w 790 fs 2D-IR spectra of* ***M1*** *dissolved in* ***(a)*** *H_2O,* ***(b)*** *D_2O,* ***(c)*** *MeOH,* ***(d)*** *CH_3CN and* ***(e)*** *DMSO for regions of the spectrum coinciding with* ***(i)*** *diagonal transitions of the ν_{CO} mode, and off-diagonal transitions when pumping* ***(ii)*** *ν_{CO} and* ***(iii)*** *ν_{CN} modes. Experimental data is shown as solid black lines, fitting of individual peaks are shown as solid green lines, and the cumulative fitting as dashed red lines. Green numbers are used to identify transitions.*

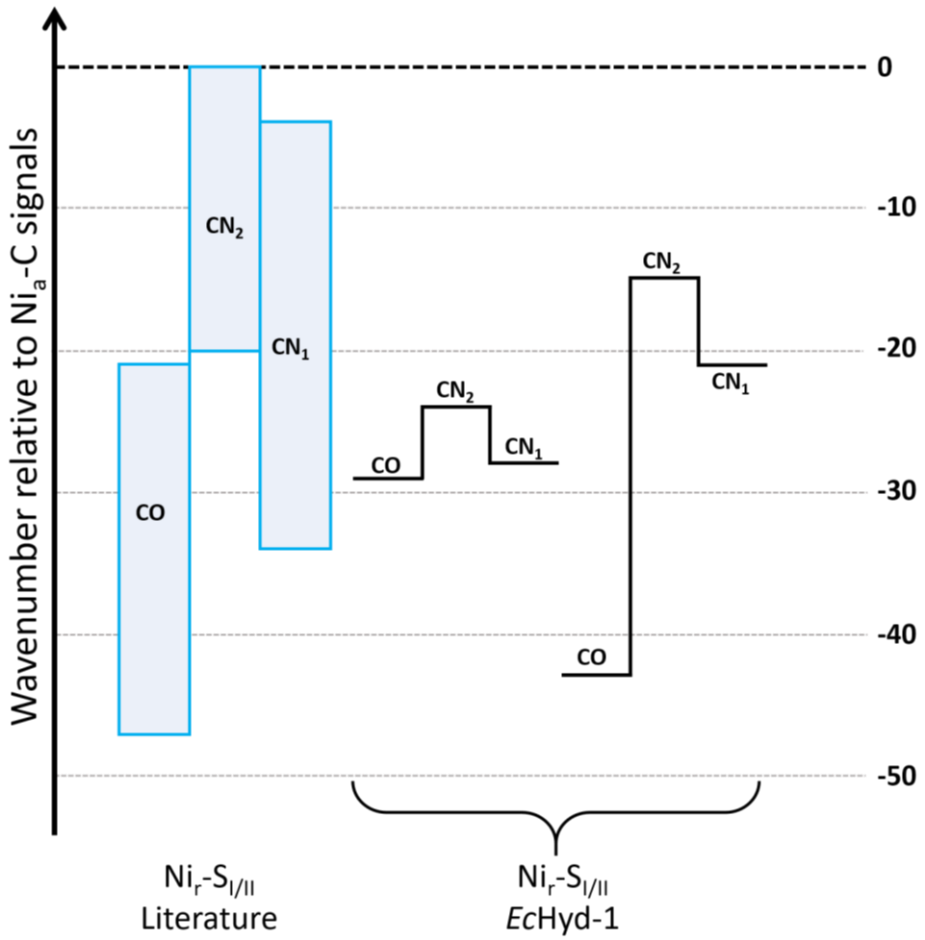

Figure 105 *Diagram showing the wavenumbers reported for CO, CN_1 and CN_2 stretching modes of NiFe-hydrogenases (DvMF, AvMBH, DgMBH and ReMBH) in the Ni_r-S states (blue) relative to Ni_a-C signals from the same enzyme. Wavenumbers for the CN_1 and CN_2 stretching modes of EcHyd-1 were estimated based on values reported for ReMBH.*[24,66,206,207]

8 References

(1) Verne, J. *L'Île Mystérieuse*; Pierre-Jules Hetzel: France, 1875.

(2) Siegbahn, P. E. M.; Tye, J. W.; Hall, M. B. Computational Studies of [NiFe] and [FeFe] Hydrogenases. *Chem. Rev.* **2007**, *107* (10), 4414–4435.

(3) Tye, J. W.; Hall, M. B.; Darensbourg, M. Y. Better than Platinum? Fuel Cells Energized by Enzymes. *Proc. Natl. Acad. Sci.* **2005**, *102* (47), 16911–16912.

(4) Shiva Kumar, S.; Himabindu, V. Hydrogen Production by PEM Water Electrolysis – A Review. *Mater. Sci. Energy Technol.* **2019**, *2* (3), 442–454.

(5) Greening, C.; Biswas, A.; Carere, C. R.; Jackson, C. J.; Taylor, M. C.; Stott, M. B.; Cook, G. M.; Morales, S. E. Genomic and Metagenomic Surveys of Hydrogenase Distribution Indicate H 2 Is a Widely Utilised Energy Source for Microbial Growth and Survival. *ISME J.* **2016**, *10* (3), 761–777.

(6) Volbeda, A.; Charon, M.-H.; Piras, C.; Hatchikian, E. C.; Frey, M.; Fontecilla-Camps, J. C. Crystal Structure of the Nickel–Iron Hydrogenase from Desulfovibrio Gigas. *Nature* **1995**, *373* (6515), 580–587.

(7) Volbeda, A.; Garcin, E.; Piras, C.; De Lacey, A. L.; Fernandez, V. M.; Hatchikian, E. C.; Frey, M.; Fontecilla-Camps, J. C. Structure of the [NiFe] Hydrogenase Active Site: Evidence for Biologically Uncommon Fe Ligands. *J. Am. Chem. Soc.* **1996**, *118* (51), 12989–12996.

(8) Peters, J. W. X-Ray Crystal Structure of the Fe-Only Hydrogenase (CpI) from Clostridium Pasteurianum to 1.8Angstrom Resolution. *Science (80-.).* **1998**, *282* (5395), 1853–1858.

(9) Nicolet, Y.; Piras, C.; Legrand, P.; Hatchikian, C. E.; Fontecilla-Camps, J. C. Desulfovibrio Desulfuricans Iron Hydrogenase: The Structure Shows Unusual Coordination to an Active Site Fe Binuclear Center. *Structure* **1999**, *7* (1), 13–23.

(10) Shima, S.; Pilak, O.; Vogt, S.; Schick, M.; Stagni, M. S.; Meyer-Klaucke, W.; Warkentin, E.; Thauer, R. K.; Ermler, U. The Crystal Structure of [Fe]-Hydrogenase Reveals the Geometry of the Active Site. *Science (80-.).* **2008**, *321* (5888), 572–575.

(11) Lubitz, W.; Ogata, H.; Rüdiger, O.; Reijerse, E. Hydrogenases. *Chem. Rev.* **2014**, *114* (8), 4081–4148.

(12) Jones, A. K.; Sillery, E.; Albracht, S. P. J.; Armstrong, F. A. Direct Comparison of the Electrocatalytic Oxidation of Hydrogen by an Enzyme and a Platinum CatalystElectronic Supplementary Information (ESI) Available: Levich Plots at 1% and 10% Hydrogen, and a Comparison of the Effect of Carbon Monoxide on Oxidation C. *Chem. Commun.* **2002**, No. 8, 866–867.

(13) Vignais, P. M.; Billoud, B. Occurrence, Classification, and Biological Function of Hydrogenases:

An Overview. *Chem. Rev.* **2007**, *107* (10), 4206–4272.

(14) Horch, M.; Hildebrandt, P.; Zebger, I. Concepts in Bio-Molecular Spectroscopy: Vibrational Case Studies on Metalloenzymes. *Phys. Chem. Chem. Phys.* **2015**, *17* (28), 18222–18237.

(15) Evans, R. M.; Ash, P. A.; Beaton, S. E.; Brooke, E. J.; Vincent, K. A.; Carr, S. B.; Armstrong, F. A. Mechanistic Exploitation of a Self-Repairing, Blocked Proton Transfer Pathway in an O 2 - Tolerant [NiFe]-Hydrogenase. *J. Am. Chem. Soc.* **2018**, *140* (32), 10208–10220.

(16) Vincent, K. A.; Parkin, A.; Lenz, O.; Albracht, S. P. J.; Fontecilla-Camps, J. C.; Cammack, R.; Friedrich, B.; Armstrong, F. A. Electrochemical Definitions of O 2 Sensitivity and Oxidative Inactivation in Hydrogenases. *J. Am. Chem. Soc.* **2005**, *127* (51), 18179–18189.

(17) Lukey, M. J.; Parkin, A.; Roessler, M. M.; Murphy, B. J.; Harmer, J.; Palmer, T.; Sargent, F.; Armstrong, F. A. How Escherichia Coli Is Equipped to Oxidize Hydrogen under Different Redox Conditions. *J. Biol. Chem.* **2010**, *285* (6), 3928–3938.

(18) Lukey, M. J.; Roessler, M. M.; Parkin, A.; Evans, R. M.; Davies, R. A.; Lenz, O.; Friedrich, B.; Sargent, F.; Armstrong, F. A. Oxygen-Tolerant [NiFe]-Hydrogenases: The Individual and Collective Importance of Supernumerary Cysteines at the Proximal Fe-S Cluster. *J. Am. Chem. Soc.* **2011**, *133* (42), 16881–16892.

(19) Pandelia, M.-E.; Fourmond, V.; Tron-Infossi, P.; Lojou, E.; Bertrand, P.; Léger, C.; Giudici-Orticoni, M.-T.; Lubitz, W. Membrane-Bound Hydrogenase I from the Hyperthermophilic Bacterium Aquifex Aeolicus : Enzyme Activation, Redox Intermediates and Oxygen Tolerance. *J. Am. Chem. Soc.* **2010**, *132* (20), 6991–7004.

(20) Pandelia, M.-E.; Infossi, P.; Giudici-Orticoni, M. T.; Lubitz, W. The Oxygen-Tolerant Hydrogenase I from Aquifex Aeolicus Weakly Interacts with Carbon Monoxide: An Electrochemical and Time-Resolved FTIR Study. *Biochemistry* **2010**, *49* (41), 8873–8881.

(21) Buhrke, T.; Lenz, O.; Krauss, N.; Friedrich, B. Oxygen Tolerance of the H2-Sensing [NiFe] Hydrogenase from Ralstonia Eutropha H16 Is Based on Limited Access of Oxygen to the Active Site. *J. Biol. Chem.* **2005**, *280* (25), 23791–23796.

(22) Van Der Linden, E.; Burgdorf, T.; Bernhard, M.; Bleijlevens, B.; Friedrich, B.; Albracht, S. P. J. The Soluble [NiFe]-Hydrogenase from Ralstonia Eutropha Contains Four Cyanides in Its Active Site, One of Which Is Responsible for the Insensitivity towards Oxygen. *J. Biol. Inorg. Chem.* **2004**, *9* (5), 616–626.

(23) Horch, M.; Lauterbach, L.; Lenz, O.; Hildebrandt, P.; Zebger, I. NAD(H)-Coupled Hydrogen Cycling - Structure-Function Relationships of Bidirectional [NiFe] Hydrogenases. *FEBS Lett.* **2012**, *586* (5), 545–556.

(24) de Lacey, A. L.; Hatchikian, E. C.; Volbeda, A.; Frey, M.; Fontecilla-Camps, J. C.; Fernandez, V.

M. Infrared-Spectroelectrochemical Characterization of the [NiFe] Hydrogenase of Desulfovibrio Gigas. *J. Am. Chem. Soc.* **1997**, *119* (31), 7181–7189.

(25) Senger, M.; Laun, K.; Soboh, B.; Stripp, S. Infrared Characterization of the Bidirectional Oxygen-Sensitive [NiFe]-Hydrogenase from E. Coli. *Catalysts* **2018**, *8* (11), 530.

(26) Ogata, H.; Lubitz, W.; Higuchi, Y. Structure and Function of [NiFe] Hydrogenases. *J. Biochem.* **2016**, *160* (5), 251–258.

(27) Ash, P. A.; Hidalgo, R.; Vincent, K. A. Proton Transfer in the Catalytic Cycle of [NiFe] Hydrogenases: Insight from Vibrational Spectroscopy. *ACS Catal.* **2017**, *7* (4), 2471–2485.

(28) Siebert, E.; Schmidt, A.; Frielingsdorf, S.; Kalms, J.; Kuhlmann, U.; Lenz, O.; Scheerer, P.; Zebger, I.; Hildebrandt, P. Resonance Raman Spectroscopic Analysis of the Iron–Sulfur Cluster Redox Chain of the <scp> *Ralstonia Eutropha* </Scp> Membrane-bound [NiFe]-hydrogenase. *J. Raman Spectrosc.* **2021**, *52* (12), 2621–2632.

(29) Beaton, S. E.; Evans, R. M.; Finney, A. J.; Lamont, C. M.; Armstrong, F. A.; Sargent, F.; Carr, S. B. The Structure of Hydrogenase-2 from Escherichia Coli : Implications for H2-Driven Proton Pumping. *Biochem. J.* **2018**, *475* (7), 1353–1370.

(30) Ogata, H.; Nishikawa, K.; Lubitz, W. Hydrogens Detected by Subatomic Resolution Protein Crystallography in a [NiFe] Hydrogenase. *Nature* **2015**, *520* (7548), 571–574.

(31) Fritsch, J.; Scheerer, P.; Frielingsdorf, S.; Kroschinsky, S.; Friedrich, B.; Lenz, O.; Spahn, C. M. T. The Crystal Structure of an Oxygen-Tolerant Hydrogenase Uncovers a Novel Iron-Sulphur Centre. *Nature* **2011**, *479* (7372), 249–253.

(32) Volbeda, A.; Darnault, C.; Parkin, A.; Sargent, F.; Armstrong, F. A.; Fontecilla-Camps, J. C. Crystal Structure of the O 2 -Tolerant Membrane-Bound Hydrogenase 1 from Escherichia Coli in Complex with Its Cognate Cytochrome B. *Structure* **2013**, *21* (1), 184–190.

(33) Ogata, H.; Kellers, P.; Lubitz, W. The Crystal Structure of the [NiFe] Hydrogenase from the Photosynthetic Bacterium Allochromatium Vinosum: Characterization of the Oxidized Enzyme (Ni-A State). *J. Mol. Biol.* **2010**, *402* (2), 428–444.

(34) Lenz, O.; Friedrich, B. A Novel Multicomponent Regulatory System Mediates H 2 Sensing in Alcaligenes Eutrophus. *Proc. Natl. Acad. Sci.* **1998**, *95* (21), 12474–12479.

(35) Ma, K.; Weiss, R.; Adams, M. W. W. Characterization of Hydrogenase II from the Hyperthermophilic Archaeon Pyrococcus Furiosus and Assessment of Its Role in Sulfur Reduction. *J. Bacteriol.* **2000**, *182* (7), 1864–1871.

(36) Kulkarni, G.; Kridelbaugh, D. M.; Guss, A. M.; Metcalf, W. W. Hydrogen Is a Preferred Intermediate in the Energy-Conserving Electron Transport Chain of Methanosarcina Barkeri. *Proc. Natl. Acad. Sci.* **2009**, *106* (37), 15915–15920.

(37) Mills, D. J.; Vitt, S.; Strauss, M.; Shima, S.; Vonck, J. De Novo Modeling of the F420-Reducing [NiFe]-Hydrogenase from a Methanogenic Archaeon by Cryo-Electron Microscopy. *Elife* **2013**, *2* (2), 1–21.

(38) Song, Y.; Liu, M.; Xie, L.; You, C.; Sun, J.; Zhang, Y. P. J. A Recombinant 12-His Tagged Pyrococcus Furiosus Soluble [NiFe]-Hydrogenase I Overexpressed in Thermococcus Kodakarensis KOD1 Facilitates Hydrogen-Powered in Vitro NADH Regeneration. *Biotechnol. J.* **2019**, *14* (4), 1800301.

(39) McDowall, J. S.; Murphy, B. J.; Haumann, M.; Palmer, T.; Armstrong, F. A.; Sargent, F. Bacterial Formate Hydrogenlyase Complex. *Proc. Natl. Acad. Sci.* **2014**, *111* (38), E3948–E3956.

(40) Teixeira, M.; Moura, I.; Xavier, A. V; Moura, J. J.; LeGall, J.; DerVartanian, D. V; Peck, H. D.; Huynh, B. H. Redox Intermediates of Desulfovibrio Gigas [NiFe] Hydrogenase Generated Under Hydrogen. *J. Biol. Chem.* **1989**, *264* (28), 16435–16450.

(41) Pandelia, M.-E.; Nitschke, W.; Infossi, P.; Giudici-Orticoni, M.-T.; Bill, E.; Lubitz, W. Characterization of a Unique [FeS] Cluster in the Electron Transfer Chain of the Oxygen Tolerant [NiFe] Hydrogenase from Aquifex Aeolicus. *Proc. Natl. Acad. Sci.* **2011**, *108* (15), 6097–6102.

(42) Roessler, M. M.; Evans, R. M.; Davies, R. A.; Harmer, J.; Armstrong, F. A. EPR Spectroscopic Studies of the Fe–S Clusters in the O 2 -Tolerant [NiFe]-Hydrogenase Hyd-1 from Escherichia Coli and Characterization of the Unique [4Fe–3S] Cluster by HYSCORE. *J. Am. Chem. Soc.* **2012**, *134* (37), 15581–15594.

(43) Pandelia, M.-E.; Bykov, D.; Izsak, R.; Infossi, P.; Giudici-Orticoni, M.-T.; Bill, E.; Neese, F.; Lubitz, W. Electronic Structure of the Unique [4Fe-3S] Cluster in O2-Tolerant Hydrogenases Characterized by 57Fe Mossbauer and EPR Spectroscopy. *Proc. Natl. Acad. Sci.* **2013**, *110* (2), 483–488.

(44) Frielingsdorf, S.; Fritsch, J.; Schmidt, A.; Hammer, M.; Löwenstein, J.; Siebert, E.; Pelmenschikov, V.; Jaenicke, T.; Kalms, J.; Rippers, Y.; Lendzian, F.; Zebger, I.; Teutloff, C.; Kaupp, M.; Bittl, R.; Hildebrandt, P.; Friedrich, B.; Lenz, O.; Scheerer, P. Reversible [4Fe-3S] Cluster Morphing in an O2-Tolerant [NiFe] Hydrogenase. *Nat. Chem. Biol.* **2014**, *10* (5), 378–385.

(45) Goris, T.; Wait, A. F.; Saggu, M.; Fritsch, J.; Heidary, N.; Stein, M.; Zebger, I.; Lendzian, F.; Armstrong, F. A.; Friedrich, B.; Lenz, O. A Unique Iron-Sulfur Cluster Is Crucial for Oxygen Tolerance of a [NiFe]-Hydrogenase. *Nat. Chem. Biol.* **2011**, *7* (5), 310–318.

(46) Shomura, Y.; Yoon, K. S.; Nishihara, H.; Higuchi, Y. Structural Basis for a [4Fe-3S] Cluster in the Oxygen-Tolerant Membrane-Bound [NiFe]-Hydrogenase. *Nature* **2011**, *479* (7372), 253–256.

(47) Roessler, M. M.; King, M. S.; Robinson, A. J.; Armstrong, F. A.; Harmer, J.; Hirst, J. Direct Assignment of EPR Spectra to Structurally Defined Iron-Sulfur Clusters in Complex I by Double Electron-Electron Resonance. *Proc. Natl. Acad. Sci.* **2010**, *107* (5), 1930–1935.

(48) Volbeda, A.; Mouesca, J. M.; Darnault, C.; Roessler, M. M.; Parkin, A.; Armstrong, F. A.; Fontecilla-Camps, J. C. X-Ray Structural, Functional and Computational Studies of the O 2 - Sensitive E. Coli Hydrogenase-1 C19G Variant Reveal an Unusual [4Fe–4S] Cluster. *Chem. Commun.* **2018**, *54* (52), 7175–7178.

(49) Wulff, P.; Thomas, C.; Sargent, F.; Armstrong, F. A. How the Oxygen Tolerance of a [NiFe]-Hydrogenase Depends on Quaternary Structure. *JBIC J. Biol. Inorg. Chem.* **2016**, *21* (1), 121–134.

(50) Kalms, J.; Schmidt, A.; Frielingsdorf, S.; Utesch, T.; Gotthard, G.; von Stetten, D.; van der Linden, P.; Royant, A.; Mroginski, M. A.; Carpentier, P.; Lenz, O.; Scheerer, P. Tracking the Route of Molecular Oxygen in O 2 -Tolerant Membrane-Bound [NiFe] Hydrogenase. *Proc. Natl. Acad. Sci.* **2018**, *115* (10), E2229–E2237.

(51) Evans, R. M.; Parkin, A.; Roessler, M. M.; Murphy, B. J.; Adamson, H.; Lukey, M. J.; Sargent, F.; Volbeda, A.; Fontecilla-Camps, J. C.; Armstrong, F. A. Principles of Sustained Enzymatic Hydrogen Oxidation in the Presence of Oxygen -the Crucial Influence of High Potential Fe-S Clusters in the Electron Relay of [NiFe]-Hydrogenases. *J. Am. Chem. Soc.* **2013**, *135* (7), 2694–2707.

(52) Volbeda, A.; Martin, L.; Cavazza, C.; Matho, M.; Faber, B. W.; Roseboom, W.; Albracht, S. P. J.; Garcin, E.; Rousset, M.; Fontecilla-Camps, J. C. Structural Differences between the Ready and Unready Oxidized States of [NiFe] Hydrogenases. *JBIC J. Biol. Inorg. Chem.* **2005**, *10* (3), 239–249.

(53) Hexter, S. V.; Grey, F.; Happe, T.; Climent, V.; Armstrong, F. A. Electrocatalytic Mechanism of Reversible Hydrogen Cycling by Enzymes and Distinctions between the Major Classes of Hydrogenases. *Proc. Natl. Acad. Sci. U. S. A.* **2012**, *109* (29), 11516–11521.

(54) Murphy, B. J.; Sargent, F.; Armstrong, F. A. Transforming an Oxygen-Tolerant [NiFe] Uptake Hydrogenase into a Proficient, Reversible Hydrogen Producer. *Energy Environ. Sci.* **2014**, *7* (4), 1426–1433.

(55) Flanagan, L. A.; Wright, J. J.; Roessler, M. M.; Moir, J. W.; Parkin, A. Re-Engineering a NiFe Hydrogenase to Increase the H 2 Production Bias While Maintaining Native Levels of O 2 Tolerance. *Chem. Commun.* **2016**, *52* (58), 9133–9136.

(56) Adamson, H.; Robinson, M.; Wright, J. J.; Flanagan, L. A.; Walton, J.; Elton, D.; Gavaghan, D. J.; Bond, A. M.; Roessler, M. M.; Parkin, A. Retuning the Catalytic Bias and Overpotential of a

[NiFe]-Hydrogenase via a Single Amino Acid Exchange at the Electron Entry/Exit Site. *J. Am. Chem. Soc.* **2017**, *139* (31), 10677–10686.

(57) Dementin, S.; Belle, V.; Bertrand, P.; Guigliarelli, B.; Adryanczyk-Perrier, G.; De Lacey, A. L.; Fernandez, V. M.; Rousset, M.; Léger, C. Changing the Ligation of the Distal [4Fe4S] Cluster in NiFe Hydrogenase Impairs Inter- and Intramolecular Electron Transfers. *J. Am. Chem. Soc.* **2006**, *128* (15), 5209–5218.

(58) Ogata, H.; Hirota, S.; Nakahara, A.; Komori, H.; Shibata, N.; Kato, T.; Kano, K.; Higuchi, Y. Activation Process of [NiFe] Hydrogenase Elucidated by High-Resolution X-Ray Analyses: Conversion of the Ready to the Unready State. *Structure* **2005**, *13* (11), 1635–1642.

(59) Flanagan, L. A.; Parkin, A. Electrochemical Insights into the Mechanism of NiFe Membrane-Bound Hydrogenases. *Biochem. Soc. Trans.* **2016**, *44* (1), 315–328.

(60) Peters, J. W.; Schut, G. J.; Boyd, E. S.; Mulder, D. W.; Shepard, E. M.; Broderick, J. B.; King, P. W.; Adams, M. W. W. [FeFe]- and [NiFe]-Hydrogenase Diversity, Mechanism, and Maturation. *Biochim. Biophys. Acta - Mol. Cell Res.* **2015**, *1853* (6), 1350–1369.

(61) Cracknell, J. A.; Wait, A. F.; Lenz, O.; Friedrich, B.; Armstrong, F. A. A Kinetic and Thermodynamic Understanding of O 2 Tolerance in [NiFe]-Hydrogenases. *Proc. Natl. Acad. Sci.* **2009**, *106* (49), 20681–20686.

(62) Armstrong, F. A.; Belsey, N. A.; Cracknell, J. A.; Goldet, G.; Parkin, A.; Reisner, E.; Vincent, K. A.; Wait, A. F. Dynamic Electrochemical Investigations of Hydrogen Oxidation and Production by Enzymes and Implications for Future Technology. *Chem. Soc. Rev.* **2009**, *38* (1), 36–51.

(63) Horch, M.; Lauterbach, L.; Mroginski, M. A.; Hildebrandt, P.; Lenz, O.; Zebger, I. Reversible Active Site Sulfoxygenation Can Explain the Oxygen Tolerance of a NAD + -Reducing [NiFe] Hydrogenase and Its Unusual Infrared Spectroscopic Properties. *J. Am. Chem. Soc.* **2015**, *137* (7), 2555–2564.

(64) Volbeda, A.; Martin, L.; Barbier, E.; Gutiérrez-Sanz, O.; De Lacey, A. L.; Liebgott, P.-P.; Dementin, S.; Rousset, M.; Fontecilla-Camps, J. C. Crystallographic Studies of [NiFe]-Hydrogenase Mutants: Towards Consensus Structures for the Elusive Unready Oxidized States. *JBIC J. Biol. Inorg. Chem.* **2015**, *20* (1), 11–22.

(65) Lubitz, W.; Reijerse, E.; van Gastel, M. [NiFe] and [FeFe] Hydrogenases Studied by Advanced Magnetic Resonance Techniques. *Chem. Rev.* **2007**, *107* (10), 4331–4365.

(66) Bleijlevens, B.; van Broekhuizen, F. A.; De Lacey, A. L.; Roseboom, W.; Fernandez, V. M.; Albracht, S. P. J. The Activation of the [NiFe]-Hydrogenase from Allochromatium Vinosum. An Infrared Spectro-Electrochemical Study. *JBIC J. Biol. Inorg. Chem.* **2004**, *9* (6), 743–752.

(67) George, S. J.; Kurkin, S.; Thorneley, R. N. F.; Albracht, S. P. J. Reactions of H 2 , CO, and O 2

with Active [NiFe]-Hydrogenase from Allochromatium Vinosum . A Stopped-Flow Infrared Study. *Biochemistry* **2004**, *43* (21), 6808–6819.

(68) Armstrong, F. A.; Albracht, S. P. J. [NiFe]-Hydrogenases: Spectroscopic and Electrochemical Definition of Reactions and Intermediates. *Philos. Trans. R. Soc. A Math. Phys. Eng. Sci.* **2005**, *363* (1829), 937–954.

(69) Krasna, A. I. Hydrogenase: Properties and Applications. *Enzyme Microb. Technol.* **1979**, *1* (3), 165–172.

(70) Pardo, A.; De Lacey, A. L.; Fernández, V. M.; Fan, H.-J.; Fan, Y.; Hall, M. B. Density Functional Study of the Catalytic Cycle of Nickel–Iron [NiFe] Hydrogenases and the Involvement of High-Spin Nickel(II). *JBIC J. Biol. Inorg. Chem.* **2006**, *11* (3), 286–306.

(71) Lill, S. O. N.; Siegbahn, P. E. M. An Autocatalytic Mechanism for NiFe-Hydrogenase: Reduction to Ni(I) Followed by Oxidative Addition. *Biochemistry* **2009**, *48* (5), 1056–1066.

(72) VIGNAIS, P. H/D Exchange Reactions and Mechanistic Aspects of the Hydrogenases. *Coord. Chem. Rev.* **2005**, *249* (15–16), 1677–1690.

(73) Brecht, M.; van Gastel, M.; Buhrke, T.; Friedrich, B.; Lubitz, W. Direct Detection of a Hydrogen Ligand in the [NiFe] Center of the Regulatory H 2 -Sensing Hydrogenase from Ralstonia e Utropha in Its Reduced State by HYSCORE and ENDOR Spectroscopy. *J. Am. Chem. Soc.* **2003**, *125* (43), 13075–13083.

(74) Foerster, S.; Stein, M.; Brecht, M.; Ogata, H.; Higuchi, Y.; Lubitz, W. Single Crystal EPR Studies of the Reduced Active Site of [NiFe] Hydrogenase from Desulfovibrio Vulgaris Miyazaki F. *J. Am. Chem. Soc.* **2003**, *125* (1), 83–93.

(75) Foerster, S.; Gastel, M. van; Brecht, M.; Lubitz, W. An Orientation-Selected ENDOR and HYSCORE Study of the Ni-C Active State of Desulfovibrio Vulgaris Miyazaki F Hydrogenase. *JBIC J. Biol. Inorg. Chem.* **2005**, *10* (1), 51–62.

(76) Shaw, W. J.; Helm, M. L.; DuBois, D. L. A Modular, Energy-Based Approach to the Development of Nickel Containing Molecular Electrocatalysts for Hydrogen Production and Oxidation. *Biochim. Biophys. Acta - Bioenerg.* **2013**, *1827* (8–9), 1123–1139.

(77) Evans, R. M.; Brooke, E. J.; Wehlin, S. A. M.; Nomerotskaia, E.; Sargent, F.; Carr, S. B.; Phillips, S. E. V; Armstrong, F. A. Mechanism of Hydrogen Activation by [NiFe] Hydrogenases. *Nat. Chem. Biol.* **2016**, *12* (1), 46–50.

(78) Szőri-Dorogházi, E.; Maróti, G.; Szőri, M.; Nyilasi, A.; Rákhely, G.; Kovács, K. L. Analyses of the Large Subunit Histidine-Rich Motif Expose an Alternative Proton Transfer Pathway in [NiFe] Hydrogenases. *PLoS One* **2012**, *7* (4), e34666.

(79) Kubas, G. J. Fundamentals of H 2 Binding and Reactivity on Transition Metals Underlying

Hydrogenase Function and H 2 Production and Storage. *Chem. Rev.* **2007**, *107* (10), 4152–4205.

(80) Kubas, G. J.; Ryan, R. R.; Swanson, B. I.; Vergamini, P. J.; Wasserman, H. J. Characterization of the First Examples of Isolable Molecular Hydrogen Complexes, M(CO)3(PR3)2(H2) (M = Molybdenum or Tungsten; R = Cy or Isopropyl). Evidence for a Side-on Bonded Dihydrogen Ligand. *J. Am. Chem. Soc.* **1984**, *106* (2), 451–452.

(81) Bruschi, M.; Tiberti, M.; Guerra, A.; De Gioia, L. Disclosure of Key Stereoelectronic Factors for Efficient H2 Binding and Cleavage in the Active Site of [NiFe]-Hydrogenases. *J. Am. Chem. Soc.* **2014**, *136* (5), 1803–1814.

(82) Isegawa, M.; Matsumoto, T.; Ogo, S. H 2 Activation by Hydrogenase-Inspired NiFe Catalyst Using Frustrated Lewis Pair: Effect of Buffer and Halide Ion in the Heterolytic H–H Bond Cleavage. *RSC Adv.* **2021**, *11* (45), 28420–28432.

(83) Escorcia, A. M.; Stein, M. QM/MM Investigation of the Role of a Second Coordination Shell Arginine in [NiFe]-Hydrogenases. *Front. Chem.* **2018**, *6* (MAY), 1–11.

(84) Greene, B. L.; Wu, C.-H.; McTernan, P. M.; Adams, M. W. W.; Dyer, R. B. Proton-Coupled Electron Transfer Dynamics in the Catalytic Mechanism of a [NiFe]-Hydrogenase. *J. Am. Chem. Soc.* **2015**, *137* (13), 4558–4566.

(85) Murphy, B. J.; Hidalgo, R.; Roessler, M. M.; Evans, R. M.; Ash, P. A.; Myers, W. K.; Vincent, K. A.; Armstrong, F. A. Discovery of Dark PH-Dependent H + Migration in a [NiFe]-Hydrogenase and Its Mechanistic Relevance: Mobilizing the Hydrido Ligand of the Ni-C Intermediate. *J. Am. Chem. Soc.* **2015**, *137* (26), 8484–8489.

(86) Bagley, K. A.; Van Garderen, C. J.; Chen, M.; Woodruff, W. H.; Duin, E. C.; Albracht, S. P. J. Infrared Studies on the Interaction of Carbon Monoxide with Divalent Nickel in Hydrogenase from Chromatium Vinosum. *Biochemistry* **1994**, *33* (31), 9229–9236.

(87) Bagley, K. A.; Duin, E. C.; Roseboom, W.; Albracht, S. P. J.; Woodruff, W. H. Infrared-Detectable Group Senses Changes in Charge Density on the Nickel Center in Hydrogenase from Chromatium Vinosum. *Biochemistry* **1995**, *34* (16), 5527–5535.

(88) Pierik, A. J.; Roseboom, W.; Happe, R. P.; Bagley, K. A.; Albracht, S. P. J. Carbon Monoxide and Cyanide as Intrinsic Ligands to Iron in the Active Site of [NiFe]-Hydrogenases. *J. Biol. Chem.* **1999**, *274* (6), 3331–3337.

(89) Horch, M.; Rippers, Y.; Mroginski, M. A.; Hildebrandt, P.; Zebger, I. Combining Spectroscopy and Theory to Evaluate Structural Models of Metalloenzymes: A Case Study on the Soluble [NiFe] Hydrogenase from Ralstonia Eutropha. *ChemPhysChem* **2013**, *14* (1), 185–191.

(90) Rippers, Y.; Horch, M.; Hildebrandt, P.; Zebger, I.; Mroginski, M. A. Revealing the Absolute

Configuration of the CO and CN − Ligands at the Active Site of a [NiFe] Hydrogenase. *ChemPhysChem* **2012**, *13* (17), 3852–3856.

(91) Rippers, Y.; Procacci, B.; Hunt, N. T.; Horch, M. Understanding 2D-IR Spectra of Hydrogenases: A Descriptive and Predictive Computational Study. *Catalysts* **2022**, *12* (9), 988.

(92) Ash, P. A.; Vincent, K. A. Spectroscopic Analysis of Immobilised Redox Enzymes under Direct Electrochemical Control. *Chem. Commun.* **2012**, *48* (10), 1400–1409.

(93) Hidalgo, R.; Ash, P. A.; Healy, A. J.; Vincent, K. A. Infrared Spectroscopy during Electrocatalytic Turnover Reveals the Ni-L Active Site State during H<inf>2</Inf> Oxidation by a NiFe Hydrogenase. *Angew. Chemie - Int. Ed.* **2015**, *54* (24), 7110–7113.

(94) Ilina, Y.; Lorent, C.; Katz, S.; Jeoung, J.; Shima, S.; Horch, M.; Zebger, I.; Dobbek, H. X-ray Crystallography and Vibrational Spectroscopy Reveal the Key Determinants of Biocatalytic Dihydrogen Cycling by [NiFe] Hydrogenases. *Angew. Chemie Int. Ed.* **2019**, *58* (51), 18710–18714.

(95) Katz, S.; Noth, J.; Horch, M.; Shafaat, H. S.; Happe, T.; Hildebrandt, P.; Zebger, I. Vibrational Spectroscopy Reveals the Initial Steps of Biological Hydrogen Evolution. *Chem. Sci.* **2016**, *7* (11), 6746–6752.

(96) Ash, P. A.; Liu, J.; Coutard, N.; Heidary, N.; Horch, M.; Gudim, I.; Simler, T.; Zebger, I.; Lenz, O.; Vincent, K. A. Electrochemical and Infrared Spectroscopic Studies Provide Insight into Reactions of the NiFe Regulatory Hydrogenase from Ralstonia Eutropha with O 2 and CO. *J. Phys. Chem. B* **2015**, *119* (43), 13807–13815.

(97) Ogata, H.; Krämer, T.; Wang, H.; Schilter, D.; Pelmenschikov, V.; van Gastel, M.; Neese, F.; Rauchfuss, T. B.; Gee, L. B.; Scott, A. D.; Yoda, Y.; Tanaka, Y.; Lubitz, W.; Cramer, S. P. Hydride Bridge in [NiFe]-Hydrogenase Observed by Nuclear Resonance Vibrational Spectroscopy. *Nat. Commun.* **2015**, *6* (1), 7890.

(98) Horch, M.; Schoknecht, J.; Mroginski, M. A.; Lenz, O.; Hildebrandt, P.; Zebger, I. Resonance Raman Spectroscopy on [NiFe] Hydrogenase Provides Structural Insights into Catalytic Intermediates and Reactions. *J. Am. Chem. Soc.* **2014**, *136* (28), 9870–9873.

(99) Siebert, E.; Horch, M.; Rippers, Y.; Fritsch, J.; Frielingsdorf, S.; Lenz, O.; Velazquez Escobar, F.; Siebert, F.; Paasche, L.; Kuhlmann, U.; Lendzian, F.; Mroginski, M.; Zebger, I.; Hildebrandt, P. Resonance Raman Spectroscopy as a Tool to Monitor the Active Site of Hydrogenases. *Angew. Chemie Int. Ed.* **2013**, *52* (19), 5162–5165.

(100) Kamali, S.; Wang, H.; Mitra, D.; Ogata, H.; Lubitz, W.; Manor, B. C.; Rauchfuss, T. B.; Byrne, D.; Bonnefoy, V.; Jenney, F. E.; Adams, M. W. W.; Yoda, Y.; Alp, E.; Zhao, J.; Cramer, S. P. Observation of the Fe□CN and Fe□CO Vibrations in the Active Site of [NiFe] Hydrogenase by

Nuclear Resonance Vibrational Spectroscopy. *Angew. Chemie Int. Ed.* **2013**, *52* (2), 724–728.

(101) Vansuch, G. E.; Wu, C.-H.; Haja, D. K.; Blair, S. A.; Chica, B.; Johnson, M. K.; Adams, M. W. W.; Dyer, R. B. Metal–Ligand Cooperativity in the Soluble Hydrogenase-1 from Pyrococcus Furiosus. *Chem. Sci.* **2020**, *11* (32), 8572–8581.

(102) Sanchez, M. L. K.; Konecny, S. E.; Narehood, S. M.; Reijerse, E. J.; Lubitz, W.; Birrell, J. A.; Dyer, R. B. The Laser-Induced Potential Jump: A Method for Rapid Electron Injection into Oxidoreductase Enzymes. *J. Phys. Chem. B* **2020**, *124* (40), 8750–8760.

(103) Sanchez, M. L. K.; Sommer, C.; Reijerse, E.; Birrell, J. A.; Lubitz, W.; Dyer, R. B. Investigating the Kinetic Competency of Cr HydA1 [FeFe] Hydrogenase Intermediate States via Time-Resolved Infrared Spectroscopy. *J. Am. Chem. Soc.* **2019**, *141* (40), 16064–16070.

(104) Greene, B. L.; Vansuch, G. E.; Chica, B. C.; Adams, M. W. W.; Dyer, R. B. Applications of Photogating and Time Resolved Spectroscopy to Mechanistic Studies of Hydrogenases. *Acc. Chem. Res.* **2017**, *50* (11), 2718–2726.

(105) Greene, B. L.; Schut, G. J.; Adams, M. W. W.; Dyer, R. B. Pre-Steady-State Kinetics of Catalytic Intermediates of an [FeFe]-Hydrogenase. *ACS Catal.* **2017**, *7* (3), 2145–2150.

(106) Greene, B. L.; Vansuch, G. E.; Wu, C.-H.; Adams, M. W. W.; Dyer, R. B. Glutamate Gated Proton-Coupled Electron Transfer Activity of a [NiFe]-Hydrogenase. *J. Am. Chem. Soc.* **2016**, *138* (39), 13013–13021.

(107) Greene, B. L.; Joseph, C. A.; Maroney, M. J.; Dyer, R. B. Direct Evidence of Active-Site Reduction and Photodriven Catalysis in Sensitized Hydrogenase Assemblies. *J. Am. Chem. Soc.* **2012**, *134* (27), 11108–11111.

(108) Darensbourg, M. Y.; Lyon, E. J.; Smee, J. J. The Bio-Organometallic Chemistry of Active Site Iron in Hydrogenases. *Coord. Chem. Rev.* **2000**, *206–207*, 533–561.

(109) Morse, P. M. Diatomic Molecules According to the Wave Mechanics. II. Vibrational Levels. *Phys. Rev.* **1929**, *34* (1), 57–64.

(110) Telle, H. *Laser Chemistry: Spectroscopy, Dynamics and Applications*; Telle, H., Urena, A., Donovan, R., Eds.; John Wiley & Sons, Ltd, 2007.

(111) Hamm, P.; Zanni, M. *Concepts and Methods of 2D Infrared Spectroscopy*; Cambridge University Press: Cambridge, 2011.

(112) Cho, M. *Two Dimensional Optical Spectroscopy*; CRC Press, 2009.

(113) Boyd, R. W. *Nonlinear Optics*, 4th ed.; Elsevier, 2020.

(114) Fayer, M. D. *Ultrafast Vibrational Spectroscopy*; Fayer, M. D., Ed.; CRC Press, 2013.

(115) Engel, T. *Quantum Chemistry and Spectroscopy*, Third.; Pearson Education, Inc, 2013; Vol. 40.

(116) Hamm, P.; Lim, M.; Hochstrasser, R. M. Structure of the Amide I Band of Peptides Measured

by Femtosecond Nonlinear-Infrared Spectroscopy. *J. Phys. Chem. B* **1998**, *102* (31), 6123–6138.

(117) Cervetto, V.; Helbing, J.; Bredenbeck, J.; Hamm, P. Double-Resonance versus Pulsed Fourier Transform Two-Dimensional Infrared Spectroscopy: An Experimental and Theoretical Comparison. *J. Chem. Phys.* **2004**, *121* (12), 5935–5942.

(118) Asplund, M. C.; Zanni, M. T.; Hochstrasser, R. M. Two-Dimensional Infrared Spectroscopy of Peptides by Phase-Controlled Femtosecond Vibrational Photon Echoes. *Proc. Natl. Acad. Sci.* **2000**, *97* (15), 8219–8224.

(119) Shim, S.-H.; Strasfeld, D. B.; Fulmer, E. C.; Zanni, M. T. Femtosecond Pulse Shaping Directly in the Mid-IR Using Acousto-Optic Modulation. *Opt. Lett.* **2006**, *31* (6), 838.

(120) Shim, S.-H.; Strasfeld, D. B.; Ling, Y. L.; Zanni, M. T. Automated 2D IR Spectroscopy Using a Mid-IR Pulse Shaper and Application of This Technology to the Human Islet Amyloid Polypeptide. *Proc. Natl. Acad. Sci.* **2007**, *104* (36), 14197–14202.

(121) Golonzka, O.; Tokmakoff, A. Polarization-Selective Third-Order Spectroscopy of Coupled Vibronic States. *J. Chem. Phys.* **2001**, *115* (1), 297–309.

(122) Hill, J. R.; Dlott, D. D.; Fayer, M. D.; Peterson, K. A.; Rella, C. W.; Rosenblatt, M. M.; Suslick, K. S.; Ziegler, C. J. Vibrational Relaxation of Carbon Monoxide in Model Heme Compounds. 6-Coordinate Metalloporphyrins (M = Fe, Ru, OS). *Chem. Phys. Lett.* **1995**, *244* (3–4), 218–223.

(123) Stewart, A. I.; Clark, I. P.; Towrie, M.; Ibrahim, S. K.; Parker, A. W.; Pickett, C. J.; Hunt, N. T. Structure and Vibrational Dynamics of Model Compounds of the [FeFe]−Hydrogenase Enzyme System via Ultrafast Two-Dimensional Infrared Spectroscopy. *J. Phys. Chem. B* **2008**, *112* (32), 10023–10032.

(124) Kaziannis, S.; Wright, J. A.; Candelaresi, M.; Kania, R.; Greetham, G. M.; Parker, A. W.; Pickett, C. J.; Hunt, N. T. The Role of CN and CO Ligands in the Vibrational Relaxation Dynamics of Model Compounds of the [FeFe]-Hydrogenase Enzyme. *Phys. Chem. Chem. Phys.* **2011**, *13* (21), 10295.

(125) Yamada, S. A.; Thompson, W. H.; Fayer, M. D. Water-Anion Hydrogen Bonding Dynamics: Ultrafast IR Experiments and Simulations. *J. Chem. Phys.* **2017**, *146* (23).

(126) Adamczyk, K.; Simpson, N.; Greetham, G. M.; Gumiero, A.; Walsh, M. A.; Towrie, M.; Parker, A. W.; Hunt, N. T. Ultrafast Infrared Spectroscopy Reveals Water-Mediated Coherent Dynamics in an Enzyme Active Site. *Chem. Sci.* **2015**, *6* (1), 505–516.

(127) Ridley, A. R.; Stewart, A. I.; Adamczyk, K.; Ghosh, H. N.; Kerkeni, B.; Guo, Z. X.; Nibbering, E. T. J.; Pickett, C. J.; Hunt, N. T. Multiple-Timescale Photoreactivity of a Model Compound Related to the Active Site of [FeFe]-Hydrogenase. *Inorg. Chem.* **2008**, *47* (17), 7453–7455.

(128) Fritzsch, R.; Brady, O.; Adair, E.; Wright, J. A.; Pickett, C. J.; Hunt, N. T. Encapsulating Subsite Analogues of the [FeFe]-Hydrogenases in Micelles Enables Direct Water Interactions. *J. Phys. Chem. Lett.* **2016**, *7* (14), 2838–2843.

(129) Mirmohades, M.; Adamska-Venkatesh, A.; Sommer, C.; Reijerse, E.; Lomoth, R.; Lubitz, W.; Hammarström, L. Following [FeFe] Hydrogenase Active Site Intermediates by Time-Resolved Mid-IR Spectroscopy. *J. Phys. Chem. Lett.* **2016**, *7* (16), 3290–3293.

(130) Caranto, J. D.; Weitz, A.; Hendrich, M. P.; Kurtz, D. M. The Nitric Oxide Reductase Mechanism of a Flavo-Diiron Protein: Identification of Active-Site Intermediates and Products. *J. Am. Chem. Soc.* **2014**, *136* (22), 7981–7992.

(131) Candelaresi, M.; Gumiero, A.; Adamczyk, K.; Robb, K.; Bellota-Antón, C.; Sangal, V.; Munnoch, J.; Greetham, G. M.; Towrie, M.; Hoskisson, P. A.; Parker, A. W.; Tucker, N. P.; Walsh, M. A.; Hunt, N. T. A Structural and Dynamic Investigation of the Inhibition of Catalase by Nitric Oxide. *Org. Biomol. Chem.* **2013**, *11* (44), 7778–7788.

(132) Thielges, M. C.; Axup, J. Y.; Wong, D.; Lee, H. S.; Chung, J. K.; Schultz, P. G.; Fayer, M. D. Two-Dimensional IR Spectroscopy of Protein Dynamics Using Two Vibrational Labels: A Site-Specific Genetically Encoded Unnatural Amino Acid and an Active Site Ligand. *J. Phys. Chem. B* **2011**, *115* (38), 11294–11304.

(133) Hall, C. R.; Tolentino Collado, J.; Iuliano, J. N.; Gil, A. A.; Adamczyk, K.; Lukacs, A.; Greetham, G. M.; Sazanovich, I.; Tonge, P. J.; Meech, S. R. Site-Specific Protein Dynamics Probed by Ultrafast Infrared Spectroscopy of a Noncanonical Amino Acid. *J. Phys. Chem. B* **2019**, *123* (45), 9592–9597.

(134) Ghosh, A.; Qiu, J.; DeGrado, W. F.; Hochstrasser, R. M. Tidal Surge in the M2 Proton Channel, Sensed by 2D IR Spectroscopy. *Proc. Natl. Acad. Sci.* **2011**, *108* (15), 6115–6120.

(135) Ghosh, A.; Wang, J.; Moroz, Y. S.; Korendovych, I. V.; Zanni, M.; Degrado, W. F.; Gai, F.; Hochstrasser, R. M. 2D IR Spectroscopy Reveals the Role of Water in the Binding of Channel-Blocking Drugs to the Influenza M2 Channel. *J. Chem. Phys.* **2014**, *140* (23).

(136) DeFlores, L. P.; Tokmakoff, A. Water Penetration into Protein Secondary Structure Revealed by Hydrogen-Deuterium Exchange Two-Dimensional Infrared Spectroscopy. *J. Am. Chem. Soc.* **2006**, *128* (51), 16520–16521.

(137) Kuroda, D. G.; Bauman, J. D.; Challa, J. R.; Patel, D.; Troxler, T.; Das, K.; Arnold, E.; Hochstrasser, R. M. Snapshot of the Equilibrium Dynamics of a Drug Bound to HIV-1 Reverse Transcriptase. *Nat. Chem.* **2013**, *5* (3), 174–181.

(138) Fang, C.; Bauman, J. D.; Das, K.; Remorino, A.; Arnold, E.; Hochstrasser, R. M. Two-Dimensional Infrared Spectra Reveal Relaxation of the Nonnucleoside Inhibitor TMC278

Complexed with HIV-1 Reverse Transcriptase. *Proc. Natl. Acad. Sci.* **2008**, *105* (5), 1472–1477.

(139) Basom, E. J.; Manifold, B. A.; Thielges, M. C. Conformational Heterogeneity and the Affinity of Substrate Molecular Recognition by Cytochrome P450cam. *Biochemistry* **2017**, *56* (25), 3248–3256.

(140) Thielges, M. C.; Chung, J. K.; Fayer, M. D. Protein Dynamics in Cytochrome P450 Molecular Recognition and Substrate Specificity Using 2D IR Vibrational Echo Spectroscopy. *J. Am. Chem. Soc.* **2011**, *133* (11), 3995–4004.

(141) Nagano, S.; Tosha, T.; Ishimori, K.; Morishima, I.; Poulos, T. L. Crystal Structure of the Cytochrome P450cam Mutant That Exhibits the Same Spectral Perturbations Induced by Putidaredoxin Binding. *J. Biol. Chem.* **2004**, *279* (41), 42844–42849.

(142) Henriksen, A.; Schuller, D. J.; Meno, K.; Welinder, K. G.; Smith, A. T.; Gajhede, M. Structural Interactions between Horseradish Peroxidase C and the Substrate Benzhydroxamic Acid Determined by X-Ray Crystallography ,. *Biochemistry* **1998**, *37* (22), 8054–8060.

(143) Simpson, N.; Adamczyk, K.; Hithell, G.; Shaw, D. J.; Greetham, G. M.; Towrie, M.; Parker, A. W.; Hunt, N. T. The Effect on Structural and Solvent Water Molecules of Substrate Binding to Ferric Horseradish Peroxidase. *Faraday Discuss.* **2015**, *177*, 163–179.

(144) Acharya, R.; Carnevale, V.; Fiorin, G.; Levine, B. G.; Polishchuk, A. L.; Balannik, V.; Samish, I.; Lamb, R. A.; Pinto, L. H.; DeGrado, W. F.; Klein, M. L. Structure and Mechanism of Proton Transport through the Transmembrane Tetrameric M2 Protein Bundle of the Influenza A Virus. *Proc. Natl. Acad. Sci.* **2010**, *107* (34), 15075–15080.

(145) Thomaston, J. L.; Polizzi, N. F.; Konstantinidi, A.; Wang, J.; Kolocouris, A.; DeGrado, W. F. Inhibitors of the M2 Proton Channel Engage and Disrupt Transmembrane Networks of Hydrogen-Bonded Waters. *J. Am. Chem. Soc.* **2018**, *140* (45), 15219–15226.

(146) Jung, H. E.; Lee, H. K. Host Protective Immune Responses against Influenza A Virus Infection. *Viruses* **2020**, *12* (5), 504.

(147) Lin, Y.-S.; Shorb, J. M.; Mukherjee, P.; Zanni, M. T.; Skinner, J. L. Empirical Amide I Vibrational Frequency Map: Application to 2D-IR Line Shapes for Isotope-Edited Membrane Peptide Bundles. *J. Phys. Chem. B* **2009**, *113* (3), 592–602.

(148) Chollet, A.; Mourey, L.; Lherbet, C.; Delbot, A.; Julien, S.; Baltas, M.; Bernadou, J.; Pratviel, G.; Maveyraud, L.; Bernardes-Génisson, V. Crystal Structure of the Enoyl-ACP Reductase of Mycobacterium Tuberculosis (InhA) in the Apo-Form and in Complex with the Active Metabolite of Isoniazid Pre-Formed by a Biomimetic Approach. *J. Struct. Biol.* **2015**, *190* (3), 328–337.

(149) Shaw, D. J.; Robb, K.; Vetter, B. V.; Tong, M.; Molle, V.; Hunt, N. T.; Hoskisson, P. A. Disruption

of Key NADH-Binding Pocket Residues of the Mycobacterium Tuberculosis InhA Affects DD-CoA Binding Ability. *Sci. Rep.* **2017**, *7* (1), 1–7.

(150) Shaw, D. J.; Hill, R. E.; Simpson, N.; Husseini, F. S.; Robb, K.; Greetham, G. M.; Towrie, M.; Parker, A. W.; Robinson, D.; Hirst, J. D.; Hoskisson, P. A.; Hunt, N. T. Examining the Role of Protein Structural Dynamics in Drug Resistance in: Mycobacterium Tuberculosis. *Chem. Sci.* **2017**, *8* (12), 8384–8399.

(151) Bernhard, M.; Schwartz, E.; Rietdorf, J.; Friedrich, B. The Alcaligenes Eutrophus Membrane-Bound Hydrogenase Gene Locus Encodes Functions Involved in Maturation and Electron Transport Coupling. *J. Bacteriol.* **1996**, *178* (15), 4522–4529.

(152) Schink, B.; Schlegel, H. G. The Membrane-Bound Hydrogenase of Alcaligenes Eutrophus. I. Solubilization, Purification, and Biochemical Properties. *Biochim. Biophys. Acta - Enzymol.* **1979**, *567* (2), 315–324.

(153) Greetham, G. M.; Burgos, P.; Cao, Q.; Clark, I. P.; Codd, P. S.; Farrow, R. C.; George, M. W.; Kogimtzis, M.; Matousek, P.; Parker, A. W.; Pollard, M. R.; Robinson, D. A.; Xin, Z.-J.; Towrie, M. ULTRA: A Unique Instrument for Time-Resolved Spectroscopy. *Appl. Spectrosc.* **2010**, *64* (12), 1311–1319.

(154) Horch, M.; Schoknecht, J.; Wrathall, S. L. D.; Greetham, G. M.; Lenz, O.; Hunt, N. T. Understanding the Structure and Dynamics of Hydrogenases by Ultrafast and Two-Dimensional Infrared Spectroscopy. *Chem. Sci.* **2019**, *10* (39), 8981–8989.

(155) Healy, A. J.; Ash, P. A.; Lenz, O.; Vincent, K. A. Attenuated Total Reflectance Infrared Spectroelectrochemistry at a Carbon Particle Electrode; Unmediated Redox Control of a [NiFe]-Hydrogenase Solution. *Phys. Chem. Chem. Phys.* **2013**, *15* (19), 7055.

(156) Roncaroli, F.; Bill, E.; Friedrich, B.; Lenz, O.; Lubitz, W.; Pandelia, M.-E. Cofactor Composition and Function of a H 2 -Sensing Regulatory Hydrogenase as Revealed by Mössbauer and EPR Spectroscopy. *Chem. Sci.* **2015**, *6* (8), 4495–4507.

(157) Lenz, O.; Bernhard, M.; Buhrke, T.; Schwartz, E.; Friedrich, B. The Hydrogen-Sensing Apparatus in Ralstonia Eutropha. *J. Mol. Microbiol. Biotechnol.* **2002**, *4* (3), 255–262.

(158) Buhrke, T.; Lenz, O.; Porthun, A.; Friedrich, B. The H2-Sensing Complex of Ralstonia Eutropha: Interaction between a Regulatory [NiFe] Hydrogenase and a Histidine Protein Kinase. *Mol. Microbiol.* **2004**, *51* (6), 1677–1689.

(159) Kleihues, L.; Lenz, O.; Bernhard, M.; Buhrke, T.; Friedrich, B. The H 2 Sensor of Ralstonia Eutropha Is a Member of the Subclass of Regulatory [NiFe] Hydrogenases. *J. Bacteriol.* **2000**, *182* (10), 2716–2724.

(160) Pierik, A. J.; Schmelz, M.; Lenz, O.; Friedrich, B.; Albracht, S. P. J. Characterization of the Active

Site of a Hydrogen Sensor from Alcaligenes Eutrophus. *FEBS Lett.* **1998**, *438* (3), 231–235.

(161) Caserta, G.; Lorent, C.; Ciaccafava, A.; Keck, M.; Breglia, R.; Greco, C.; Limberg, C.; Hildebrandt, P.; Cramer, S. P.; Zebger, I.; Lenz, O. The Large Subunit of the Regulatory [NiFe]-Hydrogenase from Ralstonia Eutropha – a Minimal Hydrogenase? *Chem. Sci.* **2020**, *11* (21), 5453–5465.

(162) Stewart, A. I.; Wright, J. A.; Greetham, G. M.; Kaziannis, S.; Santabarbara, S.; Towrie, M.; Parker, A. W.; Pickett, C. J.; Hunt, N. T. Determination of the Photolysis Products of [FeFe]Hydrogenase Enzyme Model Systems Using Ultrafast Multidimensional Infrared Spectroscopy. *Inorg. Chem.* **2010**, *49* (20), 9563–9573.

(163) Kaziannis, S.; Santabarbara, S.; Wright, J. A.; Greetham, G. M.; Towrie, M.; Parker, A. W.; Pickett, C. J.; Hunt, N. T. Femtosecond to Microsecond Photochemistry of a [FeFe]Hydrogenase Enzyme Model Compound. *J. Phys. Chem. B* **2010**, *114* (46), 15370–15379.

(164) Frederix, P. W. J. M.; Adamczyk, K.; Wright, J. A.; Tuttle, T.; Ulijn, R. V.; Pickett, C. J.; Hunt, N. T. Investigation of the Ultrafast Dynamics Occurring during Unsensitized Photocatalytic H2 Evolution by an [FeFe]-Hydrogenase Subsite Analogue. *Organometallics* **2014**, *33* (20), 5888–5896.

(165) Golonzka, O.; Khalil, M.; Demirdöven, N.; Tokmakoff, A. Coupling and Orientation between Anharmonic Vibrations Characterized with Two-Dimensional Infrared Vibrational Echo Spectroscopy. *J. Chem. Phys.* **2001**, *115* (23), 10814–10828.

(166) King, J. T.; Ross, M. R.; Kubarych, K. J. Water-Assisted Vibrational Relaxation of a Metal Carbonyl Complex Studied with Ultrafast 2D-IR. *J. Phys. Chem. B* **2012**, *116* (12), 3754–3759.

(167) Bonner, G. M.; Ridley, A. R.; Ibrahim, S. K.; Pickett, C. J.; Hunt, N. T. Probing the Effect of the Solution Environment on the Vibrational Dynamics of an Enzyme Model System with Ultrafast 2D-IRspectroscopy. *Faraday Discuss.* **2010**, *145*, 429–442.

(168) Hill, J. R.; Tokmakoff, A.; Peterson, K. A.; Sauter, B.; Zimdars, D.; Dlott, D. D.; Fayer, M. D. Vibrational Dynamics of Carbon Monoxide at the Active Site of Myoglobin: Picosecond Infrared Free-Electron Laser Pump-Probe Experiments. *J. Phys. Chem.* **1994**, *98* (43), 11213–11219.

(169) Dlott, D. D.; Fayer, M. D.; Hill, J. R.; Rella, C. W.; Suslick, K. S.; Ziegler, C. J. Vibrational Relaxation in Metalloporphyrin CO Complexes. *J. Am. Chem. Soc.* **1996**, *118* (33), 7853–7854.

(170) Hill, J. R.; Ziegler, C. J.; Suslick, K. S.; Dlott, D. D.; Rella, C. W.; Fayer, M. D. Tuning the Vibrational Relaxation of CO Bound to Heme and Metalloporphyrin Complexes. *J. Phys. Chem.* **1996**, *100* (46), 18023–18032.

(171) Carter, R. T.; Huber, J. R. Quantum Beat Spectroscopy in Chemistry. *Chem. Soc. Rev.* **2000**, *29* (5), 305–314.

(172) Hack, E.; Huber, J. R. Quantum Beat Spectroscopy of Molecules. *Int. Rev. Phys. Chem.* **1991**, *10* (3), 287–317.

(173) Du, P.; Eisenberg, R. Catalysts Made of Earth-Abundant Elements (Co, Ni, Fe) for Water Splitting: Recent Progress and Future Challenges. *Energy Environ. Sci.* **2012**, *5* (3), 6012.

(174) Fukuzumi, S.; Lee, Y.-M.; Nam, W. Thermal and Photocatalytic Production of Hydrogen with Earth-Abundant Metal Complexes. *Coord. Chem. Rev.* **2018**, *355*, 54–73.

(175) Krämer, T.; Kampa, M.; Lubitz, W.; van Gastel, M.; Neese, F. Theoretical Spectroscopy of the Ni II Intermediate States in the Catalytic Cycle and the Activation of [NiFe] Hydrogenases. *ChemBioChem* **2013**, *14* (14), 1898–1905.

(176) Kampa, M.; Lubitz, W.; van Gastel, M.; Neese, F. Computational Study of the Electronic Structure and Magnetic Properties of the Ni–C State in [NiFe] Hydrogenases Including the Second Coordination Sphere. *JBIC J. Biol. Inorg. Chem.* **2012**, *17* (8), 1269–1281.

(177) Nguyen, N. T.; Mori, Y.; Matsumoto, T.; Yatabe, T.; Kabe, R.; Nakai, H.; Yoon, K.-S.; Ogo, S. A [NiFe]Hydrogenase Model That Catalyses the Release of Hydrogen from Formic Acid. *Chem. Commun.* **2014**, *50* (87), 13385–13387.

(178) Helm, M. L.; Stewart, M. P.; Bullock, R. M.; DuBois, M. R.; DuBois, D. L. A Synthetic Nickel Electrocatalyst with a Turnover Frequency Above 100,000 s −1 for H 2 Production. *Science (80-.).* **2011**, *333* (6044), 863–866.

(179) Nath, I.; Chakraborty, J.; Verpoort, F. Metal Organic Frameworks Mimicking Natural Enzymes: A Structural and Functional Analogy. *Chem. Soc. Rev.* **2016**, *45* (15), 4127–4170.

(180) Kandemir, B.; Kubie, L.; Guo, Y.; Sheldon, B.; Bren, K. L. Hydrogen Evolution from Water under Aerobic Conditions Catalyzed by a Cobalt ATCUN Metallopeptide. *Inorg. Chem.* **2016**, *55* (4), 1355–1357.

(181) Kandemir, B.; Chakraborty, S.; Guo, Y.; Bren, K. L. Semisynthetic and Biomolecular Hydrogen Evolution Catalysts. *Inorg. Chem.* **2016**, *55* (2), 467–477.

(182) Silver, S. C.; Niklas, J.; Du, P.; Poluektov, O. G.; Tiede, D. M.; Utschig, L. M. Protein Delivery of a Ni Catalyst to Photosystem I for Light-Driven Hydrogen Production. *J. Am. Chem. Soc.* **2013**, *135* (36), 13246–13249.

(183) Esselborn, J.; Lambertz, C.; Adamska-Venkatesh, A.; Simmons, T.; Berggren, G.; Noth, J.; Siebel, J.; Hemschemeier, A.; Artero, V.; Reijerse, E.; Fontecave, M.; Lubitz, W.; Happe, T. Spontaneous Activation of [FeFe]-Hydrogenases by an Inorganic [2Fe] Active Site Mimic. *Nat. Chem. Biol.* **2013**, *9* (10), 607–609.

(184) Berggren, G.; Adamska, A.; Lambertz, C.; Simmons, T. R.; Esselborn, J.; Atta, M.; Gambarelli, S.; Mouesca, J.-M.; Reijerse, E.; Lubitz, W.; Happe, T.; Artero, V.; Fontecave, M. Biomimetic Assembly and Activation of [FeFe]-Hydrogenases. *Nature* **2013**, *499* (7456), 66–69.

(185) Wang, F.; Wen, M.; Feng, K.; Liang, W.-J.; Li, X.-B.; Chen, B.; Tung, C.-H.; Wu, L.-Z. Amphiphilic Polymeric Micelles as Microreactors: Improving the Photocatalytic Hydrogen Production of the [FeFe]-Hydrogenase Mimic in Water. *Chem. Commun.* **2016**, *52* (3), 457–460.

(186) Wu, L.-Z.; Chen, B.; Li, Z.-J.; Tung, C.-H. Enhancement of the Efficiency of Photocatalytic Reduction of Protons to Hydrogen via Molecular Assembly. *Acc. Chem. Res.* **2014**, *47* (7), 2177–2185.

(187) Simmons, T. R.; Berggren, G.; Bacchi, M.; Fontecave, M.; Artero, V. Mimicking Hydrogenases: From Biomimetics to Artificial Enzymes. *Coord. Chem. Rev.* **2014**, *270–271* (1), 127–150.

(188) Jian, J.-X.; Liu, Q.; Li, Z.-J.; Wang, F.; Li, X.-B.; Li, C.-B.; Liu, B.; Meng, Q.-Y.; Chen, B.; Feng, K.; Tung, C.-H.; Wu, L.-Z. Chitosan Confinement Enhances Hydrogen Photogeneration from a Mimic of the Diiron Subsite of [FeFe]-Hydrogenase. *Nat. Commun.* **2013**, *4* (1), 2695.

(189) Wang, H.-Y.; Wang, W.-G.; Si, G.; Wang, F.; Tung, C.-H.; Wu, L.-Z. Photocatalytic Hydrogen Evolution from Rhenium(I) Complexes to [FeFe] Hydrogenase Mimics in Aqueous SDS Micellar Systems: A Biomimetic Pathway. *Langmuir* **2010**, *26* (12), 9766–9771.

(190) Gloaguen, F.; Rauchfuss, T. B. Small Molecule Mimics of Hydrogenases: Hydrides and Redox. *Chem. Soc. Rev.* **2009**, *38* (1), 100–108.

(191) Firpo, V.; Le, J. M.; Pavone, V.; Lombardi, A.; Bren, K. L. Hydrogen Evolution from Water Catalyzed by Cobalt-Mimochrome VI*a, a Synthetic Mini-Protein. *Chem. Sci.* **2018**, *9* (45), 8582–8589.

(192) Soltau, S. R.; Dahlberg, P. D.; Niklas, J.; Poluektov, O. G.; Mulfort, K. L.; Utschig, L. M. Ru–Protein–Co Biohybrids Designed for Solar Hydrogen Production: Understanding Electron Transfer Pathways Related to Photocatalytic Function. *Chem. Sci.* **2016**, *7* (12), 7068–7078.

(193) Birrell, J. A.; Rüdiger, O.; Reijerse, E. J.; Lubitz, W. Semisynthetic Hydrogenases Propel Biological Energy Research into a New Era. *Joule* **2017**, *1* (1), 61–76.

(194) Eberhardt, N. A.; Guan, H. Nickel Hydride Complexes. *Chem. Rev.* **2016**, *116* (15), 8373–8426.

(195) Armstrong, F. A.; Fontecilla-Camps, J. C. A Natural Choice for Activating Hydrogen. *Science (80-.).* **2008**, *321* (5888), 498–499.

(196) De Lacey, A. L.; Fernández, V. M.; Rousset, M.; Cammack, R. Activation and Inactivation of Hydrogenase Function and the Catalytic Cycle: Spectroelectrochemical Studies. *Chem. Rev.* **2007**, *107* (10), 4304–4330.

(197) Hunt, N. T. Transient 2D-IR Spectroscopy of Inorganic Excited States. *Dalt. Trans.* **2014**, *43*

(47), 17578–17589.

(198) Hunt, N. T. 2D-IR Spectroscopy: Ultrafast Insights into Biomolecule Structure and Function. *Chem. Soc. Rev.* **2009**, *38* (7), 1837.

(199) Khalil, M.; Demirdöven, N.; Tokmakoff, A. Coherent 2D IR Spectroscopy: Molecular Structure and Dynamics in Solution. *J. Phys. Chem. A* **2003**, *107* (27), 5258–5279.

(200) DeLacey, A. L.; Fernandez, V. M.; Rousset, M.; Cavazza, C.; Hatchikian, E. C. Spectroscopic and Kinetic Characterization of Active Site Mutants of Desulfovibrio Fructosovorans Ni-Fe Hydrogenase. *J. Biol. Inorg. Chem.* **2003**, *8* (1–2), 129–134.

(201) Bolanos-Garcia, V. M.; Davies, O. R. Structural Analysis and Classification of Native Proteins from E. Coli Commonly Co-Purified by Immobilised Metal Affinity Chromatography. *Biochim. Biophys. Acta - Gen. Subj.* **2006**, *1760* (9), 1304–1313.

(202) Imlay, J. A. The Mismetallation of Enzymes during Oxidative Stress. *J. Biol. Chem.* **2014**, *289* (41), 28121–28128.

(203) Zhang, J. W.; Butland, G.; Greenblatt, J. F.; Emili, A.; Zamble, D. B. A Role for SlyD in the Escherichia Coli Hydrogenase Biosynthetic Pathway. *J. Biol. Chem.* **2005**, *280* (6), 4360–4366.

(204) Frielingsdorf, S.; Schubert, T.; Pohlmann, A.; Lenz, O.; Friedrich, B. A Trimeric Supercomplex of the Oxygen-Tolerant Membrane-Bound [NiFe]-Hydrogenase from Ralstonia Eutropha H16. *Biochemistry* **2011**, *50* (50), 10836–10843.

(205) Sigfridsson, K. G. V.; Leidel, N.; Sanganas, O.; Chernev, P.; Lenz, O.; Yoon, K.-S.; Nishihara, H.; Parkin, A.; Armstrong, F. A.; Dementin, S.; Rousset, M.; De Lacey, A. L.; Haumann, M. Structural Differences of Oxidized Iron–Sulfur and Nickel–Iron Cofactors in O 2 -Tolerant and O 2 -Sensitive Hydrogenases Studied by X-Ray Absorption Spectroscopy. *Biochim. Biophys. Acta - Bioenerg.* **2015**, *1847* (2), 162–170.

(206) Tai, H.; Xu, L.; Inoue, S.; Nishikawa, K.; Higuchi, Y.; Hirota, S. Photoactivation of the Ni-SI r State to the Ni-SI a State in [NiFe] Hydrogenase: FT-IR Study on the Light Reactivity of the Ready Ni-SI r State and as-Isolated Enzyme Revisited. *Phys. Chem. Chem. Phys.* **2016**, *18* (32), 22025–22030.

(207) Saggu, M.; Zebger, I.; Ludwig, M.; Lenz, O.; Friedrich, B.; Hildebrandt, P.; Lendzian, F. Spectroscopic Insights into the Oxygen-Tolerant Membrane-Associated [NiFe] Hydrogenase of Ralstonia Eutropha H16. *J. Biol. Chem.* **2009**, *284* (24), 16264–16276.

(208) Zheng, J.; Kwak, K.; Asbury, J.; Chen, X.; Piletic, I. R.; Fayer, M. D. Ultrafast Dynamics of Solute-Solvent Complexation Observed at Thermal Equilibrium in Real Time. *Science (80-.).* **2005**, *309* (5739), 1338–1343.

(209) Happe, R. P.; Roseboom, W.; Pierik, A. J.; Albracht, S. P. J.; Bagley, K. A. Biological Activition of

Hydrogen. *Nature* **1997**, *385* (6612), 126–126.

(210) Cho, M. Ultrafast Vibrational Spectroscopy in Condensed Phases. *PhysChemComm* **2002**, *5* (7), 40.

(211) Park, K.; Cho, M.; Hahn, S.; Kim, D. Two-Dimensional Vibrational Spectroscopy. II. Ab Initio Calculation of the Coherent 2D Infrared Response Function of CHCl3 and Comparison with the 2D Raman Response Function. *J. Chem. Phys.* **1999**, *111* (9), 4131–4139.

(212) Hahn, S.; Park, K.; Cho, M. Two-Dimensional Vibrational Spectroscopy. I. Theoretical Calculation of the Nonlinear Raman Response Function of CHCl3. *J. Chem. Phys.* **1999**, *111* (9), 4121–4130.

(213) Hahn, S.; Kim, D.; Cho, M. Nonlinear Optical Properties of the Linear Quadrupolar Molecule: Structure−Function Relationship Based on a Three-State Model. *J. Phys. Chem. B* **1999**, *103* (39), 8221–8229.

(214) Slenkamp, K. M.; Lynch, M. S.; Van Kuiken, B. E.; Brookes, J. F.; Bannan, C. C.; Daifuku, S. L.; Khalil, M. Investigating Vibrational Anharmonic Couplings in Cyanide-Bridged Transition Metal Mixed Valence Complexes Using Two-Dimensional Infrared Spectroscopy. *J. Chem. Phys.* **2014**, *140* (8), 084505.

(215) Lai, C.-H.; Lee, W.-Z.; Miller, M. L.; Reibenspies, J. H.; Darensbourg, D. J.; Darensbourg, M. Y. Responses of the Fe(CN) 2 (CO) Unit to Electronic Changes as Related to Its Role in [NiFe]Hydrogenase. *J. Am. Chem. Soc.* **1998**, *120* (39), 10103–10114.

(216) Darensbourg, D. J.; Reibenspies, J. H.; Lai, C.-H.; Lee, W.-Z.; Darensbourg, M. Y. Analysis of an Organometallic Iron Site Model for the Heterodimetallic Unit of [NiFe]Hydrogenase. *J. Am. Chem. Soc.* **1997**, *119* (33), 7903–7904.

(217) Park, S.; Fayer, M. D. Hydrogen Bond Dynamics in Aqueous NaBr Solutions. *Proc. Natl. Acad. Sci.* **2007**, *104* (43), 16731–16738.

(218) Ranasinghe, C.; Pagano, P.; Sapienza, P. J.; Lee, A. L.; Kohen, A.; Cheatum, C. M. Isotopic Labeling of Formate Dehydrogenase Perturbs the Protein Dynamics. *J. Phys. Chem. B* **2019**, *123* (49), 10403–10409.

(219) Ramos, S.; Horness, R. E.; Collins, J. A.; Haak, D.; Thielges, M. C. Site-Specific 2D IR Spectroscopy: A General Approach for the Characterization of Protein Dynamics with High Spatial and Temporal Resolution. *Phys. Chem. Chem. Phys.* **2019**, *21* (2), 780–788.

(220) Pagano, P.; Guo, Q.; Ranasinghe, C.; Schroeder, E.; Robben, K.; Häse, F.; Ye, H.; Wickersham, K.; Aspuru-Guzik, A.; Major, D. T.; Gakhar, L.; Kohen, A.; Cheatum, C. M. Oscillatory Active-Site Motions Correlate with Kinetic Isotope Effects in Formate Dehydrogenase. *ACS Catal.* **2019**, *9* (12), 11199–11206.

(221) Ranasinghe, C.; Guo, Q.; Sapienza, P. J.; Lee, A. L.; Quinn, D. M.; Cheatum, C. M.; Kohen, A. Protein Mass Effects on Formate Dehydrogenase. *J. Am. Chem. Soc.* **2017**, *139* (48), 17405–17413.

(222) Ishikawa, H.; Kim, S.; Kwak, K.; Wakasugi, K.; Fayer, M. D. Disulfide Bond Influence on Protein Structural Dynamics Probed with 2D-IR Vibrational Echo Spectroscopy. *Proc. Natl. Acad. Sci.* **2007**, *104* (49), 19309–19314.

(223) Ishikawa, H.; Finkelstein, I. J.; Kim, S.; Kwak, K.; Chung, J. K.; Wakasugi, K.; Massari, A. M.; Fayer, M. D. Neuroglobin Dynamics Observed with Ultrafast 2D-IR Vibrational Echo Spectroscopy. *Proc. Natl. Acad. Sci.* **2007**, *104* (41), 16116–16121.